

Development of Nickel-Titanium Based Shape Memory Alloy Actuators with Bespoke Thermo-Mechanical Action

A thesis submitted in fulfilment of the requirements for the degree of

Doctor of Philosophy (PhD)

from Dublin City University

School of Mechanical and Manufacturing Engineering

By

Josephine Ryan Murphy

December 2025

Supervisors

Prof. Dermot Brabazon

Dr Inam Ul Ahad

Declaration

I hereby certify that this material, which I now submit for assessment on the program study leading to the award of Ph.D. is entirely my own work, and that I have exercised reasonable care to ensure that the work is original and have conformed to the regulations on the use and declaration of Generative AI, and does not to the best of my knowledge breach any law of copyright, and has not been taken from the work of others save and to the extent that such work has been cited and acknowledged within the text of my work. I hereby certify that no Generative Artificial Intelligence (Gen AI) tools have been used in the creation of the thesis.

Signed: Josephine Ryan Murphy ID No.: 21266615 Date: 04/12/2025

Acknowledgements

This thesis, and the four years spent completing it, were made possible by the colleagues, family, friends, and pets who joined me along the way. I am forever grateful to every one of them.

To my supervisors, Dermot Brabazon and Inam Ul Ahad, who guided me through the last four years, thank you for your consistent patience and kindness.

To my manager, Joan Kelly, who was always around for a coffee, a chat, and a pep talk whenever it was needed, thank you for everything you do.

To my parents, Mary and Eamonn, who have always done everything they could to help me achieve anything I have ever wanted, without you none of this would have been possible.

To my grandparents, Nora and Phil, who have always believed in me, supported me, and had a place for me in their home, I am very lucky to have you both.

To my aunty Ita, who paved the way and has been a constant source of guidance and support throughout my life, thank you for always being there for me.

To my wonderful friends, too many to name, who were with me through every meltdown and milestone, I am who I am because of you.

To my beautiful cat Sheba, who was by my side through everything, I love you, and I wish you were here for what comes next.

Table of Contents

Abstract 1

Chapter 1: Introduction 2

1.1. Background and Motivation 2

1.2. Thesis Aims and Objectives 5

1.3. Thesis Format and Outline 6

Chapter 2: Literature Review 9

2.1. Crystal Phases 9

2.2. The Shape Memory Effect & Super Elasticity 10

2.3. The Martensitic Transformation 11

2.4. The R-Phase 13

2.5. Precipitates 15

2.5.1. Precipitates in Ni-rich NiTi 17

2.5.2. Precipitates in Ti-rich NiTi 20

2.6. Manufacturing of NiTi 21

2.6.1. Traditional Manufacturing 22

2.6.2. Additive Manufacturing 24

2.7. Shape Memory Alloy Actuators 27

2.7.1. NiTi Actuator Classification 28

2.7.2. Limitations 30

2.8. Summary of Existing Knowledge 31

Chapter 3: Effect of Heat Treatment Time and Temperature on the Microstructure and Shape Memory Properties of Nitinol Wires 34

3.1. Introduction 35

3.2. Materials and Methods 40

3.2.1. Heat treatment of nitinol wires 40
3.2.2. Metallography 42
3.2.3. Density 42
3.2.4. Differential Scanning Calorimetry 43
3.2.5. Vickers Microhardness 43
3.2.6. Displacement Experiment of Heat-Treated Nitinol Wires 43
3.2.7. Recovery Strain of Heat-Treated Nitinol Wires 44
3.3. Results 45
3.3.1. Effect of Heat Treatment on Density 45
3.3.2. Effect of Heat Treatment on Microstructure 47
3.3.3. Effect of Heat Treatment on the Phase Transformation Temperatures 48
3.3.4. Effect on Hardness Due to the Heat Treatment Process 48
3.3.5. Loss of Actuation Angle for the Nitinol Wires 48
3.3.6. Recovery Strain of the Heat-Treated Nitinol Wires 50
3.4. Discussion 51
3.5. Conclusions 54
Chapter 4: Investigating the Effect of Wire Drawing and Heat Treatment on the Response of $Ni_{50.9}Ti_{49.1}$ R-phase Actuators 57
4.1. Introduction 58
4.2. Materials and Method 61
4.2.1. Materials and Sample Preparation 61
4.2.2. Heat Treatment and Shape Setting 61
4.2.3. Stroke and Actuation Time 63
4.2.4. Material Characterisation 65
4.3. Results & Discussion 68

4.3.1. Effect of Low Temperature Aging on Actuator Stroke 68
4.3.2. Effect of Low Temperature Aging (350°C to 450°C) on Actuation Time 69
4.3.3. Phase Transformation Temperatures and DSC Results 72
4.3.4. Phase and Microstructure Analysis 78
4.3.5. Mechanical Properties 79
4.4. Conclusions 83
Chapter 5: Effect of PBF-LB Process Parameters and Strut Diameter on the Microstructure and Phase Transformation Behaviour of Ti-rich Nitinol Lattice Structures 86
5.1. Introduction 87
5.2. Materials and Method 89
5.2.1. Model Configuration & Dimensions 89
5.2.2. Material & Fabrication 91
5.2.3. Design of Experiment (DoE) 91
5.2.4. Material Characterisation 91
5.3. Results 93
5.3.1. Input-Output Correlations 93
5.3.2. Relative Density 94
5.3.3. Microstructure 94
5.3.4. Phase Analysis 98
5.3.5. Composition 99
5.3.6. Phase Transformation Characteristics 99
5.4. Discussion 105
5.4.1. Effect of powder composition 105
5.4.2. Effect of Strut Diameter 106
5.4.3. Effect of VED 109

5.5. Conclusions 112

Chapter 6: Investigating the Effect of VED and Lattice Strut Diameter on the Shape Memory Effect of Nitinol Actuators 114

6.1. Introduction 115

6.2. Materials and Method 117

6.2.1. Model Configuration & Dimensions 117

6.2.2. Material & Fabrication 117

6.2.3. Design of Experiment (DoE) 118

6.2.4. Material Characterisation 119

6.2.5. Mechanical Characterisation 120

6.3. Results 121

6.3.1. Input-Output Correlations 121

6.3.2. Material Characterisation 122

6.3.3. Mechanical Testing 126

6.4. Discussion 133

6.4.1. Material Characterisation 133

6.4.2. Stress-Strain Response 135

6.4.3. Shape Memory Response 137

6.5. Conclusions 139

Chapter 7: Conclusions and Future Work 141

7.1. Research Summary 141

7.2. Future work 145

List of Figures

Figure 1: Crystal structure of the NiTi (a) austenite and (b) martensite phases [218]. 9
Figure 2: Stress-strain-temperature graph for NiTi showing the SME and SE [19]..... 12
Figure 3: The symmetric case: a) schematic of the Gibbs free energy curves with black dotted line showing the path on heating and the solid black line showing the path on cooling, b) schematic of the corresponding idealised transformation strains, and c) corresponding DSC curves. [44] 15
Figure 4: The asymmetric case: a) schematic of the Gibbs free energy curves with black dotted line showing the path on heating and the solid black line showing the path on cooling illustrating that R does not have the lowest energy at any temperature, b) schematic of the corresponding idealised transformation strains, and c) corresponding DSC curves. [44] ... 16
Figure 5: Nickle-titanium phase diagram with the intermetallic NiTi phase highlighted [16]. 17
Figure 6: a) Section of the nickel-titanium phase diagram showing the region in which nitinol is stable and b) Time Temperature Transformation diagram of a $Ni_{52}Ti_{48}$ alloy [16]. 18
Figure 7: Fabrication methods for the manufacturing of NiTi [218]. 22
Figure 8: Forming methods of NiTi [60]. 24
Figure 9: Schematic of the PBF-LB process illustrating the process parameters laser power (P), scan speed (v), hatch spacing (h), and layer thickness (t) [50]. 26
Figure 10: Schematic of the linear electrical actuator system composed of an SMA spring and harmonic steel spring showing the motion of the actuator [43]. 29
Figure 11: Schematic of the cryogenic thermal switch (a) the open position and (b) the closed position. [88] 29
Figure 12: The illustration of the shape memory effect in NiTi alloy is depicted through stress, strain, and temperature variations, adapted from Yuebin Guo et al. [110]. 35
Figure 13: Process Diagram showing the implemented experimental procedure. 41
Figure 14: Schematic of the method used for the displacement and recovery strain experiments. (a) Wire and mandrel before deformation, (b) deformation of wire around mandrel, (c) wire after it has been released from the mandrel, (d) wire after controlled heating. 44

Figure 15: Density measurements (black squares) of all heat-treated nitinol samples, n = 3. 46
Figure 16: SEM image and EDX mapping of the surface of the as-received wire..... 47
Figure 17: (a) The A_f phase transformation temperatures of the wire samples (n = 2), and DSC heating curves (orange line) and cooling curves (blue line) of samples treated (b) at 400 °C for 30 min, (c) at 450 °C for 30 min, and (d) at 500 °C for 30 min. 49
Figure 18: Vickers microhardness test results for as-received and heat-treated samples, n = 5. 50
Figure 19: Loss of actuation angle from desired shape (°) for the heat-treated samples. 51
Figure 20: Recovery strain values for the heat-treated samples, n=3..... 52
Figure 21: Schematic of in-house designed and built actuator testing rig. 65
Figure 22: (a) Plot of the displacement, temperature, current, and t_1 from the LabVIEW data for sample 1. (b) plot of the original displacement, the smoothed displacement, the slope of the smoothed displacement and t_2..... 66
Figure 23**:** Graph of the average maximum stroke recorded from the heat-treated samples, n = 3..... 70
Figure 24: Graph of the actuation time and stroke for a) W1, b) W2, and c) W3 achieved by heat-treated samples, n = 3. 70
Figure 25: Thermal images (°C) and actuation timestamps (seconds) of sample 26 showing the effect over time of the current applied across the wire on the shape memory effect and temperature of the wire itself. 71
Figure 26: DSC curves of the as-received and untreated wires W1, W2, and W3 with a) heat flow vs temperature and d) heat flow vs time; S1, S4, and S7 with the same starting wire (W1) and heat treatment time (30 min) and different heat treatment temperatures of 350 °C, 400 °C, and 450 °C, respectively with b) heat flow vs temperature and e) heat flow vs time; S7, S8, and S9 with the same starting wire (W1) and heat treatment temperature (450 °C) and different heat treatment times of 30, 60, and 90 minutes respectively with c) heat flow vs temperature and f) heat flow vs time..... 74
Figure 27: Graph of the a) B19' start temperature, b) B2 finish temperature and c) R-phase finish temperature, n = 3..... 76

Figure 28: Graph of a) B2-B19' thermal hysteresis and b) B2-R thermal hysteresis of the as received and heat-treated samples calculated from DSC, n = 3. 78
Figure 29: XRD patterns showing the presence of the austenite, martensite, and R-phase in (a) W1, W2, and W3 before heat treatment with sample 6 (W1, 400 °C, 90 min) as a control, (b) samples 1-3 (W1, 350 °C, for 30, 60, and 90 minutes respectively) with sample 6 as a control, (c) sample 4-6 (W1, 400 °C, for 30, 60, and 90 minutes respectively), and (d) samples 7-9 (W1, 450 °C, for 30, 60, and 90 minutes respectively) with sample 6 as a control. 79
Figure 30: Hardness maps illustrating the measured nano hardness values at each of the 400 indentation points on each sample (a) W1 (as-received), (b) W2 (as-received), (c) W3 (as-received), (d) S3 (W1, 350 °C, 90 min), (e) S12 (W2, 350 °C, 90 min), (f) S21 (W3, 350 °C, 90 min), (g) S8 (W1, 450 °C, 60 min), (h) S17 (W2, 450 °C, 60 min), and (i) S26 (W3, 450 °C, 60 min). 84
Figure 31: CAD models of the NiTi lattice structures showing build direction, end plates, support structures, and removable pillars for DSC tests with strut diameters of a) 0.5 mm, b) 1.0 mm, and c) 1.5 mm. 90
Figure 32: (a) Scatter Plot of relative density with VED showing 95 % confidence intervals. Surface contours show the effect of the relationship between laser power and scan speed on the relative density for (b) $L_{0.5}$, (c) $L_{1.0}$, and (d) $L_{1.5}$. 95
Figure 33: SEM images show the effect of VED on the porosity of the part in the $L_{1.0}$ lattices. (a) sample 4: scan speed = 1200 mm/s, laser power = 150 W; (b) Sample 7: scan speed 800 mm/s, laser power = 175 W; (c) Sample 14: scan speed = 400 mm/s, laser power = 200 W. 97
Figure 34: BSEM images showing the grain morphology of (a) sample 4 and (b) sample 14. 98
Figure 35: SXRD reflections at low, mid, and high VED for (a) the $L_{0.5}$ lattices, (b) the $L_{1.0}$ lattices, and (c) the $L_{1.5}$ lattices. 100
Figure 36: (a) Bar chart of Ni loss showing 95 % confidence intervals. Surface contours showing the relationship between laser power and scan speed on the Ni loss for the (b) $L_{0.5}$, (c) $L_{1.0}$, and (d) $L_{1.5}$ lattices. 101
Figure 37: DSC curves of a) the as-received powder and DSC plots comparing the number of peaks with the VED for b) $L_{0.5}$, c) $L_{1.0}$, and d) $L_{1.5}$ 102

Figure 38: (a) Scatter plot of A_f with VED. Surface contours showing the effect of the relationship between laser power and scan speed on A_f for (b) $L_{0.5}$, (c) $L_{1.0}$, and (d) $L_{1.5}$...103
Figure 39: (a) Bar chart of thermal hysteresis (η) and surface Contours showing the effect of the relationship between laser power and scan speed on η for the (b) $L_{0.5}$, (c) $L_{1.0}$, and (d) $L_{1.5}$ lattices. 104
Figure 40: Enthalpy of the cooling ($\Delta H_{Cooling}$) and heating transformation ($\Delta H_{Heating}$), and enthalpy ratio (TEr) of the powder and PBF-LB samples. 106
Figure 41: CAD models of the NiTi lattice structures showing build direction, end plates, support structures, and removable pillars for DSC tests with strut diameters of a) 0.5 mm, b) 1.0 mm, and c) 1.5 mm. 118
Figure 42: a) Graph of the typical stress-strain response during the compression and heating cycles illustrating applied strain (εa), true strain (εt), elastic strain (εe), SME recovered strain (εSME), and residual strain (εr). b) Plot of the typical sample response during heating showing the sample displacement from DIC, sample temperature captured by thermal camera, with the time when the heat gun is switched on (t_1) and when actuation is complete (t_2). 121
Figure 43: SEM images showing density and porosity defects for the $L_{1.0}$ at a) low b) mid c) and high VEDs. d) Scatter Plot of relative density with VED showing 95 % confidence intervals. 123
Figure 44: Surface Contours showing the effect of the relationship between laser power and scan speed on the relative density for a) $L_{0.5}$, b) $L_{1.0}$, and c) $L_{1.5}$. 124
Figure 45: DSC curves of a) the as-received powder and DSC plots comparing the peaks with the VED for b) $L_{0.5}$, c) $L_{1.0}$, and d) $L_{1.5}$. 125
Figure 46: Surface contours of A_f temperature, Ni Loss, and thermal hysteresis of the $L_{0.5}$, $L_{1.0}$, and $L_{1.5}$ lattices. 127
Figure 47: Stress-strain response at applied compressive strains of 4 %, 8 %, 12 %, and 16 % for a) the $L_{0.5}$ lattices, b) the $L_{1.0}$ lattices, and c) the $L_{1.5}$ lattices. 129
Figure 48: Bar charts of the SME response showing ε_e, ε_{SME}, and ε_r for applied strains a) 4 %, b) 8 %, c) 12 %, and d) 16 %. 131
Figure 49: Graph comparing the recovery ratio of the lattice samples at each applied strain level. 132

Figure 50: Stroke achieved at applied compressive strains of 4 %, 8 %, 12 %, and 16 % for a) the $L_{0.5}$ lattices, b) the $L_{1.0}$ lattices, and c) the $L_{1.5}$ lattices.....133
Figure 51: Thermal images comparing rate at which the temperature of the $L_{0.5}$, $L_{1.0}$, and $L_{1.5}$ lattices increases with the application of a heat gun for the first 80 s of heating.....134

List of Tables

Table 1: Heat treatment process parameters applied to the nitinol wires..... 41
Table 2: Chemical composition of as-received and heat-treated nitinol wires 47
Table 3: DoE model of three parameters at three levels. 62
Table 4: Full table of the 27 process parameters used in this study..... 62
Table 5: Average elastic modulus (E) and hardness (H) calculated from nano-indentation results, n = 400..... 83
Table 6: Lattice Configuration & Dimensions 90
Table 7: Full DoE of strut diameter, laser process parameters, and resulting VED for the produced NiTi samples..... 91
Table 8: P-values of the relevant input-output correlations..... 93
Table 9: Lattice Configuration & Dimensions 117
Table 10: Full DoE of strut diameter, laser process parameters, and resulting VED for the produced NiTi samples.....119
Table 11: P-values of the relevant input-output correlations. 121
Table 12: Ultimate values for the $L_{0.5}$ lattices. 128
Table 13: Ultimate values for the $L_{1.0}$ lattices. 128
Table 14: Ultimate values for the $L_{1.5}$ lattices. 129
Table 15: Average strain values of the repetition samples with 95 % confidence intervals; strut diameter of 1.0 mm; scan speed of 800 mm/s; and laser power of 175 W. 131
Table 16: Table showing the actuation time of the lattice samples during the 12 % compression and heating cycle.....133
Table 17: Table summarising the maximum Rρ, σU, recovery ratio, and minimum actuation time recorded for the $L_{0.5}$, $L_{1.0}$, and $L_{1.5}$ lattices and their corresponding VED.....138

List of Publications

Josephine Ryan Murphy, Neha Agarwal, Hashemi, Theo Mossop, Darragh O'Neill, John Power, Ali Shayegh, and Dermot Brabazon. Effect of Heat Treatment Time and Temperature on the Microstructure and Shape Memory Properties of Nitinol Wires. Materials, *2023*, *16*, 6480.

Josephine Ryan Murphy, Inam Ul Ahad, Dermot Brabazon. Investigating the Effect of Printing Process Parameters on the Shape Memory Effect of Nitinol Actuators. Shape Memory and Superelastic Technologies, *2024*, *13*.

Josephine Ryan Murphy, Muhannad A. Obeidi, Inam Ul Ahad, Dermot Brabazon. Investigating the Effect of Wire Drawing and Heat Treatment on the Response of Ni50.9Ti49.1 R-phase Actuators. Materials, *2025, 18,* 4931.

Josephine Ryan Murphy, Josiah Cherian Chekotu, Paul Healy, and Dermot Brabazon. Investigating the Effect of VED and Lattice Strut Diameter on the Shape Memory Effect of Nitinol Actuators. Journal of Materials Research and Technology, *2025, 17*.

Josephine Ryan Murphy, Nicole Church, Nicholas Jones, Paul Healy, and Dermot Brabazon. Effect of PBF-LB Process Parameters and Strut Diameter on the Microstructure and Phase Transformation Behaviour of Ti-rich Nitinol Lattice Structures. Progress in Additive Manufacturing, *2026.*

List of Oral Presentations

Josephine Ryan Murphy, Inam Ul Ahad, and Dermot Brabazon, "Investigating the effect of heat treatment parameters on nitinol actuator response", Mini Project Symposium, 21st April 2022, University of Sheffield, Sheffield, UK

Josephine Ryan Murphy, Muhannad Ahmed Obeidi, Inam Ul Ahad, and Dermot Brabazon, "Additive Manufacturing of Innovative Nickel-Titanium Based Shape Memory Alloy Actuators with Bespoke Mechanical Action at Specific Temperatures", IForm 4 Year Review, 13th June 2022, Dublin, Ireland

Josephine Ryan Murphy, Muhannad Ahmed Obeidi, Inam Ul Ahad, and Dermot Brabazon, "Investigating the Effect of Heat Treatment on the Shape Memory Effect of Superelastic Electro-Mechanical Nitinol Actuators", AMSCDT Student Conference, 18-19th July 2023, University of Sheffield, Sheffield, UK

Josephine Ryan Murphy, Muhannad Ahmed Obeidi, Inam Ul Ahad, and Dermot Brabazon, "Investigating the Effect of Heat Treatment on the Shape Memory Effect of Superelastic Electro-Mechanical Nitinol Actuators", AMPT Conference, 13-16th July 2023, Kuala Lumpur, Malaysia

Josephine Ryan Murphy, Paul Healy, and Dermot Brabazon, "Investigating the Effect of LPBF Process Parameters and Lattice Strut Diameter on the SME of Nitinol Actuators" SMST Conference, 6-10th May 2024, Cascais, Portugal

List of Poster Presentations

Josephine Ryan Murphy, Inam Ul Ahad, and Dermot Brabazon, "Investigating the Effect of Heat Treatment on Nitinol Actuator Response", AMSCDT student conference, 11-12th July 2022, Dublin City University, Dublin, Ireland

Josephine Ryan Murphy, Paul Healy, and Dermot Brabazon, "Additive Manufacturing of NiTi Shape Memory Alloy Actuators: The Effect of VED & Lattice Strut Diameter", I-Form Gathering, 3-4th December 2024, Athlone, Ireland

Josephine Ryan Murphy, Nicole Church, Paul Healy, and Dermot Brabazon, "Additive Manufacturing of NiTi SMA Actuators: The Effect of VED & Lattice Strut Diameter", SMST Conference, 22nd May 2025, Galway, Ireland

Nomenclature

$\Delta H_{Cooling}$ = Enthalpy of cooling

$\Delta H_{Heating}$ = Enthalpy of heating

ε = Strain

ε_a = Applied strain

ε_e = Elastic strain

ε_r = Residual strain

ε_{SME} = SME recovered strain

ε_t = True strain

ε_U = Ultimate strain

η = Thermal hysteresis

η_M = Austenite to martensite thermal hysteresis

η_R = Austenite to R-phase thermal hysteresis

ν_s = Poissons ratio of NiTi

ν_i = Poissons ratio of Berkovich indenter

σ = Stress

σ_U = Ultimate stress

A_f = Austenite finish temperature

A_{f0} = Active austenite finish temperature

A_p = Austenite peak temperature

A_s = Austenite start temperature

E = Elastic modulus

E_r = Reduced modulus

E_i = Elastic modulus of the Berkovich indenter

H = Hardness

H = Hatch spacing

k = Stiffness

$L_{0.5}$ = 0.5 mm strut diameter lattice

$L_{1.0}$ = 1.0 mm strut diameter lattice

$L_{1.5}$ = 1.5 mm strut diameter lattice

M_f = Martensite finish temperature

M_p = Martensite peak temperature

M_s = Martensite start temperature

P_{max} = Maximum indentation load

p = Laser power

R = Radius of curvature

R_ρ = Relative density

R_{cf} = Cooling R-phase finish temperature

R_{cp} = Cooling R-phase peak temperature

t = Layer thickness

t_a = Actuation time

TEr = Enthalpy ratio

v = Scan speed

Abstract

Nitinol presents a compelling alternative to conventional actuation systems. Its unique shape memory effect (SME), combined with a high force-to-mass ratio, low stiffness, and high corrosion resistance, makes it particularly attractive for aerospace and automotive applications. In contrast, conventional actuation systems such as pneumatic or hydraulic systems are bulky, heavy, requiring assembly and regular maintenance. Nitinol can enable compact, single component solutions that provide silent actuation, lower energy consumption, reduced weight, and minimal maintenance.

Conventionally manufactured nitinol benefits from an established supply chain and reliable processing routes, with wires being among the most common forms. The thermomechanical processing of these wires introduces complex microstructural features that require careful post processing treatments to achieve desired functional properties. Chapter 3 reveals that heat treating NiTi wires between 400 °C and 500 °C results in a decrease of over 18 °C in the transformation temperatures owing to the precipitation of secondary phases. Chapter 4 shows that stroke of a NiTi wire actuator is increased by up to 230 % when aging temperature is increased from 350 °C to 450 °C.

A key limitation of traditionally manufactured nitinol is its poor machinability, which restricts components to simple geometries such as wires, coils, and sheets. This constraint has driven increasing interest into the additive manufacturing (AM) of nitinol. Techniques such as laser powder bed fusion (PBF-LB) allow the fabrication of complex geometries not previously possible as well as providing the opportunity to tailor microstructural and mechanical properties by optimizing processing parameters. Chapter 5 demonstrates that relative densities of 99.4 % can be achieved at VEDs of 42 J/mm^3 while chapter 6 demonstrates that stroke increases by 11.9 % when VED is decreased from 83 J/mm^3 to 21 J/mm^3 in PBF-LB lattice structures.

A significant gap remains in the literature concerning the effects of conventional and AM processing on the thermo-mechanical response of nitinol. This thesis focuses on filling this gap in knowledge. The effect of PBF-LB process parameters on the material properties of

martensitic nitinol and its shape memory response are evaluated and presented. By gaining a deeper understanding of how PBF-LB process parameters influence the final properties of nitinol actuators, it becomes more possible to engineer light-weight, low-maintenance actuators capable of replacing traditional actuation systems. Actuators are integral to countless systems, and such advancements could significantly reduce energy and fuel consumption during both the manufacture and operational lifetime particularly of critical industrial, aerospace, bioengineering, and automotive actuators.

Chapter 1: Introduction

1.1. Background and Motivation

It is predicted that between 2025 and 2044, global demand will reach approximately 43,420 new passenger and freighter aircraft [1]. In 2022 airlines and manufacturers agreed to an international goal of achieving net-zero CO_2 emissions by 2050. Projected emissions from the delivery of these new aircraft is expected to completely deplete the net-zero aviation budget by 2032, highlighting the need for substantial fuel efficiency improvements in new aircrafts [2]. The CO_2 emissions associated with producing these aircraft, together with the expansion of commercial space flights, drone delivery services, and thousands of satellite launches, pose a major risk to an already critical climate crisis. Achieving meaningful reductions in lifecycle emissions will therefore require innovations not only in propulsion systems and fuels, but also in aircraft materials, structures, and actuation technologies that can reduce weight, improve efficiency, and minimise resource consumption.

Among the advanced material systems being investigated for lightweight and energy-efficient engineering applications, shape memory alloys (SMAs) have attracted considerable attention. These are a unique class of materials that exhibit properties known as superelasticity (SE) and the shape memory effect (SME). The shape memory effect (SME) arises from a reversible solid-state phase transformation between martensite and austenite phases. Following deformation in the martensitic state, the material can recover its original shape upon heating through the transformation temperature range. These materials are capable of converting thermal energy directly into mechanical motion, enabling compact actuator systems with reduced complexity compared with conventional hydraulic and

pneumatic technologies [3][4]. Although the SME property can be found in alloys such as Cu-Al-Ni, Fe-Mn-Si, and Cu-Zn-Al, nickel-titanium (NiTi) has emerged as the most widely used. This is due to the superior mechanical properties including high wear resistance, excellent corrosion resistance, and biocompatibility. In addition, NiTi exhibits good cycling stability, large recoverable strains, good ductility, and response to thermal stimuli, qualifying NiTi as a suitable material for actuators and sensing elements [5][6].

Conventional hydraulic and pneumatic actuators are frequently bulky, heavy, maintenance-intensive, and often inefficient. In contrast, the high force-to-mass ratio of NiTi and direct actuation of the material itself, with reduced system complexity, offers a significant reduction in size and weight which is particularly advantageous for aerospace and automotive systems where, even modest reductions in component mass can translate into substantial fuel savings over an aircraft's operational lifetime [7]. Consequently, replacing conventional actuation systems with lightweight SMA-based alternatives offers the potential to reduce both operational emissions and manufacturing-related environmental impacts. NiTi actuators also provide silent, clean, low energy, and low-maintenance operation [8]. Replacing complex bulky actuation setups with compact SMA components reduces not only system weight but also material usage, maintenance requirements, waste generation, and associated emissions.

While both the shape memory effect (SME) and superelasticity arise from the reversible martensitic transformation in NiTi, the majority of published research has focused on superelastic behaviour. This emphasis is driven largely by biomedical applications, such as stents and orthodontic devices, where large recoverable strains at constant temperature are desirable. Consequently, considerable attention has been devoted to understanding the effects of composition, processing, and microstructure on superelastic performance. Comparatively fewer studies have investigated thermally activated shape memory actuation, despite its growing relevance in aerospace, automotive, and robotics applications. Shape memory actuators operate under fundamentally different conditions, requiring precise control of transformation temperatures, actuation strain, recovery stress, cyclic stability, and energy efficiency. As a result, many of the processing–structure–property relationships

established for superelastic NiTi cannot be directly translated to shape memory actuator design, highlighting the need for dedicated investigation of SME-driven systems.

A further limitation within the current body of literature is the separation between materials science and actuator-focused research. Materials science studies typically investigate how composition, thermomechanical processing, heat treatment, and manufacturing parameters influence microstructure and phase transformation behaviour. In contrast, actuator-oriented studies frequently evaluate metrics such as displacement, force output, response time, and cyclic performance, often without establishing direct links to the underlying material characteristics responsible for these behaviours. While both perspectives provide valuable insights, relatively few studies integrate the relationships between processing conditions, microstructure, transformation characteristics, and actuator performance within a single framework. This disconnect limits the development of predictive design methodologies and hinders the optimisation of NiTi actuators for application-specific requirements. Establishing these links is therefore essential for the reliable design and deployment of next-generation NiTi actuator systems.

At present, one of the main processing routes for NiTi actuators is ingot metallurgy, where ingots are hot worked into rods, tubes, or sheets before being laser cut or cold worked into simple geometries such as wires. These conventional routes can introduce limitations including randomly distributed dislocations, heterogeneous microstructures, excessive porosity, and the formation of secondary phases all of which can alter the phase transformation behaviour and actuator performance [9]. While heat treatment can partially mitigate microstructural defects introduced during conventional processing, the poor machinability of NiTi due to its high ductility and work-hardening remains a major obstacle to manufacturing complex actuator geometries. As a result, most commercially available NiTi actuators are limited to relatively simple forms such as wires, springs, and rods [10]. Additive manufacturing (AM), particularly laser powder bed fusion (PBF-LB), offers a potential solution to this challenge by enabling the direct fabrication of geometrically complex components that would be difficult or impossible to produce using conventional methods.

To address this constraint the additive manufacturing, particularly laser powder bed fusion (PBF-LB), of NiTi is of great interest. Additive manufacturing enables the fabrication of complex, lightweight, and application-specific geometries. The final properties of NiTi are greatly influenced by the PBF-LB process parameters which can control the microstructure, phase transformation characteristics, and actuation performance [11]. Additionally, the geometry of the part greatly influences the effect of the PBF-LB process parameters on the part properties. Leveraging geometry specific effects alongside process parameter tailoring could expand the capabilities and reliability of NiTi actuators. Although numerous studies have investigated the influence of individual PBF-LB processing parameters on NiTi microstructure and transformation behaviour, comparatively few have examined the coupled effects of processing conditions and component geometry. The interaction between these factors remains poorly understood, particularly for actuator applications where dimensional accuracy, transformation temperatures, recoverable strain, and cyclic performance are critical. This lack of understanding limits the development of predictive design methodologies and hinders the reliable deployment of additively manufactured NiTi actuators in engineering systems.

This doctoral thesis addresses these challenges through a comprehensive investigation of both conventionally manufactured and additively manufactured NiTi actuators. The research examines the effects of thermomechanical processing and post-ageing heat treatment on the functional behaviour of conventionally produced NiTi wire actuators, while also evaluating the influence of PBF-LB processing parameters and component geometry on the microstructural, thermal, mechanical, and actuation performance of additively manufactured NiTi. By establishing relationships between manufacturing conditions, geometry, and functional response, this work aims to develop performance-optimized NiTi actuators and to expand the fundamental understanding of how process parameters and geometry can be tailored for application-specific requirements.

1.2. Thesis Aims and Objectives

The aim of this thesis was to explore the material behaviour and functional response of both traditionally manufacture and additively manufactured NiTi actuators to enable the design

of bespoke SMA actuators with tailored, application specific properties and design. This aim was achieved through investigations with the following objectives:

1. Investigate the **training of NiTi wires using age heat treatment** on the material properties, transformation temperatures, and shape recovery.
2. Investigate the **thermo-mechanical training and wire drawing history of NiTi** on the material properties, transformation temperatures, and actuator performance by constraining NiTi wires with different processing routes to a mandrel and age heat treating.
3. Assess the effect of PBF-LB process parameters and part geometry on the **material properties and phase transformation characteristics** of NiTi by producing NiTi lattices of different strut thickness at different VEDs.
4. Assess the effect of PBF-LB process parameters and part geometry on the **shape memory properties and actuator performance** of NiTi by producing NiTi lattices of different strut thickness at different VEDs.

1.3. Thesis Format and Outline

This thesis is presented as a collection of published research papers and submitted manuscripts with original contributions. The contribution of the candidate in the publications is as following:

Chapter	Publication Title	Status	Candidate Contribution
3	Effect of Heat Treatment Time and Temperature on the Microstructure and Shape Memory Properties of Nitinol Wires	Published, Materials, 2023	Co-first author, conceptualisation, methodology, formal analysis, investigation, writing – original draft, writing – review and editing
4	Investigating the Effect of Wire Drawing and Heat Treatment on the Response	Published, Materials, 2025	First author, conceptualisation, methodology, formal analysis, validation, data

	of $Ni_{50.9}Ti_{49.1}$ R-phase Actuators		curation, writing – original draft, writing – review & editing;
5	Effect of PBF-LB Process Parameters and Strut Diameter on the Microstructure and Phase Transformation Behaviour of Ti-rich Nitinol Lattice Structures	Published, Progress in Additive Manufacturing, 2026	First author, conceptualisation, methodology, formal analysis, validation, data curation, writing – original draft, writing – review & editing;
6	Investigating the Effect of VED and Lattice Strut Diameter on the Shape Memory Effect of Nitinol Actuators	Published, Journal of Materials Research and Technology, 2025	First author, conceptualisation, methodology, formal analysis, validation, data curation, writing – original draft, writing – review & editing;

This thesis is comprised of 7 chapters, arranged progressively. The following is a brief description of the work performed and/or contents included in each chapter:

Chapter 1: This chapter introduces the topic of this thesis, the aims and objectives, and the structure of the thesis.

Chapter 2: This chapter provides a comprehensive review of the information fundamental to the understanding of the thesis topic as well as a discussion of the current literature providing a summary of the current limitations and existing knowledge gaps.

Chapter 3: This chapter investigates the effect of **heat treatment time and temperature** on the material properties and **shape memory** capabilities of traditionally manufactured **NiTi wires**.

Chapter 4: This chapter investigates the effect of the **thermomechanical route used during the wire drawing process and subsequent heat treatment** and shape setting on the **material properties and shape memory** of R-phase electromechanical actuators

Chapter 5: This chapter investigates the effect of **PBF-LB** process parameters and part geometry on the **microstructure and phase transformation characteristics of lattice structures**.

Chapter 6: This chapter investigates the effect of **PBF-LB** process parameters and part geometry on the **mechanical properties and actuator performance on lattice structures**.

Chapter 7: This chapter summarises the main findings of this original research and suggests future research in this area.

Chapter 2: Literature Review

NiTi is a nickel titanium shape memory alloy (SMA) with near equiatomic composition. SMAs are a class of functional materials that exhibit unique properties, including the shape memory effect (SME) and superelasticity (SE), in response to external stimuli such as thermal, mechanical, and magnetic fields. The SME describes the materials' ability to return to a pre-defined shape after deformation, when heated above the transition temperature of the material. SE refers to the materials' substantial elastic elongation range (≈ 6 to 10%, depending on phase composition and microstructure) compared to that of conventional materials such as stainless steel [5].

2.1. Crystal Phases

NiTi is stable in two main crystal phases, austenite and martensite seen in Figure 1 below. Austenite is the high temperature parent phase, with a high symmetry ordered B2 body centred cubic (BCC) lattice structure. The low temperature martensite phase has a low symmetry B19' monoclinic lattice structure characterised by a herringbone array of needle-like crystals. The martensite phase is stable in two different forms, twinned martensite, and de-twinned martensite. The B2 phase is characterised by high hardness and stiffness while the B19' phase is softer and more ductile. In certain cases, a third crystal phase known as the R-phase is favoured. The R-phase is an intermediate phase with rhombohedral crystal structure [12].

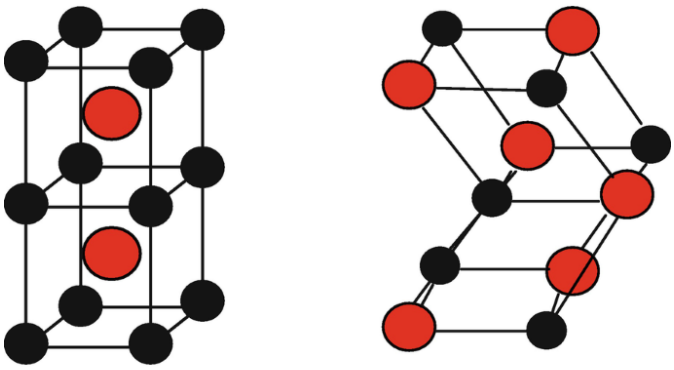


Figure 1: Crystal structure of the NiTi (a) austenite and (b) martensite phases [218].

The phase transformation between phases can be driven by either changes in temperature or stress. In either case the transformation involves a hysteresis, and therefore, there is no single temperature or stress that can define the phase change.

The temperature driven phase transformation can be described by four temperatures. The austenite start temperature (A_s) and the austenite finish temperature (A_f) on heating are the temperature at which the martensite begins to transform to austenite and the temperature at which the martensite has completely transformed to austenite respectively. The martensite start temperature (M_s) and the martensite finish temperature (M_f) on cooling are the temperatures at the austenite begins to transform to martensite, and is completely transformed to martensite, respectively [13].

The stress driven phase transformation is based on the detwinning mechanism. In crystalline solids, there are several irreversible deformation mechanisms including plastic slip and dislocations. However, in SMAs, the deformation mechanism is a reversible crystallographic reorientation between two stable phases resulting in the detwinning of martensite twins. Detwinning is a mode of plastic deformation where the twin boundaries in martensite readily shift, resulting in the twins reorienting to align preferentially along the direction that accommodates the applied stress most effectively [14][15]. In alloys without SME, martensitic transformation is not generally reversible, as the high mechanical stresses induced by the martensite transformation usually results in irreversible dislocation slips. In SMAs however, these stresses result in the detwinning process.

In both cases the transformation between phases is a diffusionless solid-state transformation meaning the only change that takes place is in the crystal structure allowing a reversible phase transformation [16][17]. This is the basis for the SME and SE in NiTi.

2.2. The Shape Memory Effect & Super Elasticity

The SME is activated via a temperature-driven transformation occurring over a range of temperatures. From Figure 2, when the temperature is below M_f the material is in the twinned martensite phase (point A). When a stress is applied to NiTi below M_f, the detwinning mechanism takes place, and twinned martensite orients to detwinned martensite (point B). When the stress is removed, some elastic recovery occurs resulting in

reoriented detwinned martensite (point C). When heated above A_s, the detwinned martensite begins to transform into austenite, causing the material to begin recovering its original shape. When the temperature reaches A_f, the martensite is entirely replaced by austenite, and the material has fully recovered the original shape (point D). As the temperature is reduced from M_s to M_f, the reverse transformation occurs, and the material undergoes a full phase transformation from austenite back to twinned martensite while maintaining the original shape (point A) [18].

SE is an isothermal stress induced transformation that occurs when a force is applied at temperatures above A_f. As stress is applied, austenite transforms to stress-induced martensite (point E). As martensite is not stable at higher temperatures, when the stress is removed the martensite immediately transforms back to austenite and the deformation is recovered through superelasticity (point O) [19].

The prevalence of either the SME or SE exhibited by NiTi depends highly on the alloy composition as any deviations in the equiatomic Ni:Ti ratio can significantly affect the transformation temperatures (TTs) of NiTi. For example a variation of 0.1 at.% of Ni can change the TTs by 10 °C or more [20][21]. Due to the lower TTs of Ni compared to TT, Ni-rich NiTi is typically austenitic at room temperature while Ti-rich NiTi is typically martensitic [22] [23]. For this reason, Ni-rich compositions are generally chosen for SE applications such as braces and stents [24], whereas Ti-rich compositions are preferred for SME applications such as sensors and actuators [25].

2.3. The Martensitic Transformation

The martensite phase transformation in NiTi is a reversible crystal reorientation between two phases. In the stress-free case the transformation between martensite and austenite is a thermally driven phase transformation. Thermodynamic equilibrium occurs at the critical temperature (T_0) which corresponds to the intersection between the energy curves for the martensite phase G_M and the austenite phase G_A. The transformation from austenite to martensite occurs when G_M is lower than G_A at a temperature below the T_0. In the absence of stress, the temperature below T_0 at which the transformation occurs is the M_s temperature. The transformation continues as the temperature continues to decrease until reaching the

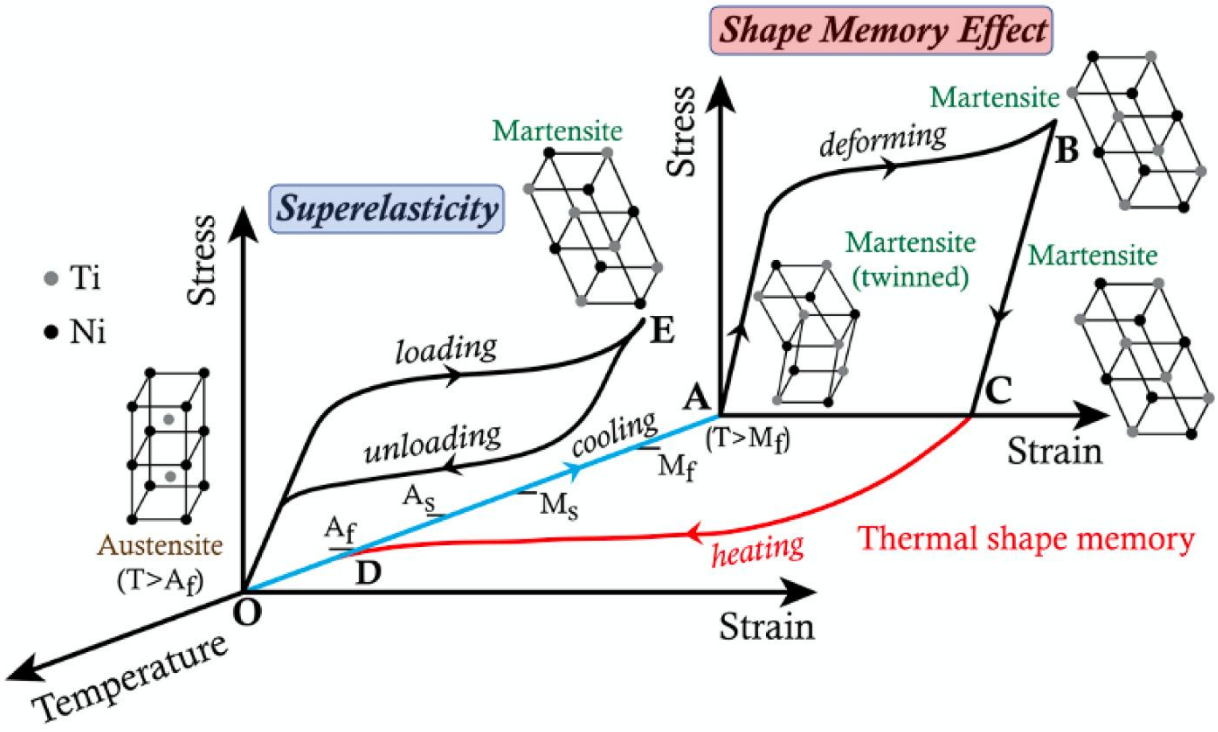


Figure 2: Stress-strain-temperature graph for NiTi showing the SME and SE [19].

M_f temperature. For the reverse stress-free transformation, transformation from martensite to austenite occurs when G_A is lower than G_M at a temperature above T_0, the A_s temperature. The transformation continues as temperature increases until the A_f temperature [26][27].

In the case of stress driven transformations in NiTi, the two main deformation modes in NiTi are twinning and dislocation slip [28]. The stress induced transformation from austenite to martensite is a two-step process that occurs when a load is applied to NiTi in the austenite phase at a critical stress level. This stress level is associated with a stress/strain plateau where stress remains constant as strain increases due to the formation of detwinned martensite accommodating the stress. If the stress is further increased passed the critical stress of the material plastic slip will occur resulting in unrecoverable strains. When the load is removed the martensite transforms back into austenite. This reverse transformation also has an associated stress/strain plateau that occurs at a lower stress than the forward transformation. This difference in the forward and reverse plateau stress is referred to as the stress/strain hysteresis [29]. This is the basis for superelasticity.

A three-step process between twinned martensite, detwinned martensite, and austenite occurs when NiTi is loaded in the martensite phase. When a load is applied to NiTi in the twinned martensite phase a transformation from twinned martensite to detwinned martensite occurs. As the load increases, the volume fraction of detwinned martensite increases until the matrix eventually transforms completely into detwinned martensite. Increasing the load at this stage will elastically deform the NiTi until a critical stress is reached resulting in plastic slip. When heated the strain is recovered as the detwinned martensite transforms into austenite. Shape recovery increases with increasing stress up until this critical stress at which point the strain associated with plastic slip is unrecoverable. To maximise the shape recovery the stress applied should be selected such that the maximum possible strain is induced in the material without inducing plastic slip [30][31].

The martensite transformation and detwinning is strongly influenced by microstructural features such as grains size, stacking-faulty energy, and dislocation density [32]. Even in the case that the applied stress remains below the critical stress for plastic deformation, some irreversible processes inevitable occur during transformation. Local plastic accomodation during transformations still occurs due to transformation-induced defects such as dislocations and leads to macroscopic plastic deformation and martensite stabilization during thermal cycling [33][34]. These small residual strains accumulate over many cycles reducing the strain recovery, leading to variation in transformation thermal and stress hysteresis [35]. Thermo-mechanical treatment can be used to facilitate the formation of stress induced martensite over dislocation slip by increasing the difference between the critical stress required for martensite transformation and for dislocation slip through effects such as grain refinement, coherent nano-precipitation and strain hardening thereby improving the strain recovery [36].

2.4. The R-Phase

NiTi has two distinct crystal structures – a high temperature austenitic phase with BCC crystal structure (B2), and a low temperature martensitic phase with monoclinic lattice structure (B19') [37]. In certain cases, an additional intermediate R-phase with a rhombohedral crystal structure (R) may be present, resulting in a multistep transformation between austenite and martensite [38]. The formation of R-phase during the phase

transformations between austenite and martensite depends on thermodynamic, and kinetic factors. At a given temperature, the formation of NiTi phase is determined by the Gibbs free energy of each phase. The phase with the lowest free energy is thermodynamically favoured. However, for a phase transformation to occur with changing temperature, a kinetic barrier must be overcome to initiate the phase change. The lower the activation energy required for a phase change, the more likely this phase will form during the transformation [39]. Martensite is more stable than the R-phase and is generally thermodynamically preferred however the R-phase has a significantly lower activation energy. Certain factors such as thermal cycling, cold work, ageing, precipitate formation, increasing Ni content above 50%, or the addition of alloying elements such as iron can affect phase stability and Gibbs free energies as well or increase the kinetic energy barrier for martensite formation causing the intermediate R-phase to form [40][41]. The R-phase also possesses unique properties, such as narrow hysteresis and high fatigue life, which are advantageous for certain applications [42].

R-phase transformations typically occur as two stage transformations in one of two ways. In the symmetric case the R-phase has the lowest free energy within a certain temperature range, making it thermodynamically favoured within this range. Additionally, the formation of the R-phase has a lower kinetic barrier compared to the direct transformation to B19', allowing the R-phase to remain stable over a broader thermal range during cooling than heating. Figure 3, shows the symmetric case where on cooling, as shown by the solid black line moving from right to left, the transition from B2 to R begins at the first vertical dotted line, and the transition from R to B19' occurs at the third vertical dashed line. On heating,indicated by the dotted line moving from left to right, the transition from B19' to R starts at the second vertical dashed line, and the transition from R to B2 occurs at the third vertical dashed line.

In the asymmetric case, seen in Figure 4, the transformation is B2 to R to B19' on cooling and B19' directly to B2 on heating. The R-phase is not thermodynamically preferred at any temperature in this scenario. However, the transformation from austenite to martensite involves significant atomic rearrangements and changes in the lattice structure, requiring a large amount of kinetic energy. Conversely, the transformation between austenite and the R-

phase has a lower kinetic barrier due to the rhombohedral structure being closer to that of austenite. This results in a particularly low recovery strain of 0.5%, compared to the 6.5 - 8.5% seen in the martensitic transformation. Therefore, the R-phase forms before B19', until sufficient supercooling allows the formation of B19'. In the reverse transformation, the kinetic barriers to form B2 are overcome before the R-phase can form [43][44].

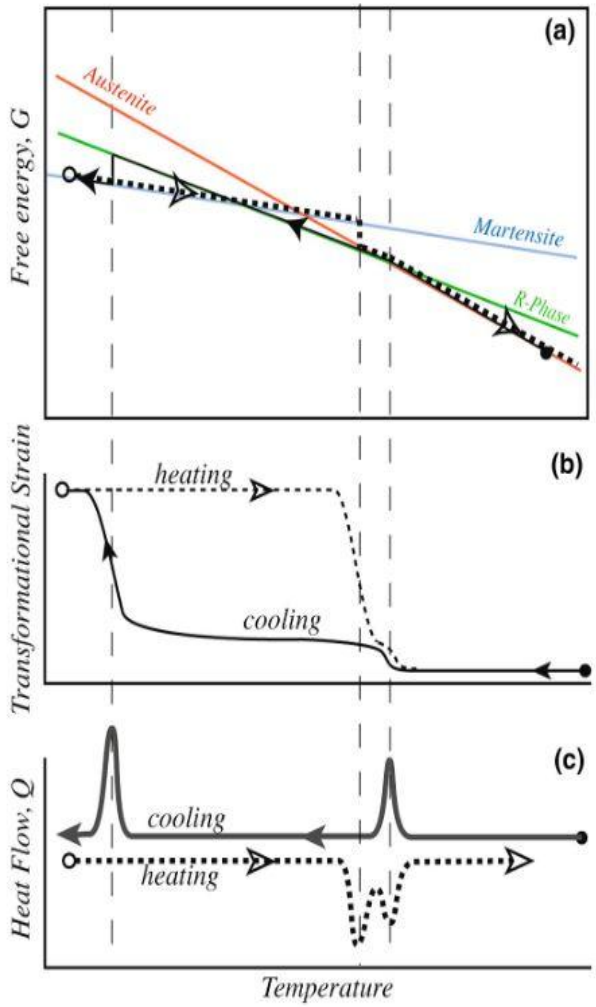


Figure 3: The symmetric case: a) schematic of the Gibbs free energy curves with black dotted line showing the path on heating and the solid black line showing the path on cooling, b) schematic of the corresponding idealised transformation strains, and c) corresponding DSC curves. [44]

2.5. Precipitates

NiTi is an intermetallic phase of the nickel-titanium of near-equiatomic composition. The NiTi phase is stable for a narrow range of compositions as seen in the nickel-titanium phase diagram in Figure 5. For thermodynamically stable conditions, the NiTi phase has a limited

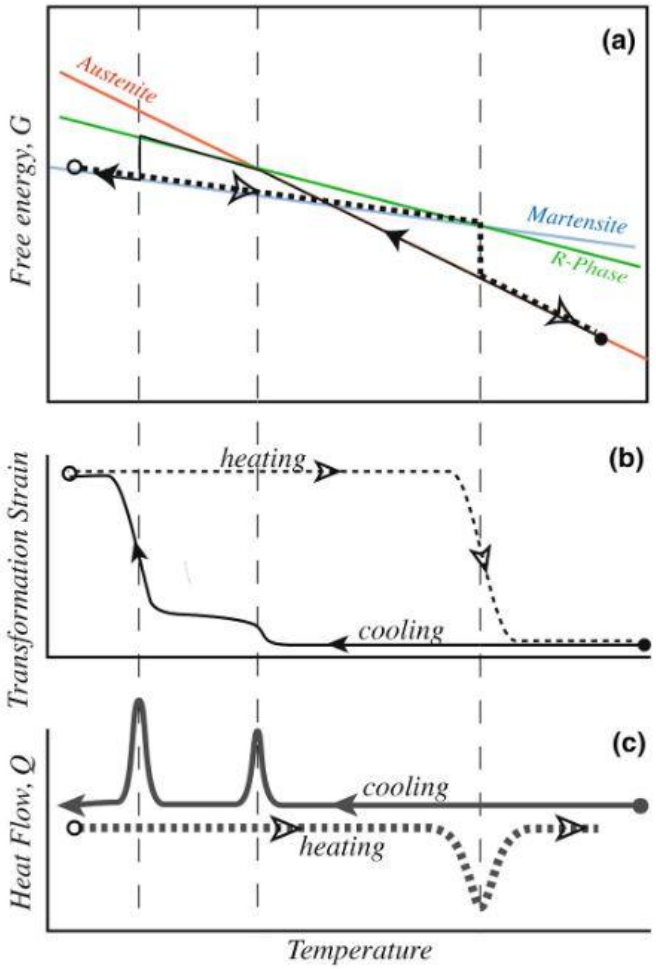


Figure 4: The asymmetric case: a) schematic of the Gibbs free energy curves with black dotted line showing the path on heating and the solid black line showing the path on cooling illustrating that R does not have the lowest energy at any temperature, b) schematic of the corresponding idealised transformation strains, and c) corresponding DSC curves. [44]

range of solubility for titanium with minimum nickel content of approximately 49 at.%. The maximum nickel content of the NiTi phase is 57 at.% at 1118 °C and decreases with temperature increase or decrease [16]. Deviations from this compositional ratio can result in the precipitation of a second phase in the microstructure, significantly altering the alloy's fatigue and functional behaviour [45].

Precipitates are a secondary intermetallic phase that can form within the primary matrix resulting in a microstructure primarily composed of a single phase with small quantities of the secondary phase dispersed throughout the matrix [13]. In the NiTi phase diagram, the boundary for the single-phase Ti-rich region is sharply defined and approaches 50 at.% Ni.

Conversely, towards the Ni-rich side, the solubility of nickel decreases as temperature decreases, leading to a microstructure composed of two phases. Depending on the alloy composition, various secondary phases like Ti_2Ni, Ti_3Ni_4, and Ni_3Ti can form within the microstructure [45]. Thermomechanical processing, cold working, and heat setting are known to induce the nucleation and growth of these precipitate in NiTi [22]. Precipitates can affect the martensite transformation by altering the local composition and inducing coherency stresses which can significantly affect the phase transformation characteristics [27].

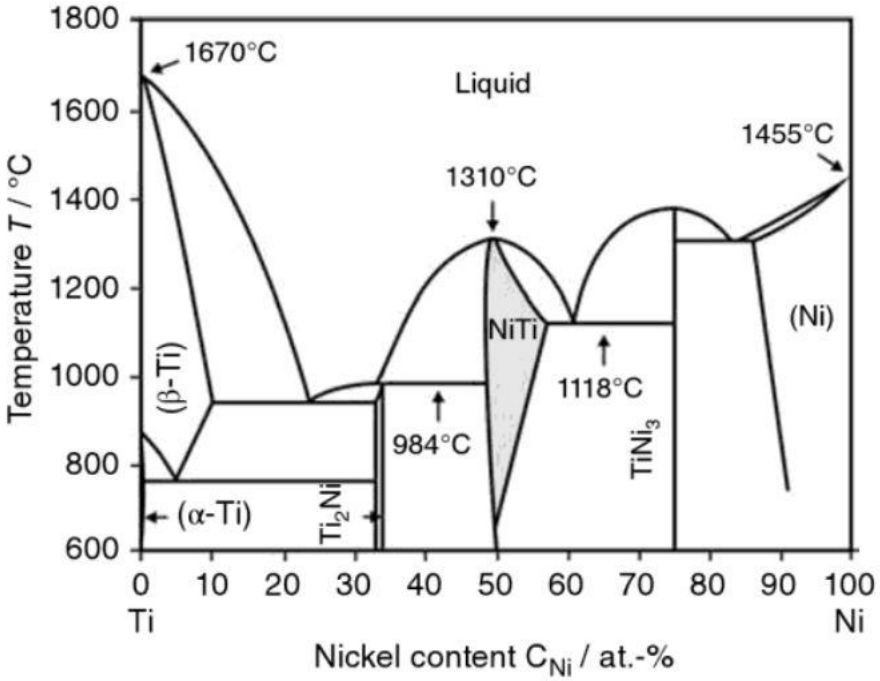


Figure 5: Nickle-titanium phase diagram with the intermetallic NiTi phase highlighted [16].

2.5.1. Precipitates in Ni-rich NiTi

The ageing process in Ni-rich NiTi causes the alloy to form more stable compounds, the nature of which is dependent on the ageing temperature and time. According to the binary phase diagram and precipitation kinetics shown in Figure 6, under lower temperatures (400 °C to 600 °C) and shorter durations, Ni_4Ti_3 forms, and higher temperature and duration leads to the formation of Ni_3Ti_2 precipitates, and at the highest temperatures and ageing durations, Ni_3Ti precipitates form. Ni_4Ti_3 is the most commonly observed precipitate in Ni-rich NiTi alloy. These precipitates strengthen the NiTi matrix and impede dislocation motion

improving SE and increasing yield stress and cycling ability [16] [13]. Ni_4Ti_3 precipitates also affect martensite transformations by increasing the transformation strain from B2 to B19', resulting R-phase transformations as well as increasing the TTs by forming nickel depletion regions in the B2 matrix around the Ni-rich precipitates [46].

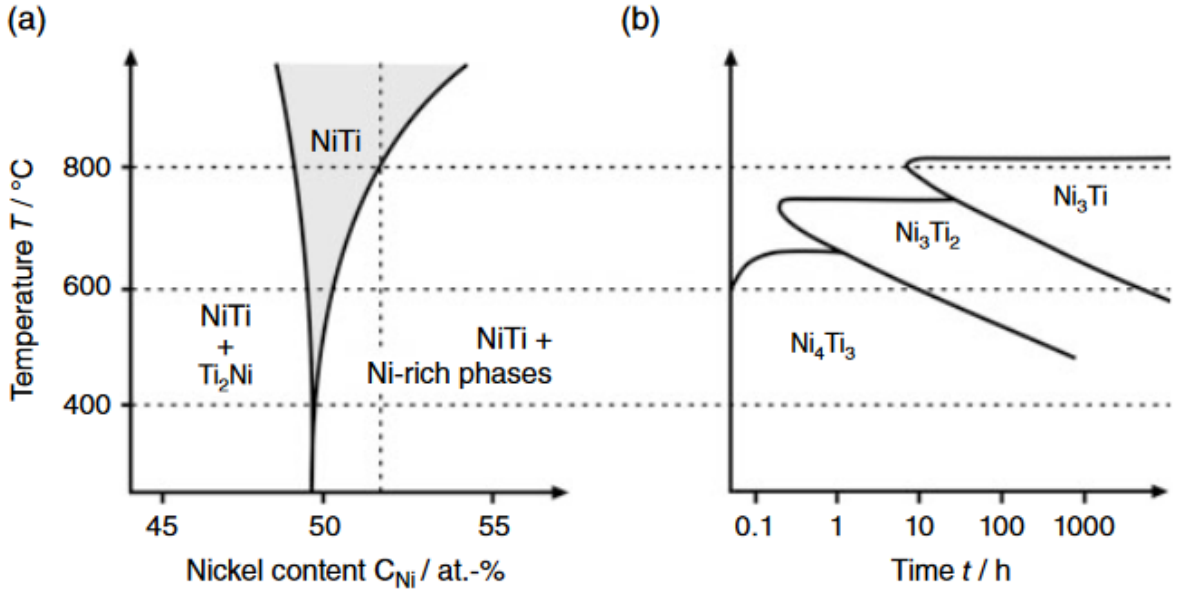


Figure 6: a) Section of the nickel-titanium phase diagram showing the region in which nitinol is stable and b) Time Temperature Transformation diagram of a $Ni_{52}Ti_{48}$ alloy [16].

Yu et al. [47] examined the influence of Ni_4Ti_3 precipitates on the superelasticity of $Ni_{50.8}Ti_{49.2}$ deformed at high strain rates. Hot-rolled rod samples were aged at 500 °C for 1 h, and 550 °C for 1 h and 4.5 h. The results indicated that mechanical properties for high strain rate deformation can be improved by selecting the appropriate ageing treatments. Specifically, strength and superelasticity increased with increasing ageing time and temperature due to the increased volume fraction and size of precipitates impeding dislocation motion and increasing critical shear stress for dislocation slip. In as-received samples, TTs increased after ageing treatment, however, among the aged samples, TTs decreased with ageing temperature due to increased Ni solubility in the matrix and increased with ageing time due to growth of Ni_4Ti_3 precipitates consuming surrounding Ni. All aged samples showed two stage R-phase transformations on heating and a three-stage transformation on cooling. The three-stage transformation is attributed to two different transformations occurring

simultaneously, B2 to B19' and B2 to R to B19', due to inhomogeneity of local stress and composition in the matrix.

Lu et al. [48] investigates the effect of Ni_4Ti_3 precipitates on the stability of SE during compressive loading up to 10 cycles of $Ni_{50.4}Ti_{49.6}$ PBF-LB (laser beam powder bed fusion technique) fabricated samples aged at 350 °C, 450 °C, and 550 °C. This study concluded that the control of Ni_4Ti_3 precipitate formation was crucial for determining the dislocation motion during compressive loading. Ni_4Ti_3 precipitates were more effective for improving the cycling ability than improving the recovery strain of the Ni-rich NiTi alloy. While strain recovery for the first cycle increased with ageing temperature, the best SE stability was observed in samples aged at 350 °C, along with formations of evenly distributed, high-density, relatively small precipitates. The study concluded that 550 °C was above the upper limit temperature for Ni_4Ti_3 precipitates resulting in and uneven distribution of precipitates and the formation of dislocation networks. The A_f temperature decreased with increasing ageing temperature. Samples treated at 350 °C and 450 °C presented intermediate R-phase during heating and cooling, however, the sample heated at 550 °C did not show the presence of R-phase during phase transformation.

In a study by Jiang et al. [49] on the effect of Ni_4Ti_3 precipitates on the microstructural evolution and phase transformation behaviour of $Ni_{50.9}Ti_{49.1}$ samples aged at 300 °C, 450 °C, and 600 °C for 2 hours. The results showed that lower ageing temperatures (300 °C) resulted in small, coherent Ni_4Ti_3 precipitates in the B2 matrix, while intermediate temperatures (450 °C) allowed for a homogeneous distribution of larger coherent precipitates. Higher ageing temperatures (600 °C) led to inhomogeneous precipitate sizes and loss of coherence with the B2 matrix. The A_f temperatures were highest for samples aged at 450 °C due to the homogeneous distribution of precipitates creating Ni-depleted regions throughout the matrix. Samples aged at 600 °C showed a one-stage transformation on heating and a two-stage transformation including the R-phase on cooling. Samples aged at 450 °C showed the two-stage R-phase transformation on heating and cooling, and samples heated at 300 °C showed a two-stage transformation on heating and a three-stage transformation on cooling. The three-stage transformation is attributed to two separate two-stage B2 to R transformations occurring simultaneously, one in the low Ni, high stress region next to the

precipitates and the other in the high Ni, low stress region away from the precipitates, followed by a single R to B19' transformation.

2.5.2. Precipitates in Ti-rich NiTi

The most commonly observed Ti-rich precipitate is Ti_2Ni [50], [51], [52], [53], [54]. The Ti_2Ni precipitate exists mostly in Ti-rich NiTi, and depending on the size and distribution, these Ti_2Ni precipitates may improve the mechanical and SME properties of NiTi. The precipitation of homogeneously distributed nanoscale Ti_2Ni can result in microstructural refinement by separating grain boundaries, thus impeding dislocation movement, however when formed preferentially along grain boundaries, it can also lead to fractures at the early stages of plastic deformation, thereby diminishing the SME performance [55]. The main factors which influence the size, morphology, and distribution of Ti_2Ni precipitates in NiTi are heat treatment, cooling rate during solidification, and thermo-mechanical processing.

Lu et al. [55] shows the effect of heat treatment on the distribution of Ti_2Ni precipitates. The study aims to improve the mechanical and SME properties of $Ni_{49.4}Ti_{50.6}$ fabricated via PBF-LB by introducing a homogeneously distributed nanoscale Ti_2Ni precipitate into the matrix. The study succeeded by solution treatment of the samples at 1000 °C. The alloy exhibited excellent tensile strength of 800 MPa due to precipitation strengthening and work hardening. The alloy had exhibited excellent plasticity with a large elongation of 22.4 % attributed to the homogeneity of the precipitates impeding the propagation of microcracks. The SME properties showed recovery rate of > 98 % and recoverable strain of 5.23 % after 10 cycles owing to the high-density dislocations, nanoscale Ti_2Ni precipitates, and abundant interfaces suppressing dislocation movement and formation of retained martensite.

Bhagyaraj et al. [45] demonstrates the influence of thermo-mechanical processing on the size, morphology, and distribution of Ti_2Ni precipitates in an as-cast NiTi alloy containing precipitates ranging from 1 μm to 10 μm preferentially located along grain boundaries. Hot rolling significantly reduced the size and altered the shape of the precipitates, elongating and fragmenting them into smaller particles oriented in the rolling direction, while maintaining their ductility at 850 °C. Cold rolling, however, resulted in less ductility, fracturing the precipitates into smaller, irregular shapes and causing separation at the precipitate-matrix

interface, forming microcracks and amorphous regions around the precipitates. As cold rolling continued with inter-pas annealing the precipitates became more round in shape and a more refined microstructure was produced. During wire drawing and inter-pass annealing, the stress concentration around Ti_2Ni precipitates caused localized amorphization and microstructural refinement near small particles, while larger particles induced these effects further into the matrix. This non-uniform deformation resulted in a complex structure that, combined with annealing, could lead to a bimodal size distribution of crystallites, significantly impacting the functional characteristics of the shape memory alloy wire.

Based on the NiTi binary phase diagram, a Ti-rich NiTi alloy is expected to form Ti_2Ni precipitates during solidification under equilibrium conditions. Cooling rate has been recognised as a significant factor. In cast Ti-rich NiTi, faster cooling rates typically lead to the formation of larger volume fractions of Ti_2Ni phase, which results in a titanium-deficient matrix phase. In contrast, slower cooling rates result in a lower volume fraction of Ti_2Ni phase and the development of a uniform single-phase martensitic structure [45]. During the PBF-LB process, heating and cooling rates as high as 10^8 K/s occur throughout the alloy during the manufacturing process. Such high cooling rates result in non-equilibrium solidification causing the formation of non-uniform distribution of Ti_2Ni precipitates. In a study by Lu et al. [56] samples printed at lower VEDs had lower cooling rates resulting in a more even distribution of Ti_2Ni precipitates (5 – 10 nm) and high dislocation density. This reduced the formation of dislocation slip leading to better strain recovery and improved strength and ductility by impeding dislocation motion. In contrast samples printed at higher VED has higher cooling rates resulting in inhomogeneous formation of Ti_2Ni (30 – 150 nm) and substantial dislocations along the grain boundary impeding martensite variant reorientation and detwinning, thereby promoting stress concentration, dislocation generation, and microcrack formation.

2.6. Manufacturing of NiTi

NiTi can be fabricated by range of different conventional and additive manufacturing methods which are summarised in Figure 7 below.

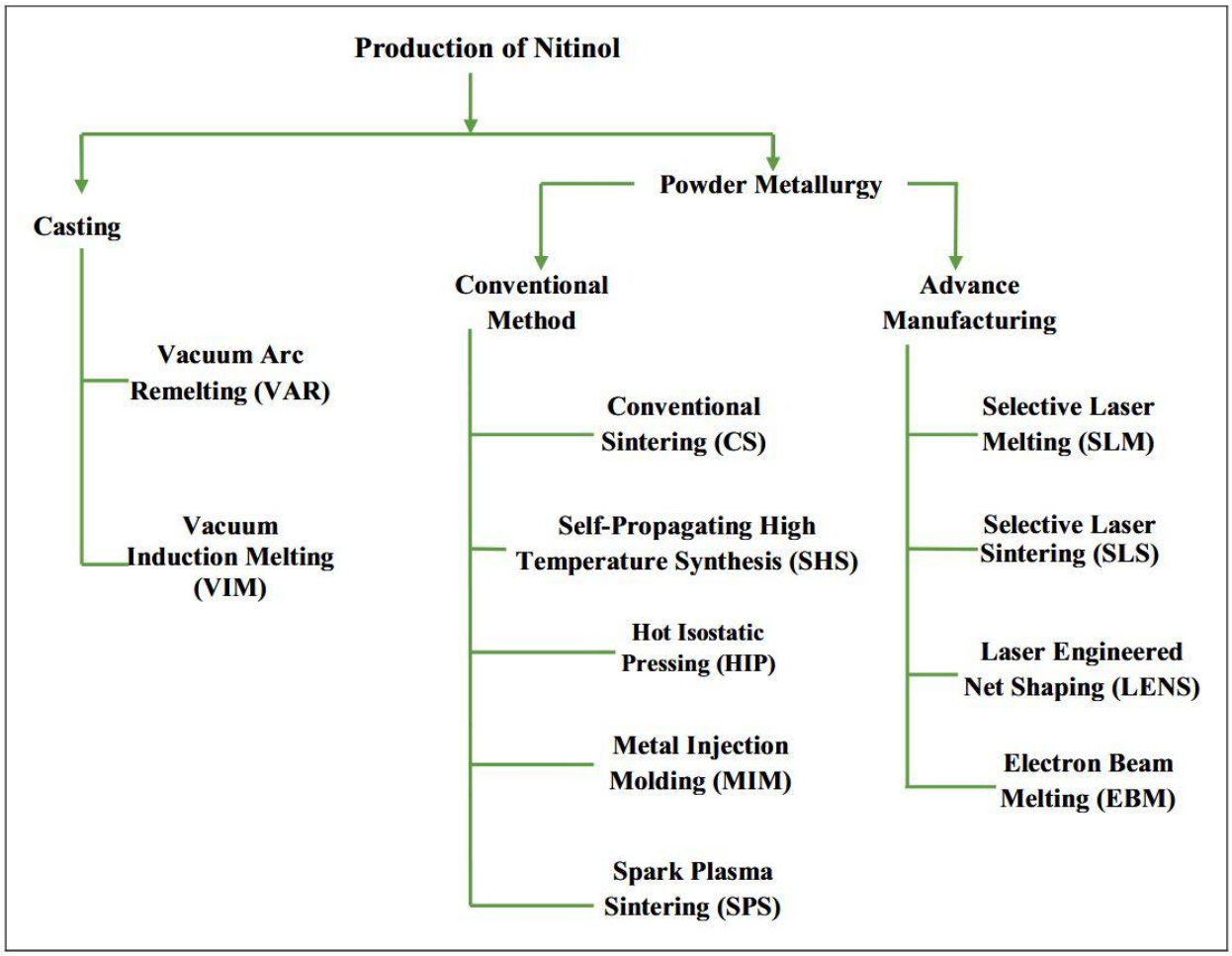


Figure 7: Fabrication methods for the manufacturing of NiTi [218].

2.6.1. Traditional Manufacturing

The two main traditional manufacturing methods of NiTi are casting and powder metallurgy. The melting processes typically used in the processing of NiTi are vacuum induction melting (VIM) and vacuum arc remelting (VAR) with VIM being the most commonly used method of NiTi melting. The two main concerns in the melting process of NiTi are compositional fluctuations and carbon and oxygen impurities. An inhomogeneous composition can result in deviations from the desired functional properties of the material while the inclusion of impurities can act as failure initiation sites reducing the mechanical performance of the part. During the VIM method, NiTi is melted by high frequency induction heating in either a vacuum or inert gas. The material is completely melted, stirred and transferred to the mould resulting in a high level of compositional uniformity. However, the main drawback of this method is carbon impurity contamination from the graphite crucible. VAR benefits from

increased purity compared to VIM however in this method the entire ingot cannot be simultaneously melted and can result in compositional heterogeneity due to the partial melting [57]. Conventional powder metallurgy processes for NiTi include conventional sintering (CS), hot isostatic pressing (HIP), spark plasma sintering (SPS), metal injection moulding (MIM), and self-propagating high temperature synthesis (SHS). These methods typically suffers from high porosity, high levels of oxygen and carbon inclusions, and poor control of intermetallic phases such as $NiTi_2$, Ni_3Ti, and Ni_4Ti_3 [58].

2.6.1.1. Forming

After conventional manufacturing methods, the ingot requires extensive post processing involving hot and cold working steps to achieve the desired geometry and part properties [59]. The forming method, route, and parameters used to shape the ingot directly influences the final properties of the part. The main aim of the initial hot working steps is to change the dimensions and modify the microstructure of the ingot. Hot working steps are carried out at temperatures between 600 and 900 °C which increases the formability of the metal, allowing large deformations and microstructural recrystallisation. Subsequently a combination of cold working and ageing treatments are carried out to further reduce the dimensions of the ingot and to achieve the desired final part properties [60].

2.6.1.2. Shape Setting

Shape setting of SME NiTi refers to the process of controlling and fixing the shape that the material will return to after deformation when the material transforms to austenite. The three most important factors in the shape setting of NiTi are the heat treatment temperature, dwell time, and the thermomechanical history/condition of raw material. Longer times and higher temperatures can lead to annealing of the material however, it also results in more exact shapes and less spring back. Shorter times and lower temperatures cause the material to remain closer to the high-strength, cold-worked state but will result in more spring back and less accurate shapes. The right conditions must be developed to optimise the shape setting of NiTi [61].

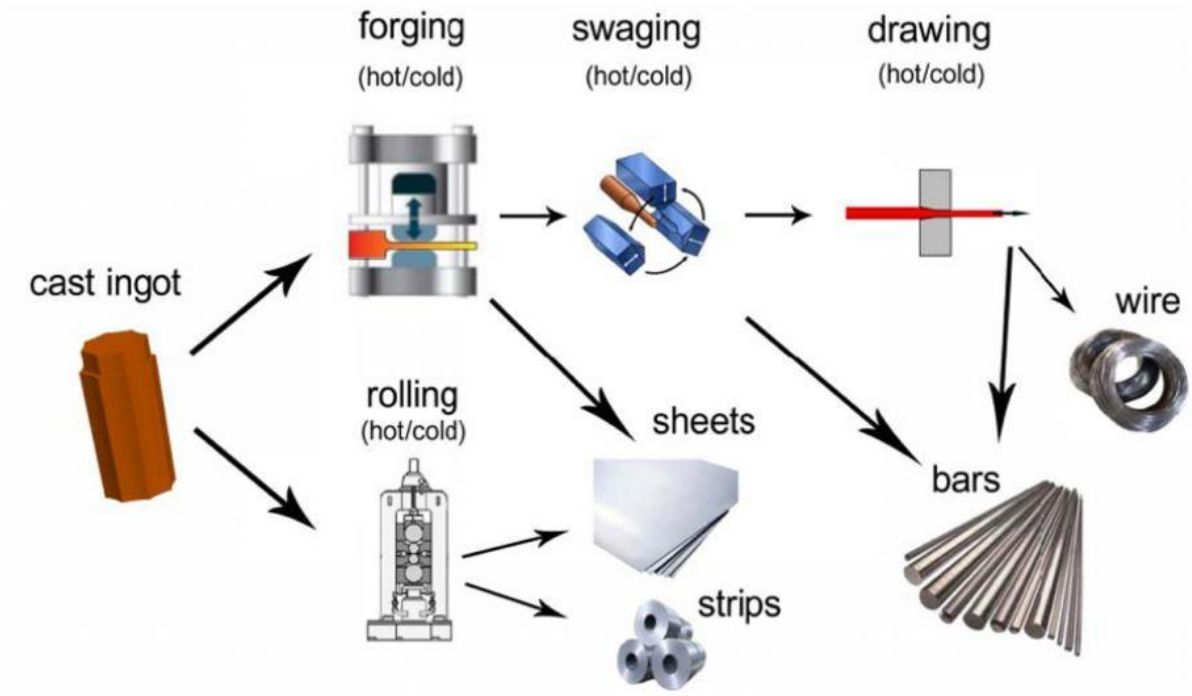


Figure 8: Forming methods of NiTi [60].

Three main methods of shape setting include mandrels and fixtures, straight annealing, and over-straining. In the first method, the material is held in the desired shape using a mandrel or fixture during heat treatment at a controlled temperature and time, and then the part is quenched. Once removed from the mandrel, NiTi retains the programmed shape, known as the "remembered" or austenitic shape [62]. Straight annealing method involves pulling long lengths of wire from one reel to another through a tube furnace at high tensions, cooling them upon exiting the furnace to maintain the straightness, and then reeling them again. These wires are generally subject to further shape setting and machining. Over-straining method involves cold working the part to the point where full recovery of the previous shape upon heating does not occur. This process is repeated until the previous austenitic shape is sufficiently removed. This process is time consuming and difficult to predict [63].

2.6.2. Additive Manufacturing

One of the main drawbacks of traditional manufacturing methods is the poor machinability of NiTi which limits the parts to simple geometries such as wire, rods, and sheets. Additive manufacturing (AM) is a layer by layer fabrication method without the need for tools or moulds with a high degree of freedom of design [64]. AM enables the manufacturing of

complex application specific geometries not previously possible via traditional manufacturing methods as well as advantages such as rapid design iteration, negligible lead time, and reduced material and energy wastage [65].

Laser powder bed fusion (PBF-LB) is an AM technique that employs lasers as a heat source which selectively scan across a powder bed, fusing the powder to form the 2D-cross section of a 3D model layer by layer [66]. The final properties of parts produced by PBF-LB are mainly determined by the following process parameters: laser power (L), scan speed (v), hatch spacing (h), and layer thickness (t) [67]. To facilitate the comparison of PBF-LB process parameters, the relationship between laser power, scan speed, and hatch spacing is often represented by a single value known as the volumetric energy density (VED). VED describes the energy input to the powder per unit volume in Joules per mm^3 (J/mm^3) and is calculated according to the following formula:

$$VED = \frac{P}{v \,.\, h \,.\, t}$$

2.6.2.1. Effect on the Properties of NiTi

The VED has a significant effect on the final properties of NiTi parts, and the optimum parameters are influenced by the material characteristics of the starting powder, the intended application, the desired part properties, and the operating environment of the final part. The layer-by-layer nature of the PBF-LB process as well as the high melt pool temperatures and the rapid solidification rates inherent to the process result in large thermal gradients and non-equilibrium solidification rates [65]. These uneven solidification rates can result in heterogeneous microstructures and phase distribution. Rapid heating and cooling can solidify meta stable phases in alloy matrix and result in insufficient time for full phase transformation while high thermal gradients can induce high thermal residual stresses resulting in porosity defect and microcracks [68]. However, it is also possible to produce parts with improved properties compared to conventionally manufactured parts. By optimising the PBF-LB parameters the fast cooling rates can produced small grain sizes and improved mechanical properties as well as making possible the production of functionally graded microstructures [69]. The process parameters used control the energy

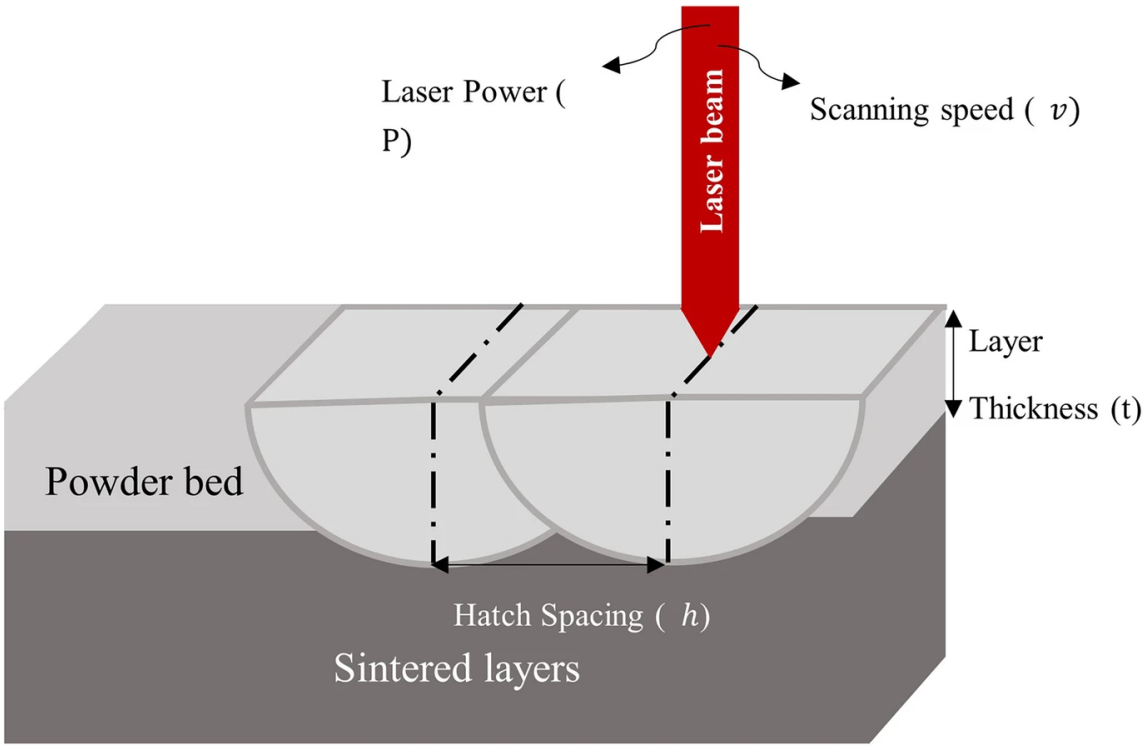


Figure 9: Schematic of the PBF-LB process illustrating the process parameters laser power (P), scan speed (v), hatch spacing (h), and layer thickness (t) [50].

supplied to the powder during the PBF-LB process and thus control the influence of these effects on the final properties of the part.

2.6.2.2. Challenges

Control of Ni Content: It is well reported in the literature that the lower boiling evaporation temperature of Ni compared to Ti results decrease in the Ni content of the PBF-LB parts from the starting powder. The TTs of NiTi are heavily influenced by the PBF-LB process parameters due to the high sensitivity alloy composition to VED. Transformation temperatures can vary greatly with VED due to changes in the alloy composition owing to Ni evaporation and precipitation of secondary phases [70]. An increase in VED due to increased laser power or reduced scan speeds leads to increased Ni evaporation which in turn increases TTs and results in Ti-rich regions which promote the precipitation of Ti-rich precipitates such as $NiTi_2$ [71]. As the composition of the alloy is essential to the functional properties and phase transformation behaviour of the alloy it is critical that the PBF-LB and starting composition of the alloy are optimised to achieve the desired final part properties.

Porosity Defects: On of the most common defects in the PBF-LB processing of NiTi are porosity defects. These pores can act as initiation sites for cracks to form, deteriorating the mechanical performance of NiTi [72]. There are three types of porosity defects which can occur during the PBF-LB process. Gas pores are caused by gas in the powder bed which becomes trapped or dissolved in the liquid metal during the rapid solidification process resulting in spherical pores of less than 20 μm in size [73]. Lack of fusion defects occur when low VED causes insufficient melting resulting in lack fusion between particles producing irregular shaped pores ranging in size from 50 μm to several millimetres [74]. Keyhole pores occur when high VED causes the evaporation of material which generates a recoil pressure that pushes the molten metal away from the laser interaction zone leading to vapour cavities [75]. These vapour cavities appear as spherical pores ranging from 20 μm to 60 μm in size.

Residual Stress & *Microcracks:* Residual stresses in PBF-LB parts primarily originates from large thermal gradients produced by the high thermal energy and localised heating inherent to the PBF-LB process. Residual stress in NiTi can influence the phase transformation characteristics, cause localised detwinning and, when sever enough, can lead to crack formation [76][77]. Post-processing heat treatments can be used to relax residual stresses and annihilate defects in the microstructure however the heat treatment itself also alters the phase transformation characteristics and microstructure of the part [78].

2.7. Shape Memory Alloy Actuators

An actuator is a device that converts energy into mechanical force to produce motion. SMA actuator systems are typically composed of the SMA element itself, a bias element that returns the SMA to its original shape after actuation, an electrical control unit, and a set of fixtures used to couple the actuator to the mechanical system. During phase transformations, SMAs can generate work in the form of force and displacement. The motion of the force and displacement can typically be divided into either linear or rotational [79]. NiTi SMAs are used as an alternative to traditional actuation systems due to their high power-to-weight ratio, making them ideal for lightweight applications and miniaturization in cases requiring high mechanical performance within limited spaces. Additionally, their low maintenance requirements, reliability, large stroke capabilities, and spark-free, clean, and silent operation

make them ideal for use in biomedical, robotics, automotive, and aerospace industries [80][81].

2.7.1. NiTi Actuator Classification

NiTi actuators are primarily classified as either thermal actuators, where a change in ambient temperature causes actuation, or electrical actuators, where actuation is initiated by the application of direct current, resulting in a temperature change [82]. Thermal actuators are typically controlled by passive heating where actuation occurs through changes in ambient temperature [83]. They can be used as sensors to detect changes in temperature and as actuators to output work. Electrical actuators are controlled by Joule heating where a current is applied to the material causing resistive electrical heating and are generally used solely as actuators to output work [84]. In either case, the application of heat is the only necessary input for actuation, allowing NiTi SMA actuators to be used as high work output actuators with reduced system complexity and volume, and higher energy densities than pneumatic actuators and direct current motors [85].

An example of an electrical actuator system is illustrated in a study by Costanza et al. [86]. Figure 10 shows a linear actuator prototype made from a NiTi spring and a harmonic steel spring. The SMA spring is heated by applying an electric current, causing it to push against and compress the harmonic steel spring. When the electric current is switched off, the SMA spring cools, and the harmonic steel spring pushes it back to its starting position. The point of intersection between the thermoelastic curve of the NiTi spring and the elastic curve of the steel spring defines the force and displacement of the spring, and thus the stroke of the actuator. This study demonstrates how the actuator's stroke can be easily tailored to a specific application by combining SMA and harmonic springs of different stiffnesses.

An example of a thermal actuator is presented in a study by Krishnan et al. [87]. In this study the SMA element works as both a sensor and an actuator in a cryogenic thermal conduction switch between dewars of liquid methane and liquid oxygen (Figure 11). In this case the bias spring exerts a tensile force on the SMA spring, stretching it and separating the copper contacts. When the temperature of the liquid methane increases beyond a certain defined temperature, the SMA spring senses the change in temperature and actuates by undergoing

a phase transformation from martensite to austenite and overcomes the tension of the bias spring bringing together the copper contacts. The copper contacts create a conductive path for the liquid oxygen to cool the liquid methane. The SMA spring senses the decrease in temperature and transforms back to martensite where the bias spring overcomes the SMA spring and breaks the heat conduction circuit.

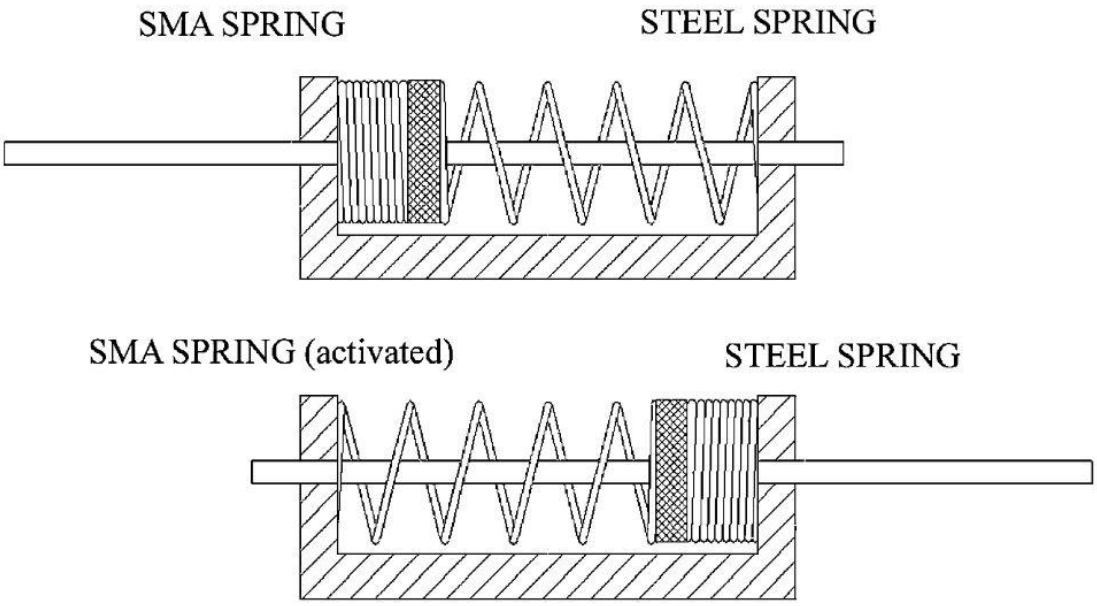


Figure 11: Schematic of the linear electrical actuator system composed of an SMA spring and harmonic steel spring showing the motion of the actuator [43].

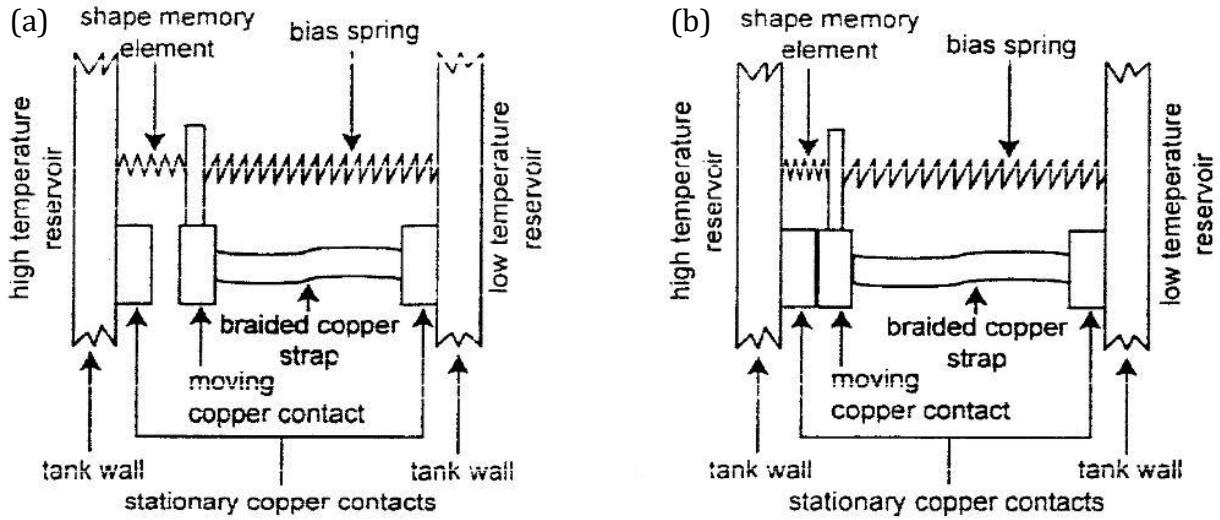


Figure 10: Schematic of the cryogenic thermal switch (a) the open position and (b) the closed position. [88]

2.7.2. Limitations

Two of the main challenges of SMA actuators are energy efficiency and actuation cycle time. During the heating part of the actuation cycle, the response time for actuation ON is determined by the time taken for the material to reach A_f and undergo phase transformation. Actuation ON time is primarily controlled by the current applied where increasing the current can increase the response time. The ON time is also affected by the efficiency of heating. The heating part of the actuation cycle can suffer from low energy efficiency due to a significant amount of heat energy being lost to the environment which also results in a slower response time. In conventional electrical SMA wire actuators, a low voltage of up to 10 V is applied continuously, depending on the volume of the material and properties such as resistivity and transformation temperatures [84]. In a study by Motzki et al. [88], a rapid pulse method of electrical heating was investigated. A wire with a diameter of 76 μm and length 225 mm, conventionally heated by a supply voltage of 8 V for 1 s, achieved a maximum displacement of 8.33 mm, corresponding to a 3.7 % stroke. Using the rapid pulse method, a wire of the same diameter heated by a supply voltage of 125 V for 2 ms, achieved a displacement of 21 mm, 38 ms after the voltage was switched off, corresponding to a 9.3% stroke. The study found that higher voltages resulted in higher forces at lower energy input levels, and shorter activation pulses increased the efficiency of the system by eliminating heat loss to the environment, achieving energy savings of up to 80 %.

Slow actuation cycle times are primarily dictated by the slow cooling of the NiTi actuator. During the cooling part of the actuation cycle, the actuation OFF is the time taken for the material to cool back to M_f. The OFF time is the more challenging part of the actuation cycle as it is controlled by the thermal conductivity of the material. Optimising the cooling of SMA actuators can be divided into either passive methods or active methods. Examples of active cooling optimisation methods include active cooling systems such as fans or forces convection through conductive fluids or coatings. The most common method of passive cooling optimisation is increasing the surface to volume ratio. This highlights the advantage of AM which allows the fabrication of geometries with high surface to volume ratios such as lattice structures [89]. Sputtering methods have been used to increase the surface area to volume ratio by producing NiTi thin films for use in microelectromechanical systems

(MEMS). The advantage of thin film SMAs is not only their small size but also the increased response rate of the NiTi actuator due to faster cooling rates [5][52].

2.8. Summary of Existing Knowledge

Nitinol has attracted considerable interest across aerospace, automotive, biomedical, and robotics industries as a promising alternative to conventional actuation systems. Its high force-to-mass ratio, superior wear and corrosion resistance, and unique shape memory and superelastic properties enable the design of lightweight, low-maintenance actuators that function as single components. Previous research has investigated both traditional manufacturing and PBF-LB processing of NiTi, highlighting the influence of the starting material, process parameters, and post-processing heat treatments on part properties.

Based on the current research traditional manufacturing methods, such as wire drawing, can produce NiTi wires that exhibit shape memory and superelastic behaviour with tailored transformation temperatures. However, the thermal and mechanical properties of these wires are strongly dependent on the production route. Ingot fabrication often results in heterogeneous microstructures with oxygen and carbon impurities, which act as sites for crack initiation during subsequent hot or cold working or later in service. While hot and cold working can refine the microstructure, these processes also introduce residual stresses and dislocation networks that can shift phase transformation characteristics and degrade shape memory performance. Post-deformation annealing and thermal ageing can relieve stresses and tune transformation temperatures, but they may also promote extensive precipitation of secondary phases. Such precipitates hinder the austenite–martensite transformation, reducing shape memory performance and increasing hysteresis.

The machining of Nitinol poses another challenge. Its high ductility and work hardening leads to significant tool wear, and processes like grinding introduce high temperatures and stresses that alter material properties. Consequently, NiTi is generally limited to simple geometries such as wires, tubes, and sheets, preventing the full realization of its potential. To overcome these limitations, additive manufacturing, particularly PBF-LB, has emerged as a promising alternative. PBF-LB enables the fabrication of complex geometries with tailored properties. Yet, the complex interactions between process parameters and material

behaviour also introduce drawbacks. The high temperatures, steep thermal gradients, and rapid cooling rates characteristic of PBF-LB can lead to composition variations, porosity defects, and significant residual stresses.

The existing literature highlights that each step of the fabrication process strongly influences the final properties of NiTi components. Nevertheless, the majority of research focuses on the superelastic performance, while relatively few address the shape memory effect (SME), especially in the context of actuator behaviour such as stroke and actuation time. A critical gap remains in understanding how PBF-LB processing parameters affect the SME of Ti-rich NiTi, which is essential for optimizing actuation performance. This thesis aims to address these gaps through the following investigations:

- It is hypothesised that ageing heat treatments can enable the fabrication of thermal actuators from conventionally manufactured Ni-rich wires. Chapter 3 examines the effects of ageing time and temperature on phase transformation characteristics, density, hardness, and shape memory performance. In this study the wires were actuated by application of heat offering insight into the effects of ageing on conventionally manufactured thermal actuators.
- It was hypothesised that the degree of cold work and subsequent ageing treatments can control the properties of conventionally manufactured NiTi wires and that actuators based on R-phase transformation exhibit reduced hysteresis. Chapter 4 analyses the influence of the effect of the level of cold work and ageing time and temperature on the phase transformation characteristics, hardness, microstructure, and R-phase actuator performance. The results of this study provide valuable insight into the performance of Ni-rich electromechanical R-phase actuators and the role of thermomechanical history.
- It is hypothesized that the interplay between PBF-LB process parameters and part geometry can be leveraged to control the material properties of Ti-rich NiTi parts. Chapter 5 examines the influence of process parameters on phase transformation behaviour and material properties across different lattice geometries and the relationship between the process parameters, the part geometry, and the material characteristics. This study provides new insights into the relationship between strut

part geometry and PBF-LB process parameters and their effect on the phase transformation temperatures and material characteristics of Ti-rich parts.

- It was hypothesised that the relationship between PBF-LB process parameters and part geometry together can be used to optimize the shape memory performance of Ti-rich thermal actuators. Chapter 6 investigates the effect of PBF-LB process parameters and lattice strut diameter on the actuator performance and strain recovery of Ti-rich thermal actuators fabricated by PBF-LB. This study presents valuable new insight into the interaction between PBF-LB process parameters and part geometry on the performance of Ti-rich actuators.

Chapter 3: Effect of Heat Treatment Time and Temperature on the Microstructure and Shape Memory Properties of Nitinol Wires

Josephine Ryan Murphy, Neha Agarwal, Hashemi, Theo Mossop, Darragh O'Neill, John Power, Ali Shayegh, and Dermot Brabazon. Effect of Heat Treatment Time and Temperature on the Microstructure and Shape Memory Properties of Nitinol Wires. Materials *2023*, *16*, 6480.

This chapter focuses on conventionally manufactured NiTi wires. Although wire drawing is a well-established manufacturing method, they remain an important area of study. Much of the existing literature concentrates on their superelastic behaviour, while comparatively less attention has been given to the shape memory effect. Given the widespread availability of conventionally manufactured NiTi wires and the significant scope for tailoring their functional properties through heat treatment, this investigation provides an essential foundation for the studies presented throughout this thesis.

Abstract

In this study, the effect of heat treatment parameters on the optimized performance of Ni-rich nickel–titanium wires (NiTi/Nitinol) were investigated that were intended for application as actuators across various industries. In this instance, the maximum recovery strain and actuation angle achievable by a nitinol wire were employed as indicators of optimal performance. Nitinol wires were heat treated at different temperatures, 400–500 ◦C, and times, 30–120 min, to study the effects of these heat treatment parameters on the actuation performance and properties of the nitinol wires. Assessment covered changes in density, hardness, phase transition temperatures, microstructure, and alloy composition resulting from these heat treatments. DSC analysis revealed a decrease in the austenite transformation temperature, which transitioned from 42.8 ◦C to 24.39 ◦C with an increase in heat treatment temperature from 400 ◦C to 500 ◦C and was attributed to the formation of Ni_4Ti_3 precipitates. Increasing the heat treatment time led to an increase in the austenite transformation temperature. A negative correlation between the hardness of the heat-

treated samples and the heat treatment temperature was found. This trend can be attributed to the formation and growth of Ni_4Ti_3 precipitates, which in turn affect the matrix properties. A novel approach involving image analysis was utilized as a simple yet robust analysis method for measurement of recovery strain for the wires as they underwent actuation. It was found that increasing heat treatment temperature from 400 ◦C to 500 ◦C above 30 min raised recovery strain from 0.001 to 0.01, thereby maximizing the shape memory effect.

3.1. Introduction

Nitinol is an intermetallic phase of the nickel–titanium alloy with near-equiatomic composition. It has two main crystal phases: a high-temperature austenitic phase with BCC crystal structure, and a low-temperature martensitic phase with a monoclinic lattice structure [90]. The transformation from austenite to twinned martensite on cooling is a diffusionless process meaning that it can occur at very low temperatures as depicted in Figure 12. As there is no diffusion of atoms, the only change that takes place is in the crystal structure of the material, as depicted in Figure 12, allowing what is known as the shape memory effect (SME) to occur [16]. When stress is applied to nitinol in the twinned

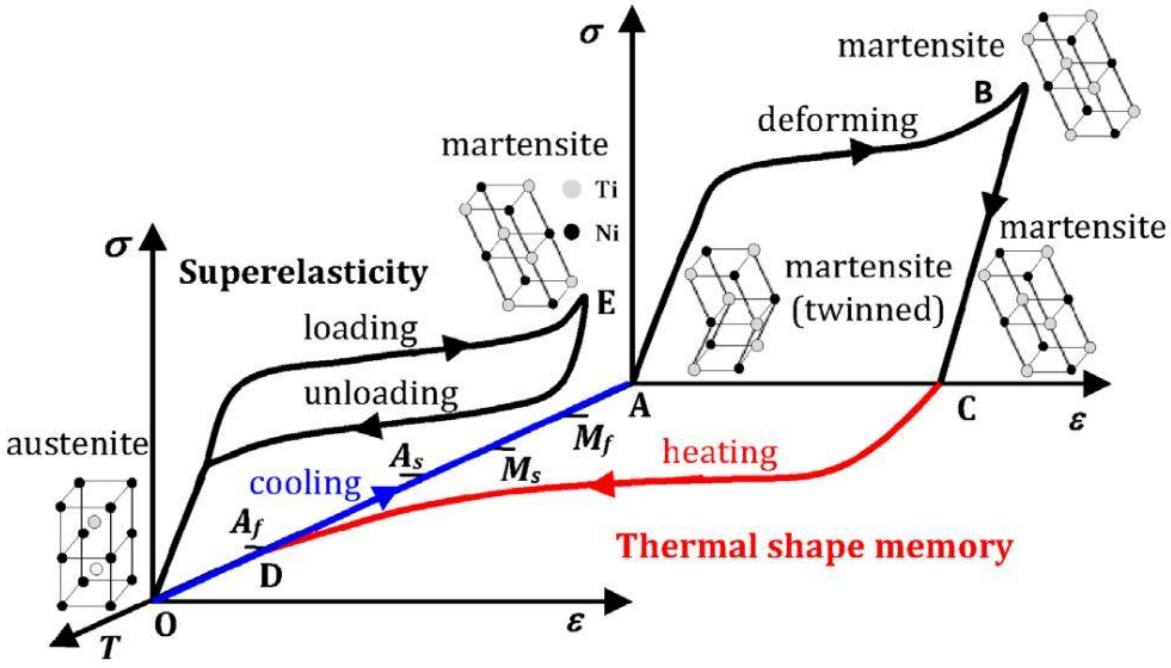


Figure 12: The illustration of the shape memory effect in NiTi alloy is depicted through stress, strain, and temperature variations, adapted from Yuebin Guo et al. [110].

martensite phase, provided the stress is sufficiently high to induce a phase transformation yet remains below the elastic limit, slip will not take place. Instead, a temporary phase change from twinned martensite to detwinned martensite will be observed [91]. This means that during the phase change, no atomic bonds are broken and thus the phase change is reversible, allowing the nitinol to recover its original shape when heated to the high-temperature austenite phase. The nitinol then remains in this shape as it cools and transforms back to twinned martensite [18].

A process known as shape setting determines the shape that nitinol will return to, the 'remembered' shape, once the trained part is heated above the austenite finish (A_f) temperature. The most common method of shape setting nitinol is by heat treatment [92], [93], [94]. The nitinol is held in the desired shape with a mandrel or fixture while it is heat treated at a controlled temperature and time and is then quenched. When the nitinol is removed from the mandrel after quenching, it retains its shape that is the austenitic or "remembered" [62]. Another method of shape setting is over-straining which involves cold working nitinol to the point at which full recovery of the previous shape on heating is not possible. This process can be repeated until the previous austenitic shape is sufficiently removed. This procedure takes time and is typically not as repeatable as heat treatment shape setting [83].

The three most important factors in the heat treatment method of shape setting nitinol are the heat treatment temperature, time spent at this temperature, and the raw material condition. Shorter times and lower temperatures result in the material retaining the properties of the high-strength, cold-worked state, but will result in more spring back and less accurate shape setting. Longer times and higher temperatures can result in annealing; however, it also results in shapes that are more exact and have less spring back [61]. The existing literature shows that heat treating nitinol between 400 and 500 °C increases the SME [90], [95], [96]. This is due to the formation of metastable Ni_4Ti_3 precipitates on heat treatment of the samples and also due to the substantial density of reorganized dislocations that remain within the samples [5].

The Ni_4Ti_3 precipitates is dominantly present in the {111}B2 plane of the NiTi matrix This is the crystallographic orientation relationship between the Ni_4Ti_3 precipitate and the B2 phase. Each of the parent phase has four {111}B2 planes with two of these variants having the same plane leading to eight variants of the Ni_4Ti_3 precipitates. These precipitates have varying size vastly depending on the heat treatment temperatures and times. The precipitate formation in the ageing temperatures generally have affinity of nucleating and grow near the grain boundaries [97]. It was shown in the work of Sadiq et al. [98] that changes in distribution of the Ni_4Ti_3 precipitates governs the SME as it prevents plastic deformation by restricting the movement of dislocations and increasing the critical stress magnitude [98]. From this work, it was also noted that heat treatments at temperatures above 400 °C show the highest extent of the SME. However, in a study by Oncel et al. [94], it was found that, at temperatures above 500 °C, the precipitates are larger, less dense, and begin to re-dissolve within the austenitic phase matrix, decreasing the SME of the material. These studies highlight the importance of finding the optimum heat treatment parameters for nitinol in order to provide the highest extent of SME.

Several research studies have demonstrated that the nickel (Ni) content within NiTi based alloys and the presence of precipitates, such as $NiTi_2$, Ni_3Ti_2, and Ni_4Ti_3, play a significant role in influencing the alloy's phase transition temperature. Additionally, the incorporation of alloying elements not only impacts the phase transition temperature but also affects the resultant phase transition products and the pathway of the phase transition [99]. In NiTi binary alloys, a typical one-step phase transition directly from B2 to B19′ is observed. However, the introduction of iron (Fe) results in a two-step phase transition, progressing from B2 to R and then to B19′. Notably, the degree of separation between these two transition steps becomes more pronounced with higher levels of Fe incorporation. The NiTi-Cu alloy system offers less sensitivity of the alloy's phase transition temperature due to compositional variations, facilitating enhanced control over memory performance. The addition of copper (Cu) imparts the alloy with a high phase transition temperature, exceeding room temperature, enabling the realization of shape memory effects even at ambient conditions. These favourable attributes position NiTi-Cu alloy as a highly promising choice for practical applications in shape memory alloys. Additionally, incorporating

palladium (Pd) into a NiTi alloy can substitute for nickel (Ni) atoms, resulting in an initial decrease in the alloy's phase transition temperature. However, as the quantity of added Pd increases, the phase transition temperature gradually rises with the Pd content [100]. The critical influence of nickel (Ni) content and precipitates on the phase transition temperature of NiTi-based alloys, as well as the profound impact of alloying elements on both the temperature and the characteristics of phase transitions, offers opportunities for tailoring shape memory alloys to suit various practical applications.

Many different methods have been presented in the literature to determine the efficacy of heat treatment parameters on the SME of nitinol. In a study conducted by Lahoz and Puertolas [101], NiTi wire with A_f temperature 29.2 °C was heated treated at 660 °C for 30 min and then quenched in water. Stress-strain and deformation-temperature curves of the NiTi wire were then obtained using a thermomechanical analyser (TMA). Several different studies used a low-friction linear variable displacement transducer (LVDT) to measure the displacement of a nitinol part. In Lou and Abel [102], NiTi wire with an A_f temperature of 80 °C, heat treated at 550 °C for 20 min, was held stationary at one end by a support structure, while the other end was attached to the central slider of a LVDT which measured the horizontal displacement produced by SME. In Speicher et al. [103], nitinol helical springs and Belleville washers are tested by using a cylindrical damper as a tension/compression device and a LVDT was used to measure the vertical displacement during actuation of the nitinol component.

In recent years, there has been a growing interest in harnessing the potential of shape memory alloys (SMAs) like nitinol to enhance structural behaviours. Nitinol, with its remarkable tensile strain recovery properties, offers the ability to generate and withstand substantial stresses and strains, making it a standout candidate for applications requiring high mechanical energy density. This feature enables more compact structural designs compared to other actuator systems and adaptive materials. Furthermore, nitinol's attributes, such as its robust tensile strength, corrosion resistance, and biocompatibility, have solidified its popularity in various fields, particularly in biomedical applications [104].

Moreover, nitinol-based single-stage bellows, shaped using the rubber bulge method, have been investigated for their compressive behaviour. These structures hold potential in energy absorption applications, providing adjustability in energy absorption and crushing forces based on their bellows' shapes. Additionally, nitinol-based bellows can be reused due to their recovery function, making them a promising choice for energy absorption devices [105], [106].

In a separate development, researchers have introduced a novel class of superelastic NiTi honeycomb structures. A unique brazing technique was employed to create nitinol based cellular structures with low relative densities. These structures exhibited impressive specific strength, high specific stiffness, and enhanced shape recovery when subjected to compression loading, outperforming monolithic shape memory alloys. This breakthrough opens the door to a wide range of engineered topologies with customizable properties and enhanced thermomechanical response [107]. These applications underscore the versatility and promise of nitinol in various fields, from seismic engineering to biomedical devices and advanced structural materials.

While these studies also investigate the effect of heat treatment parameters on the SME of nitinol, there are still several gaps in our understanding of the process and material behaviour. Achieving optimal energy consumption and SME performance for NiTi involves selecting a temperature that closely aligns with the operational environment, avoiding being too close to prevent unintended actuation. Previous investigations have shown that the initial A_f temperature of the wires were above room temperature; the A_f temperature further increased after heat treatments. There are, however, many potential applications for NiTi closer to room temperature so by selecting NiTi with a starting A_f slightly below room temperature, after heat treatment, it becomes possible to establish the resulting A_f temperature at an appropriate level above room temperature. Studies to date have also only examined a very limited range of heat treatment times and temperatures [108]. Finally, mechanical device methods of displacement and strain measurement used in past studies are known to have errors due to inherent friction and strain accommodation within the connecting mechanical elements [109]. The study involved an extensive exploration of various temperatures and durations applied to nitinol wire with initial A_f temperatures

below room temperature. The purpose was to determine the most effective heat treatment parameters to enhance shape memory effect (SME) control. Additionally, a strain recovery measurement was conducted using an image analysis methodology.

3.2. Materials and Methods

In this study, a DoE with two parameters at three levels was used to heat treat the nitinol wires in order to determine the optimum heat treatment parameters for maximum shape memory response. Wire samples of length 400 mm were heat treated and shape set as straight wires in a box furnace for 30, 60, and 120 min at 400 °C, 450 °C, and 500 °C. For each of these parameters, two samples were tested in order to validate results and calculate the repeatability. These samples underwent characterization through metallography, density, hardness, and DSC measurements. These analyses were performed to investigate the influence of the heat treatment parameters on the material properties, as depicted in Figure 13. Finally, the shape memory effect (SME) of the samples was tested by angular displacement and recovery strain experiments to determine the optimum heat treatment parameters for SME in nitinol wires. Note that throughout this study n = 2 and error bars shown are 95% confidence intervals.

3.2.1. Heat treatment of nitinol wires

The nitinol (NiTi) wire used for this study was provided by Fort Wayne Metals, Castlebar, Co. Mayo, Ireland, with a chemical composition of 55 wt.% Ni and 45 wt.% Ti. The wire supplied had a diameter of 0.468 mm with austenite finish temperature (A_f) of 13.7 °C with a lightly oxide surface finish. For heat treating the wires, a Nabertherm N60/85HA chamber furnace was used. This furnace has an operating temperature range of 30 to 850 °C and its inner chamber's dimensions are 350 × 500 × 350 mm. This furnace is heated from the bottom, sides, and the top and uses recirculating air flow to maintain temperature uniformity within 10 K according to DIN 17052-1 [110].

A summary of the heat treatment temperatures and times examined is shown in Table 1. For each specific time and temperature configuration, a 150 mm wire length was subjected to the heat treatment process. In total, nine wires were heat treated in this study. All the samples were heat treated individually to have stability at the respective temperature,

thereby avoiding opening of the furnace to add/remove samples. The samples were air cooled outside the furnace upon completion of each heat treatment process.

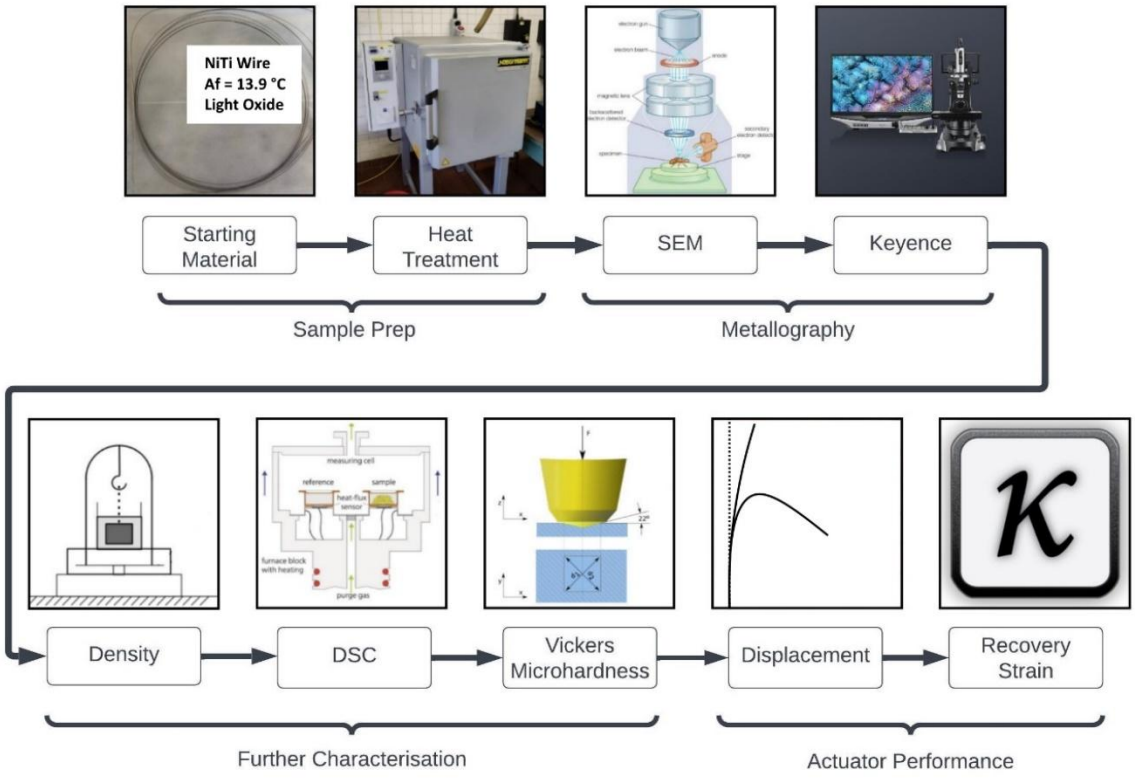


Figure 13: Process Diagram showing the implemented experimental procedure.

Table 1: Heat treatment process parameters applied to the nitinol wires.

Sample Number	Temperature (°C)	Time (min)
1	As-received	As-received
2	400	30
3	400	60
4	400	120
5	450	30
6	450	60
7	450	120
8	500	30
9	500	60
10	500	120

3.2.2. Metallography

Metallographic analysis of the surface morphology and topology was conducted using a SEM (Zeiss EVO LS15) at an accelerating voltage of 20 kV. The Zeiss EVO LS15 is a thermionic emission SEM with variable pressure option, and a maximum magnification of 300,000X with a 5-axis stage. The thin wires were mounted on conductive stubs and placed inside the SEM chamber for analysis. As the NiTi wires are conductive, no additional sample preparation was required. An Oxford Instrument EDX (Energy Dispersive X-Ray) was used for composition analysis. This analysis helped in identifying change in the Ni content as an effect of the variation in the heat treatment process parameters.

As titanium is a highly oxidizing element [111], in order to study the microstructure, samples were etched with a Kroll's reagent (HF based acid) to provide a better contrast between chemically different features of the material. Nitinol is a particularly unreactive metal in part due to the formation of an insoluble titanium oxide layer. Unlike with primarily titanium-based alloys, this etching procedure is particularly sensitive to alloy segregation, as the chemical reactivity of nickel is significantly different from that of titanium. This creates a challenge for determining the etching time for this metal. The etching times were found to be different for the as-received and heat-treated samples. The etching times used for the samples ranged between 2–5 s. There were no significant differences observed in the microstructures after etching.

3.2.3. Density

The most widely used method for calculating the density of solids is the buoyancy method, which is based on the Archimedean principle. This principle states that a body immersed in a fluid indicates an apparent loss in weight equal to the weight of the fluid it displaces. Ethanol was used as the fluid medium for density measurement in this study [112]. Density measurements were conducted on the nitinol wires, which were heat treated. Three measurements for each sample were recorded with averages and confidence intervals reported in this study.

3.2.4. Differential Scanning Calorimetry

Differential Scanning Calorimetric analysis was performed using a TA Instruments® Discovery DSC2500, New Castle, DE, USA. DSC analysis was performed on all the heat-treated samples as well on the as-received wire to study the phase transformation temperatures. The crucibles used for this experiment were made of pure aluminium, which is suitable for solid and powder samples that do not decompose or boil at temperatures between -170 °C to 600 °C [113]. The tests were conducted in the temperature range of 0 °C to 150 °C with a ramp up rate of 10 °C/min. The austenite and martensite start and peak and finish temperatures were evaluated. TZero aluminium pan with TZero lids and a sample mass of around 20 mg were used to carry out the tests. Liquid nitrogen was used as the cooling medium.

3.2.5. Vickers Microhardness

Vickers microhardness was recorded using a Leitz MiniLoad 2® equipment (Spectrographic, Leeds, UK by applying a force of 981 mN onto the surface of the samples with a holding time of 20 s [114]. Vickers hardness measurements were performed on all heat-treated samples, with each sample undergoing five measurements at randomly selected locations on its surface. The resulting average Vickers hardness values were then recorded and reported. For ease of the microhardness measurements with these thin wires, the wires were mounted in epoxy resin and grinded till the required surface finish was attained.

3.2.6. Displacement Experiment of Heat-Treated Nitinol Wires

The 150 mm long heat-treated wires were deformed into 'U' shapes by bending the wires 180° around a 6 mm diameter mandrel while both the ends were held together. This bending process was carried out with careful attention to prevent kinks in the wire. Such kinks could potentially cause a form of irreversible deformation due to elevated internal stresses compared to the surrounding wire. This deformation, if present, might diminish the overall shape memory effect. The wire was then released and secured to a reference sheet. A controlled heating was then applied to raise the temperature of the wire above the austenite finish temperature. A photograph of the wire, normal to the surface, of each sample after heating was taken, and for the measurement of deformation, an image analysis utilizing

ImageJ software (V 1.8.0) was employed [115]. A schematic representation of this entire process is visually outlined in Figure 14.

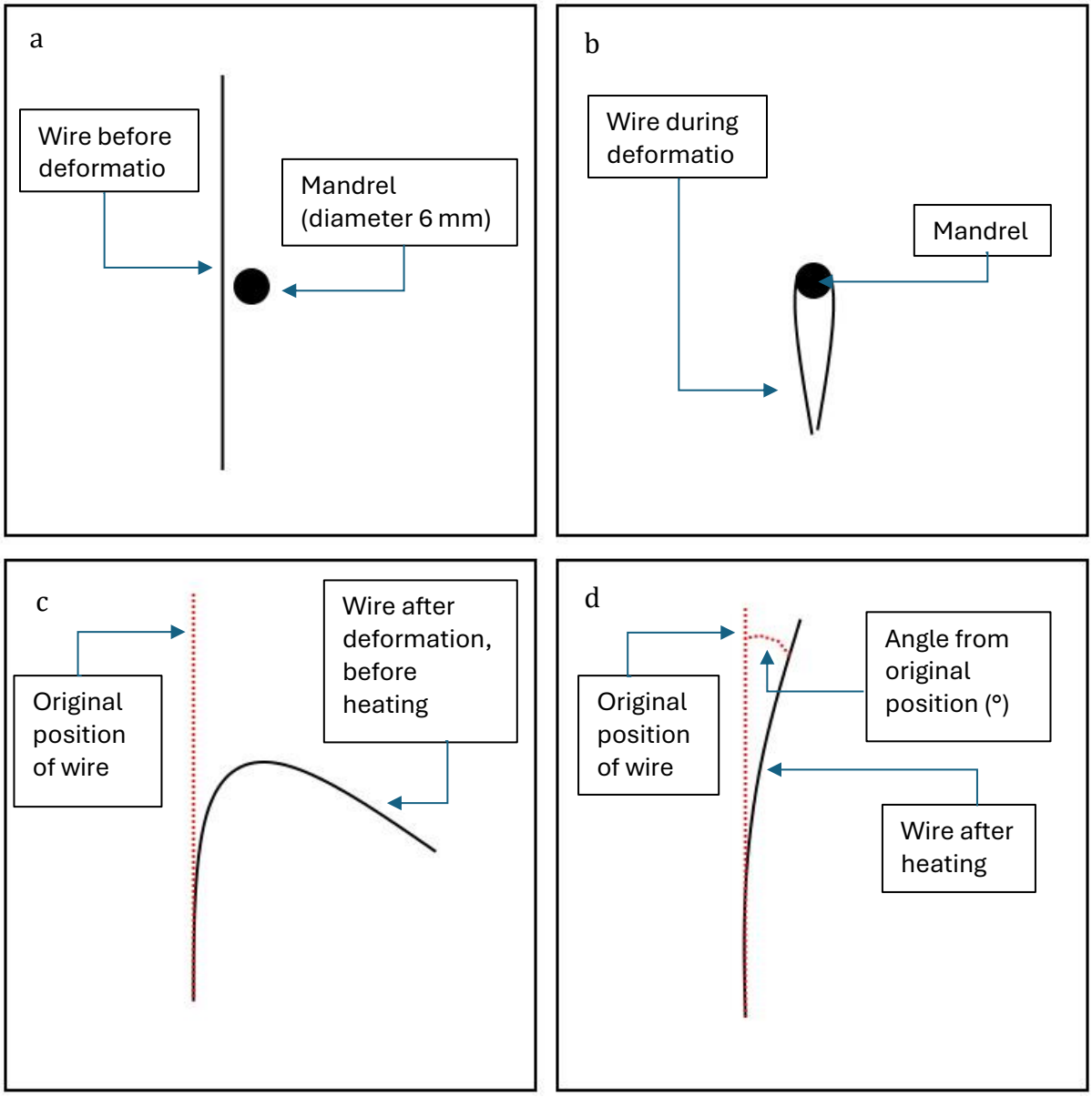


Figure 14: Schematic of the method used for the displacement and recovery strain experiments. (a) Wire and mandrel before deformation, (b) deformation of wire around mandrel, (c) wire after it has been released from the mandrel, (d) wire after controlled heating.

3.2.7. Recovery Strain of Heat-Treated Nitinol Wires

Images were captured before and after bending for all of the heat-treated nitinol wires. ImageJ software was used to calculate the radius of curvature before and after the wires were heated above the A_f temperature. The radius of curvature was calculated using a developed

ImageJ macro. Utilizing the initial radius of curvature (denoted by R), the bending stress equation was used to find the strain (denoted by ε) in the maximum bent section of the wire. The stress (denoted by σ) over the point of maximum stress equals the Young's modulus (denoted by E) divided by the radius of curvature as in Equation

(1).

$$\frac{\sigma}{y} = \frac{E}{R} \quad (1)$$

Furthermore, it is known that strain equals the Young's modulus by the stress as shown in Equation (2).

$$\sigma = E.\varepsilon \quad (2)$$

The combination of these two equations suggests that the strain within the sections of wire that is measured equals the point of maximum stress by the radius of curvature as shown in Equation (3). The point of maximum stress is relative to the neutral axis. The neutral axis within the wires is the centre point in the wires. The point of maximum stress is equal to the radius of these wires. Strain was calculated before and after the wires were exposed to the heat source. Recovery strain was calculated by subtracting the strain after recovery from the strain measured before recovery.

$$\varepsilon = \frac{y}{R} \quad (3)$$

3.3. Results

3.3.1. Effect of Heat Treatment on Density

Density measurements are conducted to evaluate the impact of heat treatment and its duration on the material's properties and characteristics. This allowed a comprehensive understanding of how changes in heat treatment conditions affect density and, by extension, the alloy's performance. While the density of the as-received nitinol was found to be close to the expected nitinol density of 6.45 g/cm^3 [116], differences in the resultant density were recorded for samples produced at the

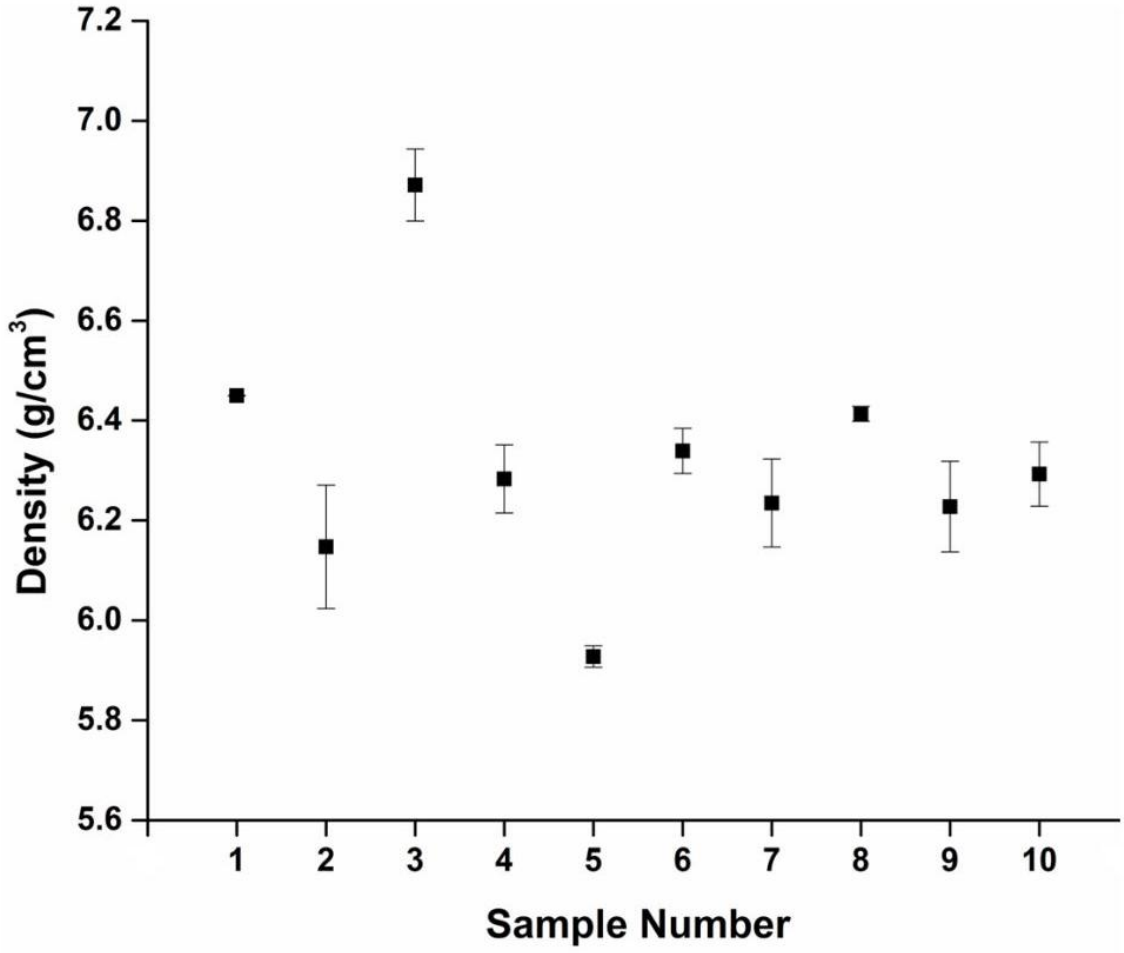


Figure 15: Density measurements (black squares) of all heat-treated nitinol samples, n = 3.

different processing parameters, see Figure 15. A slight decrease in density compared to the non-heat-treated samples was observed in the samples heat treated at 400 °C for 30 min (sample 2). Among the various heat treatment conditions, the sample treated at 400 °C for 60 min (sample 3) exhibited the highest density, with a value of 6.85 g/cm^3, while the sample subjected to heat treatment at 450 °C for 30 min (sample 5) demonstrated the lowest density of 5.95 g/cm^3. A decrease in density relative to the non-heated samples was observed for samples processed at all other heat treatment conditions. The density for the other heat treatment conditions was on average 6.25 g/cm^3. The density for the sample heat treated at 500 °C for 30 min (sample 8) was the closest to that of the as-received nitinol wire. Both samples, as received and heat treated, were also found to have the lowest standard deviation. It was observed that the heat treatment time had relatively little effect on the density value at 500 °C. Apart from one heat treatment condition, the heat treatments led to a decrease in

the density relative to that of the as-received nitinol wire, which is consistent with previous research findings [117].

3.3.2. Effect of Heat Treatment on Microstructure

The EDS results of the as-received wire showed a uniform distribution of Ni and Ti. Results of further EDS tests at different locations and areas confirmed that the surface of these samples contained a uniform composition of about 55 wt.% Ni and 45 wt.% Ti as shown in Figure 16. The chemical composition of the heat-treated wires has been tabulated in Table 2. Other observed elements were C and O but were insignificant to be mentioned.

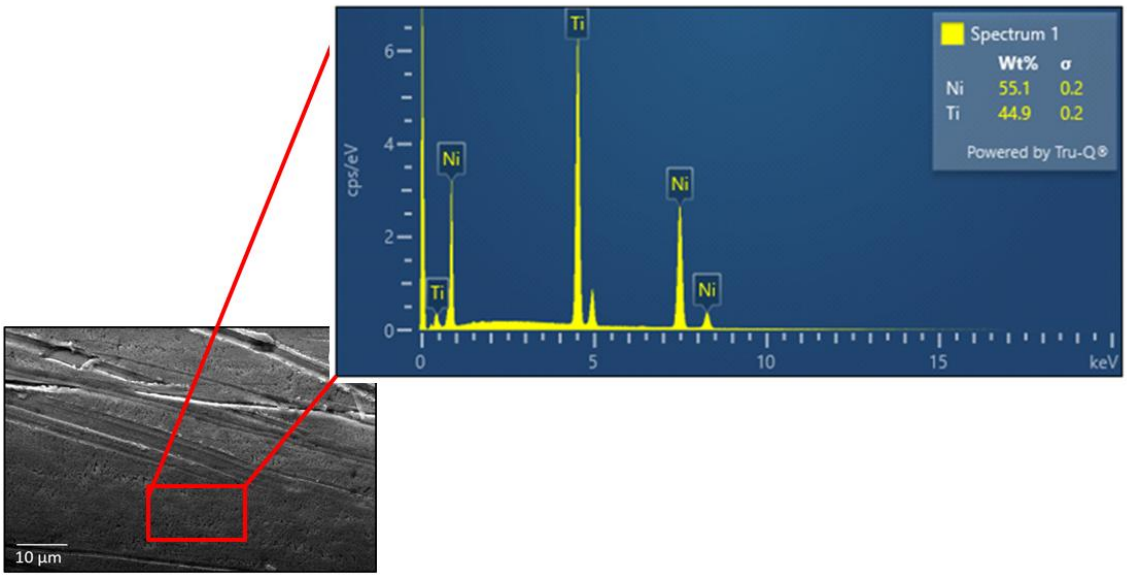


Figure 16: SEM image and EDX mapping of the surface of the as-received wire.

Table 2: Chemical composition of as-received and heat-treated nitinol wires

Sample Number	Ni (at. %)	Ti (at. %)
1	49.9	50.1
2	49.3	50.7
3	49.5	50.5
4	49.4	50.6
5	47.9	52.1
6	48.8	51.2
7	49.1	50.9
8	48	52
9	47.5	52.5

10	46	54

3.3.3. Effect of Heat Treatment on the Phase Transformation Temperatures

The phase change, including the austenite finish, temperatures (A_f) were measured using DSC, see Figure 17. These results show that there was a decrease in the A_f temperatures with increasing heat treatment temperature. The lowest A_f temperature for a specific temperature group was higher than the highest A_f temperature found in the next lower temperature treated group. On the other hand, there was an increase in A_f temperature with time for samples heated at 400 °C, a decrease in A_f temperature with time at 500 °C, and relatively little effect of time at 450 °C on the A_f temperature. From the DSC curves the phase change peaks become sharper with both heat treatment temperature and time with the broadest peak at 400 °C for 30 min and the sharpest at 500 °C for 120 min.

3.3.4. Effect on Hardness Due to the Heat Treatment Process

Figure 18 presents the results from the Vickers microhardness indentation tests. The measured hardness for all the heat-treated samples in this study was found to be lower than the measured hardness of the as-received nitinol wire. For the samples treated at 400 °C (samples 2, 3, and 4), there was an initial decrease in the hardness values between the samples treated at 30 min (sample 2) and those at 60 min (sample 3), and a subsequent increase in the hardness values from the 60 min samples (sample 3) to the 120 min (sample 4) heat-treated samples. For the samples treated at 450 °C (samples 5, 6, and 7), there was a general trend that showed a decrease in the hardness of the samples as the heat treatment time increased [53], [111]. Increasing heat treatment temperature also resulted in a reduction in average hardness. The trend of results of this work in terms of hardness matched well with those recorded previously [118].

3.3.5. Loss of Actuation Angle for the Nitinol Wires

The results in Figure 19 show that the largest deviations from the straight wire occurred in samples heat treated at 400 °C for 30 (sample 2) and 60 min (sample 3) with angles of 18.80 ° and 18.16 ° respectively. Increasing the heat treatment time to 120 min at 400 °C resulted in a reduction of this angle to 10.61 °.

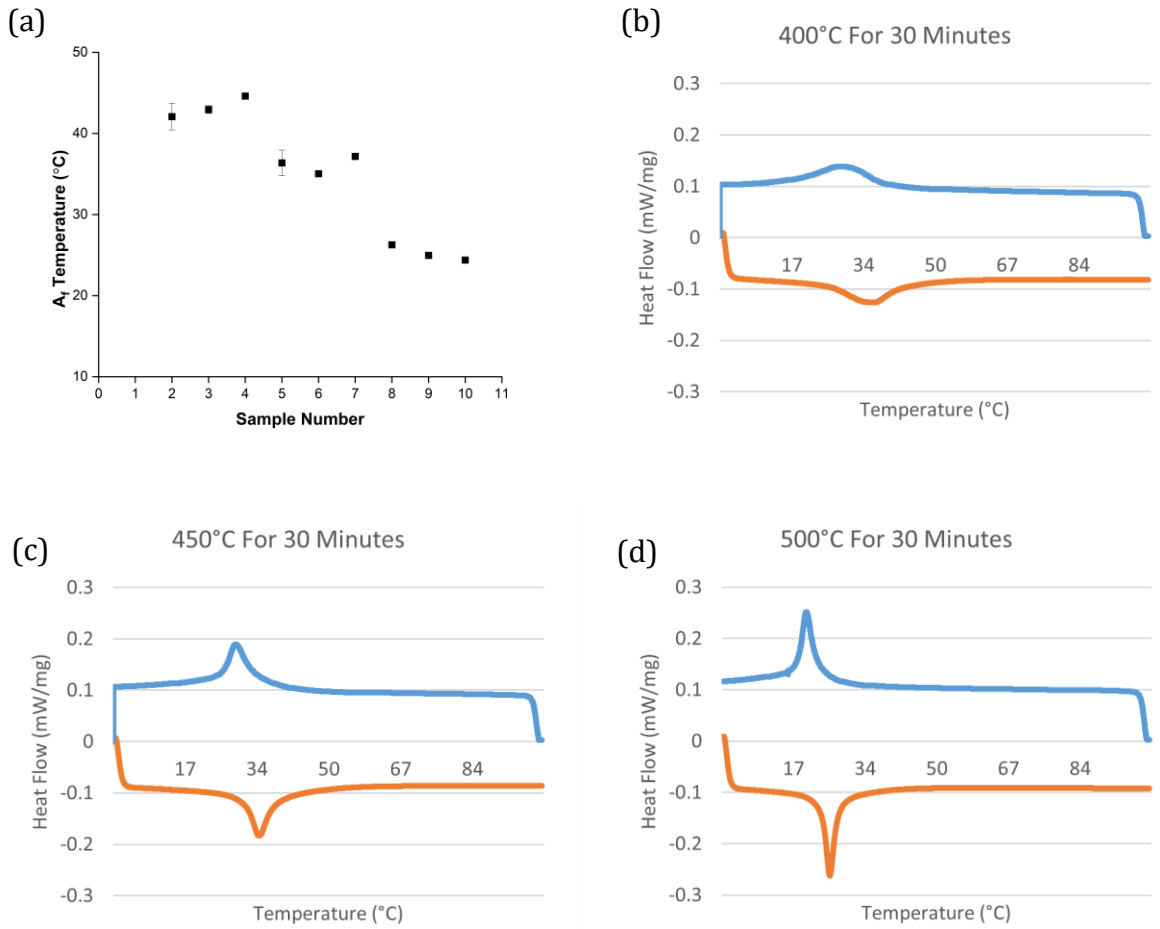


Figure 17: (a) The A_f phase transformation temperatures of the wire samples (n = 2), and DSC heating curves (orange line) and cooling curves (blue line) of samples treated (b) at 400 °C for 30 min, (c) at 450 °C for 30 min, and (d) at 500 °C for 30 min.

Samples heat treated at 450 °C show a different relationship between angle and heat treatment time. The lowest angle occurred in the sample heated for 30 min (sample 5), achieving an angle of 10.10 °. The angle increased drastically to 16.92 ° at 60 min (sample 6) and showed only a slight decrease to 16.74 ° for 120 min (sample 7).

For samples heat treated at 500 °C, a decrease in angle with increasing heat treatment time was observed. The sample treated for 30 min (sample 8) achieved an angle of 12.07 °. The samples treated at 60 min (sample 9) and 120 min (sample 10) both produced the lowest

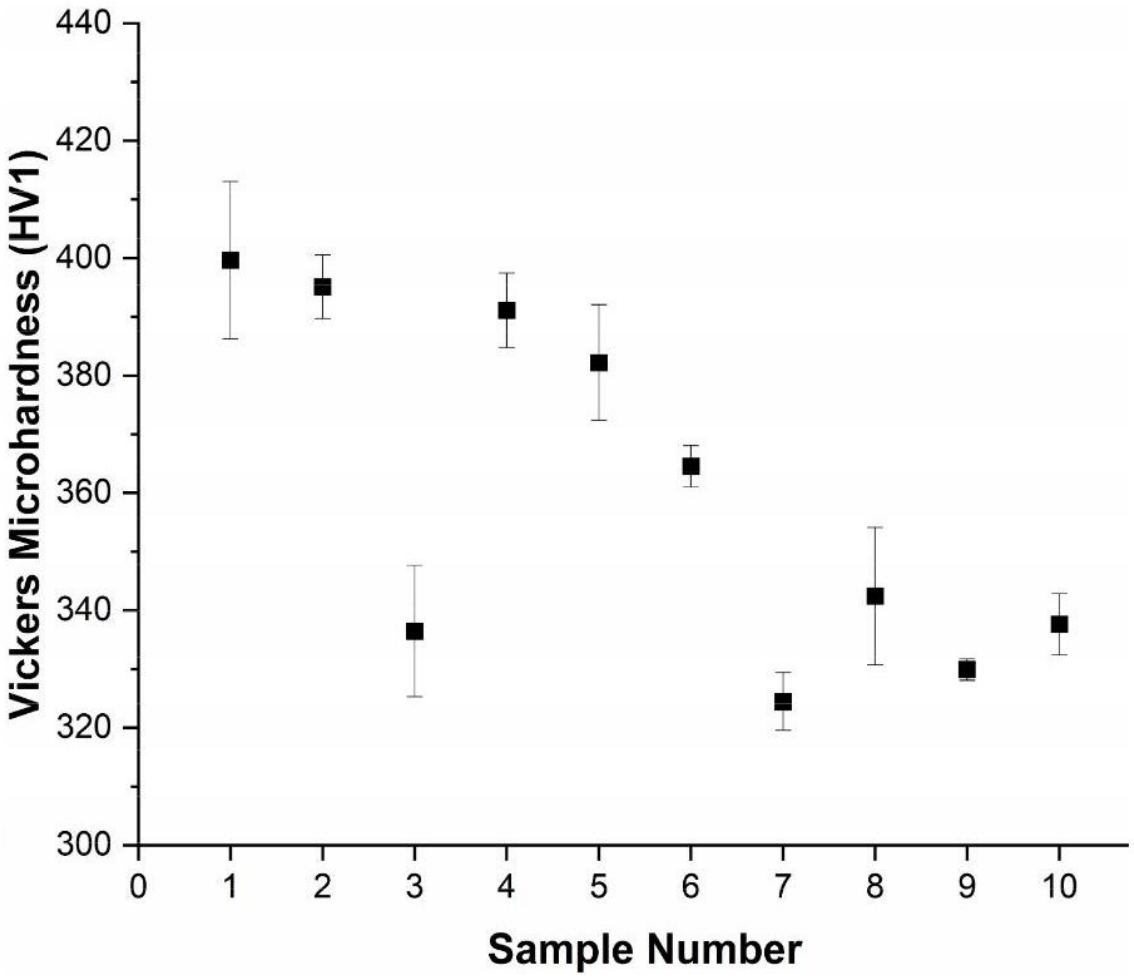


Figure 18: Vickers microhardness test results for as-received and heat-treated samples, n = 5.

actuation angular loss compared to any of the other samples at 9.22 ° and 6.75 °, respectively, as shown in Figure 19.

3.3.6. Recovery Strain of the Heat-Treated Nitinol Wires

The recorded recovery strains of the heat-treated nitinol wires, after bending the wires and then recovering once they were heated above the A_f temperature is shown in Figure 20. For the samples heat treated at 400 °C, an increasing extent of recovery in the strain values were observed with increasing heat treatment time. A similar trend was observed for the samples

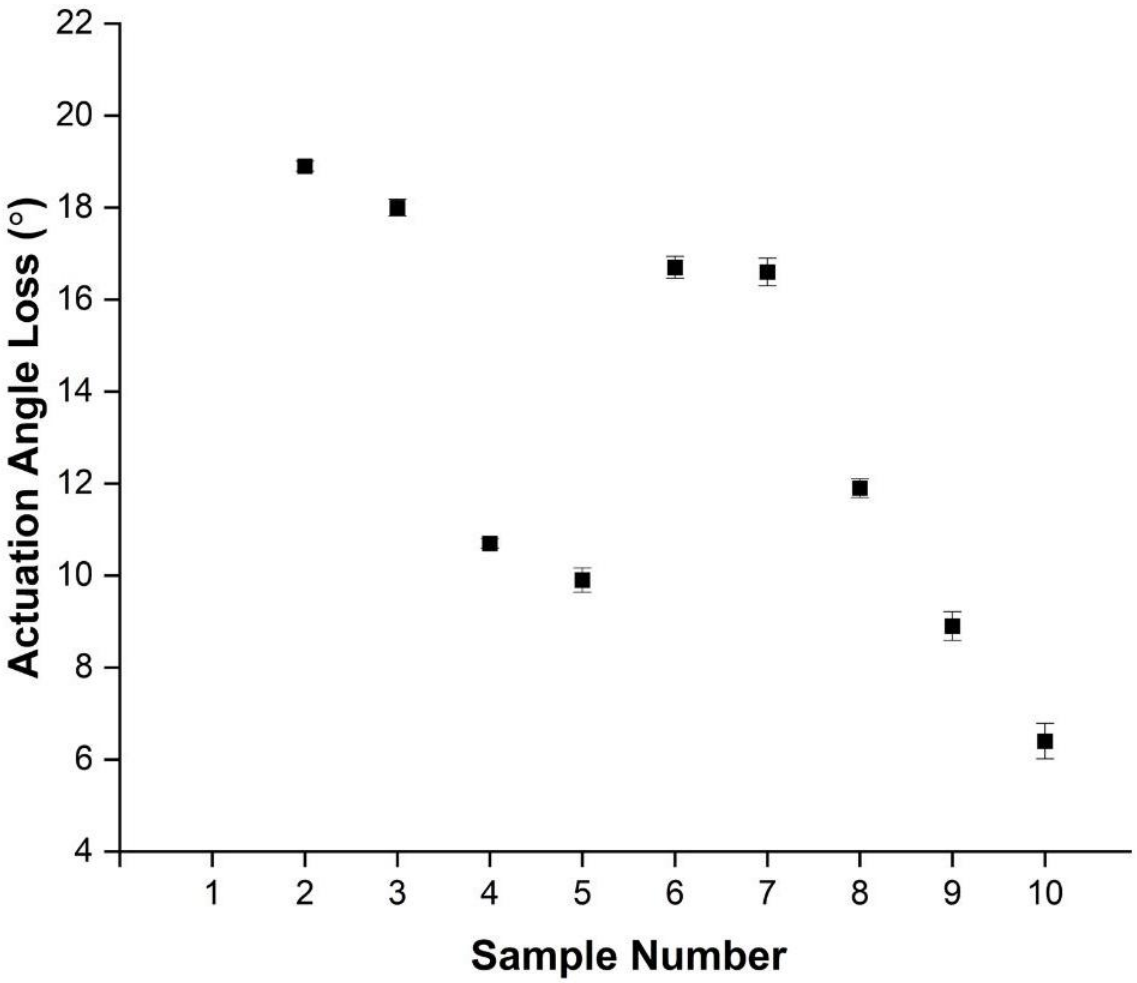


Figure 19: Loss of actuation angle from desired shape (°) for the heat-treated samples.

heat treated at 500 °C with maximum recovery strain achieved for the sample heat treated at 500 °C for the longest duration of 120 min.

For the samples heat treated at 450 °C, the lowest time of 30 min showed the lowest recovery in the strain values. Increasing the time of 60 min heat treatment showed an increase in the recovery strain value, whereas a further increase in the heat treatment time to 120 min resulted in a drop in the recovery strain value.

3.4. Discussion

Main aims of this study were to determine how the nitinol wire heat treatment process parameters relate to the resulting shape recovery response and mechanical properties. In this work, wire samples were heat treated in a box furnace at three different temperatures

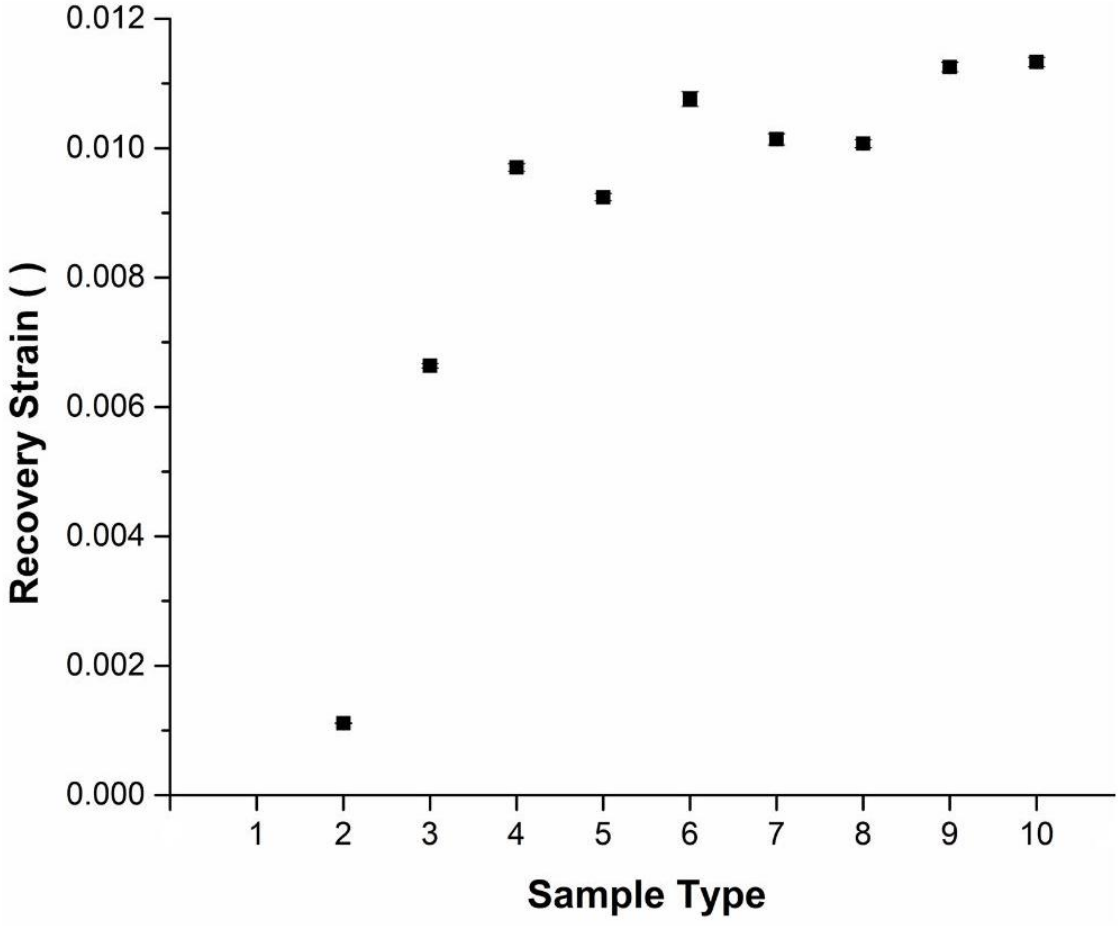


Figure 20: Recovery strain values for the heat-treated samples, n=3.

of 400 °C, 450 °C, and 500 °C with varying times of 30, 60, and 120 min for each temperature. The samples were heat treated in atmospheric conditions and air cooled outside the furnace. As shown in Figure 20, the recovery strain response of the heat-treated samples increased as the heat treatment temperature increased. A maximum recovery strain value was observed for the wires heat treated at 500 °C for 120 min. This result correlates well with the measured loss of actuation angle that was found to be the lowest for the wires heat treated in this condition, see Figure 19. There was an increase in the change in the radius of curvature of the wire as the heat treatment temperature of the wire was increased. Wires with the highest recoverable strain provide the maximum shape recovery capability.

The EDX analysis of the post-processed wires showed no significant changes in the chemical composition of the samples. The chemical composition of nitinol significantly influences the

performance of the shape memory alloy, demanding close monitoring of the sample's composition. As mentioned earlier, the chemical composition of the samples used in this study was found to be Ni55 wt.% and Ti45 wt.%. A more Ti-rich nitinol alloy exhibits better shape memory property and higher phase transformation temperature [119] [120].

The density of the phases present in the produced parts can be directly correlated to the hardness values measured. Ni_4Ti_3 precipitates have been identified in heat-treated NiTi samples with more precipitates occurring at higher ageing temperatures and with longer heat treatment periods as reported by Rondelli et al. [111]. The lower hardness values for the samples heat treated at 450 °C and 500 °C is likely caused by the increased presence of the Ni_4Ti_3 precipitates in the wire samples, thereby lowering the hardness values compared to samples heat treated at 400 °C [118], [121]. As indicated previously in the study conducted by Khalil-allafi et al. [97], at the ageing temperature range of 400 to 600 °C, heterogenous distribution of the Ni_4Ti_3 precipitates has been observed. It has also been reported that the grain size increases with increasing ageing temperature that leads to lowering of the hardness values. In the work of Adharapurapu et al. [118], the samples that were heat treated at 400 °C for 5 h exhibited the best hardness values. From this previous study, the sample heat treated at 500 °C for 5 h also displayed a lower hardness value, however, for sample heat treated at this temperature for longer periods of 10 h or more, the hardness increased. This finding directly correlates with our results. The trend of decreasing hardness values with increasing temperatures and times also is expected to be attributed to the formation of an increased Ti-rich matrix due to the formation and growth of Ni_4Ti_3 and Ni_4Ti_2 precipitates.

A clear indication of the changes in the A_f temperature has been observed because of the heat treatment process, see Figure 17. From the graph, it is apparent that there is a decrease in A_f temperature with increasing heat treatment temperature. The heat treatment time, however, has a relatively small effect on the transformation temperatures, indicating that the main driver for the reduction in A_f is the heat treatment temperature rather than time. The samples heat treated at same temperature of 400 °C but for varying times, however, show a general increase in A_f temperature with heat treatment time that has also been reported in the literature due to an increase in Ni_4Ti_3 precipitation [122], [123]. Furthermore, a noticeable increase in the sharpness of the transformation peaks was

observed with extended time and temperature. This trend was accompanied by a decrease in A_f and a heightened precision in the transformation peaks, as both temperature and time increased [98], [124]. This phenomenon can be attributed to the relaxation of residual stress and the correction of microstructural defects that hinder crystal mobility during heating. The alteration in the A_f temperature caused by the heat treatment process is advantageous, as it offers the potential for adjusting the phase change temperature according to specific application requirements.

In this work, a straightforward and quick method of calculating the actuation of a wire at the actuation angle was developed. The results show that the actuation improved with both heat treatment temperature and time. The largest shape recovery was achieved with the sample heated at the highest temperature for the longest time (500 °C for 120 min), while the lowest shape recovery was recorded at the lowest temperature and shortest time (400 °C for 30 min). The growth of the metastable finer Ti-rich precipitates with the increase in the heat treatment temperature to 500 °C resulted in more martensitic phases that increased the shape memory response.

This study explores the impact of heat treatment parameters on the performance of nitinol wires, specifically focusing on actuation characteristics. While the primary focus is on understanding the material behaviour, the results of this research can have direct applicability in industries where nitinol-based actuators are used. By optimizing the heat treatment parameters, the study shows how to enhance the actuator performance, which is valuable for the development of robotic, aerospace, and medical actuator devices. This work, therefore, adds a new scientific knowledge base to inform future practical product designs. The study utilizes a novel approach involving image analysis to measure recovery strain during wire actuation. This methodological innovation can be used by the scientific community as a new practical and robust technique for assessing shape memory alloy behaviour.

3.5. Conclusions

Wire samples of nitinol manufactured using traditional wire-drawing techniques were examined to determine the effect of heat treatment time and temperature on the density,

hardness, material composition, surface morphology, transformation temperature, angular displacement, and strain recovery. This study highlights that the homogeneity and presence of precipitates of nitinol are critical to final properties of the material. The conclusions drawn from the obtained results are as follows:

- There is a decrease in the density between the as-received samples and the heat-treated samples, except for sample 3. Sample 3 was treated at 400 °C for 60 min and an increase from the as-received density of 6.45 g/cm^3 to 6.85 g/cm^3 was observed. The results show that the heat treatment time and temperature can be used to control the density within the range of 5.85 to 6.85 g/cm^3.
- The hardness results show a general decrease in hardness with heat treatment time and temperature.
- From the EDX and SEM results, the as-received wire has a uniform distribution of Ni and Ti with a surface oxide layer due to titanium's highly oxidising nature.
- The DSC curves show that increasing heat treatment time and temperature decreases the Af temperature and increases the sharpness of the phase transition curves. This indicates that higher temperatures (500 °C) for longer times (120 min) results in an increased reduction of residual stresses and defects that impede crystal mobility.
- NiTi heat treated at 400 °C for up to 60 min and 450 °C for 60 to 120 min fails to result in a high level of shape memory response. Heat treating NiTi at 500 °C for 60 (8.9°) and 120 min (6.4°) results in an increasing shape memory effect with the greatest shape recovery observed in the sample treated for 120 min.
- The strain recovery increases with increasing heat treatment time and temperature. The maximum strain recovery occurred in the sample heated at 500 °C for 120 min.

In terms of limitations, the size of the samples was too small to allow XRD testing. Sheet samples could potentially be used to allow for XRD analysis due to its larger surface area. Future studies should prioritize in-depth investigations aimed at achieving the maximum shape memory effect tailored specifically to the desired application. Future work could also examine the heat treatment of the wire samples at higher temperatures (e.g., 550 °C or 600 °C) and for longer periods of time (e.g., 150 and 180 min). More rapid cooling of the samples

such as the use of water quenching of the wires after the heat treatment process should also be further examined.

Chapter 4: Investigating the Effect of Wire Drawing and Heat Treatment on the Response of $Ni_{50.9}Ti_{49.1}$ R-phase Actuators

Josephine Ryan Murphy, Muhannad A. Obeidi, Inam Ul Ahad, Dermot Brabazon. Investigating the Effect of Wire Drawing and Heat Treatment on the Response of Ni50.9Ti49.1 R-phase Actuators. Materials, *2025*, *18*, 4931.

This chapter builds upon the investigation of conventionally manufactured NiTi wires. The study examines the effects of both post-processing heat treatments and the thermomechanical processing history of the starting material, providing a deeper understanding of the relationship between processing conditions and the resulting functional properties. Furthermore, this work begins to establish a framework for the direct evaluation of NiTi actuator performance through experimental testing, enabling the measurement of key actuator characteristics such as stroke and actuation time.

Abstract

In this investigation, $Ni_{50.9}Ti_{49.1}$ wires which were cold rolled to 40 % and straight annealed at 480 °C, 510 °C, and 550 °C respectively were heat treated to shape set these wires as helical springs and enhance their SME for use as electro-mechanical actuators. These shape set spring actuators were heat treated at 350 °C, 400 °C, and 450 °C for 30, 60, and 90 minutes. The wires' performance as actuators was assessed on a custom-built testing rig, which measured both the stroke and actuation time for each wire. Additionally, the wires were characterised experimentally by DSC, XRD, and nano indentation. The final resulting properties of the R-phase transformation helical spring actuator is controlled by the competing mechanisms of dislocation annihilation, and precipitation of Ni_4Ti_3, as well as the prior thermomechanical treatment. The optimum conditions for actuator response in $Ni_{50.9}Ti_{49.1}$ 40 % cold worked wires was a straight annealing temperature of 480 °C and shape setting aging conditions of 450 °C for 60 minutes. These parameters resulting in the optimum combination of defect annihilation and density of precipitates resulting in a high stroke (56 mm), low hysteresis (2.68 °C) actuator with an actuation time of 6 s.

4.1. Introduction

Nitinol (NiTi) is a nickel-titanium shape memory alloy (SMA) of equiatomic composition. SMAs are alloys that exhibit two unique mechanical properties known as superelasticity (SE) and shape memory effect (SME) [125]. SE and SME are achieved due to a reversible, thermally activated transformation between the two main crystal phases of NiTi: a high-temperature austenitic phase (B2) with BCC crystal structure, and a low-temperature martensitic phase (B19') with monoclinic lattice structure [126], [127]. SE also refers to the material's ability to recover strains isothermally during a mechanical load/unload cycle without acquiring any residual stresses, while SME is defined by the material's ability to recover large deformations, returning to its original shape upon heating above a transition temperature [84].

While SE and SME have been found to exist in many different alloys, NiTi is the most popular Shape Memory Alloy (SMA) owing to its high tensile strength, corrosion resistance, and biocompatibility [105]. As a result, NiTi has numerous applications across a wide range of industries, generally availing of either SE or SME. For example, the biomedical industry makes use of NiTi's SE along with biocompatibility and corrosion resistance for devices such as catheters and stents, meanwhile the aerospace industry takes advantage of the SME, high force-to-weight ratio, and spark-free response to thermal stimuli for use as sensors and actuators [79], [80], [84]. The prevalence of either a SE or SME characteristic depends on the composition of the alloy, which in turn determines the phase. A higher titanium content results in higher transformation temperatures (TT), a martensitic phase, and an SME response, while a higher nickel content results in lower TT, an austenitic phase, and an SE response [128]. For example, Wen et al. [129] found that NiTi samples produced from powder with a Ni content of 50.73 at.% displayed SME, while NiTi with Ni content 50.93 at.% and 51.27 at.% displayed SE and had A_f temperatures of 55 °C, 31 °C, and 25 °C, respectively.

Although Ti-rich NiTi is generally used for SME, equiatomic or Ni-rich NiTi is more widely available and can - through thermomechanical processing - be used for SME applications. Ni-rich NiTi also shows reduced thermal hysteresis which is an important factor for actuators, allowing actuator activation and de-activation to occur within a smaller temperature, the mechanical properties of NiTi are dependent on the temperature of the operative

environment relative to the transformation temperatures for the alloy range [27] [130]. This means that to be able to tailor NiTi SMA actuators to a wide range of applications, SME Ni-rich NiTi must also be investigated.

As well as chemical composition, the processing routes of NiTi wire also drastically impact the material and mechanical properties. NiTi wires are produced by a thermomechanical process known as wire drawing, which involves a series of cold rolling through dies to reduce the diameter and inter-pass annealing, followed by straight annealing at various temperatures and times to control the final properties of the wire. The cold working process introduces lattice defects and randomly distributed dislocations into the microstructure, which can result in increased strength and reduce SME while annealing, depending on the annealing parameters, can rearrange or annihilate the dislocations as well as cause the formation and dissolution of precipitates such as Ni_4Ti_3, thereby altering the chemical composition of the matrix. The thermo-mechanical history is therefore instrumental in determining the material's properties [131][132][133][81].

The nanocrystalline grain structure formed due to cold work can impede B19' nucleation, resulting in the formation of the intermediate R-phase. Additionally, the strain fields introduced by precipitates such as Ni_4Ti_3 can further stabilise the R-phase [134]. R-phase can be beneficial for sensor and actuator applications due to its increased cycling stability and low temperature hysteresis, allowing it to operate in a smaller temperature range [123][135]. A trade off from the R-phase is the small recoverable strains (< 1%) compared to the martensite transformation strain (6 %) However the R-phase transformations can still be effectively used as SMA actuators when used in the form of a helical spring allowing much larger stroke per unit of length of the actuator and adequate work output despite the low recoverable strains [83][136]. In addition to having larger strokes, linear SME helical spring-based actuators are more compact than wire actuators [137].

Shape setting is performed by holding the material in the trained shape at an aging temperature for a specific duration, followed by quenching to entrain the higher austenite phase structure. Studies have also found that constraining NiTi for shape setting increases the effect of heat treatment on the material. Favier et al. [138] found that aging has a stronger

influence on the transformation and mechanical behaviour of $Ni_{50.8}Ti_{49.2}$ in constrained samples, indicating faster aging kinetics. This is attributed to the interaction between internal stresses from Ni_4Ti_3 precipitates and the externally applied stress during constrained aging.

Lenticular Ni_4Ti_3 precipitates form coherently with the matrix, generating anisotropic stress fields with compressive stress perpendicular to the precipitates. When an external stress is applied, the precipitates align preferentially with the external tensile stress to relieve internal stresses, perpendicular to the internal compressive stress. During constrained shape setting, NiTi undergoes a phase transformation to the B2 phase, attempting to recover its straight-annealed shape. However, the applied constraint prevents full recovery, leading to stress buildup, potential plastic deformation, and pinning of reoriented martensite, which hinders transformation and reduces shape recovery. Benafan et al. [85] found that heating a 10 mm rod of $Ni_{49.9}Ti_{50.1}$ at a rate of 15 °C min^{-1} relaxed these stresses, ultimately reaching zero stress at 450 °C. They also noted that isothermally holding the sample at a lower temperature above A_f for a period of time can also result in complete stress relaxation. Liu et al. [93] found that shape setting $Ni_{50.7}Ti_{49.3}$ 0.5 mm wire at temperatures above 450 °C showed negligible improvements in shape recovery compared to samples shape set at 450 °C for 60 minutes, and increased the risk of oxidation. Therefore, in this study, shape setting is performed at 350 °C, 400 °C, and 450 °C for 30, 60, and 90 minutes.

Much of the current literature focuses on the effect of wire drawing steps on the material characteristics of NiTi, wire as well as the influence of heat treatment on the R-phase. There is little research on the effect of the thermomechanical processing of NiTi wires on the functional properties of Ni-rich SMA actuators based solely on R-phase transformations. While there have been many studies on the effects of the degree of cold work and heat treatment on Ni-rich nitinol, they tend to focus on the SE [14][140]. In the case where SME is studied in Ni-rich nitinol, the actuator performance is not directly assessed but instead tested by methods such as the bend and free recovery test, which does not allow the measurement of properties such as actuator stroke [141][142]. Finally, in the case where the functional performance of SMA actuators is assessed using setups such as linear actuators, the materials used are Ti-rich NiTi [15][86][143]. This study aims to address gaps in the

literature related to the actuation performance of Ni-rich R-phase actuators. In particular, the effect of different wire drawing histories and shape setting parameters on the stroke and response times of NiTi helical springs. $Ni_{50.9}Ti_{49.1}$ wires from the same ingot with different thermomechanical histories were constrained and shape set as helical springs to investigate the effect of straight annealing and shape setting parameters on actuator performance. Actuator performance, including stroke and actuation time, were measured and reported herein using an in-house built rig and, the properties of the wires were characterised using DSC, XRD, SEM, and nano-indentation.

4.2. Materials and Method

4.2.1. Materials and Sample Preparation

In this study three distinct nitinol wires (denoted as Wire 1 (W1), Wire 2 (W2), and Wire 3 (W3).), fabricated using traditional wire drawing and straight annealing methods and supplied by Fort Wayne Metals, Castlebar, Co. Mayo, Ireland. All three wires originate from the same ingot material source with a composition of 50.90 atomic percent nickel (at. % Ni), and an ingot A_f temperature of -5.5 °C tested according to ASTM E2994 and ASTM F2063, respectively. All three wires were cold worked to 40 % resulting in a diameter of 0.46 mm, and an ultimate tensile strength (UTS) of 1450 MPa. During the straight annealing step, W1, W2, and W3 were annealed at 480 °C, 510 °C, and 550 °C, resulting in active austenite finish temperatures of 6.37 °C (W1), 23.11 °C (W2), and 44.58 °C (W3) respectively, as measured by DSC analysis in this study. The characterisation equipment utilised in this work is detailed in section 2.4. For clarity, the active austenite finish temperatures of the as-received wires are herein referred to as A_{f0} temperatures.

4.2.2. Heat Treatment and Shape Setting

A design of experiments (DoE) model with three parameters at three levels, as seen in Table 3, was employed to generate 27 distinct process parameter combinations. The complete set of process parameters, along with their respective sample numbers, is provided in Table 4. To ensure repeatability, three samples (n = 3) were prepared for each set of parameters, resulting in a total of 81 fabricated and tested samples.

From each of the three wires, 27 sections, each measuring 200 mm in length, were cut. To shape these sections into spring actuators, a helical thread with a diameter of 10mm and a pitch of 1mm was used as a mandrel. Each sample was mechanically fixed at one end and then wound around the mandrel within the thread groove. Six full rotations around the mandrel following the threaded groove were completed, and subsequently the wire was mechanically fixed at each end to maintain the spring configuration. The samples were then placed in a box furnace while attached to the threads, enabling simultaneous shape setting and aging treatments. The samples were heat treated in a box furnace at 350 °C, 400 °C, and 450 °C for 30, 60, and 90 minutes. Upon removal from the furnace, the samples were immediately quenched in water to establish a clear finish time and prevent further aging.

Table 3: DoE model of three parameters at three levels.

Level	**-1**	**0**	**+1**
Starting Wire	W1	W2	W3
Treatment Temperature (°C)	350	400	450
Treatment Time (min)	30	60	90

Table 4: Full table of the 27 process parameters used in this study.

Sample Name	**Starting Wire**	**Heat Treatment Temp (°C)**	**Heat Treatment Time (min)**
S1	W1	350	30
S2	W1	350	60
S3	W1	350	90
S4	W1	400	30
S5	W1	400	60
S6	W1	400	90
S7	W1	450	30
S8	W1	450	60
S9	W1	450	90
S10	W2	350	30
S11	W2	350	60

S12	W2	350	90
S13	W2	400	30
S14	W2	400	60
S15	W2	400	90
S16	W2	450	30
S17	W2	450	60
S18	W2	450	90
S19	W3	350	30
S20	W3	350	60
S21	W3	350	90
S22	W3	400	30
S23	W3	400	60
S24	W3	400	90
S25	W3	450	30
S26	W3	450	60
S27	W3	450	90

4.2.3. Stroke and Actuation Time

After heat treatment, the samples were removed from the threads and loaded onto the in-house-built NiTi actuator testing rig. A schematic of this experimental rig is shown in Figure 21, where the spring actuator 'A' is attached to the stationary wall of the testing rig on one side and connected to the bias load ‘D’ on the other via nylon wire, joined using floating connector blocks 'B'. The bias load, of mass 200 g, hangs from the nylon wire attached to the actuator while a Baumer Ultrasonic Distance Sensor (Model: U300.D50-DPMJ.72N) ‘E’ was employed to measure the displacement of the sample. To initiate the Shape Memory Effect (SME) and lift the bias load, a current of 2 A was applied across the actuator through electrical connections at 'C' for 10 seconds. A Fluke RSE600 Infrared Camera was used to record the temperature of the sample, and a LabVIEW program was used to control the current and to measure the data from the camera and displacement sensor. The experiments were carried out according to the steps below:

- The sample is loaded onto the rig at A and attached on either end by the connector blocks 'B'.
- Electrical connectors are attached at both ends of the sample at 'C'.
- The bias load 'D' is attached, causing the sample to stretch.
- Using a LabVIEW program, a current of 2 A is applied to the sample via the electrical connectors.
- The application of current causes the sample to contract and lift the bias load.
- The distance sensor 'E' connected to the LabVIEW program records the change in distance between the sensor and the bias load w.r.t time.
- The thermal camera connected to the LabVIEW program records the temperature of the sample w.r.t time during heating.
- After 10 seconds the current switches off and the sample is left to cool.
- The distance sensor and thermal camera continue to record data as the sample cools and stretches, lowering the bias load.
- The data from the displacement sensor is exported from the LabVIEW program and used to calculate the maximum stroke and the actuation.

This test process was repeated on each wire three times (n = 3). The data exported from LabVIEW can be used to plot the graph seen in Figure 22a. To calculate the stroke and actuation time, the noise from the displacement sensor is reduced using a Gaussian distribution function with gamma = 5. From the smoothed displacement the slope of the displacement curve is calculated, resulting in the curve seen in Figure 22b. Stroke is defined as Stroke = $s_1 - s_2$, where s_1 is the distance between the bias load and the displacement before current is applied and s_2 is the distance between the bias load and the displacement sensor after a current of 2 A has been applied for 10 seconds. Actuation time (t_a) is then defined as $t_a = t_2 - t_1$, where t_1 is the time at which the current is switched on and t_2 is the time at which the slope of the smoothed displacement curve is less than -0.5.

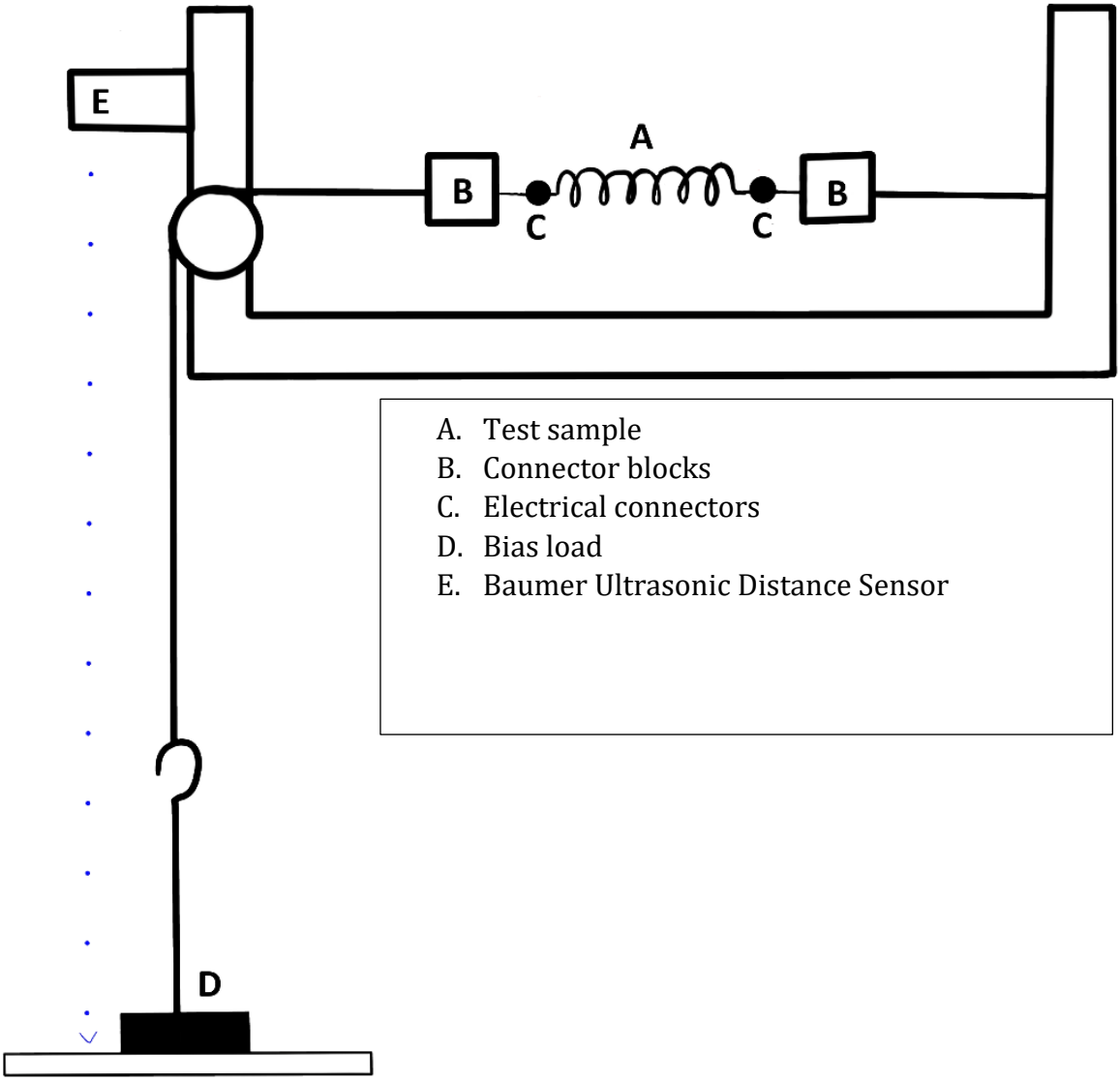


Figure 21: Schematic of in-house designed and built actuator testing rig.

4.2.4. Material Characterisation

Differential Scanning Calorimetry (DSC) analysis was conducted using a TA Instruments® Discovery DSC2500 instrument (± 0.025 °C) to determine the transformation temperatures (TT) of both the as-received and heat-treated wires. The wire samples for DSC were prepared by cutting the sample into sections using wire cutters and placing them into aluminium pan crucibles. These crucibles were then positioned in the DSC and prepared for testing by ramping the temperature to 100 °C at a rate of 100 °C/min and then holding isothermally for 5 minutes. The tests were then carried out by cooling the samples to -150

°C at a rate of 10°C/min, followed by an isothermal hold for 5 minutes, and subsequently heating to 150 °C at a rate of 10 °C/min.

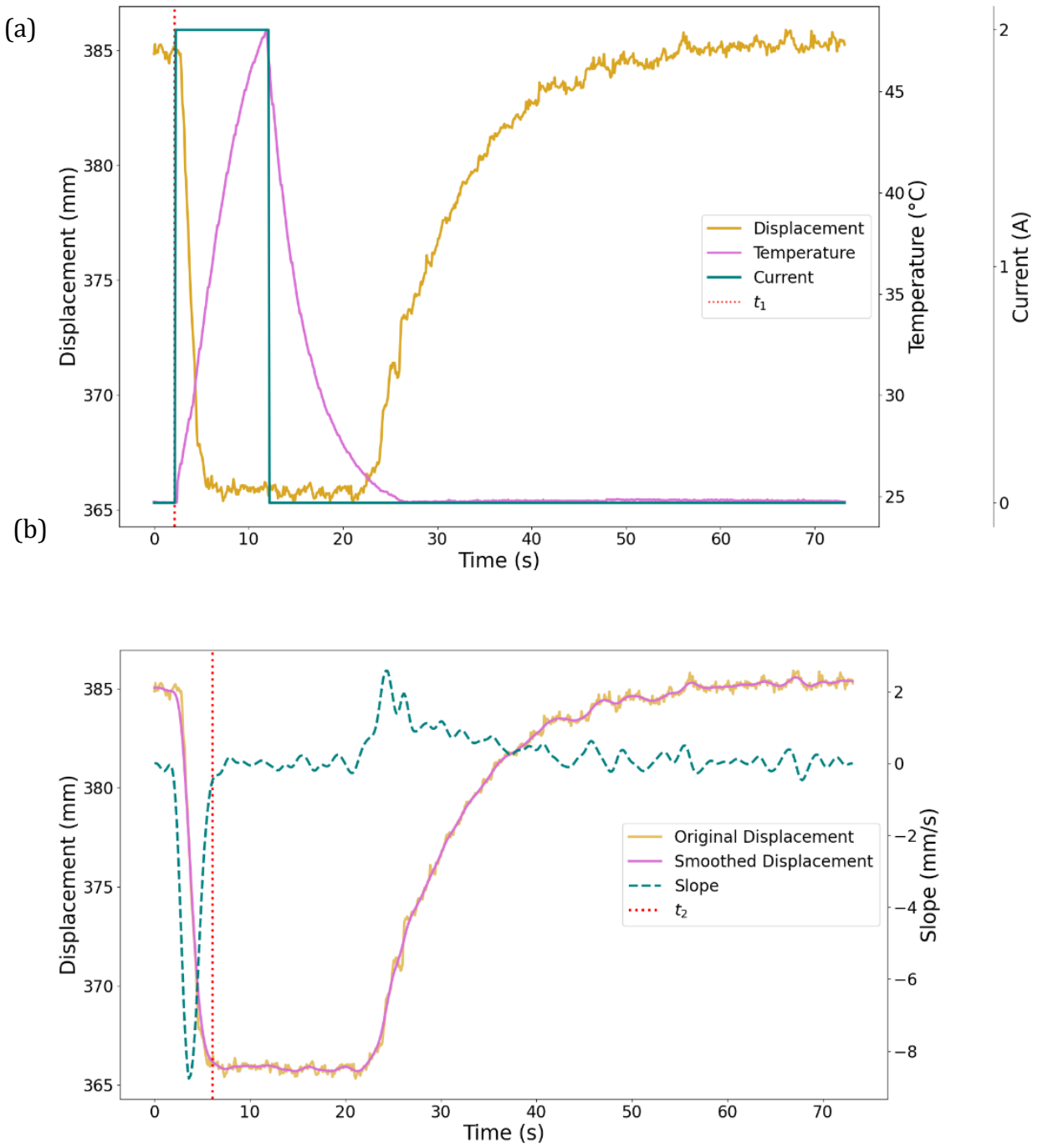


Figure 22: (a) Plot of the displacement, temperature, current, and t_1 from the LabVIEW data for sample 1. (b) plot of the original displacement, the smoothed displacement, the slope of the smoothed displacement and t_2.

X-ray Diffraction (XRD) tests were performed using the PANalytical X'Pert3 (± 0.0025 °). In preparation for XRD analysis, the wire sample segments were secured in resin. Once the resin had solidified, the resin-encased wire samples were ground down and polished to create a flat surface area suitable for XRD analysis. This process was carried out for wire samples 1 to 9, see Table 2, as well as for the as-received untreated wires W1, W2, and W3.

Nano-indentation tests were performed on a Bruker HYSITRON TI Premier using a Berkovich Indenter to measure the variation in hardness (H) and elastic modulus (E) in the wires. In these load-controlled tests, a maximum load of 5000 μN was applied at a rate of 1000 μN/s and held for 2 seconds before unloading. A total of 400 indents were made on each sample within a 300 μm by 300 μm square grid, with 15 μm spacing between individual indents. H and E were calculated from the load-displacement data for all 400 points on each sample using the Oliver-Pharr method [144]. The hardness is found from:

$$H = \frac{P_{max}}{A_p}$$

where P_{max} is the maximum indentation load and A_p is the projected area of contact which are both taken directly from the indentation test data [145]. And elastic modulus is found from:

$$E = \frac{1 - (v_s)^2}{\frac{1}{E_r} - \frac{1 - (v_i)^2}{E_i}}$$

where E_r is the reduced modulus taken directly from the indentation test data, E_i is the elastic modulus of the Berkovich indenter, and v_s and v_i are the Poisons ratio of NiTi and the indenter respectively [145]. The elastic modulus E_i and Poisson's ratio v_i of the Berkovich indenter are taken as 1141 GPa and 0.07 in this study, and the Poisson's ratio v_s used is 0.33 [146][147].

4.3. Results & Discussion

4.3.1. Effect of Low Temperature Aging on Actuator Stroke

The graph shown in Figure 23 presents the recorded displacements for each wire. The stroke achieved across all samples varies from the smallest stroke of 17 mm (± 3.0 mm) for S10 (W2, 350 °C, 30 min) to the largest stroke of 56 mm (± 1.0 mm) for S8 (W1, 450 °C, 60 min). There is a noticeable increase in actuator stroke with increasing heat treatment temperature and time until 450 °C for 60 minutes however, when aging time is increased to 90 minutes at 450 °C, actuator stroke decreases.

Dislocations introduced during the wire drawing process raises the stress required for plastic deformation, meaning that wires with a higher density of dislocations can store more energy during loading, which can be released on the reverse transformation. On the other hand, coherent Ni_4Ti_3 precipitates act in a similar way to the dislocations from cold work, acting as obstacles to dislocation motion, meaning the recovery stress of all samples increases with aging temperature and time. However, dislocations and precipitates also impede shape memory recovery and can prevent the material from undergoing the detwinning process or shape recovery during heating which is necessary for the SME [55][142][148]. It has also been reported that dislocations impede both B19' and R-phase transformation up to three times more than precipitates [40] therefore, despite the increase in precipitation with increasing aging temperatures and times, the stroke increases with aging temperature and time due to increased defect annihilation.

The overall general increase in actuator stroke with increased aging time and temperature is also attributed to the increased effectiveness of the shape setting process. As aging time and temperature increase, the shape setting improves, and the geometry of the wire becomes closer to the dimensions of the mandrel with less springback on removal. It was also clear on visual inspection that the lower aging temperature of 350 °C is insufficient for shape setting. This agrees with similar findings in the literature where Liu et al. [139] found that temperatures between 450 °C and 550 °C were best for shape setting of $Ni_{50.7}Ti_{49.3}$ wire stents, and Zhan et al. [148] found the best aging for shape setting thin $Ni_{50.53}Ti_{49.47}$ sheets was at 30 – 60 minutes.

The range of minimum and maximum stroke values observed across the tested samples varied among W1, W2, and W3. For W1, the stroke has a range of 38 mm, varying from 18 mm ± 1.5 (S1: 350 °C, 30 min) to 56 mm ± 1.0 (S8: 450 °C, 60 min). For W2 the stroke achieved has a range of 30 mm, varying from 17 mm ± 3.0 (S10: 350 °C, 30 min) to 47 mm ± 1.0 (S15: 450 °C, 60 min). In the case of W3, the stroke has a range of 27 mm, varying from 20 mm ± 2.5 (S22: 400 °C, 30 min) to 47 mm ± 3.5 (S26: 450 °C, 60 min). The variation between wire responses is due to the differences in their thermomechanical and heat treatment processing histories. Casati et al. [81] found that the drawing history carried out to achieve a given degree of cold work is crucial to the final properties of the wire. They found that the drawing history permanently alters the functional properties of the wire even after heat treatment and thermomechanical cycling. As the wires were all subject to the same degree of cold work but straight annealed at 480 °C, 510 °C, and 550 °C for W1, W2, and W3 respectively, the annihilation of defects would have been highest in W1 and lowest in W3.

At 350 °C the aging conditions are not sufficient for shape setting therefore, the stroke is primarily dictated by the degree of plastic deformation rather than shape memory recovery. For samples aged at 350 °C for 30 minutes, W3 has the highest stroke as it has the highest density of dislocations and thus the lowest plastic deformation. As aging time increases to 60 and 90 minutes, precipitation of Ni_4Ti_3 occurs, which decreases both the plastic deformation and the shape memory recovery resulting in W2 having the optimum balance between these effects. As the aging temperature increases to 400 °C and 450 °C, the aging conditions become sufficient for shape setting and thus the stroke is primarily dictated by shape memory recovery. As W1 has the lowest density of dislocations, which impede shape memory recovery, W1 achieves the highest stroke at the aging temperatures of 400 °C and 450 °C. The decrease in stroke displacement for all wires aged for 90 minutes indicates that the density of precipitates at 90 minutes could be inhibiting the SME. The optimum aging parameter for actuator stroke displacement for all wires is 450 °C for 60 minutes.

4.3.2. Effect of Low Temperature Aging (350°C to 450°C) on Actuation Time

From the results, the actuation time was found to vary between 3.4 and 7.1 seconds. At the low aging condition of 350 °C for 30 minutes, actuation time increased from W1 to W3 (4 s ± 0.1, 4 s ± 0.5, and 6 s ± 1.1 for W1, W2, and W3 respectively), which may be attributed to

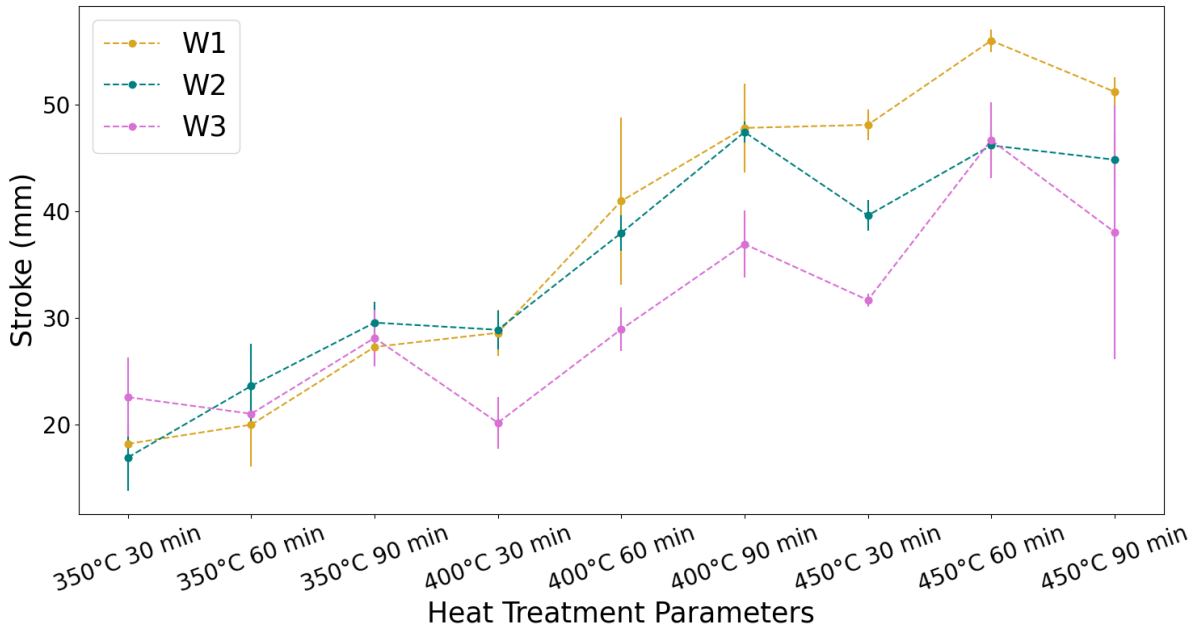


Figure 23: Graph of the average maximum stroke recorded from the heat-treated samples, n = 3.

the increase in A_f temperatures (42.72 °C, 46.15 °C, and 48.96 °C for W1, W2, and W3 respectively) requiring more time to complete actuation. However, as shown in Figure 24, there is no consistent trend in actuation time across all samples. This variability may be due to two competing factors: the increase in stroke and the decrease in A_f with higher aging temperatures. A larger stroke extends the actuator's travel distance, increasing actuation time, while a lower A_f reduces the time needed to reach the actuation temperature. Thus, actuation time is determined by the interaction between A_f temperature and stroke.

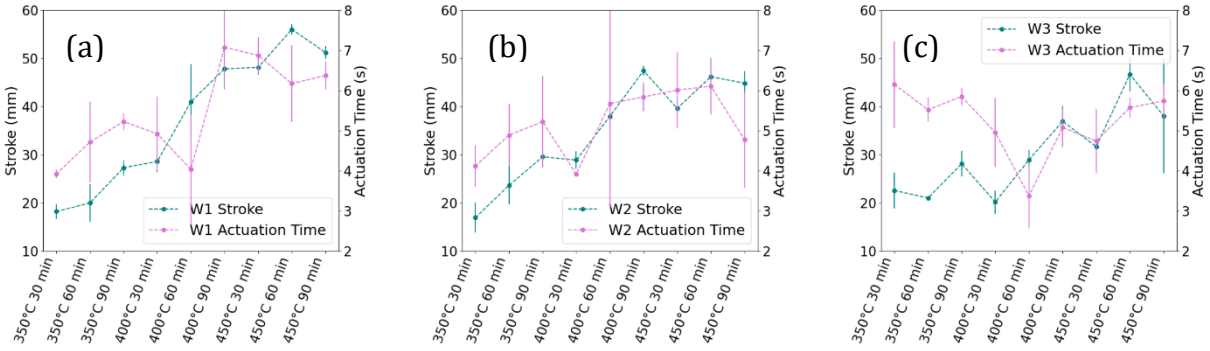


Figure 24: Graph of the actuation time and stroke for a) W1, b) W2, and c) W3 achieved by heat-treated samples, n = 3.

The thermal IR image data of S26 (450°C, 60 minutes) during testing is shown in Figure 25. Figure 25a and b show the 2 second delay that occurred between the application of current and the wire's corresponding heating and stroke response. This "dead time" is the duration required for the wire's temperature to reach the phase change temperature necessary to reverse martensite transformation [149]. Beyond this dead time, at 4 seconds, the wire's temperature has become uniform along its length, and the majority of the shape recovery has occurred. At 6 seconds, shape recovery is complete, as shown in Figure 25d which agrees with the results for sample 26 shown in Figure 24.

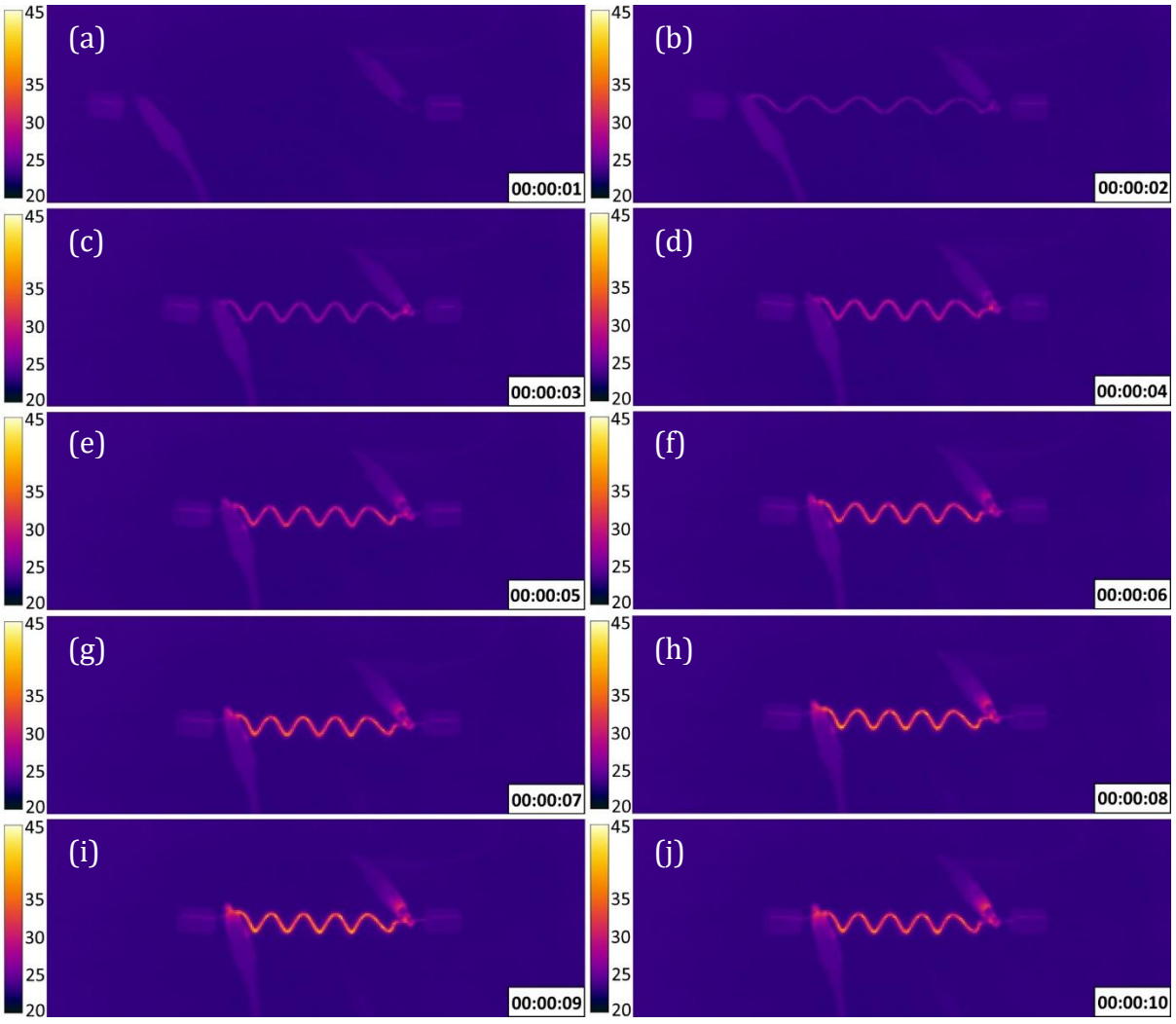


Figure 25: Thermal images (°C) and actuation timestamps (seconds) of sample 26 showing the effect over time of the current applied across the wire on the shape memory effect and temperature of the wire itself.

As rapid actuation is an important consideration in the functionality of actuators further work on the improvement of actuation time such as improved conductivity via alloying

elements such as Cu and rapid heating pulse methods to reduce the time taken for the element to become uniformly heated and reduce loss of energy to the surroundings [150][88], and reduced thermal hysteresis discussed in section 4.3.3 to decrease the deadtime.

4.3.3. Phase Transformation Temperatures and DSC Results

4.3.3.1. 3.3.1. DSC Peak Analysis

The DSC curves of all samples tested in this study exhibit a symmetric multi-step transformation (MST). Upon heating, two peaks appear: the first is the B19' to R-phase transformation and the second is the R-phase to B2 transformation. On cooling, two peaks are also observed, B2 to R-phase and R-phase to B19',.The second peak is broad and difficult to distinguish, preventing the identification of the B19' finish (M_f) or B'19 peak (M_p) and in some cases even the B19' start (M_s). It is common for the B19' transformation peak to become broad and seem not to appear at all in NiTi with high levels of retained cold work [44]. In fact, the R-phase is associated with a large decrease in M_s due to internal stresses and dislocations increasing the barrier for martensite phase transformations, thereby facilitating the formation of the intermediate R-phase [151]. Additionally, symmetric R-phase MSTs can be uniquely characterised by a large disparity in peak spacing between heating and cooling [44].

R-phase transformations occur most frequently in Ni-rich NiTi and are often reported in literature to be caused by defects induced by cold work and the presence of Ni_4Ti_3 precipitates, which increase the energy barrier to martensite formation, thus promoting the R-phase due to its lower activation energy [151][152][16][31]. The degree of cold work and annealing however, can significantly influence the transformation [44].

Figure 26 shows three plots comparing selected DSC curves to determine the effect of different parameters on the phase transformation sequence. Figure 26a compares the as-received wires. The DSC curves of the as-received wires show broad transformation peaks on both cooling and heating. On heating, W1 shows two overlapping peaks that both broaden and separate from W1 to W2 to W3. The increased separation of the two peaks from W1 to W2 and W3 suggests an increase in lattice defects, suppressing phase transformation. On

cooling, the two separate transformation peaks are present in W1 that broaden and separate from W1 to W3, such that the second peak seen in W1 is barely visible for W2 and disappears by W3. In fact, for W3, the second peak is not observed in the as-received sample or in samples heated at 350 °C for any length of time, or at 400 °C for 30 minutes.

Figure 26b compares the effect of heat treatment temperature using S1, S4, and S7, each from W1, and treated for 30 minutes at 350 °C, 400 °C, and 450 °C, respectively. There is a clear sharpening of peaks with increasing temperature across the samples for both heating and cooling curves. Additionally, the B19'→R and R→B2 peaks become closer with increasing temperature. Figure 26c compares the effect of heat treatment time using S7, S8, and S9, all from W1, and treated at 450 °C for 30, 60, and 90 minutes, respectively. There is a substantial increase in peak sharpness between S7 aged at 30 minutes and sample 8 aged at 60 minutes, and a minor decrease from S8 to S9 aged at 90 minutes. However, the difference in sharpness between samples treated at different times is considerably less significant than the difference observed between samples treated at varying temperatures. The separation between B19'→R and R→B2 peaks for all aging times at 450 °C is considerably reduced from the as-received sample, indicating a reduction in dislocations from cold work. Still there are two clear peaks visible, likely due to insufficient defect annihilation and the precipitation of secondary phases [153]. The broadening of DSC phase transformation peaks indicates the condition of stresses in the crystal. A broader peak indicates the presence of internal strains impeding the phase transformation caused by dislocations and precipitates, and the presence of stress-induced martensite [154][98][155]. Therefore, based on the DSC curves, the amount of residual stress-induced martensite and defects increases from W1 to W3. This indicates that increasing aging temperature and time reduce lattice defects and stress-induced martensite, and aging temperature has a more significant effect than aging time.

4.3.3.2. Transformation Temperatures

The M_s temperature, A_f temperature, and the cooling R-phase finish temperature (R_{cf}) obtained from the DSC experiments are shown in Figure 27 below. The results show that A_f and R_{cf} increase and the M_s temperature decreases from the as-received W1 to W3. This variation in TTs between the as-received wires is due to the differences in their thermomechanical history. Cold work, such as wire drawing, introduces dislocations and

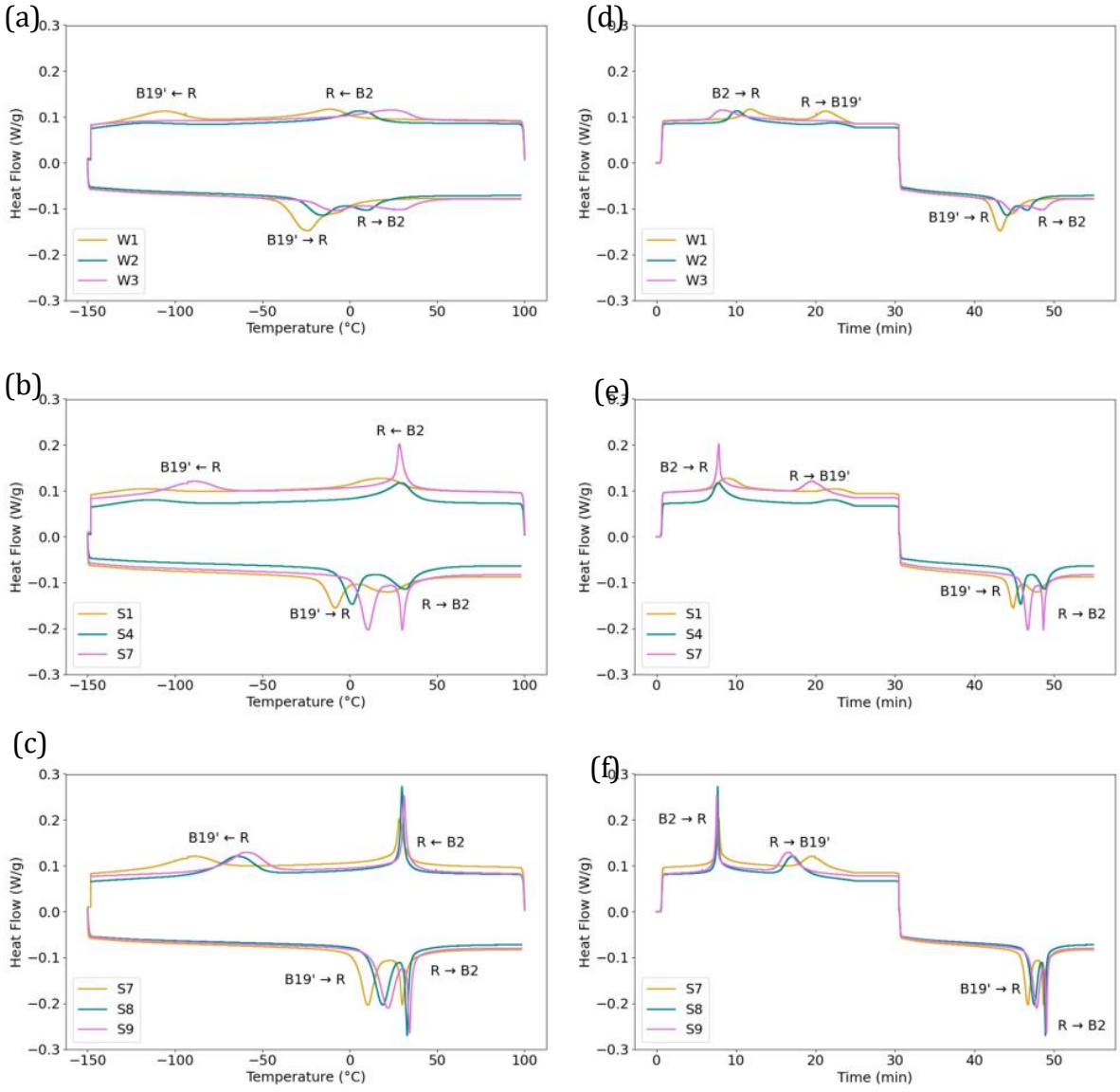


Figure 26: DSC curves of the as-received and untreated wires W1, W2, and W3 with a) heat flow vs temperature and d) heat flow vs time; S1, S4, and S7 with the same starting wire (W1) and heat treatment time (30 min) and different heat treatment temperatures of 350 °C, 400 °C, and 450 °C, respectively with b) heat flow vs temperature and e) heat flow vs time; S7, S8, and S9 with the same starting wire (W1) and heat treatment temperature (450 °C) and different heat treatment times of 30, 60, and 90 minutes respectively with c) heat flow vs temperature and f) heat flow vs time.

residual stresses that inhibit the phase transformations resulting in higher A_f temperatures, lower M_s temperatures, and stabilization of the R-phase. Annealing the wires reduces the number of dislocations and relieves the stresses, allowing phase transformation to occur more readily thus decreasing A_f and R_{cf} temperature and increasing M_s temperature [133][153][156][130][154].

The M_s temperature shows a large increase with both aging temperature and time. To fabricate room temperature SMA actuators using R-phase transformations, the M_s temperature must be kept below room temperature. Despite the large increase in the B19' transformation temperatures compared to B2 and R-phase, the aging conditions in this study maintain a low M_s temperature.

A significant reduction in the variation between W1, W2, and W3 of A_f and R_{cf} from the as-received wires to the heat-treated wires is seen in Figure 27b and c suggesting that the differences in microstructure amongst samples resulting from the thermomechanical processing were reduced through the further post-processing heat treatments.

The results also show a significant increase in A_f from the as-received wires to the samples aged at 350 °C for 30 minutes. Increases in the TTs of NiTi are commonly attributed to the precipitation of Ni-rich precipitates as they deplete Ni from the matrix, thus increasing A_f. This initial increase in A_f after 30 minutes of aging may therefore be due to the rapid precipitation of Ni_4Ti_3 at shorter times. A similar trend was seen by both Liu et al. [139] and Drexel et al. [96], who report a rapid increase in Af temperature owing to the high rate of Ni_4Ti_3 precipitation for samples annealed between 300 °C and 500 °C for 2 min to 30 min and increases only slightly at longer aging times. Additionally, as reported by Favier et al. [138], constraining the sample for shape setting during results in faster aging kinetics due to the interaction between the internal stresses from Ni4Ti3 precipitates and the applied external stress during constrained aging. Meaning that the saturation of precipitation could occur within the shorter aging times (< 30 min) in this study.

There is a general decrease in the A_f temperature with increasing aging temperature. While this may be assigned to a decrease in Ni_4Ti_3 precipitates, it is well reported in literature that the optimum temperatures for Ni_4Ti_3 precipitation occurs between 400 °C and 450 °C for Ni-rich NiTi. Therefore, it is likely that as the aging temperature increases, the dislocations and residual stress from cold work are more effectively removed while the continued precipitation of Ni_4Ti_3 prevents the A_f from returning to the pre-aged A_f for W1 and W2 [96].

For longer aging times, there is a slight increase in A_f at 350 °C, but no clear trend with aging time for higher aging temperatures. Kaya et al. [157] postulates that the increase in A_f with aging time is due to the influence of Ni_4Ti_3 precipitates on the martensite morphology. At lower aging times Ni_4Ti_3 precipitates are expected to be small and closely spaced. This creates local stress fields in the alloy matrix, facilitating the nucleation of large martensite plates at lower temperatures. As the aging time increases, the volume fraction of precipitates remains unchanged, but the size of the precipitates increases. As the precipitates grow, the distance between them increases reducing the effect of local stress fields on martensite nucleation, allowing the change in Ni content of the matrix to become the driving force for changes in A_f. The growth of Ni_4Ti_3 precipitates with time increases the Ni depletion thereby increasing A_f [157]. At higher aging temperatures, there are more factors influencing the change in A_f with aging time due to more effective recovery of retained martensite and the rearrangement and annihilation of dislocations coupled with increased volume of Ni_4Ti_3 which may account for the lack of correlation between A_f temp and aging time at 400 °C and 450 °C.

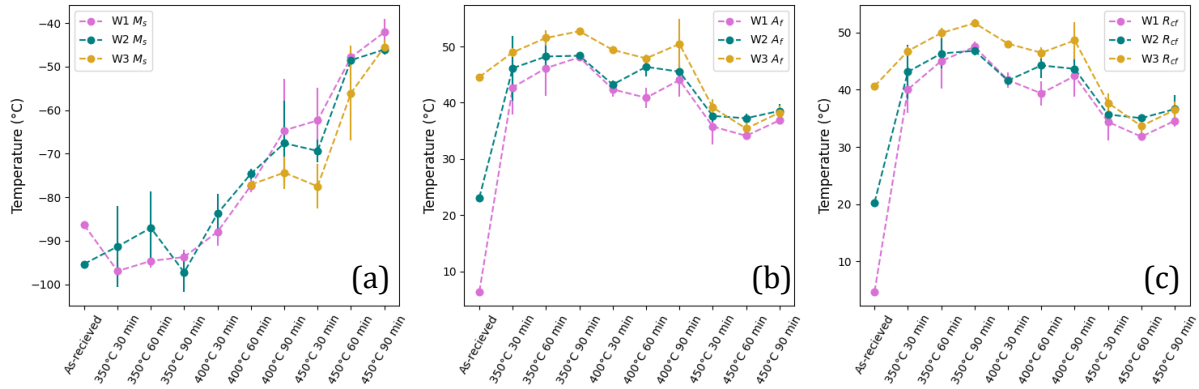


Figure 27: Graph of the a) B19' start temperature, b) B2 finish temperature and c) R-phase finish temperature, n = 3.

4.3.3.3. Thermal Hysteresis

Another characteristic of the R phase is a small thermal hysteresis of the B2-R phase transformation compared to that of the B2-B19' transformation, which decreases with increasing aging temperature [44][38]. This characteristic can be beneficial for applications in micro actuators with a high working frequency [42]. Thermal hysteresis 'η' is defined as the temperature differential between the forward and reverse phase change

transformations and can be calculated as the difference in temperature between the martensite peak or the R-phase peak on cooling and the austenite peak on heating[158]. Thermal hysteresis is attributed to the elastic misfit between phases and is generally lower in Ni-rich NiTi. However, the presence of dislocations, defects, residual stress, or chemical heterogeneity in the material, all of which are inherent to cold working, can greatly alter thermal hysteresis by either inhibiting or promoting the phase transformations [158].

Figure 28 compares the thermal hysteresis of the B19' to B2 transformation (η_M) defined as the difference between the B2 peak temperature (A_p) and M_s (note that as mentioned, the broad undefined nature of the B19' peaks in this study meant that M_p could not be identified and instead η_M was calculated as the difference in temperature between M_s and A_p and the thermal hysteresis of the R-phase to B2 transformation (η_R) defined as the difference between A_p and the R-phase peak on cooling (R_{cp}).

The results of this study, presented in Figure 28a, revealed a significant level of η_M in the wires, ranging from approximately 76.44 °C ± 3.87 to 138.19 °C ± 4.42. This level of thermal hysteresis is not uncommon in wire-drawn alloys. For example, in a study by Choi et al. [156], inducing a prestrain of 7% during wire drawing of NiTiNb alloys increased the A_f temperature from 22.02 °C to 139.18 °C and increased the thermal hysteresis from 31.59 °C to 122.5 °C. The results show that η_M for the as-received wires was lowest for W1 and highest for W3 although the exact value of η_M could not be calculated as the M_s temperature could not be identified due to the broad nature and low temperature of the martensite transformation. Among the aged samples, the results show a decrease in η_M with increasing aging temperature. The residual stresses and dislocations introduced during wire drawing can pin or stabilise the martensite, increasing the energy barrier for phase transformations and thus increasing thermal hysteresis. As annealing temperature increases the residual stress and dislocations decrease, facilitating phase transformations and reducing hysteresis [132][153]. The results also show that hysteresis increases with time for samples heated at 350 °C and decreases with time for samples heated at 400 °C and 450 °C. As discussed in section 4.3.1, precipitates have a similar effect to dislocations in terms of inhibiting phase transformation. These results indicate that 350 °C is insufficient for reducing dislocations and residual stress but sufficient for the precipitation of Ni_4Ti_3. At 350 °C, increasing aging

time results in an increase in Ni_4Ti_3 precipitates causing an increase in hysteresis. As the aging temperature is increased, it becomes sufficient for the removal of residual stress and dislocations which becomes the deciding factor for hysteresis. Thus, hysteresis decreases with aging time for aging temperatures of 400 °C and 450 °C, despite the continued precipitation of Ni_4Ti_3.

The results for η_R presented in Figure 28 b show a significantly smaller hysteresis compared to η_M ranging from 2.06 °C ± 0.01 to 4.77 °C ± 1.24. As with η_M, W1 has the smallest η_R of the as-received wires (4.79 °C) followed by W2 (5.14 °C) and then W3 (6.30 °C). Among the aged samples, there is a general decrease in η_R with aging temperature. Variations in η_R are much smaller than those of η_M due to the relatively smaller variation in A_p and R_{cp} temperatures compared to the M_s temperatures.

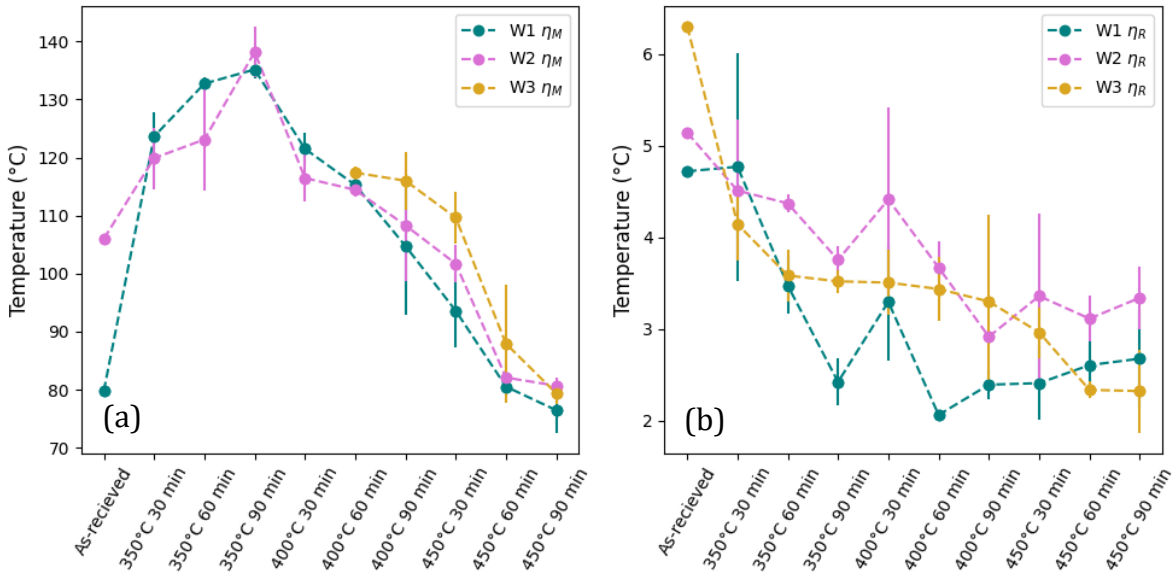


Figure 28: Graph of a) B2-B19' thermal hysteresis and b) B2-R thermal hysteresis of the as received and heat-treated samples calculated from DSC, n = 3.

4.3.4. Phase and Microstructure Analysis

NiTi wires with the same chemical composition but drastically different microstructures have been reported in literature as a consequence of the different degrees of cold work and annealing [159]. Figure 29 a-d shows the XRD patterns of as-received W1, W2, and W3 and the heat-treated wires S1 – S9. Due to the wire's small diameter of 0.46mm, achieving a sufficiently large surface area of material to obtain clear peaks was not possible for all

samples. The primary phases identified in these samples were austenite, martensite, and R-phase. In the as-received wires there is a single peak at approximately 2θ = 42 which splits into two peaks in the aged samples. The second peak at approximately 2θ = 39 represents the R-phase. This therefore indicated that aging stabilised the R-phase. As the density of defects decreases from the as-received samples to the aged samples, it can be concluded that the stabilisation of the R-phase is caused by the precipitation of Ni_4Ti_3.

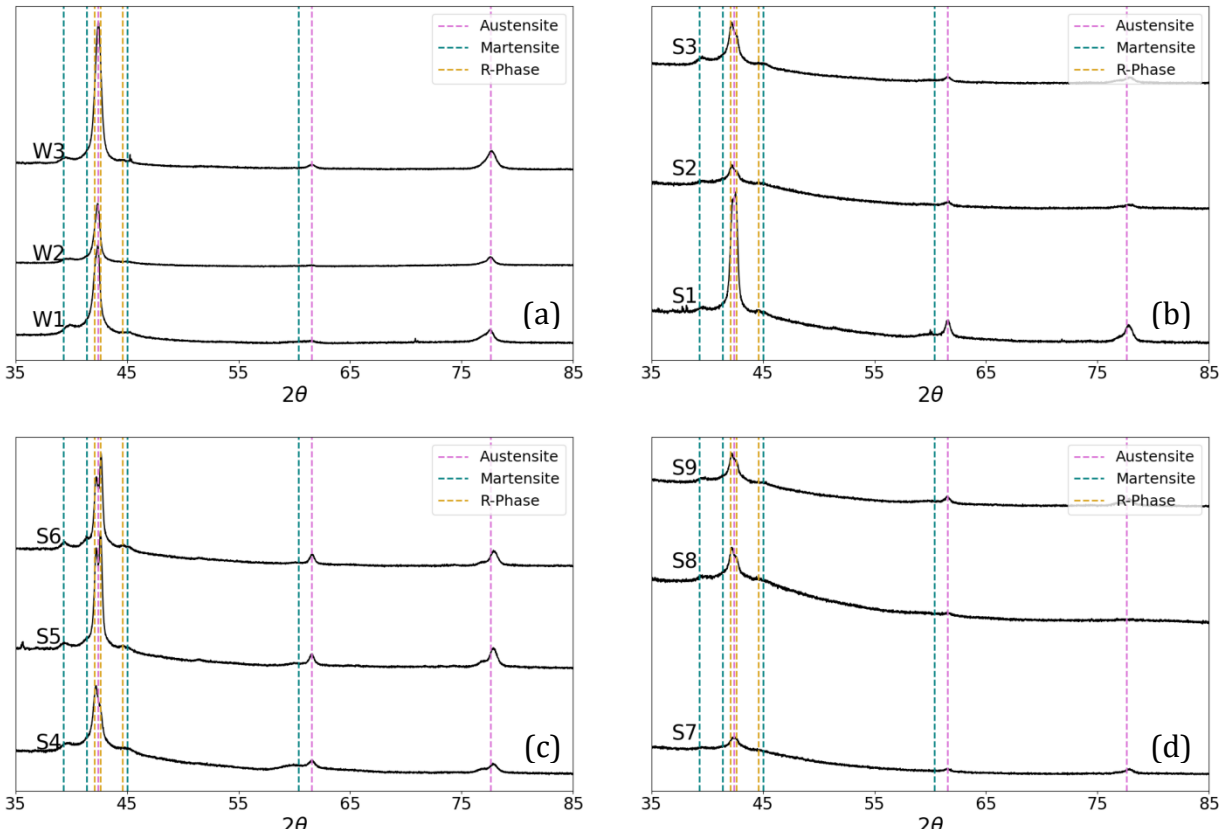


Figure 29: XRD patterns showing the presence of the austenite, martensite, and R-phase in (a) W1, W2, and W3 before heat treatment with sample 6 (W1, 400 °C, 90 min) as a control, (b) samples 1-3 (W1, 350 °C, for 30, 60, and 90 minutes respectively) with sample 6 as a control, (c) sample 4-6 (W1, 400 °C, for 30, 60, and 90 minutes respectively), and (d) samples 7-9 (W1, 450 °C, for 30, 60, and 90 minutes respectively) with sample 6 as a control.

4.3.5. Mechanical Properties

Table 5 provides a summary of the average values obtained from the nano indentation tests which represent 400 points of measurements of each sample. Hardness (H) and Elastic Modulus (E) were calculated from the nanoindentation results using the Oliver-Pharr method [144]

Table 5: Average values of the hardness and elastic modulus obtained from the nano indentation tests.

Sample	E (GPa)	H (GPa)
W1 (as-received)	55.8 ± 12.5	4.17 ± 1.36
S3 (W1, 350 °C, 90 minutes)	65.5 ± 10.5	3.52 ± 0.83
S8 (W1, 450 °C, 60 minutes)	60.7 ± 11.5	2.79 ± 0.84
W2 (as-received)	59.2 ± 8.81	4.34 ± 1.01
S12 (W2, 350 °C, 90 minutes)	64.8 ± 9.44	3.73 ± 0.84
S17 (W2, 450 °C, 60 minutes)	60.4 ± 12.6	3.06 ± 0.96
W3 (as-received)	59.9 ± 10.2	4.24 ± 1.13
S21 (W3, 350 °C, 90 minutes)	56.1 ± 14.3	3.16 ± 1.18
S26 (W3, 450 °C, 60 minutes)	60.5 ± 10.5	3.2 ± 0.82

The elastic modulus is a measure of the stiffness of a material and its ability to resist elastic deformation or deflection under an applied force and is dependent on factors including density and size of precipitates, grain size, defects, and volume fraction of phases present [160][161]. It is often reported in the literature that the B19' phase has a lower elastic modulus than the B2 phase and that the elastic modulus typically ranges from 18.45 GPa to 45 GPa for B19' and 41 GPa to 75 GPa for B2 [162][163][160]. However, a wide range of values for both phases has been reported in the literature. For example, Obeidi [164] reported an elastic modulus of between 62 GPa and 79.5 GPa for B19', and Huang et al. [165] reported an elastic modulus of 73.7 +/- 4.2 for B19' and 80.1 GPa for B2. As well as the main B2 and B19' phases, Wagner & Windl [166] reported that the elastic modulus of the pure B2 phase increased from 71 GPa to 108 GPa due to the precipitation of Ni_4Ti_3 and Yang et al. [161] reported an increase from 118 GPa in the B2 phase to 163 GPa with the addition of Ni_4Ti_3 precipitates. Fine, densely distributed Ni_4Ti_3 precipitates inhibit dislocation motion which increases the elastic modulus. An increase in density of precipitates increases this effect further, however as the size of the precipitates increases they become incoherent and the elastic modulus decreases [148][118]. In addition to the volume fraction of phases present and the precipitation of Ni_4Ti_3, it has been reported that aging causes an increase in grain size and that for grain sizes of less than 60 nm, the elastic modulus decreases with

increasing grain size due to the larger grains decreasing the stress required to form stress-induced martensite [152][167].

W1 and W2 show an initial increase in E for aging condition 350 °C for 90 minutes, followed by a decrease for aging condition 450 °C for 60 minutes. For W3, E decreases for aging condition 350 °C for 90 minutes and increases for aging condition 450 °C for 60 minutes. For W1 and W2, the increase in E from the as-received samples to those aged at 350 °C for 90 minutes may be due to the precipitation of Ni_4Ti_3, which increases E. Conversely, the decrease in E for samples aged at 450 °C for 60 minutes may be attributed to a decrease in the density of defects. The decrease in E from the as-received samples to those aged at 350 °C for 90 minutes in W3 may be due to the increase in volume fraction of the lower elastic modulus B19' phase as the results of this study show that this sample was found to have the highest TTs and the most martensitic microstructure, the increase in E for aging condition 450 °C for 60 minutes may be due to the increase in the volume fraction of the higher elastic modulus B2 phase as TTs decrease and the microstructure becomes more austenitic.

The hardness of the NiTi wire is a consequence of the microstructure owing to its thermomechanical processing and post process aging. Frick et al. found that hardness in cold-draw $Ni_{50.9}Ti_{48.1}$ wires is primarily dependent on dislocation density and that aging between 350 °C and 550 °C reduces the hardness due to the annihilation of dislocations [168]. Morawiec at al. found that hardness increased with cold rolling due to an increase in dislocation density. They also found that hardness decreases linearly with increasing aging temperature above 400 °C. They attributed the decrease in hardness between 400 °C and 500 °C to the reduction in dislocation density however, they found that although the hardness continues to decrease at temperatures above 500 °C, there is no further decrease in dislocation density. The decrease at temperatures above 500 °C is therefore said to be due to some additional factors [154].

The precipitation of Ni_4Ti_3 causes an increase in hardness and decrease in ductility due to precipitation hardening. Hardness has a complex dependence on precipitate formation and is significantly affected by the size, volume, and interparticle spacing of the precipitates [118][167]. According to Tahaei et al., the hardness and resistance to martensite

transformation are determined by the size of Ni_4Ti_3 precipitates, finding that hardness is highest when precipitates are around 10 nm and hardness decreases as precipitate size increases [167]. This is because small precipitates are coherent with the matrix, making them more effective at inhibiting dislocation motion. As aging temperature and time increase the precipitates grow and coarsen becoming incoherent with the matrix, decreasing hardness [168]. For example, Kaya et al. found that hardness was relatively unchanged by increasing aging temperature from 400 °C to 500 °C, but decreased with increasing aging time from 1 hour to 24 hours, attributing this to an increase in precipitation size and interparticle distance [157]. Increasing aging temperatures can also reduce hardness if the temperature exceeds the conditions for Ni_4Ti_3 precipitation. For example, Drexel et al. reported that aging $Ni_{50.8}Ti_{48.2}$ wires between 350 °C and 450 °C resulted in the precipitation of Ni_4Ti_3 but aging at higher temperatures caused the precipitates to dissolve [96].

The results show a general decrease in the average nano hardness of the as-received wires with aging. The presence of precipitates or a high density of dislocations essentially affects the hardness of NiTi in the same way. In either case, they inhibit plastic flow, which increases hardness. The difference is that dislocations are reduced during aging while precipitates are created. Therefore, the effect of aging on the hardness of NiTi is a function of two opposing processes – the annihilation of dislocations and growth of Ni_4Ti_3 precipitates [168]. Based on the literature and the nanoindentation results of this study, the dislocations and retained martensite introduced during the wire drawing process contributed to the relatively high hardness values of the as-received wires (4.17 GPa, 4.34 GPa, and 4.24 GPa for W1, W2, and W3, respectively). The overall decrease in hardness with increasing aging temperature suggests that hardness is determined by dislocation density, which is in agreement with the findings of Frick et al. mentioned above [168]. As the aging temperature increases, the dislocation density decreases, leading to a decrease in hardness.

The distribution of the hardness results for all 400 data points on each sample is visually illustrated in Figure 30. The hardness values for the as-received W1, W2, and W3 were distributed from 1 GPa to 10 GPa, with the main peak at 3.7 GPa, 4.6 GPa, and 4.0 GPa, respectively. The distribution of hardness values decreased from the as-received wires to the aged wires, and among the aged samples, the hardness distribution decreased with

increased aging temperature. The hardness for samples aged at 350 °C for 90 minutes were distributed from 0.75 GPa to 8.75 GPa. Main peaks were identified at 3.7 GPa and 4.2 GPa for S3 (W1) and S12 (W2), respectively. The distribution is wider for S21 (W3) and appears to have two main peaks around 2.4 GPa and 3.8 GPa. The hardness for samples aged at 450 °C for 60 minutes were distributed from 0.5 GPa to 6.25 GPa, with main peaks at 3.3 GPa, 3.6 GPa, and 3.3 GPa for S8 (W1), S72 (W2), and S26 (W3), respectively. Hardness distribution values within the same sample indicate a heterogenous distribution of precipitates and stress-induced B19' phase [152]. The high variability in the nano hardness in the as-received wires therefore indicates a high degree of stress and phase variation owing to the wire drawing process. The decrease in distribution with increased aging temperature indicates a reduction in stress-induced martensite and lattice defects from the wire drawing process and a more homogeneous distribution of precipitates. The two main peaks for S21 could represent two distinct phases in the material, potentially due to a higher degree of retained martensite or defects.

Table 6: Average elastic modulus (E) and hardness (H) calculated from nano-indentation results, n = 400.

Sample	E (GPa)	H (GPa)
W1 (as-received)	55.8 ± 12.5	4.17 ± 1.36
S3 (W1, 350 °C, 90 minutes)	65.5 ± 10.5	3.52 ± 0.83
S8 (W1, 450 °C, 60 minutes)	60.7 ± 11.5	2.79 ± 0.84
W2 (as-received)	59.2 ± 8.81	4.34 ± 1.01
S12 (W2, 350 °C, 90 minutes)	64.8 ± 9.44	3.73 ± 0.84
S17 (W2, 450 °C, 60 minutes)	60.4 ± 12.6	3.06 ± 0.96
W3 (as-received)	59.9 ± 10.2	4.24 ± 1.13
S21 (W3, 350 °C, 90 minutes)	56.1 ± 14.3	3.16 ± 1.18
S26 (W3, 450 °C, 60 minutes)	60.5 ± 10.5	3.2 ± 0.82

4.4. Conclusions

This study investigated the impact of thermomechanical processing on the actuation performance of $Ni_{50.9}Ti_{49.1}$ electromechanical helical spring actuators. The primary focus was on the effects of wire drawing history and heat treatment parameters, including straight

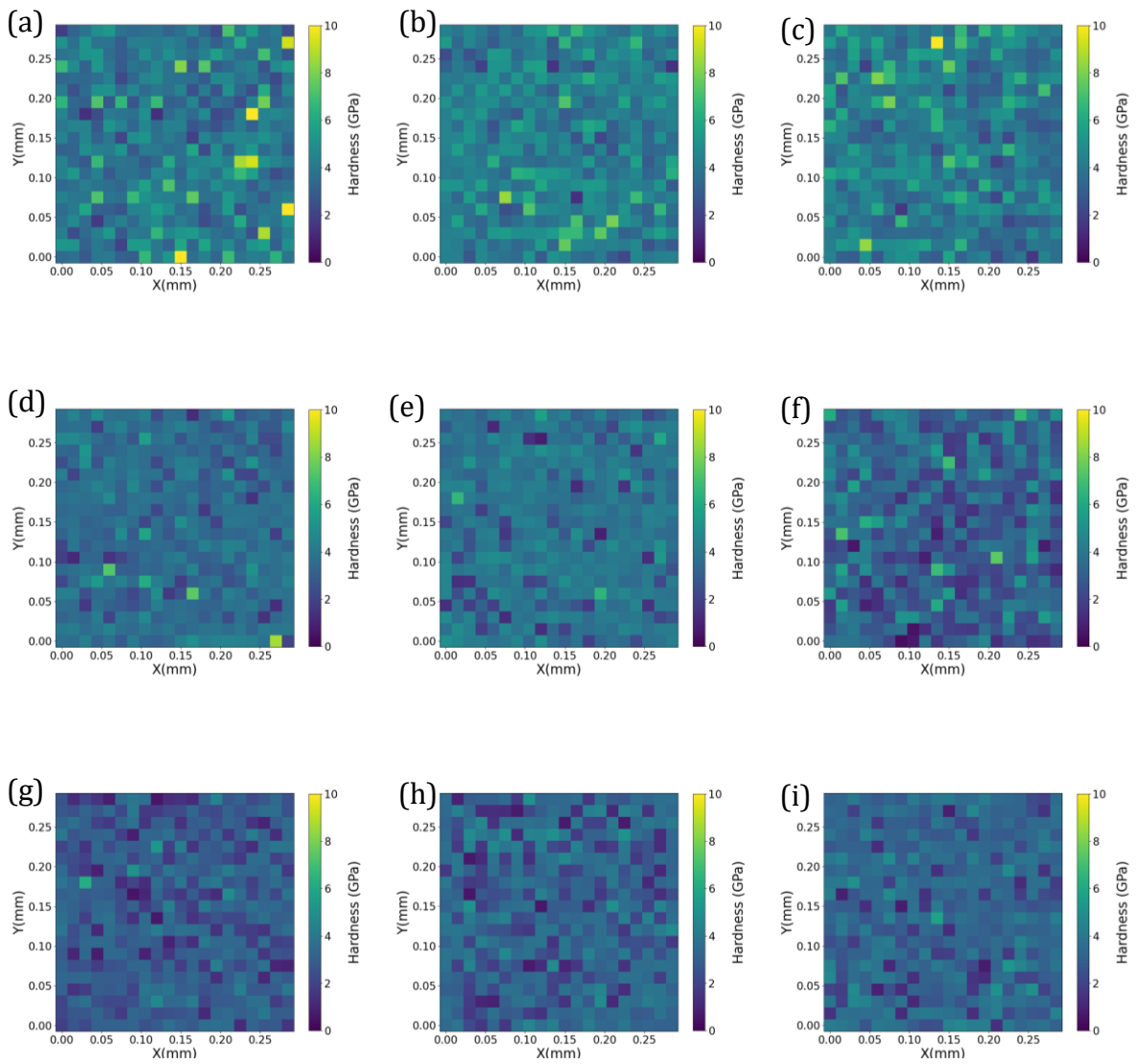


Figure 30: Hardness maps illustrating the measured nano hardness values at each of the 400 indentation points on each sample (a) W1 (as-received), (b) W2 (as-received), (c) W3 (as-received), (d) S3 (W1, 350 °C, 90 min), (e) S12 (W2, 350 °C, 90 min), (f) S21 (W3, 350 °C, 90 min), (g) S8 (W1, 450 °C, 60 min), (h) S17 (W2, 450 °C, 60 min), and (i) S26 (W3, 450 °C, 60 min).

annealing and shape setting conditions, on the stroke, actuation time, and transformation temperatures of the Ni-rich nitinol springs.

The findings highlight that the final actuator properties are influenced by a combination of dislocation annihilation, Ni_4Ti_3 precipitation, and the thermomechanical processing history. It was observed that increasing aging temperature and duration improved actuator stroke up to an optimal condition, beyond which excessive precipitation inhibited shape memory recovery. The optimal processing parameters for maximizing actuator stroke while

maintaining low hysteresis were identified as straight annealing at 480 °C, followed by shape setting at 450 °C for 60 minutes. These conditions achieved the best balance between defect annihilation and precipitation hardening, yielding a high-performing actuator with an A_f temperature of 34.11 °C ± 0.34 °C, a stroke of 56 mm ± 1.0 mm, a thermal hysteresis of 2.68 °C ± 0.26 °C, and an actuation time of 6 s ± 1 s.

Unlike conventional NiTi actuators that rely on martensite transformation, this study investigates $Ni_{50.9}Ti_{49.1}$ helical spring actuators operated through an R-phase transformation. The stabilization of the R-phase due to controlled thermomechanical processing results in lower hysteresis, making it particularly advantageous for applications requiring precise actuation. Additionally, while Ti-rich NiTi is typically preferred for actuator applications due to its superior shape memory effect, this study shows that Ni-rich NiTi can be effectively tailored through thermomechanical treatments to achieve comparable or even superior actuation performance, with the added benefits of reduced thermal hysteresis.

Microstructural and phase transformation analyses confirmed that the Ni_4Ti_3 precipitates played a crucial role in stabilizing the R-phase, which contributed to the observed actuation behaviour. Differential Scanning Calorimetry (DSC) results demonstrated a general reduction in transformation temperature hysteresis with increasing heat treatment temperature. Furthermore, nano-indentation analysis revealed a decrease in hardness with increasing aging temperature, indicating effective dislocation recovery and a transition toward a more homogeneous microstructure.

This study provides valuable insights into the processing-structure-property relationships in Ni-rich nitinol actuators, emphasizing the potential for tuning thermomechanical treatments to optimize actuator performance. Future work should explore alternative alloying strategies and advanced processing techniques, such as rapid heating pulse methods, to further enhance actuation speed and efficiency.

Chapter 5: Effect of PBF-LB Process Parameters and Strut Diameter on the Microstructure and Phase Transformation Behaviour of Ti-rich Nitinol Lattice Structures

Josephine Ryan Murphy, Nicole Church, Nicholas Jones, Paul Healy, and Dermot Brabazon. Effect of PBF-LB Process Parameters and Strut Diameter on the Microstructure and Phase Transformation Behaviour of Ti-rich Nitinol Lattice Structures. Accepted. Progress in Additive Manufacturing, *2026.*

This chapter introduces additively manufactured NiTi and represents an important progression in the work presented throughout this thesis. While additive manufacturing of NiTi has experienced rapid growth in recent years, it remains a relatively underexplored area within the literature. As such, it provides a natural extension to the investigation of NiTi shape memory alloy actuators undertaken in this research. This chapter examines the influence of both the process parameters and the part geometry on the resulting microstructure and phase transformation behaviour of NiTi produced by laser powder bed fusion.

Abstract

This study examines how volumetric energy density (VED) and lattice strut diameter affect the microstructure, composition, and thermal behaviour of Ti-rich NiTi shape memory alloy lattices produced by laser powder bed fusion (PBF-LB). Lattices with strut diameters of 0.5, 1.0, and 1.5 mm were fabricated across a range of VEDs, and their properties were systematically characterized. Results show that strut diameter critically influence density, Ni evaporation, and transformation behaviour. Thinner struts exhibited higher relative density at low VEDs (98.9 % at 31 J/mm^3), but increased Ni loss (0.32 at.% to 0.45 at.%) and chemical heterogeneity. Thicker struts exhibited reduced Ni loss (0.28 at.% to 0.40 at.%) and achieved higher maximum densities at mid-range VEDs (99.4 % at 42 J/mm^3). However, they exhibited increased residual stress resulting in higher thermal hysteresis. The 1.0 mm strut diameter provided the most stable transformation temperatures and lowest thermal

hysteresis. These findings highlight the necessity of optimizing both process parameters and geometry to engineer NiTi actuators with tailored functional properties.

5.1. Introduction

Nitinol (NiTi) is a binary nickel-titanium alloy with unique functional properties known as superelasticity (SE) and the shape memory effect (SME) arising from the reversible phase transformation between the high-temperature austenitic phase and the low-temperature martensitic phase [169]. In addition to SME and SE, NiTi exhibits superior wear and corrosion resistance [152], biocompatibility [48], high damping capacity [103], and thermomechanical performance [170]. These characteristics have led to the widespread use of NiTi in the automotive, aerospace, and biomedical industries [171]. However, due to NiTi's poor machinability - owing to its high ductility, work hardening rate, and low thermal conductivity, all of which contribute to rapid tool wear and poor surface finish during traditional processing [59][172] - traditional manufacturing techniques can only achieve simple geometries, which greatly limit its potential applications [173].

To address this, in more recent years, additive manufacturing (AM), particularly laser powder bed fusion (PBF-LB), has emerged as a promising route for fabricating geometrically complex NiTi components [174][175]. However, the high cooling rates and large thermal gradients inherent to the PBF-LB process can significantly alter the local microstructure and composition, and consequently, the functional properties of the printed part [141]. For example, Xue et al. [176] demonstrated that increasing laser power and decreasing scan speed resulted in an increase in the transformation temperatures of Ni-rich NiTi due to increased Ni evaporation. Meanwhile, Zhu et al. [177] found that while Ni evaporation in equiatomic NiTi increased linearly with decreasing hatch distance, the transformation temperatures (TTs) did not. Instead, the TTs related to a critical hatch distance, which was determined by the interplay between thermal stresses and in situ reheating effects during the build process. A study by Shen et al. [70] showed that increasing the VED from 70 J/mm^3 to 111 J/mm^3 in Ni-rich NiTi resulted in a decrease in relative density, which was attributed to overmelting and the subsequent formation of keyhole defects at higher energy inputs. In contrast, Khanlari et al. [78] demonstrated that the density of NiTi parts increased as the VED was raised from 46 J/mm^3 to 69 J/mm^3, due to insufficient melting of the powder at

lower energy densities. It should be noted that VED is a simplified metric used to describe the combined effect of the PBF-LB parameters and does not consider the geometry of the part. For this reason, while VED is used in this study, the results are mainly discussed in terms of the individual effects of scan speed, laser power, and strut diameter.

While many researchers have studied the PBF-LB of NiTi, highlighting the ability to control the material properties through process parameter optimisation [178], the majority of studies focus on conventional bulk test specimens such as cubes. This does not account for the critical effect of complex geometries on the thermal evolution of PBF-LB parts, overlooking one of the key benefits of AM over traditional manufacturing methods [179][180][71]. In addition, while several studies investigate the relationship between PBF-LB process parameters and part geometry, the majority of research focuses on Ni-rich NiTi [175][181][182][183]. For example, Chen et al. [174] looks at the effect of effect of geometry on the mechanical properties of gradient lattice structures however, this study used Ni-rich NiTi and does not investigates the relationship between the geometry and PBF-LB process parameters. Dadbakhsh et al. [180] examines the effect of scan speed and laser power on scaffold structures with different strut thickness but the study focuses on Ni-rich NiTi. Ni-rich NiTi is used in the austenitic phase for its superelastic properties in biomedical application while Ti-rich NiTi is used in the martensitic phase for its shape memory properties in the aerospace and automotive industries. The two compositions exhibit very different behaviours and functional properties, and the results of one cannot be applied to the other. This leaves a clear and critical gap in the literature of how PBF-LB process parameters and complex geometries affect the final properties of Ti-rich NiTi parts, which is key to implementing SMAs in aerospace and automotive applications.

The fabrication of lattice structures, in particular, offers significant promise for the development of high power-to-mass ratio shape memory alloy (SMA) actuators [184]. The ability to optimise both the geometry and functional properties of NiTi parts to achieve lightweight structures with tuneable material characteristics is of particular interest in the development of SMA actuators for aerospace applications [185]. PBF-LB lattice in other Ti alloys, such as Ti-6Al-4V have shown strong interactions between strut diameter and process parameters, indicating a need for similar studies of NiTi [186]. Geometrical features

such as wall thickness and strut diameters can drastically influence the final properties of the part due to differences in thermal histories and cooling rates during the PBF-LB process [181]. These differences in thermal histories owing to feature size have been reported to result in differences in Ni evaporation, grain morphology, defects, and precipitate formation within the NiTi matrix. A comprehensive understanding of the interplay between PBF-LB process parameters and part geometry is therefore essential for the fabrication of application specific designs with tailored material and mechanical properties, enabling applications and performance far beyond what can be achieved by conventional manufacturing methods [187]. By examining the interaction between process parameters and strut diameter, this work provides insight into how these factors impact the properties of the part, thereby contributing to the development of SMA lattice structures for high performance applications.

5.2. Materials and Method

5.2.1. Model Configuration & Dimensions

In this study, three model configurations were designed in SolidWorks Ver. 2023, all featuring the same geometry and differing strut diameters of 0.5 mm, 1.0 mm, and 1.5 mm as illustrated in Figure 32 and detailed in Table 7. For brevity samples with lattice strut diameter 0.5 mm, 1.0 mm, and 1.5 mm will herein be referred to $L_{0.5}$, $L_{1.0}$, and $L_{1.5}$, respectively. The Ti-rich NiTi periodic strut-based body-centred cubic (BCC) lattice structures were composed of unit cells with equal edge lengths of 6.25 mm and internal angles of 90°. These unit cells were repeated four times in the x, y, and z direction. As these samples were used for both this study and a further study on the actuator performance, BCC lattice structures were chosen based on preliminary experiments where several different geometries were printed and tested finding that the BCC structure showed the best strain recovery. The 6.25 mm cell size was selected to optimise the number of samples that could be printed together on the build plate. Each model included top and bottom endplates with the same thickness as the respective strut diameter, support structures to allow removal from the build plate without damaging the lattice structure, and removable pillars with the same thickness as the struts. These latter struts were used for material characterisation.

Table 7: Lattice Configuration & Dimensions

Lattice & unit cell type	Periodic Strut-Based BCC
Number of unit cells in each direction	4
Unit cell length (mm)	6.25
Internal angles (°)	90
Strut diameter (mm)	0.50, 1.0, 1.5
Width, depth and height of lattice (mm)	25
Solid volume fraction (%)	3.55, 13.04, 26.74

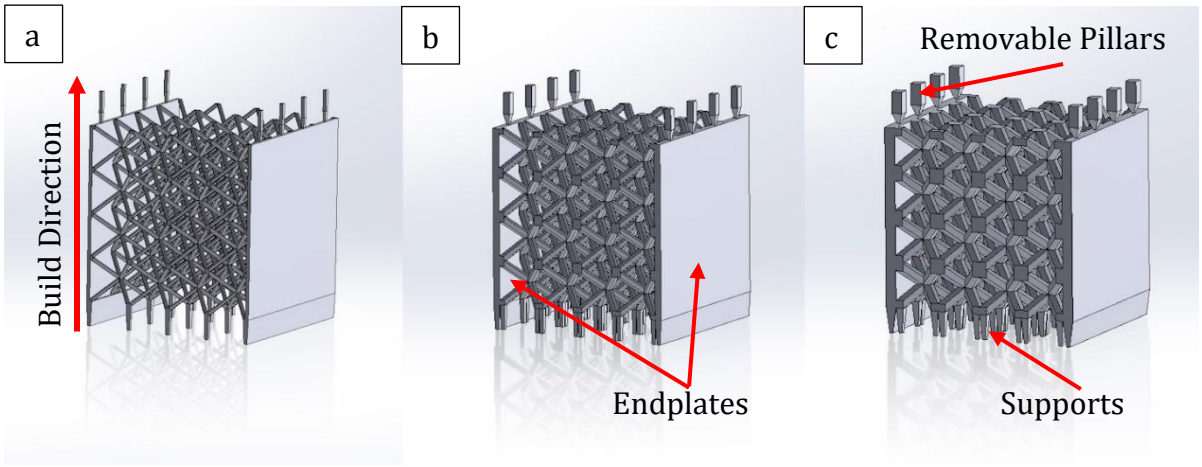


Figure 32: CAD models of the NiTi lattice structures showing build direction, end plates, support structures, and removable pillars for DSC tests with strut diameters of a) 0.5 mm, b) 1.0 mm, and c) 1.5 mm.

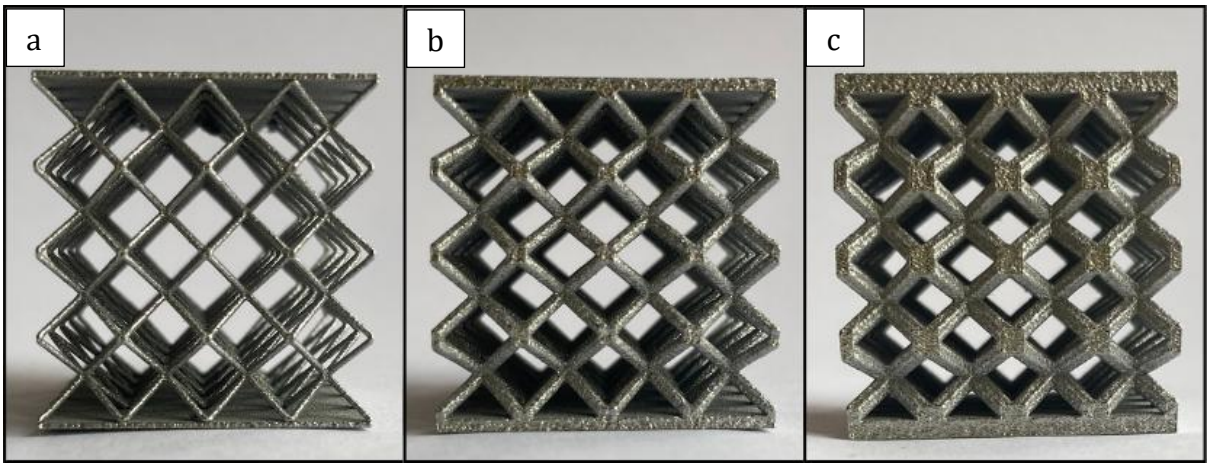


Figure 31: Printed lattices with a) 0.5 mm, b) 1.0 mm, and c) 1.5 mm strut diameter.

5.2.2. Material & Fabrication

NiTi samples were produced from virgin gas atomized Ti-rich powder with a composition of Ni (49.82 at.%) – Ti (50.18 at.%) and particle size distribution of 20 µm to 63 µm provided by Fort Wayne Metals, Castlebar, Co. Mayo, Ireland.. The NiTi samples were 3D printed

across two builds using an Aconity MINI (GmbH) PBF-LB machine, equipped with a 200 W 1068 nm Yb fibre laser. To prevent oxidation and impurity pick-up oxygen levels were kept below 20 ppm for the duration of the build using a purging gas of pure argon (99.999 %). The parts were printed with a layer thickness of 50 µm and a spot size of 60 µm. The scan strategy used was a single contour on the perimeter of the part and hatching for the interior. The scanning parameters were constant for all samples with a hatch spacing of 120 µm, a start angle of 0°, and increment angle of 67°. To investigate the effect of the PBF-LB process laser powers of 150 W, 175 W and 200 W were used along with scan speeds of 400 mm/s, 800 mm/s, and 1200 mm/s. These process parameters were selected based on preliminary experiments where mid laser power and scan speed of 175 W and 800 mm/s showed good potential.

5.2.3. Design of Experiment (DoE)

A Box-Behnken DoE was used to investigate the effect of VED, scan speed (v), laser power (P), and lattice strut diameter (d) on the material properties and actuator performance of the produced NiTi lattices. The full DoE is presented in Table 8.

Table 8: Full DoE of strut diameter, laser process parameters, and resulting VED for the produced NiTi samples.

Sample	Strut Diameter (mm)	Scan Speed (mm/s)	Laser Power (W)	VED (J/mm^3)
1	0.5	800	150	31.25
2	0.5	1200	175	24.31
3	1.0	800	175	36.46
4	1.0	1200	150	20.83
5	1.0	1200	200	27.78
6	1.5	800	150	31.25

7	1.0	800	175	36.46
8	0.5	400	175	72.92
9	1.0	800	175	36.46
10	1.5	1200	175	24.31
11	1.0	800	175	36.46
12	1.0	400	150	62.50
13	1.5	800	200	41.67
14	1.0	400	200	83.33
15	0.5	800	200	41.67
16	1.5	400	175	72.92

5.2.4. Material Characterisation

The density of the PBF-LB lattices without supports or removable pillars was measured using the Archimedes method in an isopropyl alcohol medium according to ASTM B962-23 with the use of an analytical balance, Satorius Entris II Essential BCE124I-1S which has an accuracy and repeatability of ± 0.1 mg. Each sample was tested three times, and the resulting average was taken as the sample density. SEM, BSEM, and EDX experiments were conducted on the face of the centre lattice node for each sample. The chemical compositions of the as-printed samples were obtained using the Aztec Live System EDX from Oxford Instruments in a Zeiss EVOLS15 SEM. Five point measurements were taken from each sample, and the average was taken as the sample composition. DSC analysis was conducted on the removable pillars according to ASTM F2004-17 at Fort Wayne Metals, Castlebar, Co. Mayo, Ireland using a TA Instruments® Discovery DSC2500 instrument to ascertain the phase transformation characteristics of the powder and PBF-LB samples. Samples were first ramped at 100 °C/min to 150 °C and held isothermally for 5 minutes. The samples were then cycled between -50 °C and 150 °C at 10 °C/min twice. The data from the second scanning cycle was used to plot the DSC curves and analyse the transformation characteristics. The removable pillars were also used as samples for synchrotron X-ray diffraction (SXRD) were illuminated by a monochromatic 0.5 mm square beam operated in transmission Debye-Scherrer geometry at the I12 beamline at Diamond Light Source. The X-ray energy was calibrated using a CeO_2 NIST standard at multiple sample-to-detector distances and corresponded to a wavelength of 0.15678Å. 2D data were collected on a CdTe 2M Pilatus area detector and reduced to 1D

using the DAWN software package. Multiple diffraction patterns were obtained at different locations within each sample, and these were summed to give information representative of the whole sample.

5.3. Results

5.3.1. Input-Output Correlations

To determine the significance of the DoE inputs on the results of this study p-values noting significance were calculated. P-value significance was used to determine the relevant correlations between the inputs and outputs of the model overall where a p-value of ≤ 0.05 was considered a relevant correlation. P-values were calculated using 16 samples with 4 centre points using ANOVA linear regression. All relevant correlations are shown in Table 9.

Table 9: P-values of the relevant input-output correlations.

	No. of Measurements per Sample	Strut Diameter	Laser Power	Scan Speed
Relative Density	3	0.0103		
Ni Loss	5	0.0013		0.0008
A_f Temperature	2		0.0042	< 0.0001
Enthalpy of Cooling	2	0.0004		
Enthalpy of Heating	2	0.0002		
Thermal Hysteresis	2		0.0146	

For the scan speed, laser power, and strut diameter, the coded equations for the response surface are presented below.

$$\text{Relative Density} = 99.02 - 0.5A + 0.3B - 0.275C + 0.5AB - 0.45 + 0.6BC - 1.26C^2$$

$$\text{Ni Loss} = 0.2099 - 0.652A + 0.0044B - 0.0721C + 0.0994A^2 + 0.0372B^2 + 0.0707C^2$$

$$A_f \text{ Temperature} = 85.61 - 0.495A + 1.42B - 2.99C - 1.11AC + 1.55A^2 + 1.39C^2$$

$$\text{Enthalpy of Cooling} = 27.57 - 1.43A + 0.1169C + 0.5687AC - 1.63A^2$$

Enthalpy of Heating

$$= 27.37 - 1.46A + 0.2996B + 0.1398C - 0.493AB + 0.6349AC - 1.82A^2$$

Thermal Hysteresis $= 31.2 + 0.0356A - 0.6006B + 0.3113 + 1.42A^2$

5.3.2. Relative Density

Density was measured according to the Archimedes principle and averaged across three measurements, for each sample. The average relative density (Rρ) calculated based on the theoretical density of fully dense nitinol (6.45 g/cm^3). For the centre points within the Design of Experiments, the average relative density was 99.18 % with a 95 % confidence interval of ± 0.13 %. The Rρ of the PBF-LB samples varied by strut diameter: for $L_{0.5}$ lattices, Rρ ranged from 98.22 % ± 0.06 % to 98.88 % ± 0.14 % (0.66 % variation); for $L_{1.0}$ lattices, from 96.60 % ± 0.58 % to 99.27 % ± 0.12 % (2.67 % variation); and for $L_{1.5}$ lattices, from 96.02 % ± 0.26 % to 99.36 % ± 0.03% (3.34 % variation).

As shown in Figure 33 (a), a positive correlation between VED and Rρ was observed for all samples with VED below 45 J/mm^3, while a negative correlation occurred for samples with VED above 45 J/mm^3. The SEM images in Figure 34 support this trend, showing significant lack of fusion and unmelted powder at the low VED of 21 J/mm^3, extensive cracking and keyhole formation at the high VED of 83 J/mm^3, and minimal defects at the intermediate VED of 37 J/mm^3.

Surface contour plots in Figure 33 (b)-(d) indicate that the maximum Rρ for all strut diameters occurs at a scan speed of 800 mm/s while the laser power, and consequently the VED, required to achieve maximum Rρ increased with strut diameter. The $L_{0.5}$ lattices achieved a maximum Rρ of 98.88 % ± 0.14 % at a laser power and VED of 150 W and 31.1 J/mm^3 respectively, for the $L_{1.0}$ lattices a maximum Rρ of 99.27 % ± 0.12 % was achieved at a laser power and VED of 175 W and 36.5 J/mm^3 respectively, and for the $L_{1.5}$ lattices a maximum Rρ of 99.36 % ± 0.03 % was achieved at a laser power and VED of 200 W and 41.7 J/mm^3 respectively.

5.3.3. Microstructure

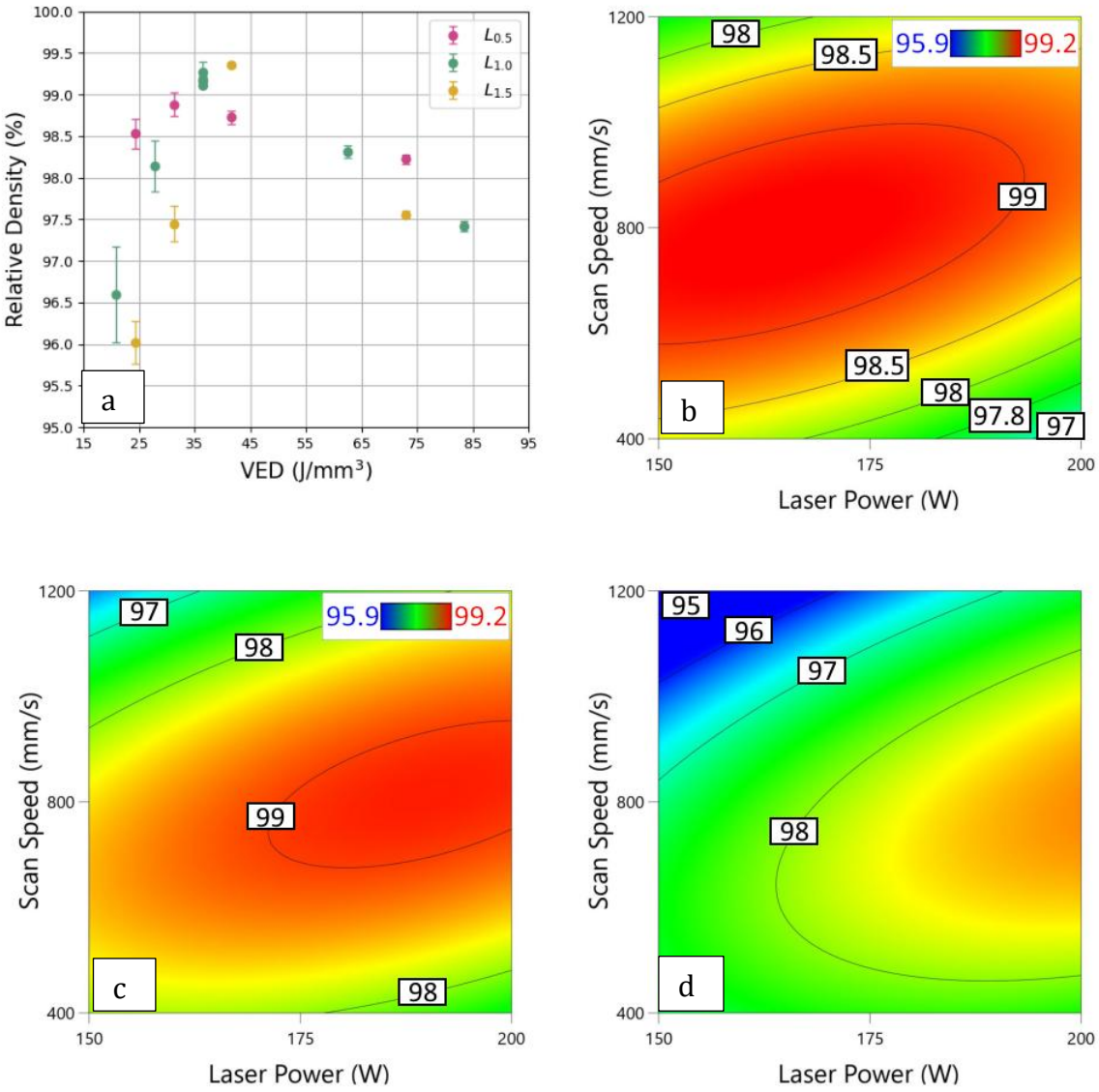


Figure 33: (a) Scatter Plot of relative density with VED showing 95 % confidence intervals. Surface contours show the effect of the relationship between laser power and scan speed on the relative density for (b) $L_{0.5}$, (c) $L_{1.0}$, and (d) $L_{1.5}$.

Representative samples were selected for microstructural examination at low (21 J/mm^3), mid (37 J/mm^3), and high (83 J/mm^3) VEDs for the mid strut diameter. SEM images of the cross sections parallel to the build direction seen in Figure 34 show the variations in pore size, pore shape, extent of porosity, and microcrack propagation with VED. In Figure 34 (a), sample 4 with a low VED of 21 J/mm^3 and a relative density of 96.6 % ± 0.58 % showed a high degree of lack of fusion. In Figure 34 (b), sample 7 with a mid VED of 37 J/mm^3 and a relative density of 99.19 % ± 0.06 % shows a significant reduction in unfused particles. In

Figure 34 (c), sample 14 with a high VED of 83 J/mm^3 and a relative density of 97.42 % ± 0.06 % displays an increased in porosity defects, exhibiting a combination of keyhole pores and microcracks.

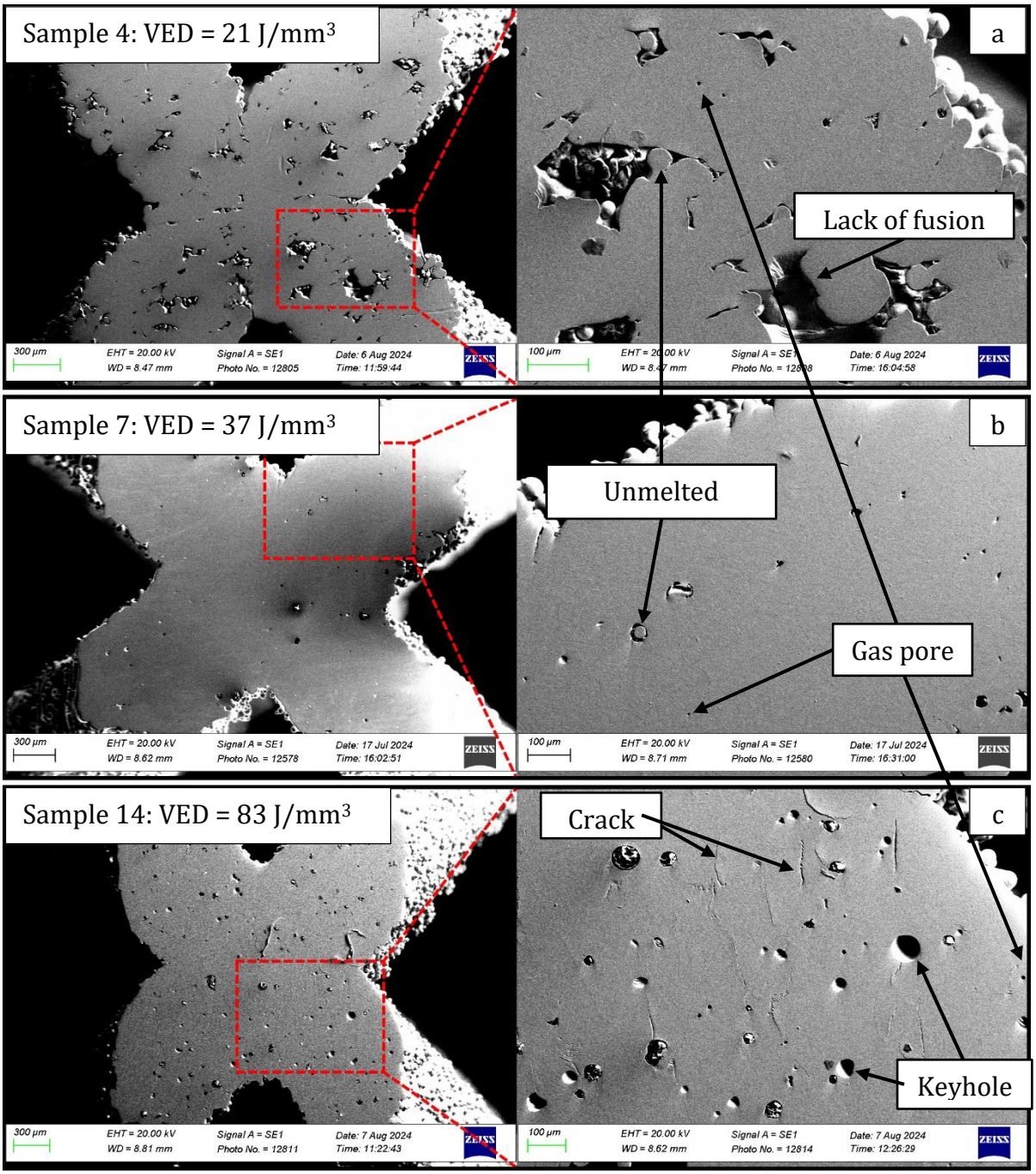


Figure 34: SEM images show the effect of VED on the porosity of the part in the $L_{1.0}$ lattices. (a) sample 4: scan speed = 1200 mm/s, laser power = 150 W; (b) Sample 7: scan speed 800 mm/s, laser power = 175 W; (c) Sample 14: scan speed = 400 mm/s, laser power = 200 W.

The BSEM images in Figure 35 show the microstructure and morphology of the $L_{1.0}$ lattice at low and high VED. Sample 4 with low VED of 21 J/mm³ shows a heterogeneous microstructure with a combination of different grain morphologies and sizes. For this sample, shown in Figure 35 (a), there is a combination of both equiaxed and columnar

dendritic grains seen at the edge of the melt pool ranging from 0.4 µm to 5 µm in size. For sample 14, with a high VED of 83 J/mm^3 the melt pool is clearly defined by columnar grains radiating towards the edge of the melt pool as well as ultra fine cellular grains (<1 µm) adjacent to the melt pool boundary, see Figure 35 (b).

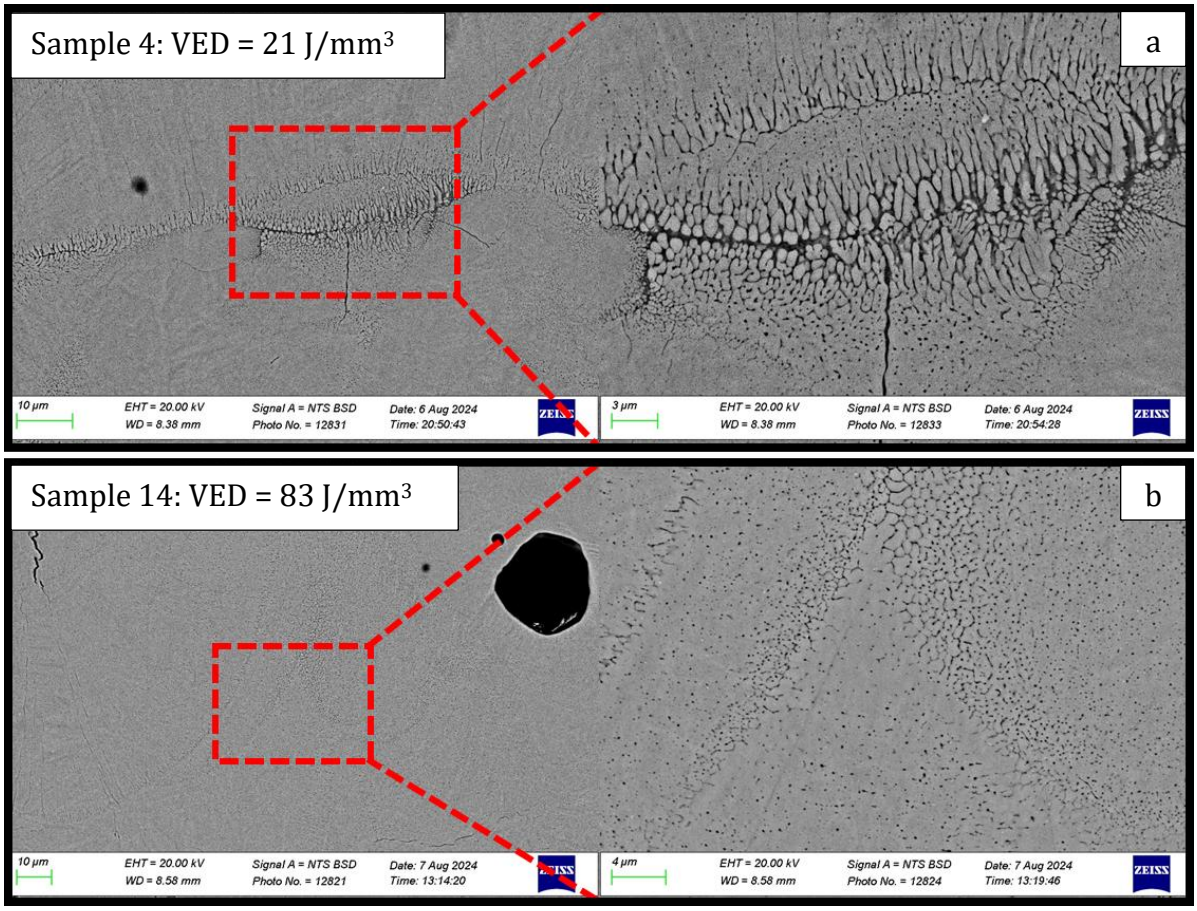


Figure 35: BSEM images showing the grain morphology of (a) sample 4 and (b) sample 14.

5.3.4. Phase Analysis

The SXRD data are presented in Figure 36. To identify the phases, CIF files of the respective structures were used to simulate powder diffraction patterns. The CIF files used were taken from the Inorganic Crystal Structure Database (ICSD): B19' - ICSD Entry: 164152 [188], Ti_2Ni - ICSD Entry: 15808 [189], B2 - ICSD Entry: 166368 [190]. Expected locations corresponding to the B2, B19′ and $NiTi_2$ phases are indicated by the markers at the top of the figure. In all samples, strong reflections consistent with the B19′ martensite phase can be seen. It is difficult to distinguish the presence and amount of $NiTi_2$ as the stronger peaks overlap with those of the B19' phase however in the high VED condition of the $L_{1.0}$ (83

J/mm^3) and $L_{1.5}$ (73 J/mm^3) lattices and the mid VED condition of the $L_{1.5}$ (42 J/mm^3) lattice, there are additional weak reflections consistent with $NiTi_2$. These additional reflections are most prominent at ~ 1.4° and 2.8° 2θ. This suggests a small volume fraction of $NiTi_2$ precipitates in these samples. This phase may also be present in the high VED condition of $L_{0.5}$ lattice (73 J/mm^3), but due to the smaller diffracting volume, could be below the resolution of the technique.

5.3.5. Composition

A decrease in Ni concentration of parts produced by PBF-LB from the starting powder is often reported in literature owing to Ni evaporation due to the high energy inputs and lower boiling point of Ni (2732 °C) compared to Ti (3287 °C) [173]. The composition was calculated based on the average of five measurements on each sample. The virgin powder contained 49.82 at. % Ni and Ni loss amongst samples was found to range from 0.2 at. % to 0.52 at. %. The results for Ni loss had a relative variation amongst samples, however the 95 % confidence intervals were also large, see Figure 37(a). One of the main limitations of EDX is that it can report large variations in composition as the X-rays generated from regions below the surface are also detected and counted during measurement [191]. Chemical heterogeneity has been found in the past to result in a high variation in composition measurement amongst different regions in the same sample [191]. However, for the centre points (samples 3, 7, 9, and 11) within the Design of Experiments, the average Ni composition was recorded as 49.61 at.% with a 95 % confidence interval of 0.02 at.%. From the P-values, the Ni evaporation has a strong negative correlation with scan speed (0.0008) and strut diameter (0.0013). The surface contours Figure 37 (b-d) show that there was negligible change in the Ni content for scan speeds above 400 mm/s in the $L_{1.0}$ and $L_{1.5}$ lattices however for the $L_{0.5}$ lattices, Ni evaporation occurred for all scan speeds. Additionally, the surface contours show that the $L_{0.5}$ lattices had the highest Ni loss, followed by the $L_{1.5}$ lattices and then the $L_{1.0}$ lattices.

5.3.6. Phase Transformation Characteristics

Two thermal cycles were conducted for two specimens from each of the samples. It was observed that the difference between the thermal profiles of the first and second cycles were

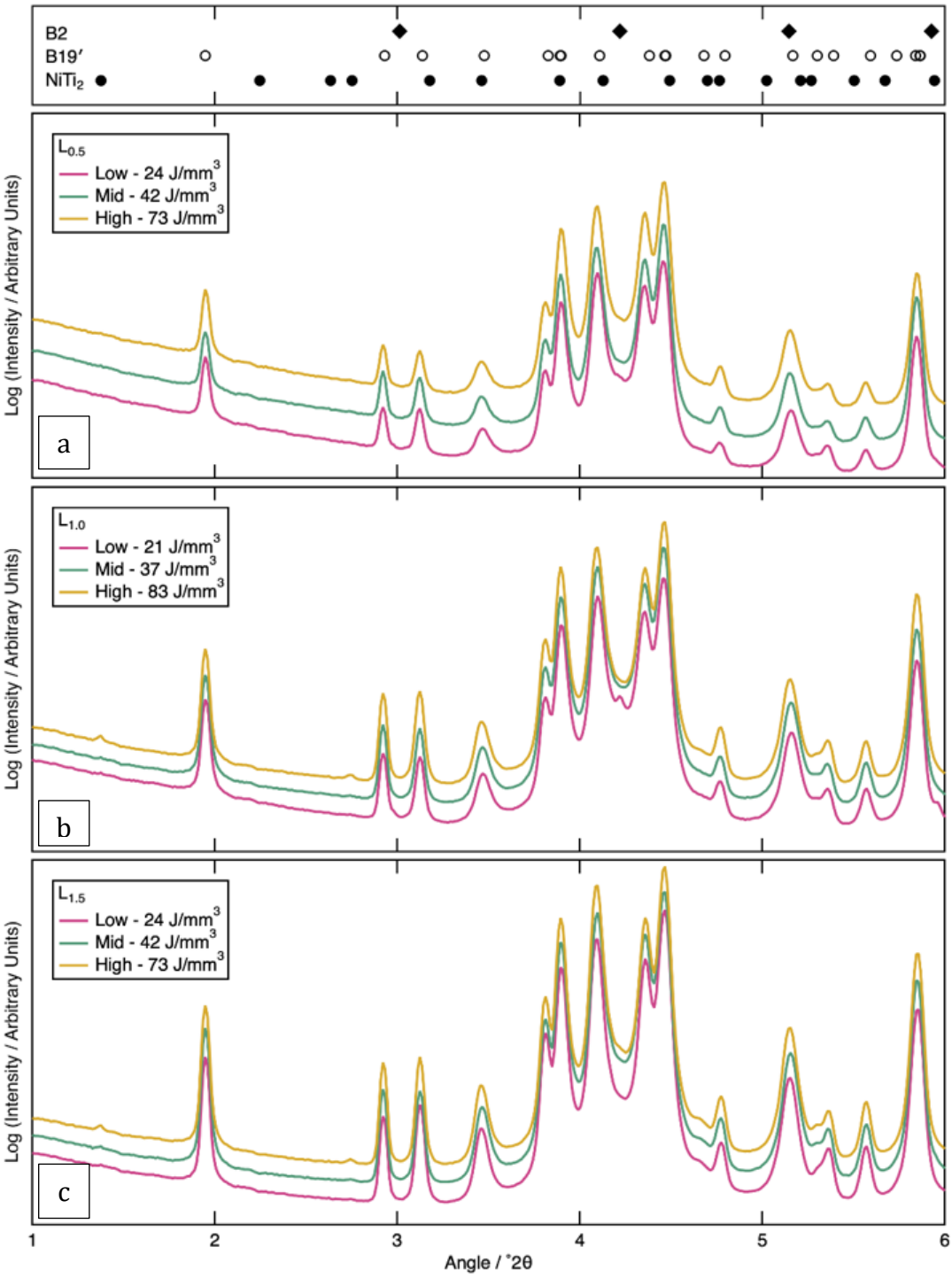


Figure 36: SXRD reflections at low, mid, and high VED for (a) the $L_{0.5}$ lattices, (b) the $L_{1.0}$ lattices, and (c) the $L_{1.5}$ lattices.

negligible showing only a minor sharpening of the peaks. For example, the difference in the A_f between cycle 1 and 2 of sample 1 was 0.25 °C.

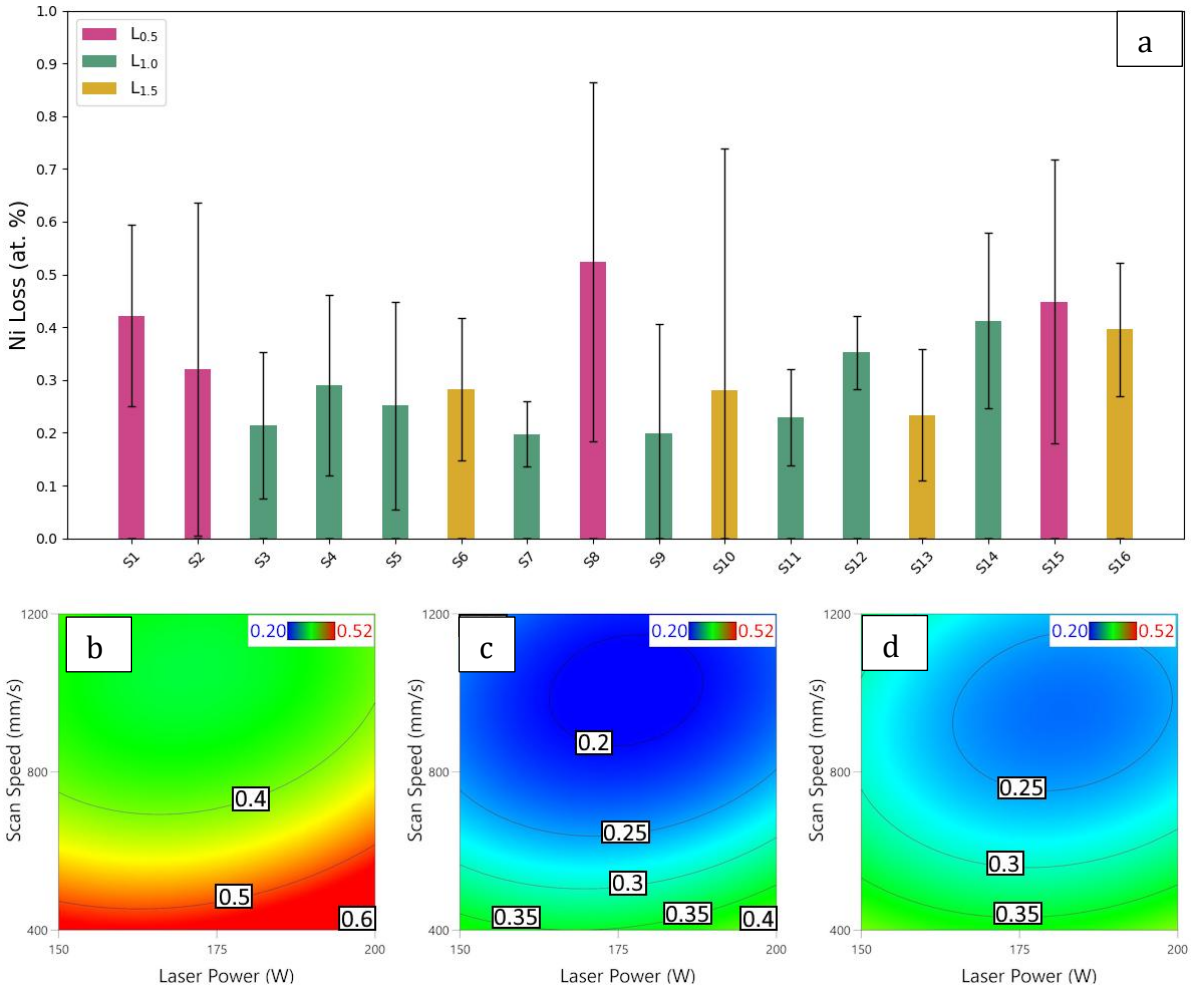


Figure 37: (a) Bar chart of Ni loss showing 95 % confidence intervals. Surface contours showing the relationship between laser power and scan speed on the Ni loss for the (b) $L_{0.5}$, (c) $L_{1.0}$, and (d) $L_{1.5}$ lattices.

From the DSC results displayed in Figure 38 (a) the powder exhibits multi-stage phase transformations with overlapping peaks. The as-received powder shows two peaks on cooling and heating with the additional peaks appearing as a shoulder to the right on the main peaks for both heating and cooling curves. In the PBF-LB samples the additional peaks are most prevalent in the $L_{0.5}$ lattices and almost completely disappear in the $L_{1.5}$ lattices. In the $L_{0.5}$ lattices the shoulders on cooling appear on either side of the main peak and are clearest S1 and S2 with VED 31 J/mm^3 and 24 J/mm^3 respectively which begin to disappear as VED increases. On heating there is a small additional peak seen in the $L_{0.5}$ lattices which disappears as VED increases.

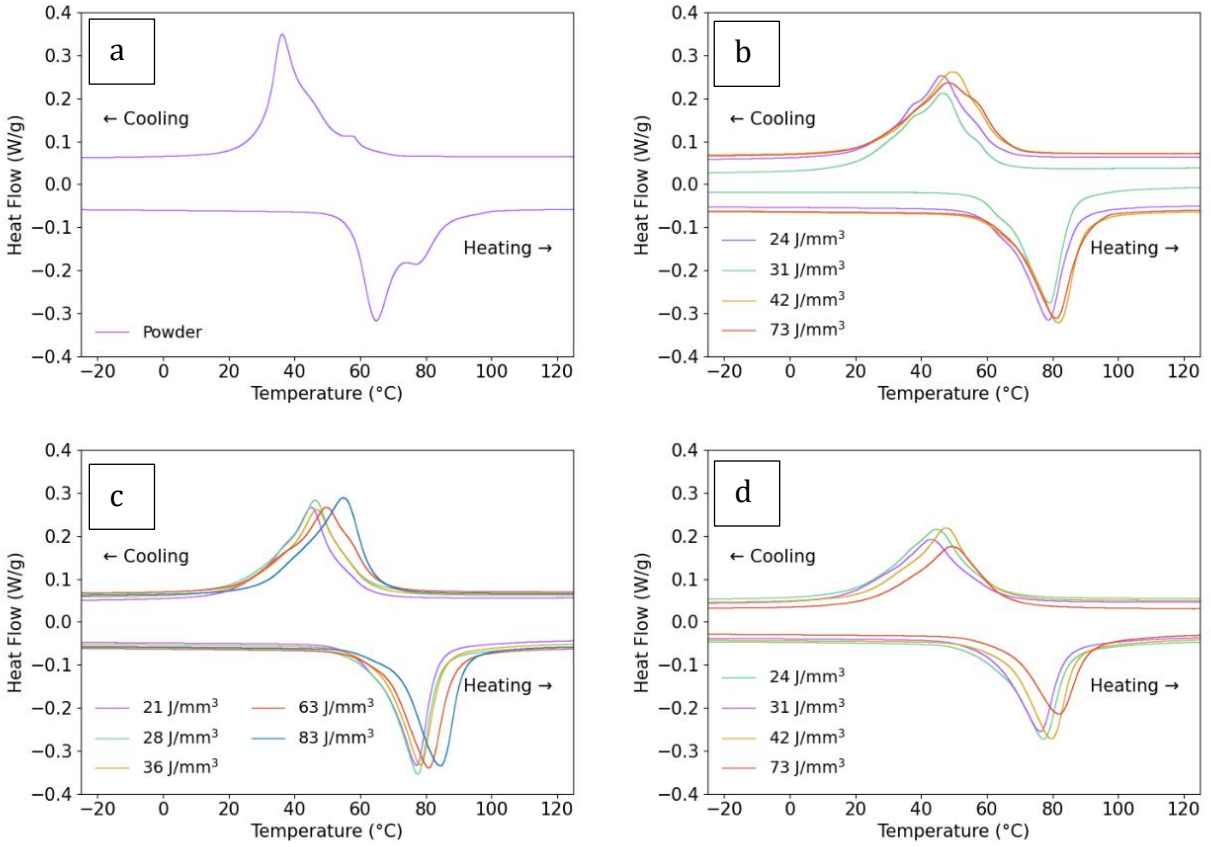


Figure 38: DSC curves of a) the as-received powder and DSC plots comparing the number of peaks with the VED for b) $L_{0.5}$, c) $L_{1.0}$, and d) $L_{1.5}$.

The A_f temperatures of the lattice samples are shown in Figure 39below. The average A_f of the four centre points was 85.52 °C with a 95 % confidence interval of 0.41 °C. A_f of the starting powder was found to be 87.53 °C and A_f of the PBF-LB samples ranges from 83.53 °C to 92.34 °C for sample 4 ($L_{1.0}$, P = 150 W, v = 1200 mm/s, VED = 20.83 J/mm³) and sample 16 ($L_{1.5}$, P = 175 W, v = 400 mm/s, VED = 72.92 J/mm³) respectively. All samples with a VED below 42 J/mm³ had an A_f lower than that of the starting powder (87.53 °C) and all samples with a VED above 42 J/mm³ had an A_f above than that of the starting powder. Amongst the PBF-LB samples there was a strong positive correlation between A_f and VED. Both laser power and scan speed were found to have significant input-output correlations with the A_f temperature. However, scan speed was found to be the controlling factor with p-value of <0.0001 compared to the laser power p-value of 0.0042.

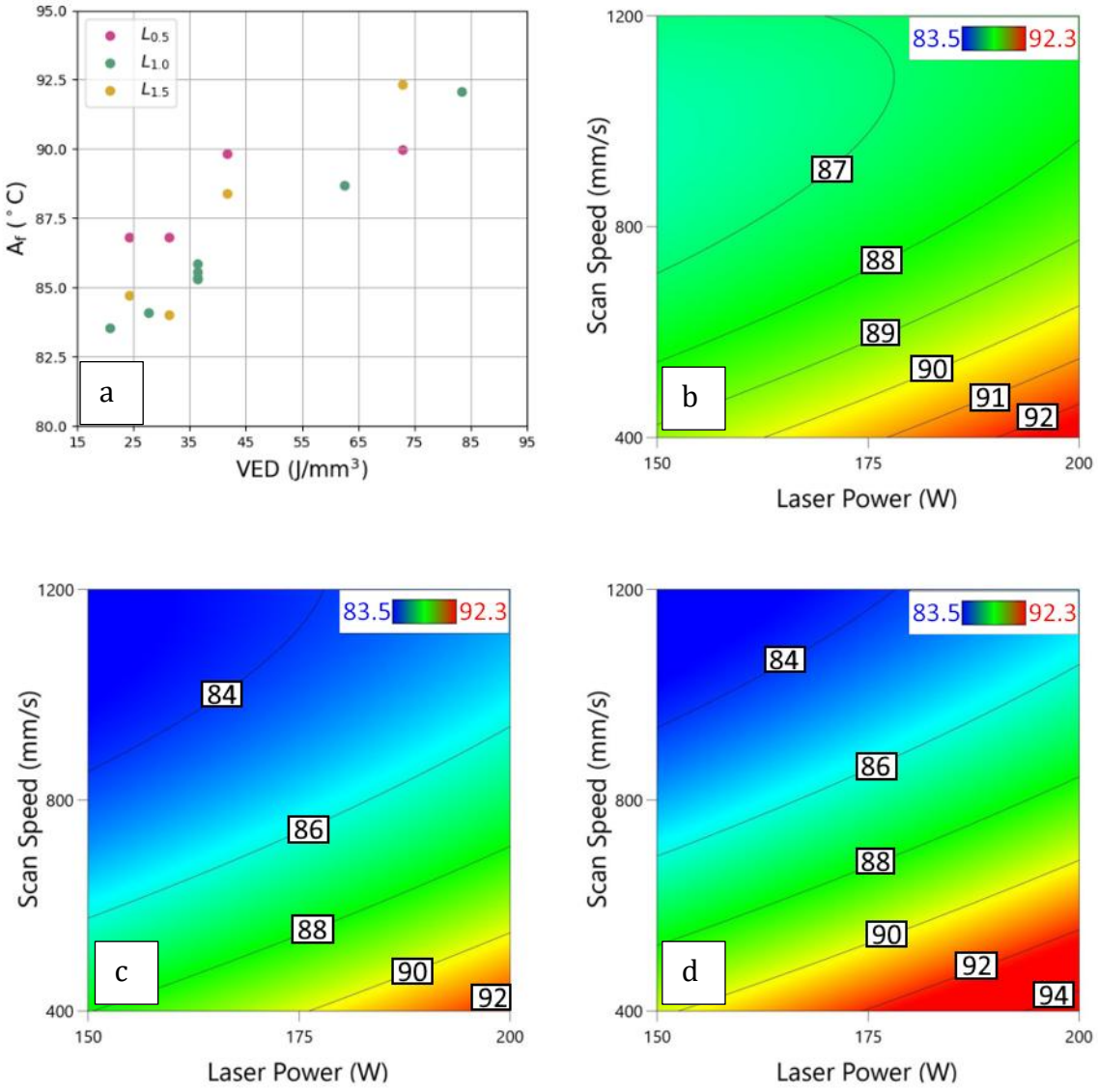


Figure 39: (a) Scatter plot of A_f with VED. Surface contours showing the effect of the relationship between laser power and scan speed on A_f for (b) $L_{0.5}$, (c) $L_{1.0}$, and (d) $L_{1.5}$.

Thermal hysteresis (η) in SMAs is defined as the difference in peak temperatures of the forward and the reverse transformation [27]. η is an important parameter in the functional behaviour of NiTi actuators as a small η results in a faster response. The results showed that the as-received powder had an η of 28.3 °C which was below that of all PBF-LB samples. The average η of the four repetition samples was 31.4 °C with a 95 % confidence interval of 0.52 °C. The η of the PBF-LB samples ranged from 29.6 °C for sample 14 ($L_{1.0,}$ P = 200 W, v = 400 mm/s, VED = 83 J/mm³) to 33.6 °C for sample 6 ($L_{1.5,}$ P = 150 W, v = 800 mm/s, VED = 31.3

J/mm^3). From the P-values, η has an inverse correlation with laser power (0.0146) showing a decrease in thermal hysteresis with increasing laser power. Additionally, from the surface plots in Figure 40 (b-d), the highest η is seen in the $L_{1.5}$ lattices and the lowest η is seen in the $L_{1.0}$ lattices.

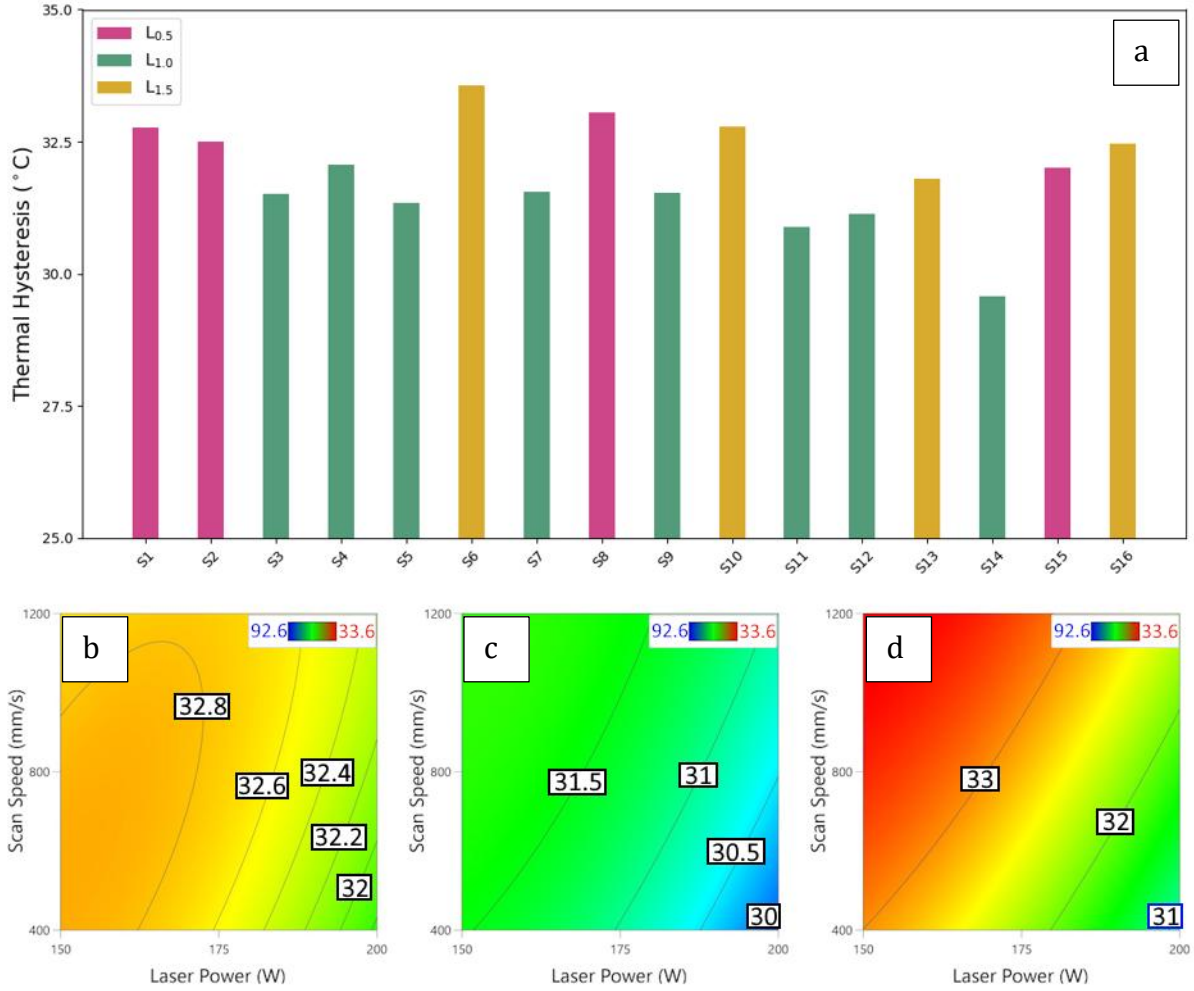


Figure 40: (a) Bar chart of thermal hysteresis (η) and surface Contours showing the effect of the relationship between laser power and scan speed on η for the (b) $L_{0.5}$, (c) $L_{1.0}$, and (d) $L_{1.5}$ lattices.

The phase transformation process involves changes in enthalpy, where the austenitic transformation during the heating cycle is an endothermic process, and the martensitic transformation during cooling is exothermic [192]. Enthalpy was calculated by plotting heat flow (W/g) against time (seconds) using Trios software and integrating the area under the transformation peaks. Specifically, the B19' transformation peak was integrated to obtain

the cooling enthalpy ($\Delta H_{Cooling}$), while the B2 peak was used to determine the heating enthalpy ($\Delta H_{Heating}$).

The average values for $\Delta H_{Cooling}$ and $\Delta H_{Heating}$ across the four repetition samples were 27.33 J/g with a 95 % confidence interval of 0.84 J/g and 27.08 with a 95 % confidence interval of 0.35 J/g, respectively. The highest $\Delta H_{Cooling}$ and $\Delta H_{Heating}$ values were observed for the powder at 28.82 J/g and 28.45 J/g respectively. Amongst the PBF-LB samples, $\Delta H_{Cooling}$ ranged from 26.31 J/g to 28.15 J/g and $\Delta H_{Heating}$ ranged from 22.99 J/g to 27.96 J/g.

Statistical analysis of the P-values for both $\Delta H_{Cooling}$ and $\Delta H_{Heating}$ revealed that the strut diameter was the most significant factor influencing these enthalpies, with p-values of 0.0004 for $\Delta H_{Cooling}$ and 0.0002 for $\Delta H_{Heating}$. As shown in Figure 41, samples 6, 10, 13, and 16 – each with strut diameters of 1.5 mm – exhibited noticeably lower values for both $\Delta H_{Cooling}$ and $\Delta H_{Heating}$ compared to the other samples.

The enthalpy ratio (TEr) is calculated as the ratio of $\Delta H_{Heating}$ to $\Delta H_{Cooling}$ ($TEr = \Delta H_{Heating}/\Delta H_{Cooling}$) No relevant input output correlation was found for TEr amongst samples however TEr ranged from 0.97 to 1.01 amongst all samples, indicating that all samples underwent nearly complete phase transformations during both heating and cooling.

5.4. Discussion

5.4.1. Effect of powder composition

A change in Ni content can have a significant effect on the performance of SMA actuators as the ratio of Ni to Ti greatly effects the transformation temperatures (TT) and functional properties of NiTi. Specifically, Ni-rich NiTi tends to have lower TTs and exhibit SE, while Ti-rich NiTi exhibits higher TTs and exhibit SME [193][50]. The majority of research to date on the effects of PBF-LB process parameters and part geometry on NiTi focuses on Ni-rich powders. This leaves a gap in the literature required to understand how these parameters affect powders used for a whole range of applications requiring the higher TTs and SME of Ti-rich NiTi. In this study the effect of scan speed, laser power, and lattice strut diameter on the microstructure and phase transformation behaviour of Ti-rich NiTi lattice structures is investigated. Ti-rich NiTi is typically chosen for applications requiring the SME. Due to the

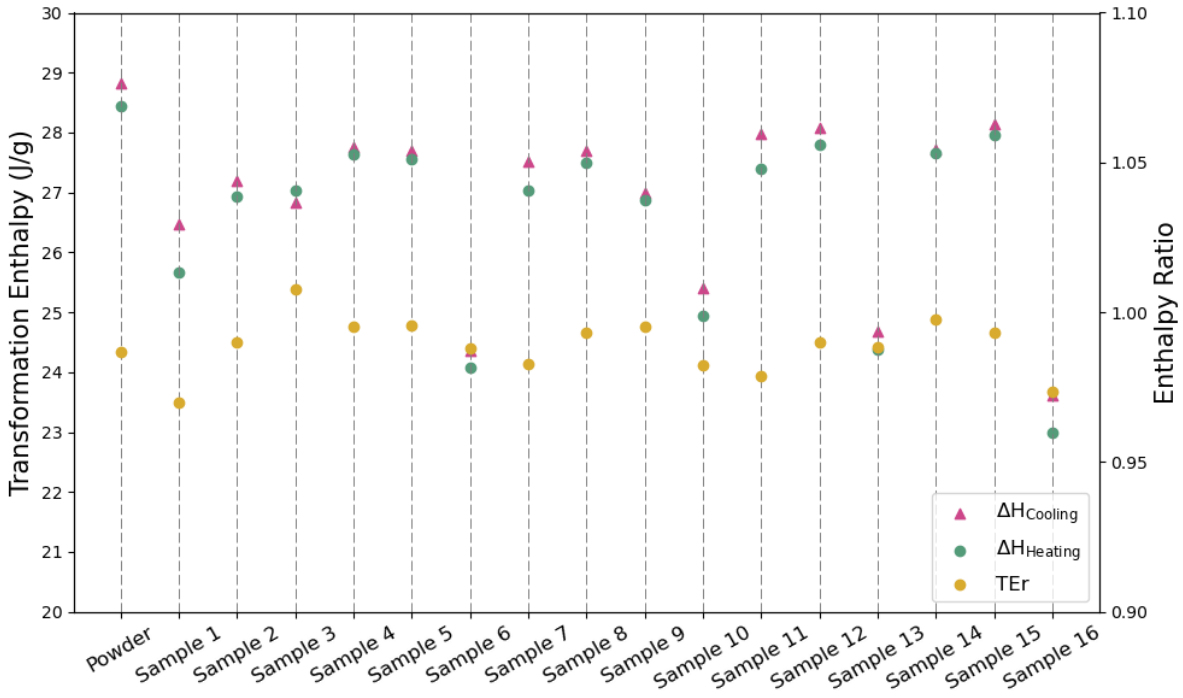


Figure 41: Enthalpy of the cooling ($\Delta H_{Cooling}$) and heating transformation ($\Delta H_{Heating}$), and enthalpy ratio (TEr) of the powder and PBF-LB samples.

higher TTs of titanium, Ti-rich NiTi is in the martensite phase at room temperature and therefore the SME is the more prevalent mechanical property. In addition, Ti-rich powders benefit from the transformation temperatures of the final part having a reduced sensitivity to Ni evaporation during the PBF-LB process compared to Ni-rich powders. In Ni-rich NiTi a change of 0.1 at. % Ni can cause the TT to change by 10 °C [27]. Meanwhile in this study despite a maximum Ni loss of 0.52 at. % (see Figure 37) from the composition of the starting powder, the A_f of the printed parts varied from the A_f of the starting powder by a maximum of 4.8 °C (see Figure 39). This is beneficial for actuator applications as the TTs is a critical parameter of actuators and requires precision and reliability.

5.4.2. Effect of Strut Diameter

The results show that the strut diameter has a critical influence on the material characteristics of the PBF-LB lattice structures. This can mainly be attributed to the effect of strut diameter on cooling rates during the PBF-LB process. A study by Biffi et al. [194] demonstrated that the heat extraction from melted Ni-rich NiTi powder was slower at the borders of the part closer to the unmelted surrounding powder and that this was because of

the lower thermal conductivity of the loose powder compared the solidified metal. Similarly a study by Qu et al. [181] demonstrates that as wall thickness decreases, the energy density should be decreased to balance the effect of decreasing cooling rate with decreasing wall thickness. The researchers found that decreasing the wall thickness of Ni-rich NiTi lattices from 260 μm to 130 μm required the VED to be decreased from 167 J/m^3 to 140 J/m^3 to compensate for the slower cooling rate of the thinner walls. Thinner strut diameters therefore exhibit slower cooling due to the increased ratio of surface area to volume, where the powder acts as a thermal insulator due to the lower thermal conductivity of the powder compared to the solidified metal [195].

The current study addresses a gap in the literature by examining this effect on Ti-rich NiTi lattices. The results for the relative density presented in Figure 33 show that the maximum Rρ achieved increased with increasing strut diameter . Additionally, while the maximum Rρ was achieved at a mid-scan speed of 800 mm/s across all strut diameters, the laser power and corresponding VED required to attain this maximum increased with strut diameter ($L_{0.5}$: 98.88 %, 150 W, $L_{1.0}$: 99.27 %, 175 W, $L_{1.5}$: 99.36 % 200 W). This can be attributed to the slower cooling rates of the thinner lattices. At lower VEDs the reduced cooling rate in thinner lattices result in slower solidification rates allowing more complete melting, reduced porosity, and increased Rρ. At higher VEDs, the slower cooling rates in these thinner lattices result in overmelting. This is evident in the lower density and higher keyhole formation found within these smaller lattice structures at higher VEDs. This concept is illustrated in Figure 42.

Similar results have been reported for Ti-6Al-4V in a study by Casata et al. [186] which found that the differences in porosity levels of different sample sizes could be attributed to the difference in thermal profiles caused by the lower thermal conductivity of the powder compared to the solidified part. The EDX results presented in Figure 37 showed that the Ni loss was highest in the $L_{0.5}$ lattices, ranging from 0.32 at. % to 0.52 at. %. The higher Ni evaporation in the $L_{0.5}$ lattices can be attributed to the decrease in melt pool solidification rates resulting in more time for Ni evaporation to occur [196]. This is in agreement with a study by Guo et al. [182] who demonstrates that the reduced solidification rate of the thinner

walls owing to reduced thermal conductivity of the Ni-rich NiTi powder compared to the solidified metal resulting in increased Ni evaporation.

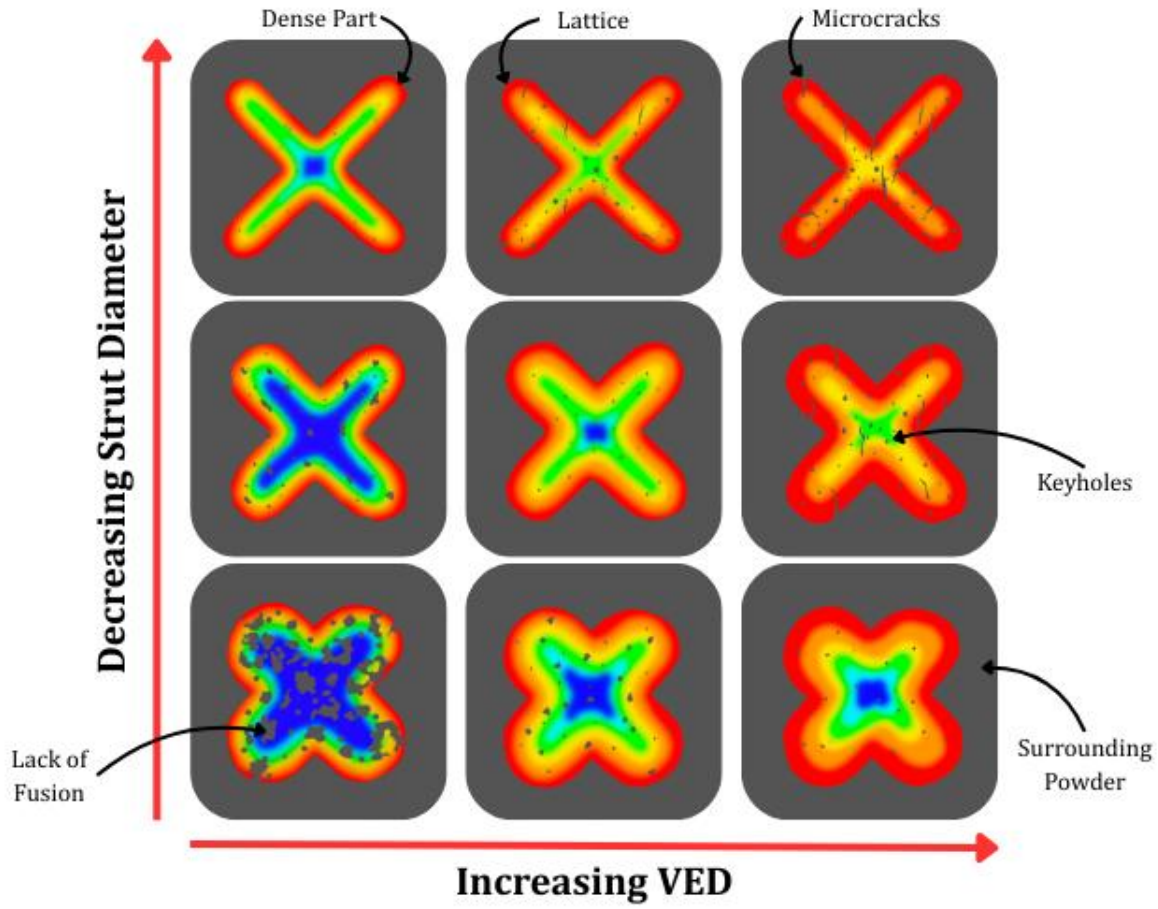


Figure 42: Schematic demonstrating the insulating effect of the surrounding powder on the density of the lattices during the PBF-LB process.

Thermal hysteresis is another critical parameter in the functional performance of NiTi actuators, as a smaller η leads to faster response times and improved efficiency. The results seen in Figure 40 showed that the $L_{1.5}$ lattices exhibited the highest η. This result is attributed to the larger surface area per layer in the thicker struts. As the strut diameter increases, the cross sectional area of the build layer increases and extends the time taken for the laser to scan across each section of the lattice. This provides more time for the beginning of the melt pool to cool as the laser completes the hatching of the current section. The elongated melt pool therefore is subject to higher thermal gradients [197]. Furthermore, the increased surface area in the thicker struts amplifies the thermal differential between the centre of the

part and the border of the part due to differences in heat extraction at the border caused by the surrounding powder [194]. Increased thermal gradients have been reported to generate higher thermal residual stresses resulting in higher thermal hysteresis [193]. Therefore, while not directly observed, it can be assumed that higher thermal residual stresses due to increased thermal gradients is the reason for the increased thermal hysteresis in the $L_{1.5}$ lattices. Additionally, the $L_{0.5}$ lattices exhibit higher η than the $L_{1.0}$ lattices. This is attributed to the lower cooling rates of the $L_{0.5}$ lattices resulting in higher Ni evaporation which alters the local composition, affecting phase transformation temperatures and hysteresis behaviour [198][199]. Amongst the PBF-LB samples, the $L_{1.0}$ lattices exhibited the lowest η overall demonstrating the optimum balance between the effect of reduced cooling rates in the thinner lattices and increased thermal gradients in the thicker lattices.

The DSC experiments also showed that the $L_{0.5}$ lattices exhibited MSTs on both heating and cooling. MSTs are generally attributed to the formations of the intermediate R-phase, which forms when it is thermodynamically favoured or the activation energy is lower than for other phases [200]. This is often associated with Ni_4Ti_3 precipitates supressing the martensitic transformation, acting as nucleation sites for R-phase [133]. However, Ni4Ti3 precipitates tend to occur in Ni-rich NiTi. In this case, the additional peaks are likely due to local chemical and microstructural inhomogeneity, causing some regions of the matrix to transform before others [200][47]. The disappearance with increasing strut diameter is due to reduced Ni evaporation and higher cooling rates increasing microstructural homogeneity. The complete disappearance of the additional peaks in the $L_{1.5}$ lattices is also evident in the enthalpy results. As shown in section 5.3.6 the enthalpy of heating and cooling is noticeably lower than that of the $L_{0.5}$ and $L_{1.0}$. This indicates that there is a single, complete phase change between B2 and B19'.

5.4.3. Effect of VED

The Rρ measurements presented in Figure 33 demonstrated a distinct dependence on VED, with a positive correlation observed for all samples processed below 45 J/mm^3 and a negative correlation for those above this threshold. At low VED values (below ~45 J/mm^3), insufficient energy input leads to incomplete melting and poor fusion between powder particles, resulting in lack of fusion and partially melted pore defects, increasing porosity

and decreasing Rρ [201]. As VED increases up to 45 J/mm^3, enhanced energy input promotes more complete melting allowing the melted powder to more easily flow to fill interparticle pores, reducing porosity and increasing density [202]. When VED increases above 45 J/mm^3, the excessive energy input causes overheating of the melt pool, which is known to induce higher thermal residual stresses and promotes over-melting phenomena such as keyhole formation. These effects contribute to the formation of microcracks and keyhole pores, which degrade the part's integrity and cause a reduction in Rρ [59]. These trends are corroborated by the SEM micrographs presented in Figure 34. Sample 7, processed at a VED of 37 J/mm^3 with an Rρ of 99.2%, exhibits a dense microstructure with minimal defects. In contrast, sample 4 at a lower VED of 21 J/mm^3 and Rρ of 96.6% shows extensive unmelted powder particles and lack-of-fusion defects. Meanwhile, sample 14, processed at a high VED of 83 J/mm^3 with Rρ of 97.4%, reveals significant keyhole pores and microcracks consistent with over-melting.

The EDX results presented in Figure 37 revealed that the Ni evaporation was primarily affected by scan speed. The results showed that for the $L_{1.0}$ and $L_{1.5}$ lattices, increasing VED had minimal effect on the Ni concentration until scan speeds reduced to 400 mm/s at which point Ni evaporation occurred. For scan speeds of above 400 mm/s the Ni content only varied between 0.20 and 0.28 at. % for the $L_{1.0}$ and $L_{1.5}$ lattices. Meanwhile at scan speeds of 400 mm/s the Ni content varied between 0.35 and 0.41 at. %. The higher Ni evaporation at the lower scan speeds of 400 mm/s can be attributed to the decrease in melt pool solidification rate resulting in more time for Ni evaporation to occur [196]. Additionally, the SXRD results presented in Figure 36 showed the appearance of $NiTi_2$ precipitates in the $L_{1.0}$ and $L_{1.5}$ lattices at mid to high VED. $NiTi_2$ precipitates deplete Ti from the matrix resulting in an apparent increase in Ni content. As scan speed decreases, Ni evaporation increases and surpasses the effect of the $NiTi_2$ precipitates on the matrix composition [178].

The DSC results presented in Figure 39 demonstrated a direct positive correlation between Af temperature and VED, with scan speed being the more significant factor. During the PBF-LB process, two main factors alter the Af temperature: Ni evaporation and precipitate formation [203]. Ni loss, which increases with higher VED, leads to a higher Ti:Ni ratio and thus an increase in Af. Conversely, the formation of Ti-rich precipitates depletes Ti from the

matrix, resulting in a decrease in A_f. A third factor which can affect the A_f PBF-LB NiTi parts is thermal residual stress. Biffi et al. [194] demonstrated that thermal residual stresses from the selective laser melting process resulted in an increase in the TTs of NiTi lattice structures following the Clausius-Clapeyron stress-temperature relationship. SXRD results indicated the presence of $NiTi_2$ in the samples, which would typically reduce the A_f temperature. However, since the peaks representing $NiTi_2$ were relatively weak, it can be concluded that the primary driver for the observed increase in A_f was the increase in the Ti:Ni ratio due to Ni evaporation. As discussed, the EDX results show that the Ni content in the $L_{1.0}$ and $L_{1.5}$ lattices is not significantly affected by the laser process parameters at lower VEDs (< 60 J/mm^3). The steady increase in A_f with increasing VED must therefore be attributed to both Ni evaporation and increasing the inferred increasing thermal residual stress.

BSEM images presented in Figure 35 revealed heterogeneous microstructures between the melt pool edges and interior for both high and low VED conditions, characterized by distinct grain structures. This heterogeneity arises from interactions between the liquid-solid interface and overlapping melt pools during solidification. Perumal et al. [204] demonstrated that melt pool boundaries and their intersections act as preferential sites for recrystallization and nucleation, thereby explaining the distinct microstructural variations observed at these regions in the present study. While both conditions produced heterogeneous microstructures, the low VED samples exhibited greater variation in grain morphology and size, featuring a mix of equiaxed and columnar dendritic grains. In contrast, the high VED samples displayed more uniform ultrafine cellular grains. This aligns with findings by Lu et al. [56], who attributed such differences to melt pool geometry. Higher energy densities generate deeper, wider melt pools that promote homogeneous nucleation and growth, whereas lower energy densities produce narrower, shallower melt pools which increase thermal gradients between the melt pool interior and edges, driving heterogeneous grain formation. The smaller grain size found in high VED samples (see Section 5.3.3) is consistent with result from Lin et al. [205], where it was observed that elevated VEDs enhance remelting and grain boundary nucleation. These mechanisms simultaneously halt grain growth prematurely and initiate new grain formation, ultimately yielding finer microstructures.

5.5. Conclusions

In this study the effect of scan speed, laser power, and lattice strut diameter on the microstructure, composition, and thermal behaviour of Ti-rich NiTi lattices produced by PBF-LB is investigated. A Box Behnken design of experiments was employed to systematically study the final properties of the part across three strut diameters (0.5 mm, 1.0 mm, and 1.5 mm), three scan speeds (400 mm/s, 800 mm/s, and 1200 mm/s), and three laser powers (150 W, 175 W, and 200 W). The key conclusions are summarised below:

1. The strut diameter has a significant influence on the final properties of the part. Thinner struts exhibit slower cooling and solidification rates during the PBF-LB process due to the lower thermal conductivity of the surrounding powder compared to the solid part. This resulted in overmelting in the thinner lattices, leading to a reduction in relative density for smaller strut diameters ($L_{0.5}$: 98.88 %, $L_{1.0}$: 99.27 %, $L_{1.5}$: 99.36 %). The smaller strut diameters had slower cooling rates which resulted in a higher Ni evaporation ($L_{0.5}$: 0.52 at. %, $L_{1.0}$: 0.41 at. %, $L_{1.5}$: 0.40 at. %).
2. Faster cooling in the larger diameter stuts resulted in reduced Ni evaporation and increased microstructural homogeneity resulting in more complete phase transformations. However, the thicker struts exhibited higher thermal residual stress owing to the increased surface area causing higher temperature differentials across each layer of the part relative to the smaller strut diameters. This resulting in increased thermal hysteresis.
3. The 1.0 mm struts exhibited the best balance between the effects of decreased cooling rates in the 0.5 mm lattice and increased thermal gradients in the 1.5 mm showing the smallest thermal hysteresis ($L_{0.5}$: 33.06 °C, $L_{1.0}$: 32.07 °C, $L_{1.5}$: 33.56 °C).
4. The process parameters are shown the have various effects on the lattice properties at different strut diameters. At VEDs above 45 J/mm^3 defects were observed within the printed lattices for all geometries however, the optimum VED for relative density increased with increasing strut diameter ($L_{0.5}$: 31.1 J/mm^3, $L_{1.0}$: 36.5 J/mm^3, $L_{1.5}$: 41.7 J/mm^3). Additionally, Ni evaporation occurred at all scan speeds including at the higher scan speeds of 1200 mm/s in the $L_{0.5}$ lattices while no significant Ni

evaporation occurred in the $L_{1.0}$ and $L_{1.5}$ lattices until the scan speed reduced to 400 mm/s.

5. The VED was also shown to control the A_f and microstructure of the lattices. A_f was shown to increase with VED due to Ni evaporation and increased thermal residual stress. Grain structure varied significantly with VED. Lower VEDs exhibited greater variation in grain morphology and size, featuring a mix of equiaxed and columnar dendritic grains due to narrower, shallower melt pools increasing thermal gradients between the melt pool interior and edges, driving heterogeneous grain formation. While higher VEDs displayed more uniform ultrafine cellular grains due to higher VEDs generating deeper, wider melt pools that promote homogeneous nucleation and growth.

In summary, strut diameter fundamentally alters the thermal dynamics during PBF-LB processing and, when combined with VED, dictates key structural and functional outcomes. Optimizing VED and lattice geometry enables tailored control over transformation temperatures, hysteresis, and microstructure, providing a pathway for engineering NiTi actuators with application-specific properties. The intermediate strut diameter of 1 mm exhibited the best properties over the range of VEDs, achieving a high density, stable phase transformations, and the lowest thermal hysteresis, all of which are critical to reliable design of NiTi actuators. Further studies carried out on the mechanical properties also find that the $L_{1.0}$ lattice is the optimum geometry for actuator performance [206]. The results of this study provide for the first time knowledge of how of the functional properties of PBF-LB processed Ti-rich NiTi lattice structures can be controlled. In particular, this work highlights how both geometry and process parameters can be set to achieve precise control over the characteristics of PBF-LB NiTi, enabling the engineering of NiTi SMA tailored properties.

Chapter 6: Investigating the Effect of VED and Lattice Strut Diameter on the Shape Memory Effect of Nitinol Actuators

Josephine Ryan Murphy, Josiah Cherian Chekotu, Paul Healy, and Dermot Brabazon. Investigating the Effect of VED and Lattice Strut Diameter on the Shape Memory Effect of Nitinol Actuators. Journal of Materials Research and Technology, *2025, 17*

This chapter builds directly upon the work presented in Chapter 5. It investigates the influence of PBF-LB process parameters and component geometry on the functional performance of NiTi actuators. By establishing direct links between the functional characteristics examined in this chapter and the material characteristics discussed in Chapter 5, a comprehensive understanding of the relationships between processing, geometry, microstructure, and actuator performance is developed. As the final experimental chapter of this thesis, it provides a crucial connection between the process–geometry–property relationships of additively manufactured NiTi and its resulting functional behaviour as a shape memory alloy actuator.

Abstract

This study examines the combined effect of volumetric energy density (VED) and lattice strut diameter on the microstructure, mechanical properties, and shape memory performance of NiTi lattice structures fabricated by laser powder bed fusion (PBF-LB). Lattices with 0.5, 1.0, and 1.5 mm strut diameters were produced by VEDs ranging from 21 J/mm^3 to 83 J/mm^3. Results reveal a strong process-geometry-property relationship. Optimum VED increased with strut diameter, resulting in relative densities of up to 99.36 %. Larger struts achieved higher ultimate strength, but reduced SME recovered strain and slower actuation. Thinner struts achieved greater SME recovery, larger stroke, and faster actuation, but reduced strength. The findings highlight a trade-off between strength and actuator performance and highlight the importance of considering both geometry and process parameters when designing NiTi actuators with application specific properties.

6.1. Introduction

Shape memory alloys (SMA) are a class of smart materials that exhibit the shape memory effect (SME) and superelasticity (SE) [13]. By utilizing the SME, SMA actuators are a promising alternative to traditional actuation systems, offering high power-to-mass ratios, low maintenance, and clean, silent actuation [16]. NiTi is currently the most widely used SMA due to its superior functional properties, such as low stiffness, high wear and corrosion resistance, and biocompatibility [207]. However, the implementation of NiTi actuators is typically limited by the use of simple geometries, such as traditionally manufactured wires and springs, due to NiTi's poor machinability [208]. To overcome these limitations, there has been much research into the additive manufacturing (AM), and particularly laser powder bed fusion (PBF-LB), of NiTi in recent years. Beyond enabling the manufacturing of complex geometries, AM offers additional advantages such as weight reduction, reduced waste material, part consolidation, and reduced lead times [209].

Recent studies carried out on the mechanical response of NiTi with complex geometries have demonstrated the potential of PBF-LB NiTi for a range of applications. Lightweight origami structures have shown potential for lightweight actuator applications, achieving complete recovery of 1000 N loads and strokes of 3.2 mm [208]. Auxetic meta-structures have exhibited efficient energy dissipation, superelasticity, and high deformation capacity, demonstrating potential for energy dissipation and damping applications [175]. Triply periodic minimal surface structures have demonstrated high accuracy and energy absorption, showing excellent potential for applications such as vibration isolators and crash cushioning [187]. However, despite these promising results, a systematic understanding of how specific geometric parameters influence functional performance remains limited. Furthermore, the relationship between geometry, thermal evolution during AM processing, and the resulting functional properties has not been thoroughly investigated.

The functional performance of SME-based actuators depends on the complex interplay between part geometry, microstructure, and composition [178]. The microstructure and composition of NiTi have been shown to be significantly altered by the high cooling rates and large thermal gradients involved in the PBF-LB process, which in turn, can control the functional properties of the printed part through parameter optimisation [141]. For

example, Saghaian et al. [171] demonstrated that decreasing the hatch distance from 120 to 80 µm in Ni-rich NiTi resulted in improved thermo-mechanical and SE response due to the increased crystallographic texture. Zhao et al. [173] investigated the effect of volumetric energy density (VED) on the phase transformation and SME of equiatomic NiTi, finding that although the samples fabricated at the lower VEDs of 375 J/mm^3 and 525 J/mm^3 had a higher proportion of NiTi phase, the samples fabricated at the higher VED of 625 J/mm^3 showed the best shape memory performance. The authors attributed this to more complete melting of the powder during the PBF-LB process. Yu et al. [210] showed that the pore generation on the surface of Ni-rich NiTi was determined by the combined effect of the VED and the ratio of laser power (P) to scan speed (V). They found that the combination of high VED (86.81 J/mm^3) and low P/V (0.21) resulted in the highest density and higher tensile strength, as well as better shape memory performance. Garrido et al. [71] demonstrated that increasing the VED for Ni-rich NiTi increased Ni evaporation, leading to higher transformation temperatures and promoting the formation of Ti-rich precipitates, which in turn reduced shape memory performance.

Despite significant advances in understanding PBF-LB processing of NiTi, a critical research gap persists. Current studies focus predominantly on Ni-rich conventional bulk samples, thereby neglecting one of the main advantages of AM while overlooking the critical impact of the geometry itself on the thermal development of PBF-LB parts [179][180]. Geometry specific variations, such as wall thickness and surface area, result in drastically different thermal gradients and cooling rates during the PBF-LB process, which directly influence microstructure development, chemistry, and the functional properties of the part [181][182][197]. This gap in the literature is critical for the design and optimization of application specific geometries with tailored actuator properties, enabling the implementation of SMA actuators across a wide range of applications. Therefore, this study aims to address this gap in the geometry-dependent thermal-microstructural-functional property relationships in PBF-LB NiTi components and to advance the practical implementation of AM NiTi actuators.

6.2. Materials and Method

6.2.1. Model Configuration & Dimensions

In this study, three model configurations were created using SolidWorks Ver. 2023. Each model had the same overall geometry but featured different strut diameters of 0.5 mm, 1.0 mm, and 1.5 mm as shown in Figure 32 and summarised in Table 10. For brevity, samples with lattice strut diameter of 0.5 mm, 1.0 mm, and 1.5 mm will herein be referred to $L_{0.5}$, $L_{1.0}$, and $L_{1.5}$, respectively throughout this paper. The periodic strut-based body-centred cubic (BCC) lattice structures consisted of unit cells with similar edge length of 6.25 mm and internal angles of 90°. These unit cells were repeated four times in the x, y, and z direction. Each configuration included top and bottom endplates matching the diameter of the corresponding strut diameter, as well as support structures to allow safe removal from the build plate without damaging the lattice structures. Additionally, removable pillars with the same diameter as the struts were incorporated for material characterisation purposes.

Table 10: Lattice Configuration & Dimensions

Lattice & Unit Cell Type	Periodic Strut-Based BCC
Number of unit cells in each direction	4
Unit cell length (mm)	6.25
Internal angles (°)	90
Strut Diameter (mm)	0.5, 1.0, 1.5
Width, Depth, and Height of Lattice (mm)	25

6.2.2. Material & Fabrication

NiTi samples were fabricated from Ti-rich powders with a composition of 49.82 at.% Ni and 50.18 at.% Ti, provided by Fort Wayne Metals, Castlebar, Co. Mayo, Ireland. The powders were sieved to achieve particle sizes ≤ 75 µm. The NiTi samples were 3D printed using an Aconity MINI (GmbH) PBF-LB system featuring a 200 W, 1068 nm Nd:YAG fibre laser. To minimise oxidation and contamination, the oxygen concentration was maintained below 20 ppm throughout the build using a purging gas of pure argon (99.999 %). Printing was performed with a layer thickness of 50 µm and a spot size of 60 µm. Constant scanning

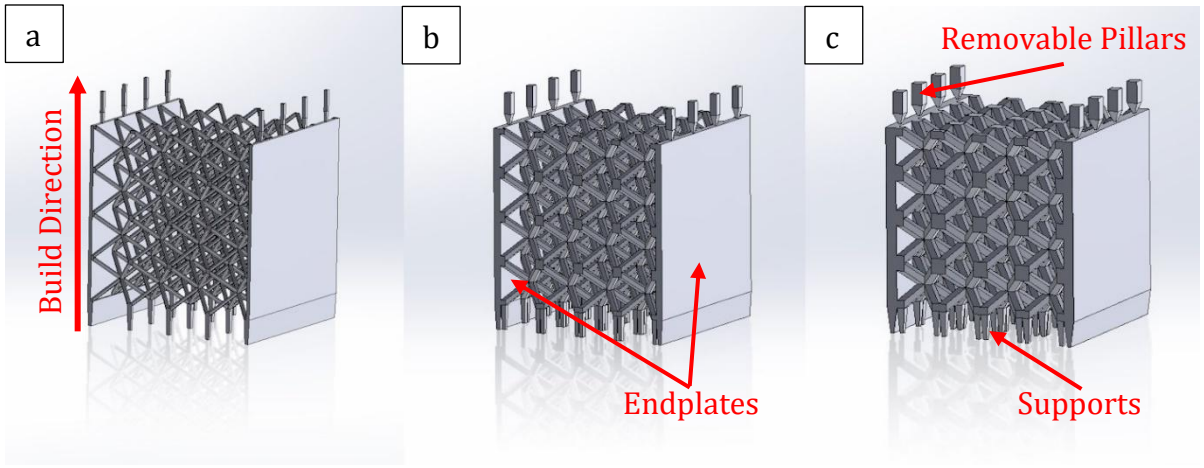


Figure 43: CAD models of the NiTi lattice structures showing build direction, end plates, support structures, and removable pillars for DSC tests with strut diameters of a) 0.5 mm, b) 1.0 mm, and c) 1.5 mm.

parameters were applied to all samples with a hatch spacing of 12 µm, a start angle of 0°, and increment angle of 67°.

6.2.3. Design of Experiment (DoE)

To investigate the effect of the PBF-LB process, laser powers of 150 W, 175 W and 200 W were used in combination with scan speeds of 400 mm/s, 800 mm/s, and 1200 mm/s; to build struts with diameters of 0.5, 1.0 and 1.5 mm. A Box-Behnken Design of Experiment (DoE) was employed to examine the influence of scan speed, laser power, and lattice strut diameter on the material properties and actuator performance of the PBF-PB fabricated NiTi lattices. The VED for each sample is calculated according to the following equation:

$$VED = \frac{P}{v.h.t}$$

Where;

P = Laser Power

v = Scan Speed

h = Hatch Spacing

t = Layer Thickness

The full DoE and corresponding VED is presented in Table 11.

Table 11: Full DoE of strut diameter, laser process parameters, and resulting VED for the produced NiTi samples.

Sample	Strut Diameter (mm)	Scan Speed (mm/s)	Laser Power (W)	VED (J/mm^3)
1	0.5	800	150	31.25
2	0.5	1200	175	24.31
3	1.0	800	175	36.46
4	1.0	1200	150	20.83
5	1.0	1200	200	27.78
6	1.5	800	150	31.25
7	1.0	800	175	36.46
8	0.5	400	175	72.92
9	1.0	800	175	36.46
10	1.5	1200	175	24.31
11	1.0	800	175	36.46
12	1.0	400	150	62.50
13	1.5	800	200	41.67
14	1.0	400	200	83.33
15	0.5	800	200	41.67
16	1.5	400	175	72.92

6.2.4. Material Characterisation

The density of the PBF-LB parts was measured using the Archimedes method in an isopropyl alcohol medium, following ASTM B962-23, with an analytical balance (Satorius Entris II Essential BCE124I-1S) having an accuracy and repeatability of ± 0.1 mg. Each sample was tested three times, and the average value was recorded as the sample density. The chemical compositions of the as-printed samples were determined using the Aztec Live System EDX from Oxford Instruments, operated within a Zeiss EVO-LS15 SEM. Five point measurements were taken at different locations on each sample, and the average was used to represent the sample composition. Differential scanning calorimetry (DSC) analysis was performed according to ASTM F2004-17 at Fort Wayne Metals, Castlebar, Co. Mayo, Ireland using a TA

Instruments® Discovery DSC2500 to evaluate the phase transformation behaviour of the powder and PBF-LB samples. The samples were initially ramped at a rate of 100 °C/min to 150 °C and held isothermally for 5 minutes. The data was then switched on, and the samples were cycled twice between -50 °C and 150 °C at a rate of 10 °C/min. The data from the second scanning cycle was used to plot the DSC curves and analyse the transformation characteristics.

6.2.5. Mechanical Characterisation

To investigate the actuator performance of the PBF-LB lattice structures, the samples were tested using compression-heat recovery cycling. During direct compression, the samples were compressed using a Zwick 50 kN Universal Testing Machine by employing an increasing level of displacement-controlled loads (1 mm, 2 mm, 3 mm, and 4 mm) at a loading rate of 2 mm/min at room temperature. Following unloading at each compressive load, the compressed samples were heated using a heat gun set to 500 °C for 5 minutes, which heated the samples to approximately 160 °C to enable shape recovery, and then left to cool with the aid of two fans at 12 V and 0.07 A for 10 minutes to reverse thermal expansion. For the experimental procedure, a dial gauge was placed on the sample and zeroed at the starting sample height. The sample was then compressed to the applied strain (ε_a), which refers to the displacement-controlled load applied during compression as a percentage of the height, $\%\, H$, of the lattice. The starting height of the lattice was 25 mm, excluding the base plate thickness. The ε_a for 1mm, 2 mm, 3 mm, and 4 mm, therefore, is 4%, 8%, 12%, and 16% respectively. The load was subsequently removed and the change in height from H was measured and referred to as ΔH_1. The sample was then heated to induce the SME and left to cool and the change in height from H after shape recovery was measured and referred to as ΔH_2. The true strain (ε_t), elastic strain (ε_e), residual strain (ε_r), and SME recovered strain (ε_{SME}) illustrated in Figure 44a are then calculated according to the following equations:

$$\varepsilon_t = \frac{\Delta H_1}{H} \times 100$$

$$\varepsilon_e = \varepsilon_a - \varepsilon_t$$

$$\varepsilon_r = \frac{\Delta H_2}{H_0} \times 100$$

$\varepsilon_{SME} = \varepsilon_t - \varepsilon_r$

Furthermore, the temperature of the sample was captured using a thermal imaging camera, and actuation time was assessed by recording a video and analysing the results with GOM Digital Image Correlation (DIC) software. Actuation time is defined as the time between when the heat gun is switched on (t_1) and when the slope of the displacement curve becomes less than 0.01 (t_2), as illustrated in Figure 44b.

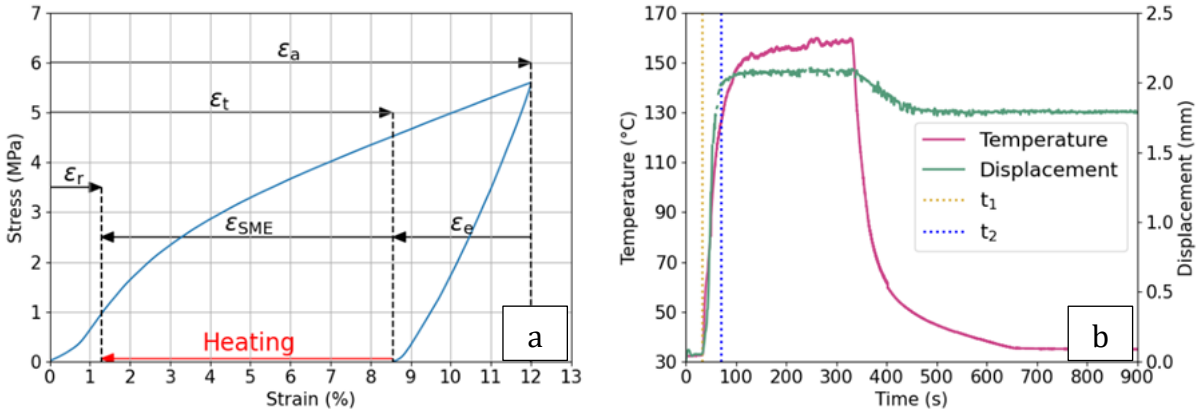


Figure 44: a) Graph of the typical stress-strain response during the compression and heating cycles illustrating applied strain (ε_a), true strain (ε_t), elastic strain (ε_e), SME recovered strain (ε_{SME}), and residual strain (ε_r). b) Plot of the typical sample response during heating showing the sample displacement from DIC, sample temperature captured by thermal camera, with the time when the heat gun is switched on (t_1) and when actuation is complete (t_2).

6.3. Results

6.3.1. Input-Output Correlations

To assess the significance of the DoE input variables on the outputs, p-values were calculated to evaluate statistical significance ($p \leq 0.05$). All relevant correlations in this study are shown in Table 12. As three samples with 0.5 mm stut diameter failed during the first compression and heating cycle, it was not possible to calculate the p-values for the shape memory response parameters of the lattices (strain values, stroke, and actuation time).

Table 12: P-values of the relevant input-output correlations.

	Strut Diameter	Laser Power	Scan Speed
Relative Density	0.0103		

Ni Loss	0.0013		0.0008
A_f Temperature		0.0042	< 0.0001
M_s Temperature	0.0007		0.0221
Thermal Hysteresis		0.0146	
Stiffness	< 0.0001	0.0274	0.0002
Ultimate Strength	< 0.0001	0.0263	0.0023
Ultimate Strain	0.0046		

6.3.2. Material Characterisation

6.3.2.1. Relative Density

Density was measured using the Archimedes principle and averaged across three measurements for each sample. The average relative density (Rρ) was calculated based on the theoretical density of fully dense nitinol (6.45 g/cm^3). For repeated samples within the Design of Experiments, the average relative density was 99.18 ± 0.13% (95 % confidence interval).

As shown in Figure 45 d, a positive correlation was observed between VED and Rρ for all samples with VED below 45 J/mm^3, whereas a negative correlation was found for samples with VED above 45 J/mm^3. At low VEDs, insufficient melting results in poor fusion of partially melted particles at the particle-particle interface, resulting in large, irregular interparticle porosity, increasing porosity and decreasing Rρ [201]. Therefore, the increase in Rρ at VEDs below 45 J/mm^3 is attributed to the increased energy input enabling more complete melting of the powder. Conversely, as VED increases above 45 J/mm^3, excessive energy input causes overmelting, leading to keyhole formation and increased thermal residual stresses which promote microcrack formation resulting in a decrease in Rρ [59]. Figure 33 illustrates this trend, showing significant lack of fusion and unmelted powder at the low VED of 21 J/mm^3, extensive cracking and keyhole formation at the high VED of 83 J/mm^3, and minimized defects at the intermediate VED of 37 J/mm^3.

Statistical analysis indicated that strut diameter was the dominant factor ($p = 0.0103$) influencing Rρ. The Rρ of the PBF-LB samples ranged from 98.22 % ± 0.06 % to 98.88 % ± 0.14 % (0.66 % variation) for $L_{0.5}$ lattices, 96.60 % ± 0.58 % to 99.27 % ± 0.12 % (2.67 %

variation) for $L_{1.0}$ lattices, and 96.02 % ± 0.26 % to 99.36 % ± 0.03% (3.34 % variation) for $L_{1.5}$ lattices. Surface contour plots in Figure 46 indicate that the maximum Rρ for all strut diameters occurs at a scan speed of 800 mm/s. The laser power, and consequently the VED, required to achieve maximum Rρ increased with strut diameter. The $L_{0.5}$ lattices achieved a maximum Rρ of 98.88 % at a laser power and VED of 150 W and 31.1 J/mm^3 respectively; for the $L_{1.0}$ lattices, a maximum Rρ of 99.27 % was achieved at a laser power and VED of 175 W and 36.5 J/mm^3 respectively; and for the $L_{1.5}$ lattices a maximum Rρ of 99.36 % was achieved at a laser power and VED of 200 W and 41.7 J/mm^3 respectively.

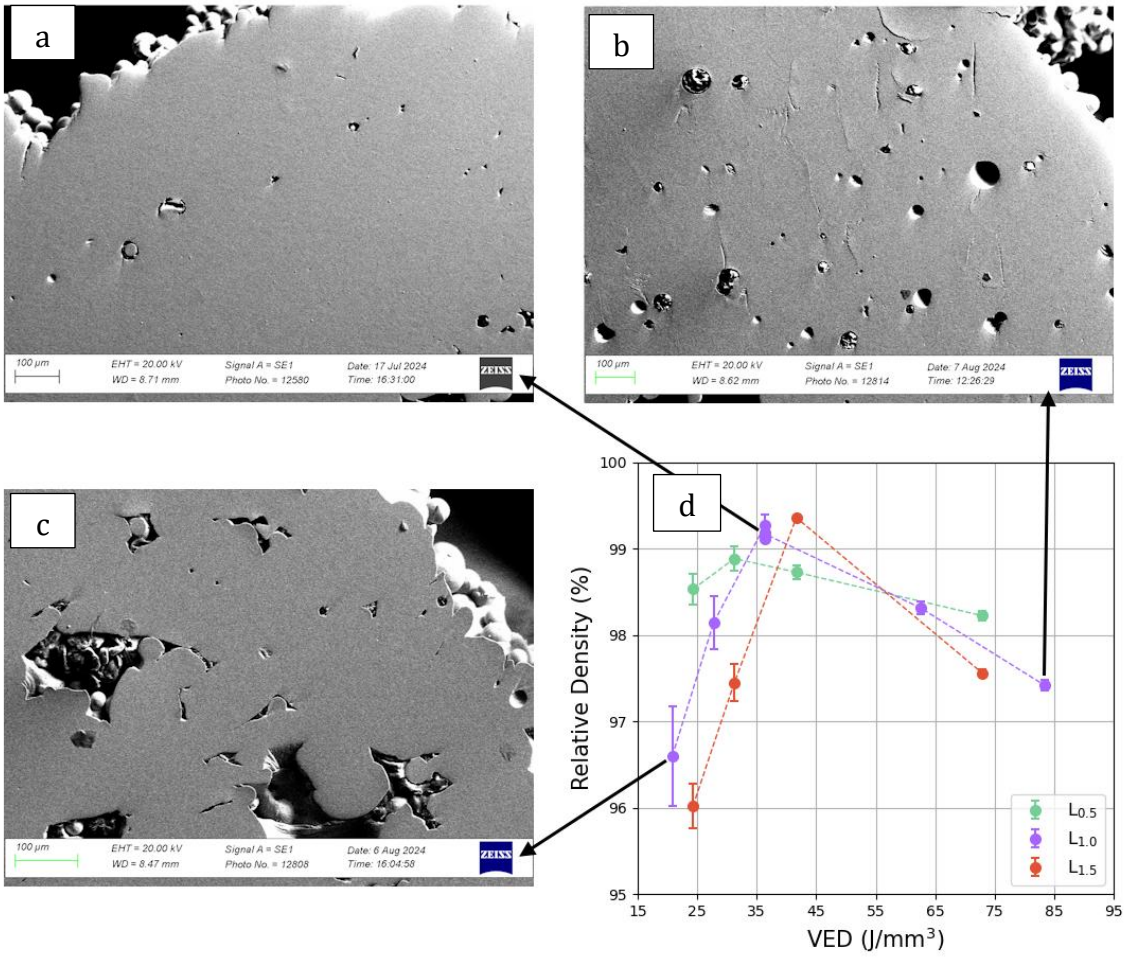


Figure 45: SEM images showing density and porosity defects for the $L_{1.0}$ at a) low b) mid c) and high VEDs. d) Scatter Plot of relative density with VED showing 95 % confidence intervals.

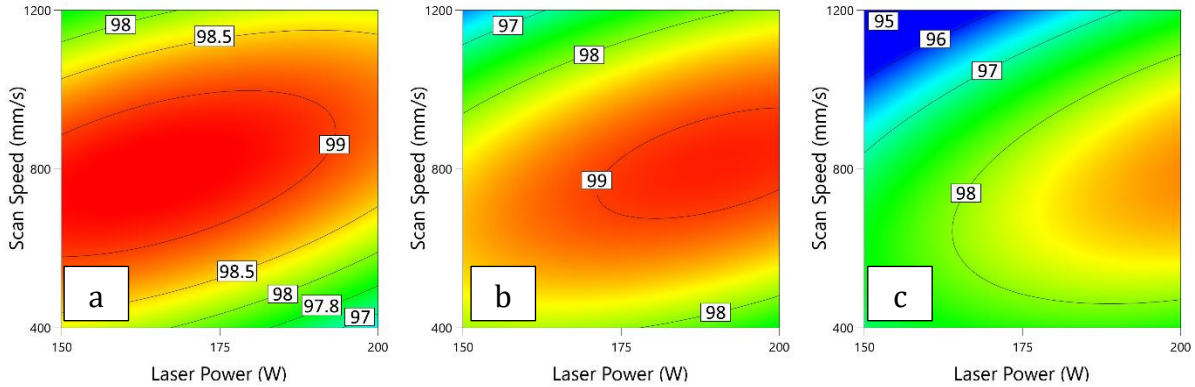


Figure 46: Surface Contours showing the effect of the relationship between laser power and scan speed on the relative density for a) $L_{0.5}$, b) $L_{1.0}$, and c) $L_{1.5}$.

6.3.2.2. Phase Transformation and Ni Loss

Phase transformation characterisation was carried out using DSC for the powder and PBF-LB samples. The DSC curves were analysed to determine the number of phase changes, the transformation temperatures, and the thermal hysteresis. The results in Figure 47 showed that the powder exhibited multi-stage transformations (MSTs) with overlapping peaks, attributed to the intermediate R-phase transformation [200]. These additional peaks were most visible in the $L_{0.5}$ lattices at low VED and disappeared as lattice strut diameter and VED increased.

The M_s of the powder was 62.4 °C, which was lower than that of any of the PBF-LB samples. However, there was very little variation in M_s amongst the PBF-LB samples. The average M_s for the repeated samples in the design of experiments was 64.4 °C with a 95 % confidence interval of ± 0.3 °C. The M_s of the PBF-LB samples ranged from 63.2 °C to 66.0 °C for the $L_{0.5}$ lattices, 64.1 °C to 65.0 °C for the $L_{1.0}$ lattices, and 64.7 °C to 66.4 °C for the $L_{1.5}$ lattices. The p-values demonstrate that the A_f temperature had a strong positive correlation with laser power (0.0042) and an even stronger negative correlation with scan speed (<0.0001). The A_f temperature of the powder was 87.5 °C, and the average A_f across the repeated samples in the design of experiments was 85.9 °C, with a 95 % confidence interval of ± 0.4 °C. All PBF-LB samples with a VED below 42 J/mm^3 had an A_f below the powder, ranging from 83.5 °C to 86.8 °C. Meanwhile, all PBF-LB samples with a VED above 42 J/mm^3 had an A_f above the powder, ranging from 88.4 °C to 92.3 °C. While the p-values showed no relevant correlation between strut diameter and A_f temperature, the surface contours presented in Figure 48

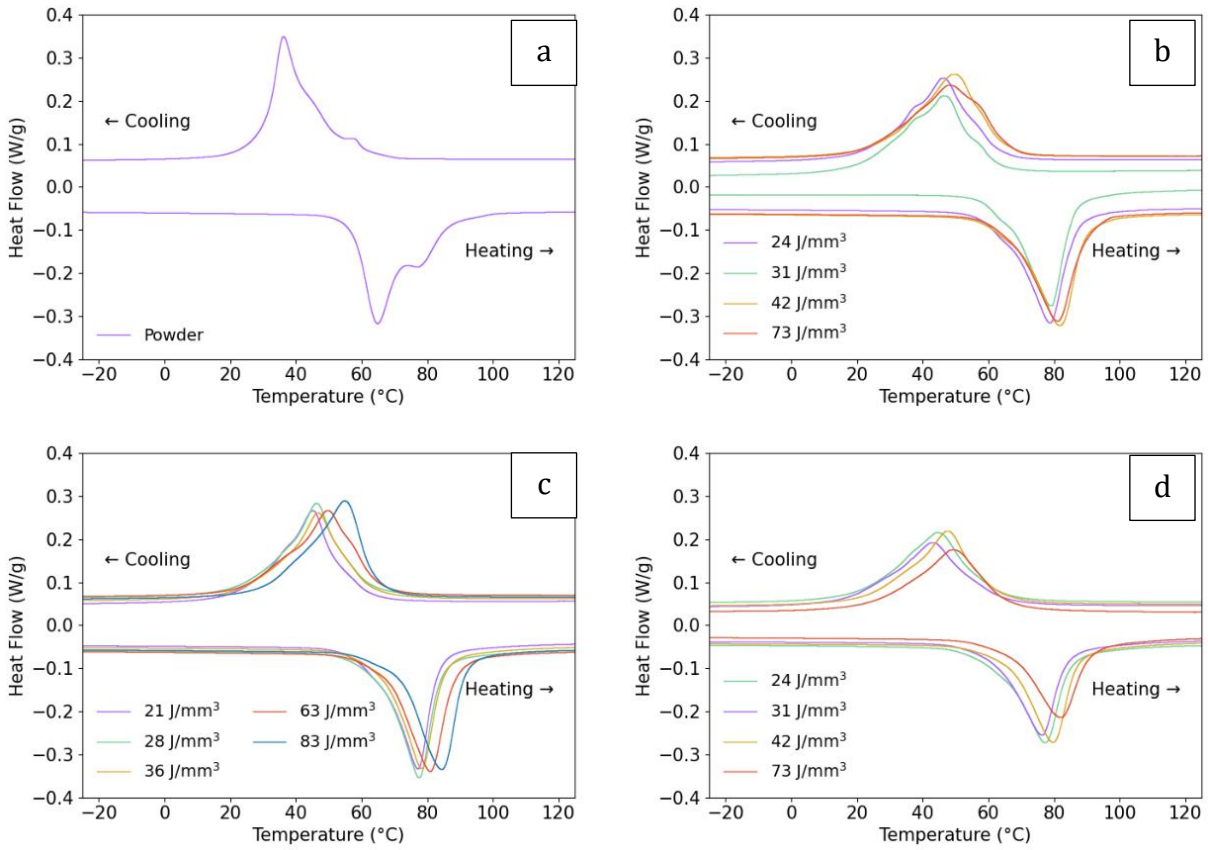


Figure 47: DSC curves of a) the as-received powder and DSC plots comparing the peaks with the VED for b) $L_{0.5}$, c) $L_{1.0}$, and d) $L_{1.5}$.

show that initially at lower VEDs, the $L_{0.5}$ have higher A_f temperatures. This is likely related to the relationship between strut diameter and Ni loss.

Ni loss during the PBF-LB process is often reported in the literature owing to the lower boiling point of Ni (2732 °C) compared to Ti (3287 °C) [173]. Ni loss amongst the PBF-PB samples ranged from 0.20 to 0.45 at.% Ni and the average Ni loss for the repeated samples in the design of experiments was 0.21 at. % with a 95 % confidence interval of ± 0.02 at. % Ni. Ni loss showed a strong negative correlation with scan speed (0.0008) however conversely to A_f temperature Ni loss did not have any relevant correlation with laser power but did have a negative correlation with strut diameter (0.0013). The $L_{0.5}$ lattices showed a directly proportional decrease in Ni content with increasing VED across all samples, while the $L_{1.0}$ and $L_{1.5}$ lattices showed no significant change in Ni concentration until higher VEDs (>60 J/mm^3) at the low scan speed of 400 mm/s at which point Ni content decreased. In addition, SXRD results from a prior work showed that $NiTi_2$ precipitation occurred from mid

to high VEDs, which can be attributed to the evaporation of Ni resulting in Ti saturated regions.

Thermal hysteresis (η) was also calculated, defined as the difference in peak temperature between the forward and reverse transformation ($\eta = A_p - M_p$). The powder had a lower η than all PBF-LB samples of 28.3 °C. The η of the PBF-LB samples ranged from 29.6 °C to 33.6 °C, and the average η for the repeated samples in the design of experiments was 31.4 °C with a 95 % confidence interval of ± 0.5 °C. The p-values indicate that η is primarily determined by laser power (0.0164), showing a decrease in η with increasing laser power. However, the surface contours in Figure 47 also reveal a correlation between η and strut diameter, showing that the $L_{1.0}$ lattices have the lowest η and the $L_{1.5}$ lattices have the highest η.

6.3.3. Mechanical Testing

6.3.3.1. Compression Behaviour

The compression behaviour of the PBF-LB samples was examined using a universal testing machine. Samples were compressed separately to compressive strains of 4 %, 8 %, 12 %, and 16 % with a heat recovery cycle in between each level of compression. The ultimate strength (σ_U) and ultimate strain (ε_U) of the samples were taken as the maximum stress and strain reached by the sample before failure, and the stiffness (k) was calculated as the maximum force divided by the change in height of the sample at this displacement during the 4 % compression cycle. The average σ_U, ε_U, and k of the repetition samples were 6.63 ± 0.38 MPa, 15.95 ± 0.04 %, and $20.76 \times 10^5 \pm 2.05 \times 10^5$ N/m, respectively.

The results show that σ_U and k increase with both VED and strut diameter. The p-values showed that for both σ_U and k, strut diameter is the most relevant parameter with a p-value of <0.0001 for both. Stiffness is also highly dependent on scan speed (p-value: 0.0002). Scan speed has a reduced effect on σ_U compared to k, however it is still a significant input (p-value: 0.0023). Laser power has the least influence of the inputs on both σ_U and k but remains a significant factor with p-values of 0.0263 and 0.0274 for σ_U and k respectively. The ultimate strain showed a non-monotonic relationship with VED. The maximum ε_U of

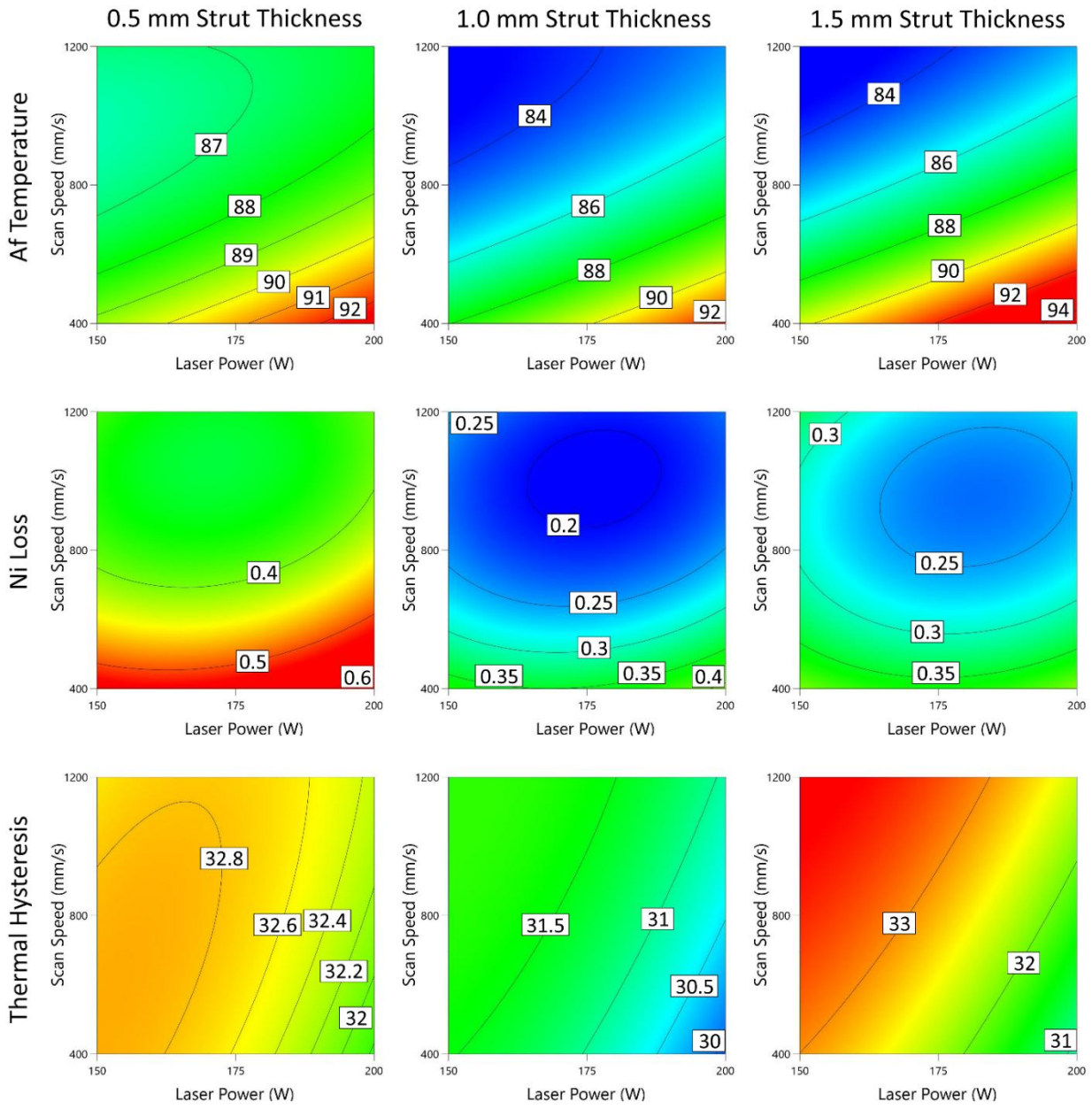


Figure 48: Surface contours of A_f temperature, Ni Loss, and thermal hysteresis of the $L_{0.5}$, $L_{1.0}$, and $L_{1.5}$ lattices.

14.75 % occurred at a VED of 73 J/mm^3 for the $L_{0.5}$ lattices, 16.00 % at 36 J/mm^3 for the $L_{1.0}$ lattices, and 14.14 % at 42 J/mm^3 for the $L_{1.5}$ lattices.

Figure 49a shows the stress-strain response of the $L_{0.5}$ lattices. Sample 1, sample 2, and sample 15 with VEDs of 31, 24, and 42 J/mm^3, respectively, all failed during the 4 % compression cycle. Crack initiation occurs at lower stress values of approximately 0.21, 0.12, and 0.34 MPa for samples 1, 2, and 15, respectively, seen by sharp drops in stress. However,

strain continues to increase and further fractures occur until complete failure at an ultimate strength of 0.23, 0.18, and 0.43 MPa with corresponding strains of 3.99, 3.98, and 3.32 % ,respectively. Among the $L_{0.5}$ lattices, only sample 8 (VED = 73 J/mm^3) withstood the 16 % compression cycle, exhibiting an ultimate strength of 0.81 MPa and strain of 14.75 %.

Table 13: Ultimate values for the $L_{0.5}$ lattices.

Sample	VED (J/mm^3)	σ_U (MPa)	ε_U (%)	k (*10^5)(N/m)	Failure Cycle
1	31	0.23	3.99	1.53	4%
2	24	0.18	3.98	1.20	4%
8	73	0.81	14.75	4.41	16%
15	42	0.43	3.32	3.44	4%

Figure 49b shows the stress-strain response of the $L_{1.0}$ lattices. While all samples failed during the 16 % compressive cycle. Sample 14 had the highest VED (83 J/mm^3), ultimate strength (7.48 MPa), and stiffness (25.48×10^5 N/m), and the lowest ultimate strain (14.36 %) of the $L_{1.0}$ lattices. The lowest ultimate strength (4.13 MPa) and stiffness (13.56×10^5 N/m) of the $L_{1.0}$ lattices were for sample 4, which also had the lowest VED (21 J/mm^3).

Table 14: Ultimate values for the $L_{1.0}$ lattices.

Sample	VED (J/mm^3)	σ_U (MPa)	ε_U (%)	k (*10^5)(N/m)	Failure Cycle
3	36	6.41	15.38	20.29	16%
4	21	4.13	15.26	13.56	16%
5	28	5.34	15.91	17.94	16%
7	36	7.18	16.00	22.29	16%
9	36	6.56	15.98	21.21	16%
11	36	6.37	15.93	19.26	16%
12	63	7.09	15.49	23.09	16%
14	83	7.48	14.36	25.48	16%

Figure 49c shows the stress-strain response of the $L_{1.5}$ lattices, which all failed during the 16 % compressive strain cycle. All the $L_{1.5}$ lattices exhibited sudden failure, evidenced by a drop in stress as strain continues to increase beyond their ultimate strain values. Ultimate

strength and stiffness ranged from 20.68 MPa and 59.75 × 10^5 N/m for sample 10 with VED of 24 J/mm^3 to 28.03 MPa and 84.76 × 10^5 N/m for sample 16 with VED of 73 J/mm^3.

Table 15: Ultimate values for the $L_{1.5}$ lattices.

Sample	VED (J/mm^3)	σ_U (MPa)	ε_U (%)	k (*10^5)(N/m)	Failure Cycle
6	31	22.81	13.86	66.91	16%
10	24	20.68	13.68	59.75	16%
13	42	28.61	14.14	74.02	16%
16	73	28.03	14.04	84.76	16%

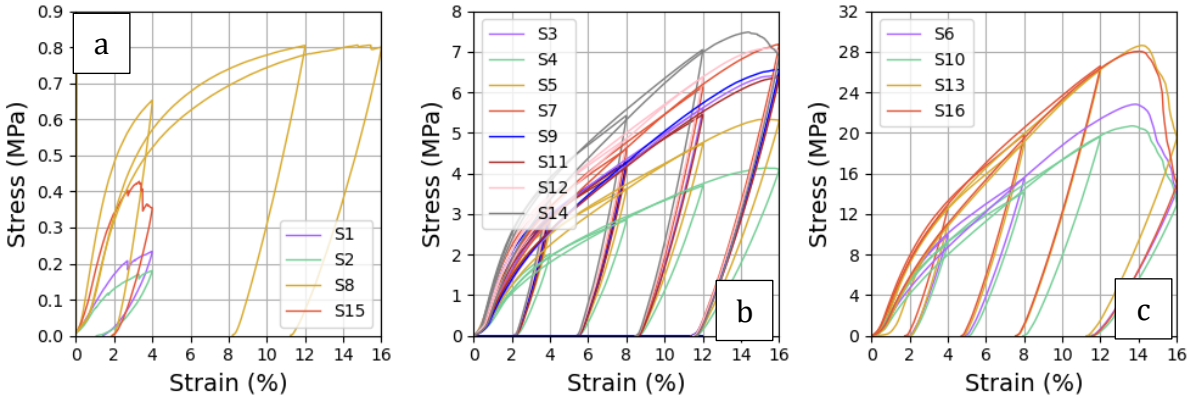


Figure 49: Stress-strain response at applied compressive strains of 4 %, 8 %, 12 %, and 16 % for a) the $L_{0.5}$ lattices, b) the $L_{1.0}$ lattices, and c) the $L_{1.5}$ lattices.

6.3.3.2. Shape Memory Response

The SME response of the PBF-LB samples was examined using compression and heat recovery cycles (as described in section 6.2.5). The strain recovery after compression and heating is a sum of both the elastic strain (ε_e) and the SME recovered strain (ε_{SME}). The ε_e is the proportion of strain that recovers upon removal of the compressive load. This component of the strain is attributed to the regions of the matrix that undergoes elastic deformation only as the applied strain is insufficient to induce a complete transformation to detwinned martensite during compression [211]. The true strain (ε_t) is the strain that remains after the load has been removed. In other words, ε_t is equal to the applied strain (ε_a) less ε_e. The ε_{SME} is the proportion of the strain that recovers after the sample was heated. This strain component is attributed to the region of the matrix that undergoes detwinned due to

the applied load exceeding the critical stress for the detwinning of martensite [212]. The residual strain (ε_r) is the proportion of strain that does not recover after heating. This irreversible component of the strain is attributed to the applied load exceeding the critical stress for plastic deformation [35].

Figure 50 illustrates the ε_e, ε_{SME}, and ε_r of the samples subjected to compression and heating cycles at ε_a of 4 %, 8 %, 12 %, and 16 %. The results showed that as strut diameter and VED increase, ε_r increases, while ε_{SME} decreases. At ε_a 12 %, before fracturing at higher strain levels, the $L_{0.5}$ lattice (sample 8) achieved ε_{SME} of 7.8 % and ε_r of 1.0 %. Amongst the $L_{1.0}$ lattices, both sample 4 (VED of 21 J/mm^3) and sample 5 (28 J/mm^3) achieved the highest ε_{SME} of 7.3 % and a ε_r of 1.4 %. The highest ε_r (1.6 %) was achieved by sample 14 with VED of 83 J/mm^3. For the $L_{1.5}$ lattices the highest ε_{SME} (6.0 %) was achieved by sample 6 with ε_r of 1.4 % and VED of 31 J/mm^3; and the highest ε_r (1.7 %) was achieved by sample 16 with VED of 73 J/mm^3.

The recovery ratio (Figure 51) is the ratio of ε_{SME} to ε_t and is an indication of the shape memory recovery ability of the material. From the results presented in Figure 50, as ε_a increased from 4 % to 16 %, the ε_{SME} increased and the ε_e decreased. However, it is also seen that ε_r increased and Figure 51 shows that there is an overall decrease in the recovery ratio with increasing ε_a. For example, despite the fracture of the lattice structures, from the ε_a of 12 % to 16 % the ε_{SME} increased from 7.8 to 10.5 % for sample 8 ($L_{0.5}$), 7.3 to 9.8 % for sample 4 ($L_{1.0}$), and 6.0 to 9.0 % sample 6 ($L_{1.5}$). Additionally, the ε_r increased from 1.0 to 1.6 %, 1.4 to 2.2 %, and 1.4 to 2.5 % for samples 8, 4, and 6, respectively. While this could indicate that the increase in ε_{SME} is substantial enough to outweigh the increase in ε_r, the recovery ratio gives a more accurate indication of the relationship between ε_a and SME performance. As ε_a increases from 12 to 16 %, the recovery ratio decreases from 88.2 to 87.0 % for sample 8, from 83.9 to 81.9 % for sample 4, and from 80.6 to 78.1 % for sample 6.

The average ε_e, ε_{SME}, ε_r, and the recovery ratio of the repetition samples at applied strains of 4 %, 8 %, 12 %, and 16 % are listed in Table 16 below.

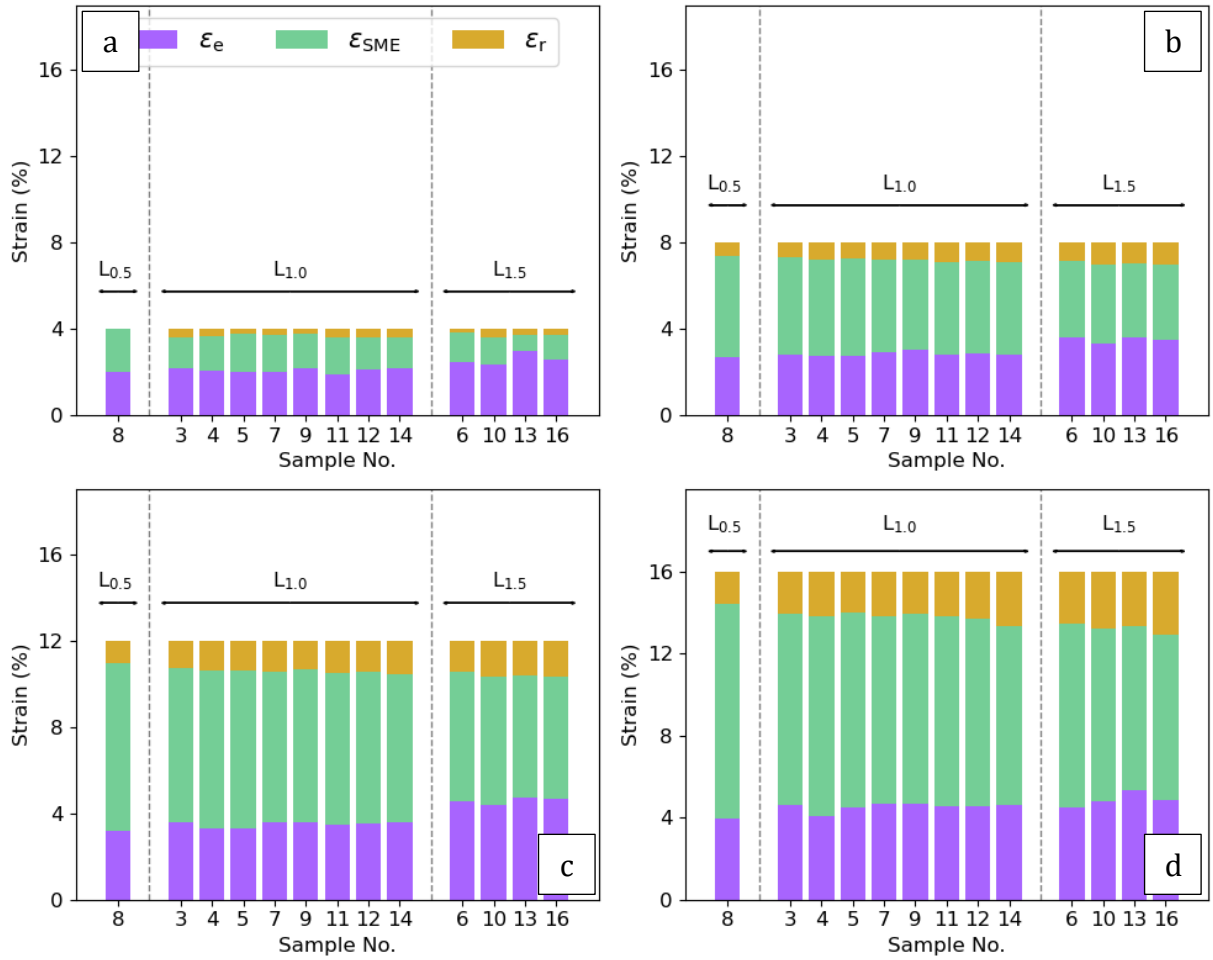


Figure 50: Bar charts of the SME response showing ε_e, ε_{SME}, and ε_r for applied strains a) 4 %, b) 8 %, c) 12 %, and d) 16 %.

Table 16: Average strain values of the repetition samples with 95 % confidence intervals; strut diameter of 1.0 mm; scan speed of 800 mm/s; and laser power of 175 W.

ε_a (%)	4	8	12	16
ε_e (%)	2.06 ± 0.21	2.90 ± 0.17	3.56 ± 0.09	4.64 ± 0.09
ε_{SME} (%)	1.64 ± 0.19	4.32 ± 0.19	7.06 ± 0.08	9.25 ± 0.10
ε_r (%)	0.30 ± 0.12	0.78 ± 0.13	1.38 ± 0.15	2.11 ± 0.10
Recovery Ratio (%)	84.57 ± 5.93	84.71 ± 2.49	83.65 ± 1.64	81.43 ± 0.78

6.3.3.3. Stroke and Actuation Time

The stroke of a linear actuator is defined as the distance that the actuator either extends or contracts in one direction when activated. In the present study, the stroke is therefore the

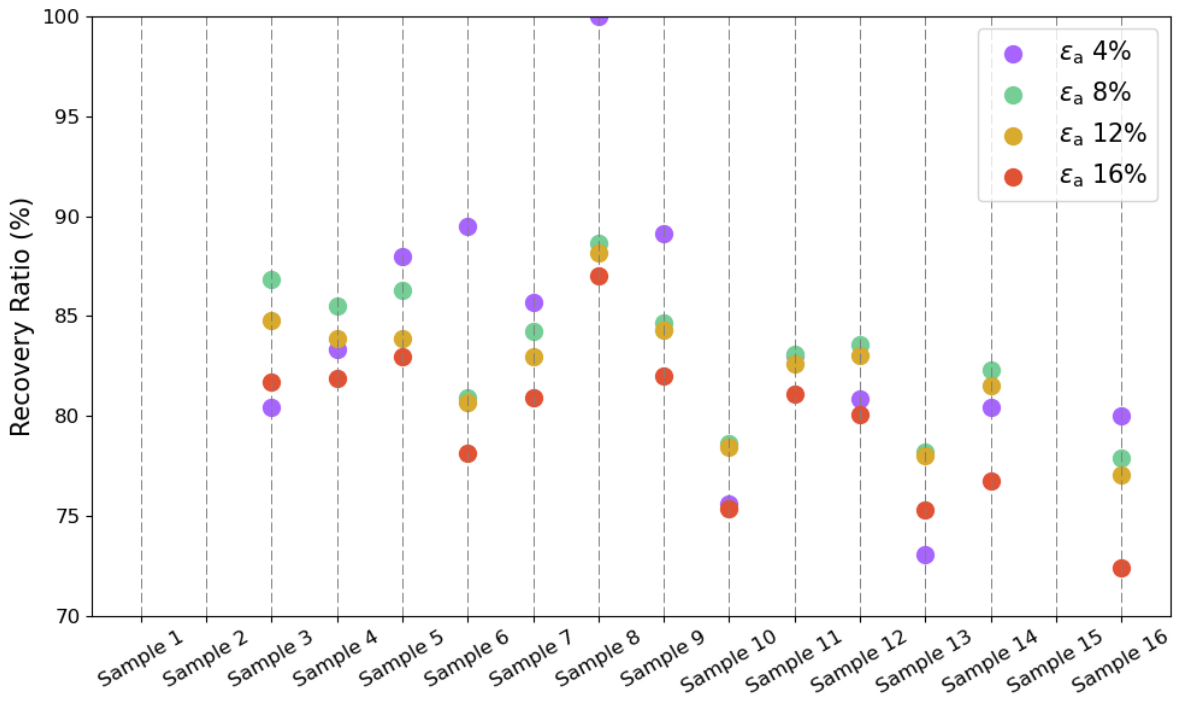


Figure 51: Graph comparing the recovery ratio of the lattice samples at each applied strain level.

difference in mm between ΔH_1 and ΔH_2. The average maximum stroke of the four repetition point samples when compressed to 3 mm was 1.77 ± 0.01 mm.

Figure 52 shows the strokes achieved by the lattices at each applied displacement. The results show that the resulting stroke increases with increasing displacement. There was also a general decrease in stroke with increasing VED and a clear increase in stroke with decreasing strut diameter. Despite the failure of all $L_{0.5}$ lattices with lower VEDs, sample 8, which had the highest VED of the $L_{0.5}$ lattices, achieved the maximum stroke across all samples at 2.62 mm when compressed to 4 mm. The stroke of the $L_{1.0}$ lattices at applied displacement of 4 mm ranged from 2.18 mm to 2.44 mm for sample 14 with VED 83 J/mm^3 and sample 4 with VED 21 J/mm^3, respectively, and the stroke of the $L_{1.5}$ lattices ranged from 2.01 mm to 2.25 mm for sample 13 with VED 42 J/mm^3 and sample 6 with VED 31 J/mm^3, respectively.

Table 17 shows the actuation time for each sample during the 12 % compressive strain cycle. The actuation time was calculated using DIC (following the method in section 6.2.5). It was not possible to extract DIC results for all samples due to computational limitations, therefore, the relationship between VED and actuation time remains unclear. However, the actuation

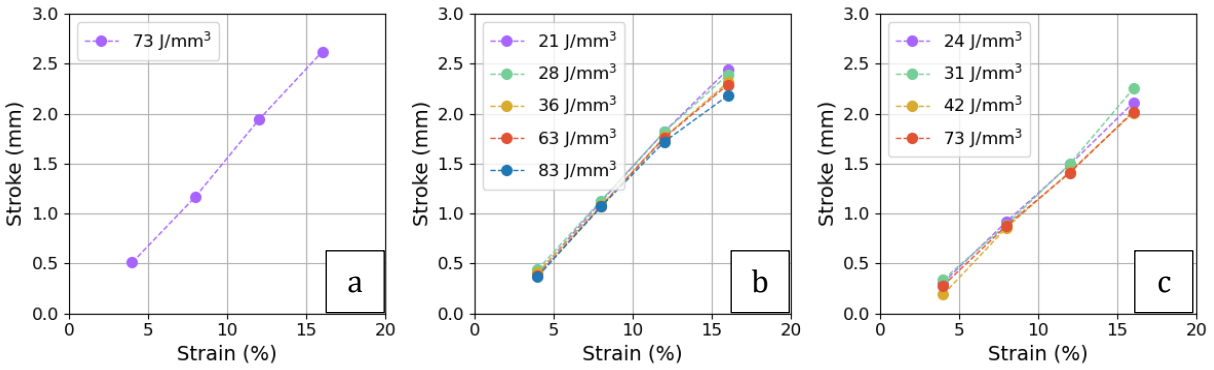


Figure 52: Stroke achieved at applied compressive strains of 4 %, 8 %, 12 %, and 16 % for a) the $L_{0.5}$ lattices, b) the $L_{1.0}$ lattices, and c) the $L_{1.5}$ lattices.

time clearly increased with increasing strut diameter. Of the two repetition samples from which an actuation time could be calculated, the average was 36.29 ± 1.47 s. Sample 8, $L_{0.5}$, achieved an actuation time of 17 s. The $L_{1.0}$ lattices ranged from 27 to 38 s, and the $L_{1.5}$ lattices ranged from 51 to 73 s.

The increase in actuation time with increasing strut diameter can be attributed to NiTi's low thermal conductivity and greater mass of solid material, which increases the time required to heat the entire sample. This can be seen in Figure 53, which shows the temperature change for the three sample geometries as the heat gun is applied over an 80 s period.

Table 17: Table showing the actuation time of the lattice samples during the 12 % compression and heating cycle.

Sample	3	4	5	6	7	8	12	13	14	16
Strut Diameter (mm)	$L_{1.0}$	$L_{1.0}$	$L_{1.0}$	$L_{1.5}$	$L_{1.0}$	$L_{0.5}$	$L_{1.0}$	$L_{1.5}$	$L_{1.0}$	$L_{1.5}$
VED (J/mm³)	36	21	28	31	36	73	63	42	83	73
Time (s)	37	27	34	73	36	17	33	51	38	69

6.4. Discussion

6.4.1. Material Characterisation

The density experiments revealed that higher absolute Rρ values were recorded for larger strut diameters. In particular, the maximum density measured for the $L_{0.5}$, $L_{1.0}$, and $L_{1.5}$ lattices was 98.88 %, 99.27 %, and 99.36 %, respectively, as shown in Figure 33. It was also noted from these results that the highest Rρ for each strut diameter occurred at higher VEDs,

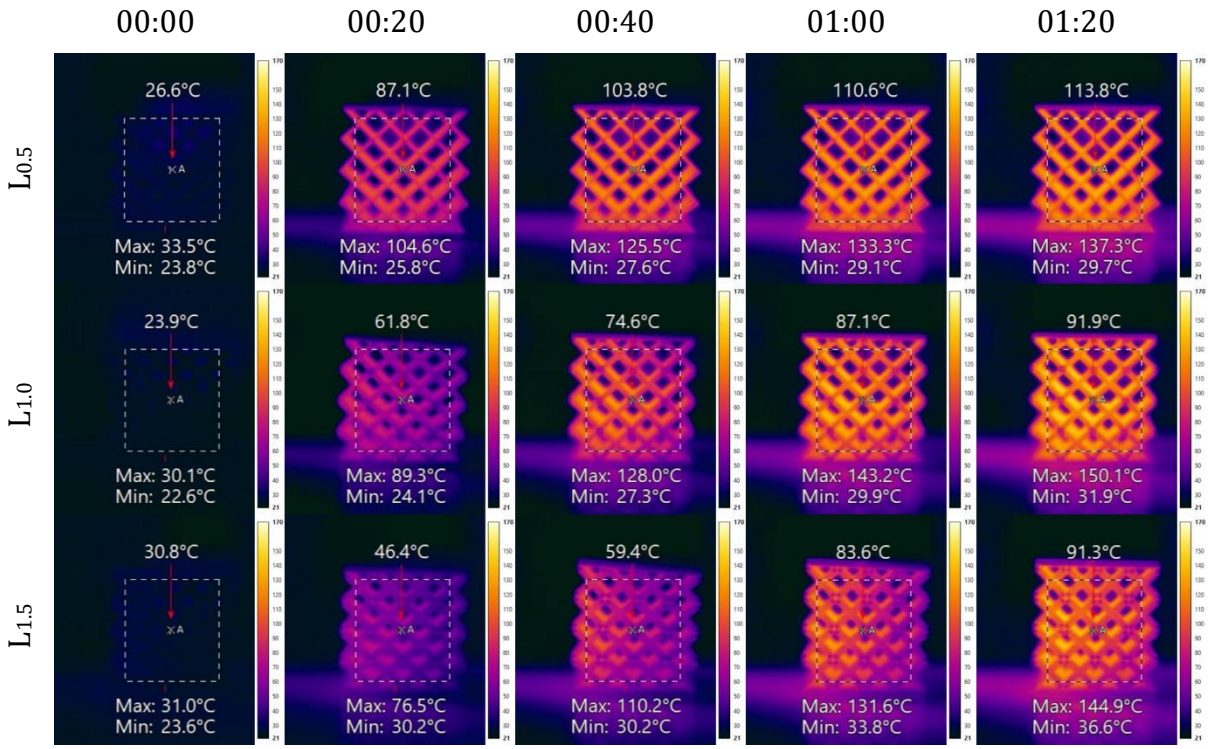


Figure 53: Thermal images comparing rate at which the temperature of the $L_{0.5}$, $L_{1.0}$, and $L_{1.5}$ lattices increases with the application of a heat gun for the first 80 s of heating.

as the strut diameter increased (31 J/mm^3 for the $L_{0.5}$ lattices, 37 J/mm^3 for the $L_{1.0}$ lattices, and 42 J/mm^3 for the $L_{1.5}$ lattices).

This is attributed to the slower cooling rates in the thinner lattices. Thinner features produced by PBF-LB have been observed to exhibit reduced cooling rates due to a higher ratio of surface area in contact with the surrounding powder to internal volume [181][182][194][195]. The surrounding powder acts as a thermal insulator because of its lower thermal conductivity compared to the solid part. Therefore, in thinner lattices, heat transfer from the melt pool is less effective, resulting in slower cooling. This means that at lower VEDs, the slower solidification in the $L_{0.5}$ lattices allows additional time for the melted powder to fill interparticle porosities more effectively, resulting in higher Rρ. This effect is also reflected in the EDX and DSC results, where Ni evaporation and, consequently, the A_f temperature are higher in the $L_{0.5}$ lattices at lower VEDs. However, this effect also limits the maximum achievable Rρ. As VED increases to mid VEDs, overmelting occurs, causing the $L_{0.5}$ lattices to have the lowest maximum Rρ amongst the three examined strut diameters.

Meanwhile, at the higher levels of VED, the $L_{1.5}$ lattices have lower Rρ than the $L_{0.5}$ lattices. This is attributed to the higher cooling rates and greater surface area in the thicker lattices, which increases thermal gradients. Increased thermal gradients result in higher porosity defects, thereby decreasing Rρ. This effect is also seen in the results for thermal hysteresis, where η is highest in the $L_{1.5}$ lattices, indicating higher thermal residual stress [193].

6.4.2. Stress-Strain Response

The mechanical stress-strain response of the PBF-LB lattice samples was a result of both the material properties and the structural geometry.

The stress-strain results presented in section 6.3.3.1 showed that σ_U increased with increasing VED. This is due to the formation of $NiTi_2$ precipitates, strengthen the alloy by pinning dislocations, hindering their motion and increasing strength [56]. SXRD results from prior work on the lattices found that $NiTi_2$ precipitates formed from the mid VEDs and increased with increasing VED. According to the nickel-titanium phase diagram, the NiTi phase is stable only for a narrow range of compositions (49 at.% Ni to 57 at.% Ni). Deviations from this range can lead to precipitation of secondary phases [16]. In Ti-rich NiTi, the resulting secondary phase most commonly observed is $NiTi_2$ [52], [53], [54]. The increase in σ_U with increasing VED in this study therefore, is attributed to the pinning effect of $NiTi_2$ precipitates formed due to the Ti-rich composition of the starting powder, fast solidification rates of the PBF-LB process [45] and the increasing Ni depletion with increasing VED.

The results for the $L_{1.0}$ and $L_{1.5}$ lattices showed that the ultimate strain is strongly correlated with Rρ. As with Rρ, ε_U increased with VED from low to mid VEDs and decreased with VED from mid to high VEDs. From Table 14 and Table 15, maximum ε_U values of 16.00 % and 14.14 % occurred at mid-range VED levels of 36 J/mm^3 and 42 J/mm^3 for the $L_{1.0}$, and $L_{1.5}$ lattices, respectively. An increase in ductility with increasing Rρ is often reported in the literature and is attributed to a decrease in porosity, which can act as a stress concentrator, leading to crack initiation and permanent deformation [213]. From Table 13, a maximum ε_U of 14.75 % was recorded at a higher VED of 73 J/mm^3 for the $L_{0.5}$ lattices. This maximum ε_U being at higher VEDs, compared to the $L_{1.0}$ and $L_{1.5}$ lattices, can be explained by the fact

that all $L_{0.5}$ lattices with a VED below 73 J/mm^3 failed during the 4% compressive strain cycle due to their lower σ_U.

The stress-strain results showed a strong positive correlation between ultimate strength and strut diameter. The ultimate strengths recorded ranged between 0.18 – 0.81 MPa, 4.13 – 7.48 MPa, and 20.68 – 28.61 MPa for the $L_{0.5}$, $L_{1.0}$, and $L_{1.5}$ lattices respectively. This was coupled with an increased in stiffness whereby k ranged between 1.20 – 4.41 N/m, 13.56 – 25.48 N/m, and 59.75 – 84.76 N/m for the $L_{0.5}$, $L_{1.0}$, and $L_{1.5}$ lattices, respectively. Meanwhile, the ultimate strains ranged from 3.32 % to 14.75 %, 14.36 % to 16.00 %, and 13.86 % to 14.14 % for the $L_{0.5}$, $L_{1.0}$, and $L_{1.5}$ lattices, respectively. The combination of the highest ultimate strength and lowest ultimate strain in the $L_{1.5}$ lattices indicates that these lattices were the least ductile among the tested geometries [214]. The higher strength and stiffness in the thicker lattices were due to the higher solid fraction in the direction of loading, which resisted structural deformation [180][179]. Additionally, as previously discussed, the increased strut diameter results in higher cooling rates. Increased cooling rates result in a finer grain structure. The fine grain structure can impede dislocation motion, resulting in increased fracture strength but reduced fracture strain [215]. Similar results were reported by Dadbakhsh et al. [180], who found that while higher sample volume led to a higher strength, faster cooling also produced a finer microstructure, resulting in higher overall strength.

The difference in ductility amongst the lattice geometries is evident in the stress-strain curves of the $L_{0.5}$ and $L_{1.5}$ lattices, as shown in Figure 49. The $L_{1.5}$ lattices exhibited a failure mode characterised by a single peak in the stress-strain curve, with failure occurring at the maximum stress, followed by a sharp drop in stress. In contrast, the $L_{0.5}$ lattices displayed a more progressive failure mechanism. Crack initiation occurs in multiple stages, as evidenced by small, sharp drops in stress, until complete fracture at the maximum stress due to localised stress concentration [175].

Variation in failure modes can be attributed to differences in bending resistance among the lattice geometries. As the strut diameter increases, bending deformation decreases for similar stress levels while compressive deformation becomes more dominant. This results

in a more homogeneous deformation behaviour, where failure occurs when all struts have reached their maximum shear stress, at which point cracks develop along the max shear plane seen by the 45°. In contrast, thinner struts exhibit greater bending, leading to barrelling and random distortions of the struts in multiple directions. These distortions create strain localisation, causing individual struts to fail sequentially, represented by the sharp stress drops, and leading to a premature decrease in overall strength [216].

6.4.3. Shape Memory Response

VED had a generally negative correlation with ε_{SME} and a positive correlation with ε_r. A similar finding was reported by Garrido et al. [71], who found that lower VEDs resulted in higher recoverable strains. The author attributed this to the increased presence of $NiTi_2$ precipitates as VED increased.

The results showed that ε_{SME} was highly dependent on strut diameter, decreasing as strut diameter increased. Despite the high VED (73 J/mm^3) of the only $L_{0.5}$ lattice to withstand mechanical testing, sample 8 had the highest ε_{SME} and the lowest ε_r at each strain level (see Figure 50), achieving a maximum ε_{SME} of 10.48 % and a corresponding ε_r of 1.56 %, at ε_a 16 %.

This can be attributed to the higher residual stress in the thicker lattices, resulting from their higher cooling rates. Thermal residual stresses caused by the PBF-LB process can increase the stress required for detwinning and martensite reorientation, and in addition, hardening due to the accumulation of dislocations during compression testing can impede the transformation from martensite to austenite during heating, causing plastic deformation via slip to occur, resulting in a decrease in ε_{SME} and an increase in ε_r [50].

The highest ε_{SME} achieved from the $L_{1.0}$ and $L_{1.5}$ lattices, respectively, was 9.76 % and 9.00 % at VEDs of 21 and 31 J/mm^3, with the corresponding ε_r of 2.16 % and 2.52 %. The increase in optimum VED for ε_{SME} with increasing strut diameter (21 J/mm^3 for $L_{1.0}$ and 31 J/mm^3 for $L_{1.5}$) was also reported by Qu et al. [181]. The author reported that while samples with larger wall thickness showed the best strain recovery at mid VEDs, those with smaller wall thickness required lower VEDs. They attributed this to slower cooling in the thinner samples, leading to greater Ni evaporation and a higher degree of $NiTi_2$ precipitation.

The performance of the PBF-LB lattices, compared to that in the literature, is promising. For example, in a study by sun et al. [187] on triply periodic minimal surface (TPMS) lattice structures at ε_a 12 % they reported a maximum ε_{SME} of 6.7 % with a corresponding ε_r of 2.5 %. In this study, at ε_a 12 %, the maximum ε_{SME} and corresponding ε_r for each of the strut diameters were 7.8 % and 1.0 % for the $L_{0.5}$ lattices, 7.3 % and 1.4 % for the $L_{1.0}$ lattices, and 6.0 % and 1.4 % for the $L_{1.5}$ lattices, respectively.

The results displayed in Figure 50 showed that ε_{SME} increased with increasing ε_a, implying that a greater proportion of the material undergoes martensite variant reorientation, thereby increasing the recoverable strain [171]. However, although ε_{SME} increases with ε_a, the recovery ratio decreases (as seen in Figure 51). This is due to stress accumulation from thermal residual stress in the PBF-LB process as well as from dislocations and precipitates, which cause localised slip deformations before the yield stress, resulting in a higher degree of irreversible deformation and thereby reducing the recovery ratio [51][187].

Table 18: Table summarising the maximum Rρ, σ_U, recovery ratio, and minimum actuation time recorded for the $L_{0.5}$, $L_{1.0}$, and $L_{1.5}$ lattices and their corresponding VED.

	$L_{0.5}$	**$L_{1.0}$**	**$L_{1.5}$**
Relative Density (%)	98.88	99.27	99.36
VED (J/mm³)	31	36	42
	$L_{0.5}$	**$L_{1.0}$**	**$L_{1.5}$**
Ultimate Strength (MPa)	0.81	7.48	28.61
VED (J/mm³)	73	83	42
	$L_{0.5}$	**$L_{1.0}$**	**$L_{1.5}$**
SME Recovered Strain (%)	10.48	9.76	9.00
VED (J/mm³)	73	21	31
	$L_{0.5}$	**$L_{1.0}$**	**$L_{1.5}$**
Actuation Time (s)	17	27	42
VED (J/mm³)	73	21	42

6.5. Conclusions

This study systematically examined the interplay between process parameters, lattice geometry, and functional performance in NiTi shape memory actuators fabricated by PBF-LB. The findings highlight a strong process-geometry-property relationship, governed by geometry dependent thermal evolution during the PBF-LB process, which directly influences density, mechanical behaviour, and shape memory performance.

Relative density was found to depend on both VED and strut diameter. VED values below 45 J/mm^3 lead to insufficient melting and poor particle fusion, while VED values above 45 J/mm^3 cause keyhole formation and induce thermal residual stresses. The optimum VED for achieving maximum density increased with increasing strut diameter.

Mechanical testing revealed that ultimate strength increased with VED due to $NiTi_2$ precipitation, whereas ductility strongly correlated with relative density. Larger strut diameters exhibited higher strength but reduced ductility, attributed to higher solid fraction and finer microstructure.

Shape memory response was influenced by VED and lattice geometry. Lower VEDs generally produced higher ε_{SME} and lower ε_r. Smaller strut diameters achieved higher ε_{SME} and faster actuation, while larger strut diameters showed reduced ε_{SME} and slower response due to higher thermal residual stresses and greater material volume.

In summary, this study reveals a trade-off between the strength and the actuator performance. Larger strut diameters and higher VEDs are suited for high-load applications where strength is prioritised over actuator stroke and speed, while smaller struts and moderate VEDs are recommended for lightweight, high-stroke actuators with rapid response. These insights provide a valuable framework for tailoring NiTi actuator performance, enabling the design of SMA actuators for a range of applications from rapid biomedical actuators to structural aerospace systems.

Recommended future work includes investigating the effect of post process heat treatments to relieve residual stresses from printing and produce a more homogeneous microstructure. Further investigation is required to optimise the actuation time of the samples which may

be achieved through shape training. Further studies could be carried out to further optimise the geometry by testing different variations of lattice structures.

Chapter 7: Conclusions and Future Work

7.1. Research Summary

The work presented in this doctoral thesis provides a detailed investigation into the development of NiTi-based SMA actuators. The aims and objectives outlined in chapter one were successfully achieved, leading to a comprehensive understanding of how process parameters, ageing heat treatments, and part geometry influence the physical, mechanical, and functional properties of both traditionally manufactured and additively manufactured NiTi actuators. This research thesis addresses a critical gap in the knowledge and provides new insight into the design and optimisation of NiTi SMA actuators.

Chapter 3 examines the influence of heat treatment time and temperature on the microstructure and strain recovery of traditionally manufactured Ni-rich NiTi wires used as thermal actuators. Density, hardness, phase transformation temperatures, microstructure, and alloy composition were evaluated. The results demonstrated that increasing the heat treatment time and temperature from 400 °C to 500 °C and from 30 to 120 min improved the strain recovery, with wires heat treated at 500 °C for 120 minutes achieving the highest recovery. Hardness decreased with both higher temperatures and longer times, attributed to the presence of Ni_4Ti_3 precipitates and subsequent changes in the matrix. DSC results showed that increasing the heat treatment temperature reduced the austenite transformation temperature from 42.8 °C to 24.4 °C due to the formation of Ni_4Ti_3 precipitates. In contrast, longer heat treatment times resulted in a slight increase in the austenite finish temperature. Increasing heat treatment time and temperature also sharpened the phase transformation curves, indicating reduced residual stresses and defects, thereby improving crystal mobility. These findings highlight that controlling heat treatment conditions enables precise tailoring of the material properties, phase transformation characteristics, and strain recovery of traditionally manufactured NiTi wires.

Chapter 4 investigated the combined effect of wire drawing history and post-processing heat treatment on the microstructure and actuator performance of traditionally manufactured Ni-rich NiTi wires used as electrical R-phase actuators. Phase transformation characteristics, hardness, microstructure, stroke, and actuation time were assessed. The results of the study

showed that the wire drawing steps strongly influence the final properties of the wire, even after subsequent heat treatments, due to residual stresses, dislocations, and precipitates introduced during the wire drawing and straight annealing steps. Defects were shown to be detrimental to performance, while ageing was demonstrated to be effective in reducing defects from the wire drawing process and improving actuator behaviour. Increasing ageing temperatures lowered austenite finish temperature, thermal hysteresis, and nano-hardness due to defect annihilation. The highest actuator stroke and lowest hysteresis were observed in wires with minimal dislocations. Notably, the thermal hysteresis of the R-phase transformation was significantly lower than that of the martensite transformation. The R-phase hysteresis ranged from 2.1 °C to 4.8 °C, while the martensite hysteresis ranged from 76.4 °C to 138.2 °C, demonstrating that R-phase actuators exhibit drastically reduced thermal hysteresis, which is a critical parameter in SMA actuators.

Chapter 5 focuses on the effect of PBF-LB process parameters and strut diameter on the microstructure, composition, and phase change characteristics of Ti-rich lattice structures. Results revealed that geometry critically influences density, Ni evaporation, and transformation behaviour. Thinner lattices exhibited slower cooling due to the insulating effect of surrounding powder, leading to lower density, greater Ni evaporation, and higher chemical heterogeneity caused by the slower cooling rate, resulting in more overmelting and allowing for more time for Ni evaporation to occur. Thicker lattices, in contrast, achieved higher density, reduced Ni evaporation, and more homogeneous microstructure, resulting in more complete phase transformations. However, they also exhibited an increase in thermal hysteresis due to the higher thermal gradients caused by the increased surface area of each layer of the parts built. The mid strut diameter of 1.0 mm provided the best balance between the effects of decreased cooling rates in the 0.5 mm lattice and increased thermal gradients in the 1.5 mm lattice, resulting in the smallest thermal hysteresis. VED was found to control austenite finish temperature, with higher VED increasing Af through enhanced Ni evaporation and thermal stresses. The results of this study emphasise the importance of part geometry and provide critical insights into the relationship between geometry, process parameters, and the final properties of NiTi PBF-LB parts.

Chapter 6 evaluates the impact of PBF-LB process parameters and strut diameter on the mechanical and functional performance of Ti-rich NiTi lattice actuators. Lattices with strut diameters of 0.5 mm, 1.0 mm, and 1.5 mm were fabricated via PBF-LB with scan speeds ranging from 400 to 1200 mm/s and laser powers of 150 to 200 W. Compression and thermal cycling tests revealed a strong process–geometry–property relationship. Strength and stiffness increased with both strut diameter and VED, indicating that the thinner struts exhibited ductile failure at lower compressive stresses, while the thicker struts exhibited more brittle failure at significantly higher compressive stresses. The increase in strength and stiffness with VED was attributed to $NiTi_2$ precipitation, which pinned dislocations but reduced ductility. Meanwhile, the increase in strength and stiffness with increasing strut diameter is due to the higher volume fraction of solid material in the direction of loading, which resists deformation and increases bending resistance. However, increased strut diameter and VED reduced shape memory recovery and increased residual strain. The increased with applied strain, but the recovery ratio decreased. This demonstrated that the increase in stroke was due to the higher applied strain providing more displacement for recovery, but the decrease in recovery ratio shows that, despite this, there was an increase in the amount of unrecovered strain, indicating that there was residual permanent deformation, which would result in faster degradation upon cycling. Actuation time increased with increasing strut diameter but showed little variation with VED, indicating that actuation time is primarily determined by the time required to heat the volume of material. The results of this study highlight a trade-off between strength and shape memory. Larger strut diameters and higher VEDs are beneficial for applications that require high loads, while smaller strut diameters and lower VEDs are beneficial for applications that require high stroke and rapid actuation.

Taken collectively, the findings of this thesis demonstrate that the performance of NiTi shape memory actuators cannot be understood solely through either a materials science perspective or an actuator performance perspective. Instead, actuator behaviour is governed by a complex interaction between processing history, microstructure, phase transformation characteristics, and geometry. By systematically investigating both conventionally manufactured and additively manufactured NiTi, this work establishes direct links between

process parameters, microstructural evolution, transformation behaviour, and functional actuator performance. These relationships provide a more holistic understanding of NiTi actuator design and contribute towards the development of predictive processing–structure–property–performance frameworks for SMAs.

A significant contribution of this research is its focus on thermally activated SME actuation, an area that has received considerably less attention than SE despite its growing importance in aerospace, automotive, and robotics. While many previous studies have focused primarily on transformation temperatures, phase transformations, or SE response, this thesis demonstrates how these material characteristics directly influence actuator properties such as stroke, recovery ratio, actuation time, and thermal hysteresis. The results therefore provide important insights into the optimisation of SMA actuators rather than simply the optimisation of SMA materials.

Furthermore, this thesis highlights the importance of geometry as a design parameter in additively manufactured NiTi actuators. The results demonstrate that geometry does not merely influence the mechanical response of the final component but also affects thermal history during manufacturing, chemical homogeneity, phase transformation behaviour, and ultimately actuator performance. This finding challenges the common assumption that process parameter optimisation can be performed independently of part geometry and demonstrates the necessity of considering process–geometry interactions during actuator design.

From a practical perspective, the outcomes of this research provide guidance for the manufacture of application-specific NiTi actuators. For conventionally manufactured NiTi wires, the results demonstrate how thermomechanical processing and ageing treatments can be tailored to minimise defects, reduce hysteresis, and maximise strain recovery. For PBF-LB fabricated NiTi lattices, the work establishes clear trade-offs between strength, stiffness, actuation displacement, recovery ratio, and actuation speed, enabling process parameters and geometries to be selected according to the functional requirements of a given application.

Ultimately, this thesis advances the understanding of how processing conditions and geometry influence the functional behaviour of NiTi shape memory actuators. The knowledge generated contributes towards the reliable design and manufacturing of high-performance SMA actuators and supports the broader adoption of lightweight, energy-efficient actuation technologies. In doing so, this work contributes to the development of next-generation SMA systems capable of reducing weight, improving efficiency, and supporting sustainability objectives within aerospace and other advanced engineering sectors.

7.2. Future work

The current study achieved its aim of developing NiTi-based SMA actuators, and the key findings of this work make a significant contribution to the understanding of optimizing both traditionally manufactured and additively manufactured NiTi actuators. Although the findings of this work address the existing knowledge gaps, it also highlights several additional gaps and challenges that require further investigation. The following proposals are recommendations for future areas of research:

- A more effective digital image correlation methodology is needed to accurately record changes in displacement, strain, and temperature over time, thereby facilitating a deeper understanding of the development of stress and actuator stroke in relation to both temperature and time. This would also enable a more thorough examination of the transfer of heat to the material, as well as the actuator cooling, which is the primary limitation to increasing actuation time.
- Further investigation into shape training and post-processing heat treatments of the PBF-LB parts should be conducted to enhance the shape memory response and determine the optimal training parameters to minimize residual strain and increase actuation time. This would help to develop a better understanding of optimization and performance of PBF-LB NiTi actuators.
- Further investigation should be undertaken to investigate the effect of geometry on the thermal development throughout the build. In-situ thermal investigation to develop a deeper understanding of the thermal development across each layer of the build. This would further enhance the understanding of the interaction between part

geometry and PBF-LB process parameters, as well as their influence on the final properties of the part.

- Fatigue tests should be investigated, as this is another key parameter of the functional performance of actuators. Fatigue testing of SMA actuators poses several challenges, including the cycle time limited by the cooling time of NiTi and the need to precisely control the actuator's temperature throughout the experiments. Developing a method for fatigue testing NiTi that records key actuator properties, such as actuator time, stroke, and force, would greatly benefit the understanding of NiTi actuator performance in use.
- Investigations should be conducted on the conductivity of NiTi and methods for improving it, such as adding alloying elements like copper. Improving the conductivity of NiTi would aid in the electrical heating of NiTi, which is crucial to its implementation as an actuator, and enhance the actuation time, necessary for a rapid response.

References

[1] Airbus (corporate author), 'Airbus Global Market Forecast 2025–2044', Jun. 2025. Accessed: Aug. 19, 2025. [Online]. Available: https://www.airbus.com/en/products-services/commercial-aircraft/global-market-forecast

[2] S. N. Kumar and D. Rutherford, 'Lifetime emissions from aircraft under a net-zero carbon budget'.

[3] Suraj, A. Kumar, and T. Nath, 'The synergy of NiTi shape memory alloys and additive manufacturing: Applications and future directions', *Journal of Micromanufacturing*, p. 25165984251348309, Jun. 2025, doi: 10.1177/25165984251348309.

[4] T. A. Farooqui, V. Belwanshi, K. Rane, K. S. Bhole, and S. Oak, 'Numerical Analysis of Joule Heating in a Ni–Ti Segmented Wire used in Sensing Applications', *J. Inst. Eng. India Ser. D*, vol. 104, no. 1, pp. 301–308, Jun. 2023, doi: 10.1007/s40033-022-00392-4.

[5] K. Otsuka and X. Ren, 'Physical metallurgy of Ti–Ni-based shape memory alloys', *Progress in Materials Science*, vol. 50, no. 5, pp. 511–678, Jul. 2005, doi: 10.1016/j.pmatsci.2004.10.001.

[6] N. Vasudha and K. Uma Rao, 'Shape memory alloy properties, modelling aspects and potential applications - a review', *J. Phys.: Conf. Ser.*, vol. 1706, no. 1, p. 012190, Dec. 2020, doi: 10.1088/1742-6596/1706/1/012190.

[7] W. Wang, Y. Xiang, J. Yu, and L. Yang, 'Development and Prospect of Smart Materials and Structures for Aerospace Sensing Systems and Applications', *Sensors*, vol. 23, no. 3, p. 1545, Jan. 2023, doi: 10.3390/s23031545.

[8] A. M. Nizamani, J. Daudpoto, and Nizamani M.A., 'Development of faster SMA actuators', in *Shape memory alloys - fundamentals and applications*, vol. 106, InTech, 2017, p. 126.

[9] Ch. Grossmann *et al.*, 'Processing and property assessment of NiTi and NiTiCu shape memory actuator springs', *Materialwissenschaft Werkst*, vol. 39, no. 8, pp. 499–510, Aug. 2008, doi: 10.1002/mawe.200800271.

[10] J. P. Oliveira, R. M. Miranda, and F. M. Braz Fernandes, 'Welding and Joining of NiTi Shape Memory Alloys: A Review', *Progress in Materials Science*, vol. 88, pp. 412–466, Jul. 2017, doi: 10.1016/j.pmatsci.2017.04.008.

[11] K. Kubášová *et al.*, 'A Review on Additive Manufacturing Methods for NiTi Shape Memory Alloy Production', *Materials*, vol. 17, no. 6, p. 1248, Mar. 2024, doi: 10.3390/ma17061248.

[12] A. Bhardwaj, A. K. Gupta, S. K. Padisala, and K. Poluri, 'Characterization of mechanical and microstructural properties of constrained groove pressed nitinol shape memory alloy for biomedical applications', *Materials Science and Engineering: C*, vol. 102, pp. 730–742, Sep. 2019, doi: 10.1016/j.msec.2019.04.070.

[13] T. W. Duerig, Ed., *Engineering aspects of shape memory alloys*. London ; Boston: Butterworth-Heinemann, 1990.

[14] Y. Liu and Z. Xie, 'Detwinning in Shape Memory Alloy', in *Progress in Smart Materials and Structures*, Nova Science Publishers, Inc., 2007, pp. 29–65.

[15] F. M. Weafer, Y. Guo, and M. S. Bruzzi, 'The effect of crystallographic texture on stress-induced martensitic transformation in NiTi: A computational analysis', *Journal of the Mechanical Behavior of Biomedical Materials*, vol. 53, pp. 210–217, Jan. 2016, doi: 10.1016/j.jmbbm.2015.08.023.

[16] M. Elahinia, *Shape Memory Alloy Actuators: Design, Fabrication, and Experimental Evaluation*, 1st edn. Ohio: John Wiley & Sons, 2016.
[17] D. R. Reynolds, 'A Nonlinear Thermodynamic Model for Phase Transitions in Shape Memory Alloy Wires', 2003.
[18] C. H. Fu, M. P. Sealy, Y. B. Guo, and X. T. Wei, 'Austenite–martensite phase transformation of biomedical Nitinol by ball burnishing', *Journal of Materials Processing Technology*, vol. 214, no. 12, pp. 3122–3130, Dec. 2014, doi: 10.1016/j.jmatprotec.2014.07.019.
[19] R. Srivastava, S. H. Alsamhi, N. Murray, and D. Devine, 'Shape Memory Alloy-Based Wearables: A Review, and Conceptual Frameworks on HCI and HRI in Industry 4.0', *Sensors*, vol. 22, no. 18, p. 6802, Sep. 2022, doi: 10.3390/s22186802.
[20] M. Bram, A. Ahmad-Khanlou, A. Heckmann, B. Fuchs, H. P. Buchkremer, and D. Stöver, 'Powder metallurgical fabrication processes for NiTi shape memory alloy parts', *Materials Science and Engineering: A*, vol. 337, no. 1–2, pp. 254–263, Nov. 2002, doi: 10.1016/S0921-5093(02)00028-X.
[21] V. Antonucci, G. Faiella, M. Giordano, F. Mennella, and L. Nicolais, 'Electrical resistivity study and characterization during NiTi phase transformations', *Thermochimica Acta*, vol. 462, no. 1–2, pp. 64–69, Oct. 2007, doi: 10.1016/j.tca.2007.05.024.
[22] G. Tadayyon, M. Mazinani, Y. Guo, S. M. Zebarjad, S. A. M. Tofail, and M. J. P. Biggs, 'Study of the microstructure evolution of heat treated Ti-rich NiTi shape memory alloy', *Materials Characterization*, vol. 112, pp. 11–19, Feb. 2016, doi: 10.1016/j.matchar.2015.11.017.
[23] S. Wen, Y. Liu, Y. Zhou, A. Zhao, C. Yan, and Y. Shi, 'Effect of Ni content on the transformation behavior and mechanical property of NiTi shape memory alloys fabricated by laser powder bed fusion', *Optics & Laser Technology*, vol. 134, p. 106653, Feb. 2021, doi: 10.1016/j.optlastec.2020.106653.
[24] S. K. Patel, B. Behera, B. Swain, R. Roshan, D. Sahoo, and A. Behera, 'A review on NiTi alloys for biomedical applications and their biocompatibility', *Materials Today: Proceedings*, vol. 33, pp. 5548–5551, 2020, doi: 10.1016/j.matpr.2020.03.538.
[25] A. Behera, A. K. Sahoo, and S. S. Mohapatra, 'Nickel–titanium smart hybrid materials for automotive industry', in *Nickel-Titanium Smart Hybrid Materials*, Elsevier, 2022, pp. 271–295. doi: 10.1016/B978-0-323-91173-3.00015-8.
[26] E. Patoor, D. C. Lagoudas, P. B. Entchev, L. C. Brinson, and X. Gao, 'Shape memory alloys, Part I: General properties and modeling of single crystals', *Mechanics of Materials*, vol. 38, no. 5–6, pp. 391–429, May 2006, doi: 10.1016/j.mechmat.2005.05.027.
[27] J. Frenzel, E. P. George, A. Dlouhy, Ch. Somsen, M. F.-X. Wagner, and G. Eggeler, 'Influence of Ni on martensitic phase transformations in NiTi shape memory alloys', *Acta Materialia*, vol. 58, no. 9, pp. 3444–3458, May 2010, doi: 10.1016/j.actamat.2010.02.019.
[28] S. Wang, K. Tsuchiya, L. Wang, and M. Umemoto, 'Martensitic stabilization and defects induced by deformation in TiNi shape memory alloys', *Int J Miner Metall Mater*, vol. 18, no. 1, pp. 66–69, Feb. 2011, doi: 10.1007/s12613-011-0401-5.
[29] T. Birk, S. Biswas, J. Frenzel, and G. Eggeler, 'Twinning-Induced Elasticity in NiTi Shape Memory Alloys', *Shap. Mem. Superelasticity*, vol. 2, no. 2, pp. 145–159, Jun. 2016, doi: 10.1007/s40830-016-0064-1.
[30] J. C. Chekotu *et al.*, 'Control of mechanical and shape memory characteristics in martensitic NiTi by setting L-PBF parameters and build orientation', *Journal of*

Materials Research and Technology, vol. 25, pp. 6407–6431, Jul. 2023, doi: 10.1016/j.jmrt.2023.07.092.
[31] S. Jiang, J. Yu, L. Hu, and Y. Zhang, 'Investigation on Deformation Mechanisms of NiTi Shape Memory Alloy Tube under Radial Loading', *Metals*, vol. 7, no. 7, p. 268, Jul. 2017, doi: 10.3390/met7070268.
[32] M. S. Khan, 'Martensitic detwinning microstructures in crystalline materials - mechanical modeling with exact computation of relaxed energy: A time incremental formulation', *AIP Advances*, vol. 9, no. 6, p. 065012, Jun. 2019, doi: 10.1063/1.5097882.
[33] B. Kockar, I. Karaman, J. I. Kim, Y. I. Chumlyakov, J. Sharp, and C.-J. (Mike) Yu, 'Thermomechanical cyclic response of an ultrafine-grained NiTi shape memory alloy', *Acta Materialia*, vol. 56, no. 14, pp. 3630–3646, Aug. 2008, doi: 10.1016/j.actamat.2008.04.001.
[34] N. Nayan, V. Buravalla, and U. Ramamurty, 'Effect of mechanical cycling on the stress–strain response of a martensitic Nitinol shape memory alloy', *Materials Science and Engineering: A*, vol. 525, no. 1–2, pp. 60–67, Nov. 2009, doi: 10.1016/j.msea.2009.07.038.
[35] T. Ezaz, J. Wang, H. Sehitoglu, and H. J. Maier, 'Plastic deformation of NiTi shape memory alloys', *Acta Materialia*, vol. 61, no. 1, pp. 67–78, Jan. 2013, doi: 10.1016/j.actamat.2012.09.023.
[36] S. Jiang, Y. Wang, X. Xing, and Y. Zhang, 'Stress-induced martensite phase transformation of FeMnSiCrNi shape memory alloy subjected to mechanical vibrating polishing', *Transactions of Nonferrous Metals Society of China*, vol. 30, no. 6, pp. 1582–1593, Jun. 2020, doi: 10.1016/S1003-6326(20)65321-3.
[37] M. Honarvar *et al.*, 'Study of Unrecovered Strain and Critical Stresses in One-Way Shape Memory Nitinol', *J. of Materi Eng and Perform*, vol. 23, no. 8, pp. 2885–2893, Aug. 2014, doi: 10.1007/s11665-014-1077-6.
[38] J. Uchil, K. P. Mohanchandra, K. K. Mahesh, and K. Ganesh Kumara, 'Thermal and electrical characterization of R-phase dependence on heat-treat temperature in Nitinol', *Physica B: Condensed Matter*, vol. 253, no. 1–2, pp. 83–89, Oct. 1998, doi: 10.1016/S0921-4526(98)00378-0.
[39] P. C. Chang, M. L. Ko, B. Ramachandran, Y. K. Kuo, C. Chien, and S. K. Wu, 'Comparative study of R-phase martensitic transformations in TiNi-based shape memory alloys induced by point defects and precipitates', *Intermetallics*, vol. 84, pp. 130–135, May 2017, doi: 10.1016/j.intermet.2017.01.008.
[40] S. Miyazaki and K. Otsuka, 'Deformation and transition behavior associated with the R-phase in Ti-Ni alloys', *Metall Trans A*, vol. 17, no. 1, pp. 53–63, Jan. 1986, doi: 10.1007/BF02644442.
[41] H. C. Ling and K. Roy, 'Stress-Induced Shape Changes and Shape Memory in the R and Martensite Transformations in Equiatomic NiTi', *Metall Trans A*, vol. 12, no. 12, pp. 2101–2111, Dec. 1981, doi: 10.1007/BF02644180.
[42] X. B. Wang, B. Verlinden, and J. Van Humbeeck, 'R-phase transformation in NiTi alloys', *Materials Science and Technology*, vol. 30, no. 13, pp. 1517–1529, Nov. 2014, doi: 10.1179/1743284714Y.0000000590.
[43] Y. Liu, J. I. Kim, and S. Miyazaki, 'Thermodynamic analysis of ageing-induced multiple-stage transformation behaviour of NiTi', *Philosophical Magazine*, vol. 84, no. 20, pp. 2083–2102, Jul. 2004, doi: 10.1080/14786430410001678262.

[44] T. W. Duerig and K. Bhattacharya, 'The Influence of the R-Phase on the Superelastic Behavior of NiTi', *Shap. Mem. Superelasticity*, vol. 1, no. 2, pp. 153–161, Jun. 2015, doi: 10.1007/s40830-015-0013-4.
[45] J. Bhagyaraj, K. V. Ramaiah, C. N. Saikrishna, S. K. Bhaumik, and Gouthama, 'Behavior and effect of Ti2Ni phase during processing of NiTi shape memory alloy wire from cast ingot', *Journal of Alloys and Compounds*, vol. 581, pp. 344–351, Dec. 2013, doi: 10.1016/j.jallcom.2013.07.046.
[46] J. Zhu *et al.*, 'Influence of Ni4Ti3 precipitation on martensitic transformations in NiTi shape memory alloy: R phase transformation', *Acta Materialia*, vol. 207, p. 116665, Apr. 2021, doi: 10.1016/j.actamat.2021.116665.
[47] H. Yu, Y. Qiu, and M. L. Young, 'Influence of Ni4Ti3 precipitate on pseudoelasticity of austenitic NiTi shape memory alloys deformed at high strain rate', *Materials Science and Engineering: A*, vol. 804, p. 140753, Feb. 2021, doi: 10.1016/j.msea.2021.140753.
[48] H. Z. Lu *et al.*, 'Effect of heat treatment on the microstructure and superelasticity of NiTi alloy via selective laser melting', *Journal of Materials Research and Technology*, vol. 30, pp. 1044–1055, May 2024, doi: 10.1016/j.jmrt.2024.03.148.
[49] S. Jiang, Y. Zhang, Y. Zhao, S. Liu, L. Hu, and C. Zhao, 'Influence of Ni4Ti3 precipitates on phase transformation of NiTi shape memory alloy', *Transactions of Nonferrous Metals Society of China*, vol. 25, no. 12, pp. 4063–4071, Dec. 2015, doi: 10.1016/S1003-6326(15)64056-0.
[50] J.-N. Zhu *et al.*, 'Effect of heat treatment on microstructure and functional properties of additively manufactured NiTi shape memory alloys', *Journal of Alloys and Compounds*, vol. 967, p. 171740, Dec. 2023, doi: 10.1016/j.jallcom.2023.171740.
[51] A. Fink, Z. Fu, and C. Körner, 'Functional properties and shape memory effect of Nitinol manufactured via electron beam powder bed fusion', *Materialia*, vol. 30, p. 101823, Aug. 2023, doi: 10.1016/j.mtla.2023.101823.
[52] A. Ishida, M. Sato, and S. Miyazaki, 'Mechanical properties of Ti–Ni shape memory thin films formed by sputtering', *Materials Science and Engineering: A*, vol. 273–275, pp. 754–757, Dec. 1999, doi: 10.1016/S0921-5093(99)00410-4.
[53] J. Lee and Y. C. Shin, 'Effects of Composition and Post Heat Treatment on Shape Memory Characteristics and Mechanical Properties for Laser Direct Deposited Nitinol', *Lasers Manuf. Mater. Process.*, vol. 6, no. 1, pp. 41–58, Mar. 2019, doi: 10.1007/s40516-019-0079-5.
[54] J. X. Zhang, M. Sato, and A. Ishida, 'On the Ti2Ni precipitates and Guinier–Preston zones in Ti-rich Ti–Ni thin films', *Acta Materialia*, vol. 51, no. 11, pp. 3121–3130, Jun. 2003, doi: 10.1016/S1359-6454(03)00124-1.
[55] H. Z. Lu *et al.*, 'Simultaneous enhancement of mechanical and shape memory properties by heat-treatment homogenization of Ti2Ni precipitates in TiNi shape memory alloy fabricated by selective laser melting', *Journal of Materials Science & Technology*, vol. 101, pp. 205–216, Feb. 2022, doi: 10.1016/j.jmst.2021.06.019.
[56] H. Z. Lu *et al.*, 'Ultrahigh-performance TiNi shape memory alloy by 4D printing', *Materials Science and Engineering: A*, vol. 763, p. 138166, Aug. 2019, doi: 10.1016/j.msea.2019.138166.
[57] T. Nakahata, 'Industrial processing of titanium–nickel (Ti–Ni) shape memory alloys (SMAs) to achieve key properties', in *Shape Memory and Superelastic Alloys*, Elsevier, 2011, pp. 53–62. doi: 10.1533/9780857092625.1.53.

[58] J. W. Mwangi, L. T. Nguyen, V. D. Bui, T. Berger, H. Zeidler, and A. Schubert, 'Nitinol manufacturing and micromachining: A review of processes and their suitability in processing medical-grade nitinol', *Journal of Manufacturing Processes*, vol. 38, pp. 355–369, Feb. 2019, doi: 10.1016/j.jmapro.2019.01.003.
[59] M. A. Obeidi *et al.*, 'Laser beam powder bed fusion of nitinol shape memory alloy (SMA)', *Journal of Materials Research and Technology*, vol. 14, pp. 2554–2570, Sep. 2021, doi: 10.1016/j.jmrt.2021.07.126.
[60] R. Kocich, I. Szurman, and M. Kurs, 'The Methods of Preparation of Ti-Ni-X Alloys and Their Forming'', in *Shape Memory Alloys - Processing, Characterization and Applications*, InTech, 2013.
[61] A. R. Pelton, S. M. Russell, and J. DiCello, 'The physical metallurgy of nitinol for medical applications', *JOM*, vol. 55, no. 5, pp. 33–37, May 2003, doi: 10.1007/s11837-003-0243-3.
[62] FW Metals, 'Shape Setting', FW Metals. Accessed: Aug. 17, 2023. [Online]. Available: https://www.fwmetals.com/materials/nitinol/nitinol-shapesetting/
[63] S. A. Smith and D. E. Hodgson, 'Shape Setting Nitinol', in *Medical Device Materials: Proceedings from the Materials & Processes for the Materials & Processes for Medical Devices Conference*, Anaheim, California: ASM International, 2004, pp. 266–270. Accessed: Feb. 03, 2022. [Online]. Available: https://books.google.ie/books?hl=en&lr=&id=Jv1Wysf1jv8C&oi=fnd&pg=PA266&dq=shape+setting+nitinol&ots=HE9TVBeDhN&sig=Lo2VhDXzPazr6OEGYFpkLtYmrgQ&redir_esc=y#v=onepage&q=shape%20setting%20nitinol&f=false
[64] M. A. Dechet *et al.*, 'A novel, precipitated polybutylene terephthalate feedstock material for powder bed fusion of polymers (PBF): Material development and initial PBF processability', *Materials & Design*, vol. 197, p. 109265, Jan. 2021, doi: 10.1016/j.matdes.2020.109265.
[65] A. K. Mishra and A. Kumar, 'Effect of Process Parameters on Melt Pool Characteristics and Solidification Process During Laser Powder Bed Fusion of AlSi10Mg Alloy', *Lasers Manuf. Mater. Process.*, vol. 11, no. 2, pp. 260–283, Jun. 2024, doi: 10.1007/s40516-023-00243-4.
[66] ISO/ASTM 52900:2021, *Additive manufacturing - general principles - fundamentals and vocabulary.*, 2021. Accessed: Aug. 25, 2025. [Online]. Available: https://www.iso.org/standard/74514.html
[67] A. Marques *et al.*, 'Inconel 718 produced by laser powder bed fusion: an overview of the influence of processing parameters on microstructural and mechanical properties', *Int J Adv Manuf Technol*, vol. 121, no. 9–10, pp. 5651–5675, Aug. 2022, doi: 10.1007/s00170-022-09693-0.
[68] M. Mehrpouya *et al.*, 'Additive manufacturing of architected shape memory alloys: a review', *Virtual and Physical Prototyping*, vol. 19, no. 1, p. e2414395, Dec. 2024, doi: 10.1080/17452759.2024.2414395.
[69] J. P. Oliveira, A. D. LaLonde, and J. Ma, 'Processing parameters in laser powder bed fusion metal additive manufacturing', *Materials & Design*, vol. 193, p. 108762, Aug. 2020, doi: 10.1016/j.matdes.2020.108762.
[70] F. L. Shen, H. Q. Li, H. Guo, N. N. Guo, and X. Y. Fang, 'Effect of energy density on the superelastic property of Ni-rich NiTi alloy fabricated by laser powder bed fusion',

Materials Science and Engineering: A, vol. 854, p. 143874, Sep. 2022, doi: 10.1016/j.msea.2022.143874.
[71] C. Garrido, S. Perosanz, A. Elliott, M. Simoes, and D. Barba, 'On the effect of the processing parameters in microstructure and thermomechanical properties of LPBF NiTi shape memory alloys', *Journal of Materials Research and Technology*, vol. 33, pp. 2414–2429, Nov. 2024, doi: 10.1016/j.jmrt.2024.09.155.
[72] M. A. L. Phan, O. Dew, and I. Todd, 'Predictive process diagram for parameters selection in laser powder bed fusion to achieve high-density and low-cracking built parts', *Additive Manufacturing*, vol. 85, p. 104145, Apr. 2024, doi: 10.1016/j.addma.2024.104145.
[73] B. Feng *et al.*, 'Effect of laser hatch spacing on the pore defects, phase transformation and properties of selective laser melting fabricated NiTi shape memory alloys', *Materials Science and Engineering: A*, vol. 840, p. 142965, Apr. 2022, doi: 10.1016/j.msea.2022.142965.
[74] J. Schröder, T. Fritsch, B. Ferrari, M. L. Altmann, G. Bruno, and A. Toenjes, 'Laser powder bed fusion: Defect type influences critical porosity re-growth during reheating after hot isostatic pressing', *Journal of Materials Processing Technology*, vol. 340, p. 118839, Jun. 2025, doi: 10.1016/j.jmatprotec.2025.118839.
[75] Y. Huang *et al.*, 'Keyhole fluctuation and pore formation mechanisms during laser powder bed fusion additive manufacturing', *Nat Commun*, vol. 13, no. 1, p. 1170, Mar. 2022, doi: 10.1038/s41467-022-28694-x.
[76] M. S. Seyam, P. Koshy, and M. A. Elbestawi, 'Laser Powder Bed Fusion of Unalloyed Tungsten: A Review of Process, Structure, and Properties Relationships', *Metals*, vol. 12, no. 2, p. 274, Feb. 2022, doi: 10.3390/met12020274.
[77] S. Rangaswamy *et al.*, 'Evaluating residual stress in additively manufactured nitinol shape memory alloy', *npj Adv. Manuf.*, vol. 2, no. 1, p. 16, Apr. 2025, doi: 10.1038/s44334-025-00027-y.
[78] K. Khanlari, Q. Shi, K. Li, K. Hu, P. Cao, and X. Liu, 'Effects of printing volumetric energy densities and post-processing treatments on the microstructural properties, phase transformation temperatures and hardness of near-equiatomic NiTinol parts fabricated by a laser powder bed fusion technique', *Intermetallics*, vol. 131, p. 107088, Apr. 2021, doi: 10.1016/j.intermet.2021.107088.
[79] A. Nespoli, 'The high potential of shape memory alloys in developing miniature mechanical devices: A review on shape memory alloy mini-actuators', *Sensors and Actuators A: Physical*, vol. 158, no. 1, pp. 149–160, 2010.
[80] C. Haberland, M. Elahinia, J. Walker, and H. Meier, 'Visions, Concepts and Strategies for Smart Nitinol Actuators and Complex Nitinol Structures Produced by Additive Manufacturing', in *Volume 1: Development and Characterization of Multifunctional Materials; Modeling, Simulation and Control of Adaptive Systems; Integrated System Design and Implementation*, Snowbird, Utah, USA: American Society of Mechanical Engineers, Sep. 2013, p. V001T01A006. doi: 10.1115/SMASIS2013-3072.
[81] R. Casati, A. Tuissi, S. Belochapkine, C. Dickinson, and S. A. M. Tofail, 'Thin NiTi Wires with Reduced Thermal Hysteresis for Shape Memory Actuators', *Funct. Mater. Lett.*, vol. 05, no. 01, p. 1250009, Mar. 2012, doi: 10.1142/S1793604712500099.

[82] A. Concilio, L. Lecce, A. Concilio, and S. Ameduri, *Shape memory alloy engineering : for aerospace, structural and biomedical applications*, 1st edition. Kidlington, England ; Butterworth-Heinemann, 2015.
[83] O. Benafan *et al.*, 'Shape memory alloy actuator design: CASMART collaborative best practices and case studies', *Int J Mech Mater Des*, vol. 10, no. 1, pp. 1–42, Mar. 2014, doi: 10.1007/s10999-013-9227-9.
[84] A. El Naggar, M. A. Youssef, and Civil and Environmental Engineering, Western University, London, ON, N6A 5B9, Canada, 'Shape memory alloy heat activation: State of the art review', *AIMS Materials Science*, vol. 7, no. 6, pp. 836–858, 2020, doi: 10.3934/matersci.2020.6.836.
[85] O. Benafan, S. A. Padula, R. D. Noebe, D. W. Brown, B. Clausen, and R. Vaidyanathan, 'An in situ neutron diffraction study of shape setting shape memory NiTi', *Acta Materialia*, vol. 61, no. 10, pp. 3585–3599, Jun. 2013, doi: 10.1016/j.actamat.2013.02.040.
[86] G. Costanza, M. E. Tata, and C. Calisti, 'Nitinol one-way shape memory springs: Thermomechanical characterization and actuator design', *Sensors and Actuators A: Physical*, vol. 157, no. 1, pp. 113–117, Jan. 2010, doi: 10.1016/j.sna.2009.11.008.
[87] V. B. Krishnan, 'A Shape Memory Alloy Based Cryogenic Thermal Conduction Switch', in *AIP Conference Proceedings*, Anchorage, Alaska (USA): AIP, 2004, pp. 26–33. doi: 10.1063/1.1774548.
[88] P. Motzki, T. Gorges, M. Kappel, M. Schmidt, G. Rizzello, and S. Seelecke, 'High-speed and high-efficiency shape memory alloy actuation', *Smart Mater. Struct.*, vol. 27, no. 7, p. 075047, Jul. 2018, doi: 10.1088/1361-665X/aac9e1.
[89] J. Mohd Jani, M. Leary, and A. Subic, 'Designing shape memory alloy linear actuators: A review', *Journal of Intelligent Material Systems and Structures*, vol. 28, no. 13, pp. 1699–1718, Aug. 2017, doi: 10.1177/1045389X16679296.
[90] K. Sadrnezhaad, F. Mashhadi, and R. Sharghi, 'Heat Treatment of Ni-Ti Alloy for Improvement of Shape Memory Effect', *Materials and Manufacturing Processes*, vol. 12, no. 1, pp. 107–115, Jan. 1997, doi: 10.1080/10426919708935124.
[91] C. Mao, J. Dong, H. Li, and J. Ou, 'Seismic performance of RC shear wall structure with novel shape memory alloy dampers in coupling beams', presented at the SPIE Smart Structures and Materials + Nondestructive Evaluation and Health Monitoring, M. Tomizuka, C.-B. Yun, and J. P. Lynch, Eds, San Diego, California, Apr. 2012, p. 83454G. doi: 10.1117/12.917304.
[92] D. Vojt, 'Influence of Heat Treatment of Shape Memory NiTi Alloy on Its Mechanical Properties', p. 5, 2010.
[93] X. Liu, Y. Wang, D. Yang, and M. Qi, 'The effect of ageing treatment on shape-setting and superelasticity of a nitinol stent', *Materials Characterization*, vol. 59, no. 4, pp. 402–406, Apr. 2008, doi: 10.1016/j.matchar.2007.02.007.
[94] L. Oncel and M. E. Acma, 'Effect of Heat Treatment Temperature and Heat Treatment Time on Properties and use of NiTi Shape Memory Implant Material', *International Advanced Research Journal in Science, Engineering and Technology*, vol. 4, no. 1, pp. 64–69, Jan. 2017, doi: 10.17148/IARJSET.2017.4115.
[95] M. Kök, F. Dağdelen, A. Aydoğdu, and Y. Aydoğdu, 'The change of transformation temperature on NiTi shape memory alloy by pressure and thermal ageing', *J. Phys.: Conf. Ser.*, vol. 667, p. 012011, Jan. 2016, doi: 10.1088/1742-6596/667/1/012011.

[96] M. J. Drexel, G. S. Selvaduray, and A. R. Pelton, 'The Effects of Cold Work and Heat Treatment on the Properties of Nitinol Wire', p. 9, 2007.
[97] J. Khalil-Allafi, A. Dlouhy, and G. Eggeler, 'Ni4Ti3-precipitation during aging of NiTi shape memory alloys and its influence on martensitic phase transformations', *Acta Materialia*, vol. 50, no. 17, pp. 4255–4274, Oct. 2002, doi: 10.1016/S1359-6454(02)00257-4.
[98] H. Sadiq, M. B. Wong, R. Al-Mahaidi, and X. L. Zhao, 'The effects of heat treatment on the recovery stresses of shape memory alloys', *Smart Mater. Struct.*, vol. 19, no. 3, p. 035021, Mar. 2010, doi: 10.1088/0964-1726/19/3/035021.
[99] X. Ma, Y. Zhou, X. Chen, G. Lu, J. Ji, and S. Zhao, 'Effect of Temperature on Phase Transformation of NiTi-based Shape Memory Alloy', *J. Phys.: Conf. Ser.*, vol. 2109, no. 1, p. 012001, Nov. 2021, doi: 10.1088/1742-6596/2109/1/012001.
[100] D. Golberg, Y. Xu, Y. Murakami, K. Otsuka, T. Ueki, and H. Horikawa, 'High-temperature shape memory effect in Ti50Pd50 − xNix (x = 10, 15, 20) alloys', *Materials Letters*, vol. 22, no. 5–6, pp. 241–248, Mar. 1995, doi: 10.1016/0167-577X(94)00256-8.
[101] R. Lahoz and J. A. Puértolas, 'Training and two-way shape memory in NiTi alloys: influence on thermal parameters', *Journal of Alloys and Compounds*, p. 7, 2004.
[102] H. Y. Luo and E. W. Abel, 'A comparison of methods for the training of NiTi two-way shape memory alloy', p. 8, 2007.
[103] M. Speicher, D. E. Hodgson, R. DesRoches, and R. T. Leon, 'Shape Memory Alloy Tension/Compression Device for Seismic Retrofit of Buildings', *J. of Materi Eng and Perform*, vol. 18, no. 5–6, pp. 746–753, Aug. 2009, doi: 10.1007/s11665-009-9433-7.
[104] H. Aryan and M. Ghassemieh, 'A superelastic protective technique for mitigating the effects of vertical and horizontal seismic excitations on highway bridges', *Journal of Intelligent Material Systems and Structures*, vol. 28, no. 12, pp. 1533–1552, Jul. 2017, doi: 10.1177/1045389X16672593.
[105] B. Reedlunn, S. Daly, and J. Shaw, 'Superelastic shape memory alloy cables: Part I – Isothermal tension experiments', *International Journal of Solids and Structures*, vol. 50, no. 20–21, pp. 3009–3026, Oct. 2013, doi: 10.1016/j.ijsolstr.2013.03.013.
[106] H. Semba, N. Okabe, T. Yamaji, K. Okita, and K. Yamauchi, 'Axial Compressive Behavior of Single-Stage Bellows of TiNi Shape Memory Alloy for Seismic Applications', *MSF*, vol. 475–479, pp. 2055–2058, Jan. 2005, doi: 10.4028/www.scientific.net/MSF.475-479.2055.
[107] J. A. Shaw, D. S. Grummon, and J. Foltz, 'Superelastic NiTi honeycombs: fabrication and experiments', *Smart Mater. Struct.*, vol. 16, no. 1, pp. S170–S178, Feb. 2007, doi: 10.1088/0964-1726/16/1/S17.
[108] O. M. A. Taha, M. B. Bahrom, O. Y. Taha, and M. S. Aris, 'Experimental study on two way shape memory effect training procedure for NiTiNOL shape memory alloy', vol. 10, no. 17, p. 6, 2015.
[109] 'Mechanical errors', in *Precision Manufacturing*, Boston, MA: Springer US, 2008, pp. 121–166. doi: 10.1007/978-0-387-68208-2_4.
[110] NaberTherm, 'NaberTherm Laboratory Furnaces Brochure 2021'. 2013.
[111] G. Rondelli, 'Localized corrosion behaviour in simulated human body fluids of commercial Ni–Ti orthodontic wires', *Biomaterials*, vol. 20, no. 8, pp. 785–792, Apr. 1999, doi: 10.1016/S0142-9612(98)90233-2.

[112] B09 Committee, *Test Methods for Density of Compacted or Sintered Powder Metallurgy (PM) Products Using Archimedes Principle*. doi: 10.1520/B0962-23.
[113] P. Elmer, 'Guide to Selection of Differential Scanning Calorimetry (Dsc) Sample Pans'. 2021. Accessed: Aug. 17, 2023. [Online]. Available: https://resources.perkinelmer.com/lab-solutions/resources/docs/tch_guide-to-dsc-selection-pans.pdf
[114] Aoli Shenzhen Technology Co., 'Vickers Hardness Testing'. Accessed: Aug. 17, 2023. [Online]. Available: https://www.hardnessgauge.com/testing-types/vickers-hardness-testing/
[115] C. T. Rueden *et al.*, 'ImageJ2: ImageJ for the next generation of scientific image data', *BMC Bioinformatics*, vol. 18, no. 1, p. 529, Dec. 2017, doi: 10.1186/s12859-017-1934-z.
[116] W. J. Buehler and F. E. Wang, 'A summary of recent research on the nitinol alloys and their potential application in ocean engineering', *Ocean Engineering*, vol. 1, no. 1, pp. 105–120, Jul. 1968, doi: 10.1016/0029-8018(68)90019-X.
[117] L. Xu and R. Wang, 'The Effect of Annealing and Cold-drawing on the Super-elasticity of the Ni-Ti Shape Memory Alloy Wire', *MAS*, vol. 4, no. 12, p. p109, Nov. 2010, doi: 10.5539/mas.v4n12p109.
[118] R. R. Adharapurapu, F. Jiang, and K. S. Vecchio, 'Aging effects on hardness and dynamic compressive behavior of Ti–55Ni (at.%) alloy', *Materials Science and Engineering: A*, vol. 527, no. 7–8, pp. 1665–1676, Mar. 2010, doi: 10.1016/j.msea.2009.10.069.
[119] C. Haberland, H. Meier, and J. Frenzel, 'On the Properties of Ni-Rich NiTi Shape Memory Parts Produced by Selective Laser Melting', in *Volume 1: Development and Characterization of Multifunctional Materials; Modeling, Simulation and Control of Adaptive Systems; Structural Health Monitoring*, Stone Mountain, Georgia, USA: American Society of Mechanical Engineers, Sep. 2012, pp. 97–104. doi: 10.1115/SMASIS2012-8040.
[120] C. Haberland, M. Elahinia, J. M. Walker, H. Meier, and J. Frenzel, 'On the development of high quality NiTi shape memory and pseudoelastic parts by additive manufacturing', *Smart Mater. Struct.*, vol. 23, no. 10, p. 104002, Oct. 2014, doi: 10.1088/0964-1726/23/10/104002.
[121] D. Stockel, 'Nitinol - A material with unusual properties', *Endovascular Update - News and reviews on developments in endovascular intervention and technique*, no. 1, pp. 1–8, 1998.
[122] T. S. Spini, F. P. Valarelli, R. H. Cançado, K. M. S. D. Freitas, and D. J. Villarinho, 'Transition temperature range of thermally activated nickel-titanium archwires', *J. Appl. Oral Sci.*, vol. 22, no. 2, pp. 109–117, Apr. 2014, doi: 10.1590/1678-775720130133.
[123] J. M. Gallardo Fuentes, P. Gümpel, and J. Strittmatter, 'Phase Change Behavior of Nitinol Shape Memory Alloys', *Adv. Eng. Mater.*, vol. 4, no. 7, pp. 437–452, Jul. 2002, doi: 10.1002/1527-2648(20020717)4:7%3C437::AID-ADEM437%3E3.0.CO;2-8.
[124] J. J. Marattukalam, V. K. Balla, M. Das, S. Bontha, and S. K. Kalpathy, 'Effect of heat treatment on microstructure, corrosion, and shape memory characteristics of laser deposited NiTi alloy', *Journal of Alloys and Compounds*, vol. 744, pp. 337–346, May 2018, doi: 10.1016/j.jallcom.2018.01.174.
[125] S. Kujala, A. Pajala, M. Kallioinen, A. Pramila, J. Tuukkanen, and J. Ryhänen, 'Biocompatibility and strength properties of nitinol shape memory alloy suture in rabbit tendon', *Biomaterials*, vol. 25, no. 2, pp. 353–358, Jan. 2004, doi: 10.1016/S0142-9612(03)00488-5.

[126] J. M. McNaney, V. Imbeni, Y. Jung, P. Papadopoulos, and R. O. Ritchie, 'An experimental study of the superelastic effect in a shape-memory Nitinol alloy under biaxial loading', *Mechanics of Materials*, vol. 35, no. 10, pp. 969–986, Oct. 2003, doi: 10.1016/S0167-6636(02)00310-1.
[127] Z. Wang, J. Everaerts, E. Salvati, and A. M. Korsunsky, 'Evolution of thermal and mechanical properties of Nitinol wire as a function of ageing treatment conditions', *Journal of Alloys and Compounds*, vol. 819, p. 153024, Apr. 2020, doi: 10.1016/j.jallcom.2019.153024.
[128] J. Chekotu, R. Groarke, K. O'Toole, and D. Brabazon, 'Advances in Selective Laser Melting of Nitinol Shape Memory Alloy Part Production', *Materials*, vol. 12, no. 5, p. 809, Mar. 2019, doi: 10.3390/ma12050809.
[129] S. Wen, Y. Liu, Y. Zhou, A. Zhao, C. Yan, and Y. Shi, 'Effect of Ni content on the transformation behavior and mechanical property of NiTi shape memory alloys fabricated by laser powder bed fusion', *Optics & Laser Technology*, vol. 134, p. 106653, Feb. 2021, doi: 10.1016/j.optlastec.2020.106653.
[130] F. Jahanbazi Asl, M. Kadkhodaei, and F. Karimzadeh, 'The effects of shape-setting on transformation temperatures of pseudoelastic shape memory alloy springs', *Journal of Science: Advanced Materials and Devices*, vol. 4, no. 4, pp. 568–576, Dec. 2019, doi: 10.1016/j.jsamd.2019.10.005.
[131] M. Patel, D. Plumley, R. Bouthot, and J. Proft, 'The Effects of Varying Active Af Temperatures on the Fatigue Properties of Nitinol Wire', 2005.
[132] M. E. Mitwally and M. Farag, 'Effect of cold work and annealing on the structure and characteristics of NiTi alloy', *Materials Science and Engineering: A*, vol. 519, no. 1–2, pp. 155–166, Aug. 2009, doi: 10.1016/j.msea.2009.04.057.
[133] A. Dos Santos Paula, K. K. Mahesh, and F. M. Braz Fernandes, 'Stability in Phase Transformation After Multiple Steps of Marforming in Ti-Rich Ni-Ti Shape Memory Alloy', *J. of Materi Eng and Perform*, vol. 20, no. 4–5, pp. 771–775, Jul. 2011, doi: 10.1007/s11665-011-9920-5.
[134] K. Lygin, S. Langbein, P. Labenda, and T. Sadek, 'A Methodology for the Development, Production, and Validation of R-Phase Actuators', *J. of Materi Eng and Perform*, vol. 21, no. 12, pp. 2657–2662, Dec. 2012, doi: 10.1007/s11665-012-0285-1.
[135] Y. Luo, T. Takagi, S. Maruyama, and M. Yamada, 'A Shape Memory Alloy Actuator Using Peltier Modules and R-Phase Transition', *Journal of Intelligent Material Systems and Structures*, vol. 11, no. 7, pp. 503–511, Jul. 2000, doi: 10.1106/92YH-9YU9-HVW4-RVKT.
[136] A. Spaggiari, E. Dragoni, and A. Tuissi, 'NiTi Alloy Negator Springs for Long-Stroke Constant-Force Shape Memory Actuators: Modeling, Simulation and Testing', *J. of Materi Eng and Perform*, vol. 23, no. 7, pp. 2412–2419, Jul. 2014, doi: 10.1007/s11665-014-0946-3.
[137] P.-A. Gédouin, L. Pino, S. Arbab Chirani, S. Calloch, E. Delaleau, and J.-M. Bourgeot, 'R-phase shape memory alloy helical spring based actuators: Modeling and experiments', *Sensors and Actuators A: Physical*, vol. 289, pp. 65–76, Apr. 2019, doi: 10.1016/j.sna.2019.02.024.
[138] D. Favier, Y. Liu, L. Orgéas, A. Sandel, L. Debove, and P. Comte-Gaz, 'Influence of thermomechanical processing on the superelastic properties of a Ni-rich Nitinol shape

memory alloy', *Materials Science and Engineering: A*, vol. 429, no. 1–2, pp. 130–136, Aug. 2006, doi: 10.1016/j.msea.2006.05.018.
[139] X. Liu, Y. Wang, D. Yang, and M. Qi, 'The effect of ageing treatment on shape-setting and superelasticity of a nitinol stent', *Materials Characterization*, vol. 59, no. 4, pp. 402–406, Apr. 2008, doi: 10.1016/j.matchar.2007.02.007.
[140] T. Assawakawintip, P. Santiwong, A. Khantachawana, K. Sipiyaruk, and R. Chintavalakorn, 'The Effects of Temperature and Time of Heat Treatment on Thermo-Mechanical Properties of Custom-Made NiTi Orthodontic Closed Coil Springs', *Materials*, vol. 15, no. 9, p. 3121, Apr. 2022, doi: 10.3390/ma15093121.
[141] G. Li, T. Yu, N. Zhang, and M. Chen, 'The effect of Ni content on phase transformation behavior of NiTi alloys: An atomistic modeling study', *Computational Materials Science*, vol. 215, p. 111804, Dec. 2022, doi: 10.1016/j.commatsci.2022.111804.
[142] E. Choi, A. Ostadrahimi, and J. Park, 'On mechanical properties of NiTi SMA wires prestrained by cold rolling', *Smart Mater. Struct.*, vol. 29, no. 6, p. 065009, Jun. 2020, doi: 10.1088/1361-665X/ab84bb.
[143] S. De Oliveira, S. A. Silva, C. R. Souto, and A. Ries, 'Experimental Characterization and Control of a Force Actuator Based on Shape Memory Alloy Wire', *J Control Autom Electr Syst*, vol. 29, no. 6, pp. 670–676, Dec. 2018, doi: 10.1007/s40313-018-0416-5.
[144] W. C. Oliver and G. M. Pharr, 'An improved technique for determining hardness and elastic modulus using load and displacement sensing indentation experiments', *J. Mater. Res.*, vol. 7, no. 6, pp. 1564–1583, Jun. 1992, doi: 10.1557/JMR.1992.1564.
[145] A. C. Fischer-Cripps, *Nanoindentation*. in Mechanical Engineering Series. New York, NY: Springer New York, 2011. doi: 10.1007/978-1-4419-9872-9.
[146] S.-R. Jian, G.-J. Chen, and T.-C. Lin, 'Berkovich Nanoindentation on AlN Thin Films', *Nanoscale Res Lett*, vol. 5, no. 6, pp. 935–940, Jun. 2010, doi: 10.1007/s11671-010-9582-5.
[147] E. Farber *et al.*, 'TiNi Alloy Lattice Structures with Negative Poisson's Ratio: Computer Simulation and Experimental Results', *Metals*, vol. 12, no. 9, p. 1476, Sep. 2022, doi: 10.3390/met12091476.
[148] Y. Zhan, L. He, X. Lu, X. Zhu, and Q. Chen, 'The Effect of Ageing Treatment on Shape-Setting and Shape Memory Effect of a NiTi SMA Corrugated Structure', *Advances in Materials Science and Engineering*, vol. 2020, pp. 1–11, Jun. 2020, doi: 10.1155/2020/2846721.
[149] S. Vollach, D. Shilo, and H. Shlagman, 'Mechanical Response of Shape Memory Alloys Under a Rapid Heating Pulse - Part II', *Exp Mech*, vol. 56, no. 8, pp. 1465–1475, Oct. 2016, doi: 10.1007/s11340-016-0172-z.
[150] K. D. Salman, 'Manufacture of shape memory alloys NiTi and NiTiCu by casting method and studying the effect of adding the copper element in different proportions to the binary alloy on the microstructure, phase transformations and conductivity', *J. Phys.: Conf. Ser.*, vol. 1973, no. 1, p. 012108, Aug. 2021, doi: 10.1088/1742-6596/1973/1/012108.
[151] J. Uchil, K. G. Kumara, and K. K. Mahesh, 'Effect of thermal cycling on R-phase stability in a NiTi shape memory alloy', *Materials Science and Engineering: A*, vol. 332, no. 1–2, pp. 25–28, Jul. 2002, doi: 10.1016/S0921-5093(01)01711-7.
[152] K. Yan, S. Yang, J. Xu, F. Ren, and Q. Sun, 'Effects of Gradient Annealing on the Microstructure and Rate-Dependent Thermomechanical Behavior of Nanocrystalline

NiTi Shape Memory Alloy', *Shap. Mem. Superelasticity*, vol. 8, no. 4, pp. 308–319, Dec. 2022, doi: 10.1007/s40830-022-00390-1.
[153] M. Pattabi and M. S. Murari, 'Effect of Cold Rolling on Phase Transformation Temperatures of NiTi Shape Memory Alloy', *J. of Materi Eng and Perform*, vol. 24, no. 2, pp. 556–564, Feb. 2015, doi: 10.1007/s11665-014-1344-6.
[154] H. Morawiec, D. Stróz, and D. Chrobak, 'Effect of Deformation and Thermal Treatment of NiTi Alloy on Transition Sequence', *J. Phys. IV France*, vol. 05, no. C2, pp. C2-205-C2-210, Feb. 1995, doi: 10.1051/jp4:1995232.
[155] X. Wang *et al.*, 'Effect of process parameters on the phase transformation behavior and tensile properties of NiTi shape memory alloys fabricated by selective laser melting', *Additive Manufacturing*, vol. 36, p. 101545, Dec. 2020, doi: 10.1016/j.addma.2020.101545.
[156] E. Choi, Y.-W. Kim, Y.-S. Chung, and K.-T. Yang, 'Bond strength of concrete confined by SMA wire jackets', *Physics Procedia*, vol. 10, pp. 210–215, 2010, doi: 10.1016/j.phpro.2010.11.100.
[157] I. Kaya, H. E. Karaca, M. Nagasako, and R. Kainuma, 'Effects of aging temperature and aging time on the mechanism of martensitic transformation in nickel-rich NiTi shape memory alloys', *Materials Characterization*, vol. 159, p. 110034, Jan. 2020, doi: 10.1016/j.matchar.2019.110034.
[158] H. Sehitoglu, R. Hamilton, H. J. Maier, and Y. Chumlyakov, 'Hysteresis in NiTi alloys', *J. Phys. IV France*, vol. 115, pp. 3–10, Jun. 2004, doi: 10.1051/jp4:2004115001.
[159] P. Sedmák, P. Šittner, J. Pilch, and C. Curfs, 'Instability of cyclic superelastic deformation of NiTi investigated by synchrotron X-ray diffraction', *Acta Materialia*, vol. 94, pp. 257–270, Aug. 2015, doi: 10.1016/j.actamat.2015.04.039.
[160] M. C. C. Monu, S. Kumar S., and D. Brabazon, 'Heat treatment of NiTi alloys: Influence of volumetric energy density on ageing parameters and the resulting physical properties', *Journal of Materials Research and Technology*, vol. 26, pp. 9532–9555, Sep. 2023, doi: 10.1016/j.jmrt.2023.09.251.
[161] Z. Yang, W. Tirry, D. Lamoen, S. Kulkova, and D. Schryvers, 'Electron energy-loss spectroscopy and first-principles calculation studies on a Ni–Ti shape memory alloy', *Acta Materialia*, vol. 56, no. 3, pp. 395–404, Feb. 2008, doi: 10.1016/j.actamat.2007.10.001.
[162] S. Kumar S *et al.*, 'Microstructure – Property correlations for additively manufactured NiTi based shape memory alloys', *Materialia*, vol. 8, p. 100456, Dec. 2019, doi: 10.1016/j.mtla.2019.100456.
[163] S. Kumar S, I. A. Kumar, L. Marandi, and I. Sen, 'Assessment of small-scale deformation characteristics and stress-strain behavior of NiTi based shape memory alloy using nanoindentation', *Acta Materialia*, vol. 201, pp. 303–315, Dec. 2020, doi: 10.1016/j.actamat.2020.09.080.
[164] M. A. Obeidi, 'Achieving high quality nitinol parts with minimised input thermal energy by optimised pulse wave laser powder bed fusion process', *Results in Materials*, vol. 14, p. 100279, Jun. 2022, doi: 10.1016/j.rinma.2022.100279.
[165] X. Huang, J. Nohava, B. Zhang, and A. G. Ramirez, 'Nanoindentation of NiTi shape memory thin films at elevated temperatures', *International Journal of Smart and Nano Materials*, vol. 2, no. 1, pp. 39–49, Feb. 2011, doi: 10.1080/19475411.2011.558179.

[166] M. F.-X. Wagner and W. Windl, 'Elastic anisotropy of Ni4Ti3 from first principles', *Scripta Materialia*, vol. 60, no. 4, pp. 207–210, Feb. 2009, doi: 10.1016/j.scriptamat.2008.09.028.
[167] A. Tahaei, A. Aghajani, M. Abbasi, B. Bagheri, M. Merlin, and G. L. Garagnani, 'Effects of Predefined Thermomechanical Procedure on the Microstructure and Mechanical Properties of the Two-Way Shape Memory Effect in the NiTi Alloy', *Advances in Materials Science and Engineering*, vol. 2023, pp. 1–11, Jun. 2023, doi: 10.1155/2023/1524836.
[168] C. P. Frick *et al.*, 'Thermal processing of polycrystalline NiTi shape memory alloys', *Materials Science and Engineering: A*, vol. 405, no. 1–2, pp. 34–49, Sep. 2005, doi: 10.1016/j.msea.2005.05.102.
[169] Z. Wang, J. Everaerts, E. Salvati, and A. M. Korsunsky, 'Evolution of thermal and mechanical properties of Nitinol wire as a function of ageing treatment conditions', *Journal of Alloys and Compounds*, vol. 819, p. 153024, Apr. 2020, doi: 10.1016/j.jallcom.2019.153024.
[170] G. Shimoga, T.-H. Kim, and S.-Y. Kim, 'An Intermetallic NiTi-Based Shape Memory Coil Spring for Actuator Technologies', *Metals*, vol. 11, no. 8, p. 1212, Jul. 2021, doi: 10.3390/met11081212.
[171] S. E. Saghaian *et al.*, 'Enhancing Shape Memory Response of Additively Manufactured NiTi Shape Memory Alloys by Texturing and Post-Processing Heat Treatment', *Shap. Mem. Superelasticity*, vol. 9, no. 1, pp. 192–206, Mar. 2023, doi: 10.1007/s40830-023-00425-1.
[172] K. Weinert and V. Petzoldt, 'Machining of NiTi based shape memory alloys', *Materials Science and Engineering: A*, vol. 378, no. 1–2, pp. 180–184, Jul. 2004, doi: 10.1016/j.msea.2003.10.344.
[173] C. Zhao, H. Liang, S. Luo, J. Yang, and Z. Wang, 'The effect of energy input on reaction, phase transition and shape memory effect of NiTi alloy by selective laser melting', *Journal of Alloys and Compounds*, vol. 817, p. 153288, Mar. 2020, doi: 10.1016/j.jallcom.2019.153288.
[174] W. Chen, D. Gu, J. Yang, Q. Yang, J. Chen, and X. Shen, 'Compressive mechanical properties and shape memory effect of NiTi gradient lattice structures fabricated by laser powder bed fusion', *Int. J. Extrem. Manuf.*, vol. 4, no. 4, p. 045002, Dec. 2022, doi: 10.1088/2631-7990/ac8ef3.
[175] C. A. Biffi *et al.*, 'Additive manufacturing of NiTi architected metamaterials', *Additive Manufacturing Letters*, vol. 10, p. 100216, Jul. 2024, doi: 10.1016/j.addlet.2024.100216.
[176] L. Xue *et al.*, 'Laser Powder Bed Fusion of Defect-Free NiTi Shape Memory Alloy Parts with Superior Tensile Superelasticity', *Acta Materialia*, vol. 229, p. 117781, May 2022, doi: 10.1016/j.actamat.2022.117781.
[177] J.-N. Zhu *et al.*, 'Controlling microstructure evolution and phase transformation behavior in additive manufacturing of nitinol shape memory alloys by tuning hatch distance', *J Mater Sci*, vol. 57, no. 10, pp. 6066–6084, Mar. 2022, doi: 10.1007/s10853-022-07007-z.
[178] E. Borisov, K. Starikov, A. Popovich, and T. Tihonovskaya, 'Investigation of the Possibility of Tailoring the Chemical Com-Position of the NiTi Alloy by Selective Laser Melting', *Metals*, vol. 11, no. 9, p. 1470, Sep. 2021, doi: 10.3390/met11091470.

[179] H. M. A. Ali, M. Abdi, and Y. Sun, 'Insight into the mechanical properties of 3D printed strut-based lattice structures', *Prog Addit Manuf*, vol. 8, pp. 919–931, Dec. 2022, doi: 10.1007/s40964-022-00365-9.
[180] S. Dadbakhsh, M. Speirs, J.-P. Kruth, and J. Van Humbeeck, 'Influence of SLM on shape memory and compression behaviour of NiTi scaffolds', *CIRP Annals*, vol. 64, no. 1, pp. 209–212, 2015, doi: 10.1016/j.cirp.2015.04.039.
[181] S. Qu *et al.*, 'Superelastic NiTi Functional Components by High-Precision Laser Powder Bed Fusion Process: The Critical Roles of Energy Density and Minimal Feature Size', *Micromachines*, vol. 14, no. 7, p. 1436, Jul. 2023, doi: 10.3390/mi14071436.
[182] F. Guo, Y. Guo, X. Kong, Z. Xiong, and S. Hao, 'The Effect of Wall Thickness and Scanning Speed on the Martensitic Transformation and Tensile Properties of Selective Laser Melted NiTi Thin-Wall Structures', *Metals*, vol. 12, no. 3, p. 519, Mar. 2022, doi: 10.3390/met12030519.
[183] R. Weber, E. Tosoratti, A. B. Spierings, and K. Wegener, 'Functional graded NiTi manufactured with powder bed fusion', *Prog Addit Manuf*, vol. 9, no. 6, pp. 2313–2326, Dec. 2024, doi: 10.1007/s40964-024-00584-2.
[184] C. G. Ferro, S. Varetti, G. De Pasquale, and P. Maggiore, 'Lattice structured impact absorber with embedded anti-icing system for aircraft wings fabricated with additive SLM process', *Materials Today Communications*, vol. 15, pp. 185–189, Jun. 2018, doi: 10.1016/j.mtcomm.2018.03.007.
[185] B. Li *et al.*, 'Effect of post-heat treatments on the microstructure, martensitic transformation and functional performance of EBF3-fabricated NiTi shape memory alloy', *Materials Science and Engineering: A*, vol. 871, p. 144897, Apr. 2023, doi: 10.1016/j.msea.2023.144897.
[186] M. Casata, S. Perosanz, C. Garrido, and D. Barba, 'A holistic study of the effect of geometrical and processing conditions on the static mechanical performance of LPBF strut elements', *Materials & Design*, vol. 247, p. 113387, Nov. 2024, doi: 10.1016/j.matdes.2024.113387.
[187] L. Sun, K. Chen, P. Geng, Y. Zhou, S. Wen, and Y. Shi, 'Mechanical and shape memory properties of NiTi triply periodic minimal surface structures fabricated by laser powder bed fusion', *Journal of Manufacturing Processes*, vol. 101, pp. 1091–1100, Sep. 2023, doi: 10.1016/j.jmapro.2023.06.034.
[188] H. Sitepu, '*In situ* structural and texture analyses of monoclinic phase for polycrystalline Ni-rich $Ti_{49.86}$ $Ni_{50.14}$ alloy from neutron diffraction data', *Powder Diffr.*, vol. 23, no. 1, pp. 35–40, Mar. 2008, doi: 10.1154/1.2839141.
[189] M. H. Mueller and H. W. Knott, 'The Crystal Structures of Ti2Cu, Ti2Ni, Ti4Ni2, and Ti4Cu2O', *Transactions of American Institute of Metallurgical Engineers*, vol. 227, 1963, [Online]. Available: https://www.osti.gov/biblio/4712302
[190] H. Sitepu, 'Texture and structural refinement using neutron diffraction data from molybdite (MoO_3) and calcite ($CaCO_3$) powders and a Ni-rich $Ni_{50.7}$ $Ti_{49.30}$ alloy', *Powder Diffr.*, vol. 24, no. 4, pp. 315–326, Dec. 2009, doi: 10.1154/1.3257906.
[191] P. R. Halani and Y. C. Shin, 'In Situ Synthesis and Characterization of Shape Memory Alloy Nitinol by Laser Direct Deposition', *Metall Mater Trans A*, vol. 43, no. 2, pp. 650–657, Feb. 2012, doi: 10.1007/s11661-011-0890-x.
[192] T. G. Bradley, W. A. Brantley, and B. M. Culbertson, 'Differential scanning calorimetry (DSC) analyses of superelastic and nonsuperelastic nickel-titanium orthodontic wires',

American Journal of Orthodontics and Dentofacial Orthopedics, vol. 109, no. 6, pp. 589–597, Jun. 1996, doi: 10.1016/S0889-5406(96)70070-7.
[193] J. C. Chekotu, R. Goodall, D. Kinahan, and D. Brabazon, 'Control of Ni-Ti phase structure, solid-state transformation temperatures and enthalpies via control of L-PBF process parameters', *Materials & Design*, vol. 218, p. 110715, Jun. 2022, doi: 10.1016/j.matdes.2022.110715.
[194] C. A. Biffi, P. Bassani, J. Fiocchi, and A. Tuissi, 'Microstructural and Mechanical Response of NiTi Lattice 3D Structure Produced by Selective Laser Melting', *Metals*, vol. 10, no. 6, p. 814, Jun. 2020, doi: 10.3390/met10060814.
[195] C. A. Biffi *et al.*, 'Effects of the scanning strategy on the microstructure and mechanical properties of a TiAl6V4 alloy produced by electron beam additive manufacturing', *Int J Adv Manuf Technol*, vol. 107, no. 11–12, pp. 4913–4924, Apr. 2020, doi: 10.1007/s00170-020-05358-y.
[196] Q. Chen, L. Xu, L. Zhao, K. Hao, and Y. Han, 'Effect of scanning speed on microstructure and mechanical properties of as-printed Ti–22Al–25Nb intermetallic by laser powder bed fusion', *Materials Science and Engineering: A*, vol. 885, p. 145652, Oct. 2023, doi: 10.1016/j.msea.2023.145652.
[197] D. Barba, C. Alabort, Y. T. Tang, M. J. Viscasillas, R. C. Reed, and E. Alabort, 'On the size and orientation effect in additive manufactured Ti-6Al-4V', *Materials & Design*, vol. 186, p. 108235, Jan. 2020, doi: 10.1016/j.matdes.2019.108235.
[198] G. Tadayyon *et al.*, 'Effect of different stages of deformation on the microstructure evolution of Ti-rich NiTi shape memory alloy', *Materials Characterization*, vol. 125, pp. 51–66, Mar. 2017, doi: 10.1016/j.matchar.2017.01.024.
[199] W. Li *et al.*, 'Large thermal hysteresis NiTi Belleville washer fabricated by metal injection moulding', *Powder Metallurgy*, vol. 63, no. 3, pp. 212–219, May 2020, doi: 10.1080/00325899.2020.1797293.
[200] A. Ahadi and E. Rezaei, 'Microstructure and Phase Transformation Behavior of a Stress-Assisted Heat-Treated Ti-Rich NiTi Shape Memory Alloy', *J. of Materi Eng and Perform*, vol. 21, no. 8, pp. 1806–1812, Aug. 2012, doi: 10.1007/s11665-011-0082-2.
[201] W. Di, Y. Yongqiang, S. Xubin, and C. Yonghua, 'Study on energy input and its influences on single-track,multi-track, and multi-layer in SLM', *Int J Adv Manuf Technol*, vol. 58, no. 9–12, pp. 1189–1199, Feb. 2012, doi: 10.1007/s00170-011-3443-y.
[202] B. V. Krishna, S. Bose, and A. Bandyopadhyay, 'Fabrication of porous NiTi shape memory alloy structures using laser engineered net shaping', *J Biomed Mater Res*, vol. 89B, no. 2, pp. 481–490, May 2009, doi: 10.1002/jbm.b.31238.
[203] K. Safaei, M. Nematollahi, P. Bayati, H. Dabbaghi, O. Benafan, and M. Elahinia, 'Torsional behavior and microstructure characterization of additively manufactured NiTi shape memory alloy tubes', *Engineering Structures*, vol. 226, p. 111383, Jan. 2021, doi: 10.1016/j.engstruct.2020.111383.
[204] G. Perumal *et al.*, 'Exploring the role of volume energy density in altering microstructure and corrosion behavior of nitinol alloys produced by laser powder bed fusion', *Sci Rep*, vol. 15, no. 1, p. 2055, Jan. 2025, doi: 10.1038/s41598-024-84222-5.
[205] Z. Lin *et al.*, 'Controlling the crystal texture and microstructure of NiTi alloy by adjusting the thermal gradient of laser powder bed melting', *Materials Science and Engineering: A*, vol. 912, p. 146970, Oct. 2024, doi: 10.1016/j.msea.2024.146970.

[206] J. Ryan Murphy, J. C. Chekotu, P. Healy, and D. Brabazon, 'Investigating the effect of VED and lattice strut diameter on the shape memory effect of nitinol actuators', *Journal of Materials Research and Technology*, vol. 41, pp. 423–434, Mar. 2026, doi: 10.1016/j.jmrt.2025.12.069.
[207] S. Khademzadeh, 'Precision additive manufacturing of NiTi shape memory parts using micro-laser powder bed fusion', *Prog Addit Manuf*, vol. 7, pp. 419–432, Nov. 2021, doi: 10.1007/s40964-021-00239-6.
[208] T. Biasutti, P. Bettini, A. M. Grande, G. Sala, B. M. Colosimo, and A. Nespoli, 'An in-depth study of a thin-wall origami-inspired NiTi structure fabricated through laser powder bed fusion', *Prog Addit Manuf*, vol. 10, pp. 7803–7814, Apr. 2025, doi: 10.1007/s40964-025-01073-w.
[209] E. Yasa, 'Selective laser melting', in *Additive Manufacturing*, Elsevier, 2021, pp. 77–120. doi: 10.1016/B978-0-12-818411-0.00017-3.
[210] Z. Yu *et al.*, 'Study on properties of SLM-NiTi shape memory alloy under the same energy density', *Journal of Materials Research and Technology*, vol. 13, pp. 241–250, Jul. 2021, doi: 10.1016/j.jmrt.2021.04.058.
[211] D. C. Lagoudas, *Shape Memory Alloys: Modeling and Engineering Applications*. Boston, MA: Springer US, 2008. doi: 10.1007/978-0-387-47685-8.
[212] H. Sehitoglu *et al.*, 'Detwinning in NiTi alloys', *Metall Mater Trans A*, vol. 34, no. 1, pp. 5–13, Jan. 2003, doi: 10.1007/s11661-003-0203-0.
[213] N. Kurgan, 'Effect of porosity and density on the mechanical and microstructural properties of sintered 316L stainless steel implant materials', *Materials & Design*, vol. 55, pp. 235–241, Mar. 2014, doi: 10.1016/j.matdes.2013.09.058.
[214] K.-N. Hong, Y.-M. Yeon, W.-B. Shim, and S.-W. Ji, 'Fatigue Characteristics of Fe-Based Shape-Memory Alloys', *Applied Sciences*, vol. 10, no. 17, p. 5812, Aug. 2020, doi: 10.3390/app10175812.
[215] D. C. Ren *et al.*, 'Microstructure and properties of equiatomic Ti–Ni alloy fabricated by selective laser melting', *Materials Science and Engineering: A*, vol. 771, p. 138586, Jan. 2020, doi: 10.1016/j.msea.2019.138586.
[216] S. Dadbakhsh, B. Vrancken, J.-P. Kruth, J. Luyten, and J. Van Humbeeck, 'Texture and anisotropy in selective laser melting of NiTi alloy', *Materials Science and Engineering: A*, vol. 650, pp. 225–232, Jan. 2016, doi: 10.1016/j.msea.2015.10.032.

Appendix

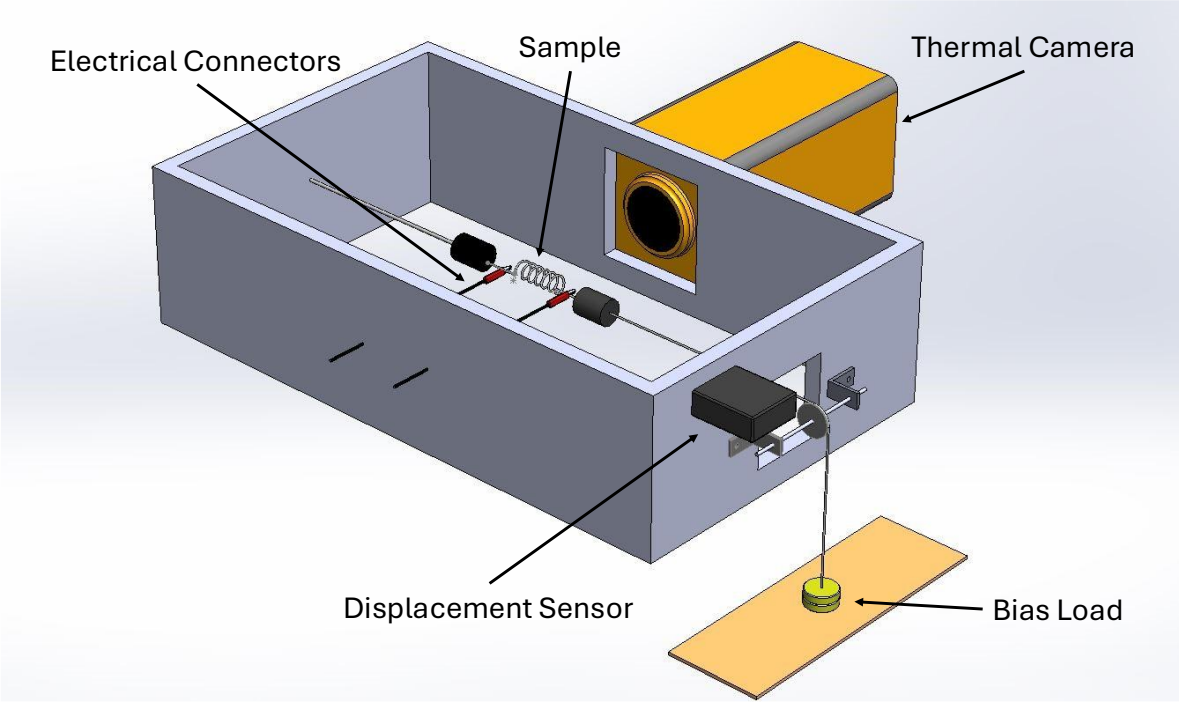


Figure 54: Schematic of wire testing rig.

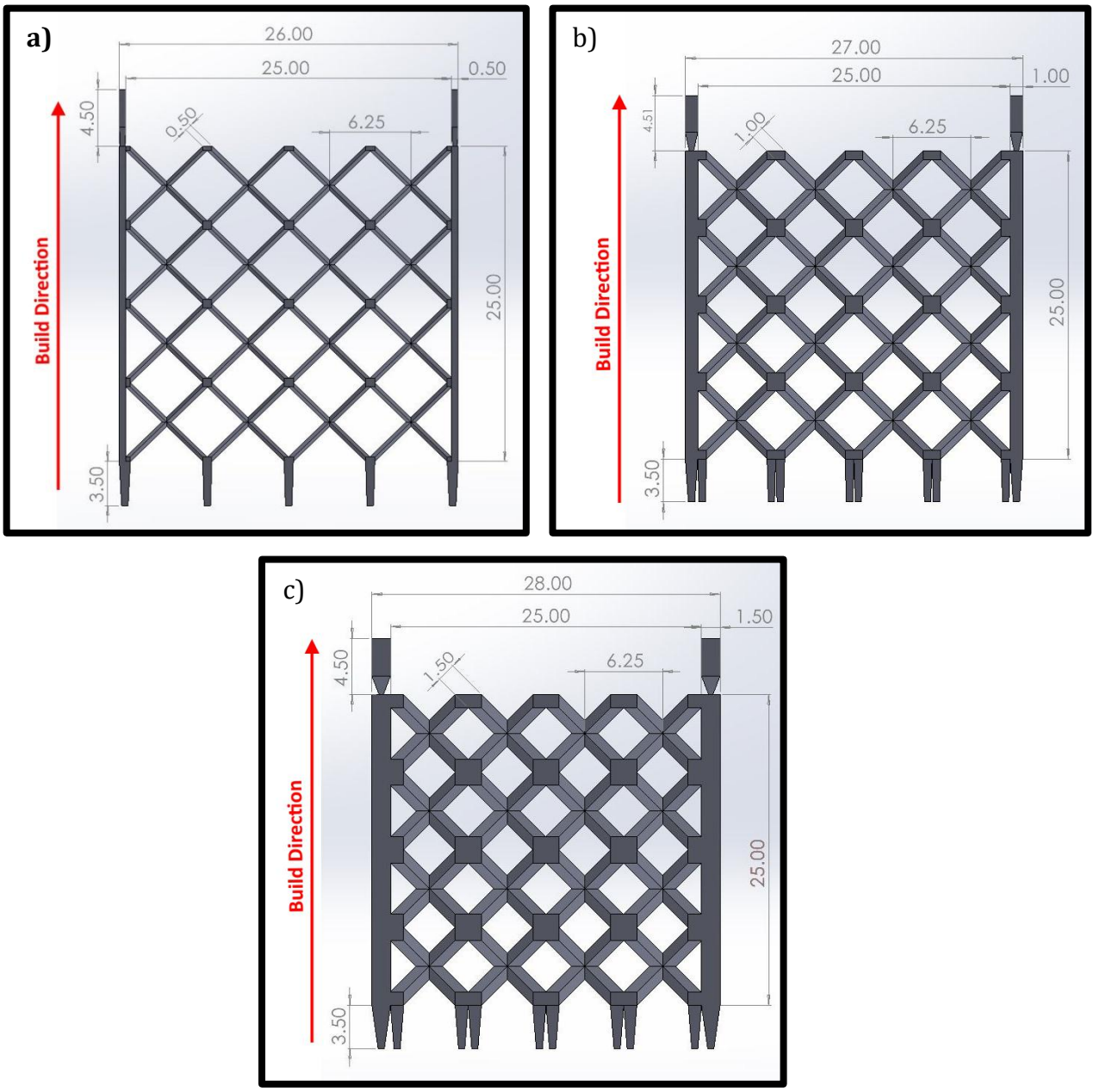


Figure 55: CAD drawing with dimensions including supports and removable pillars of the a) 0.5 mm lattice, b) 1.0 mm lattice, and c) 1.5 mm lattice.

Declaration of Authorship for PhD by Publication

Candidates are required to submit a separate **Declaration of Authorship** form for each co-authored paper submitted for examination as part of a PhD by Publication thesis. Further information is available from the accompanying guideline document.[1]

Paper 1 Declaration of Authorship

Section 1: Candidate's Details	
Candidate's Name	Josephine Ryan Murphy
DCU Student Number	21266615
School	School of Mechanical & Manufacturing Engineering
Principal Supervisor	Prof. Dermot Brabazon
Title of PhD by Publication Thesis	Development of Nickel-Titanium Based Shape Memory Alloy Actuators with Bespoke Thermo-Mechanical Action
Section 2: Paper Details	
Title of co-authored paper included in the thesis under examination	Effect of Heat Treatment Time and Temperature on the Microstructure and Shape Memory Properties of Nitinol Wires.
List of authors as in order given on accepted/published version	Neha Agarwal, Josephine Ryan Murphy, Tina Sadat Hashemi, Theo Mossop, Darragh O'Neill, John Power, Ali Shayegh, and Dermot Brabazon.
Publication Details (e.g. Year of Publication, Journal Name, Issue	September 2023, Materials, Volume 16, DOI: https://doi.org/10.3390/ma16196480

[1] 'Guidelines for candidates, supervisors and examiners on the 'PhD by Publication' format': https://www.dcu.ie/graduatestudies/A_Z-of-GSO-Policies.shtml

Number, Page Numbers, Place of Publication, DOI, ISSN, URL etc.)	
Publication Status (e.g. Published, Accepted)	Published
Provide a brief statement here on the disciplinary ranking of this publication and the peer-review process involved (e.g. how many reviewers, single blinded or other, initial decision, revision timeline etc and any other details that speak to the rigour of the peer review process)	Q2 journal, 4 reviewers, 2-month timeline, 2 set of reviews needed.

This paper (Chapter 3) is one of 4 co-authored papers to be submitted as part of the PhD by publication thesis submitted for examination.

Section 3: Candidate's Contribution to the Paper

Provide details below of the **nature** and **extent of your contribution** to the paper (include both your intellectual and practical contributions) and your overall contribution in **percentage terms**. Note that these categories can be customised according to disciplinary norms

Overall contribution: 50 %

Briefly outline your contribution to the **conception** of the work described in this paper:

I was one of two main contributors to the conception of the work outlined in this paper.
Briefly outline your contribution to the **literature review** in this paper:

I wrote the literature review for this paper with minor edits from the contributing authors.

Briefly outline your contribution to the **methodological design**:

I was one of two main contributors to the design of experiments in this study.

Briefly outline your contribution to **data collection**:

I conducted the majority of the experiments in this study with the assistance of the contributing authors.

Briefly outline your contribution to **data analysis**:

I was one of two main contributors to the data analysis in this study with the assistance of the contributing authors.

Briefly outline your contribution to the **synthesis and summary of findings**:

I was one of two main contributors to the synthesis and summary of findings.

Finally, outline your contribution to the **writing** and **revision** of the paper:

I was one of two main contributors to the writing of the paper with minor input and edits from the contributing authors.

Section 4: Signature and Validation

I confirm that the following statements are true:

(a) the information I have provided in this form is correct
(b) this paper is based on research undertaken during my candidature at DCU

Signature of PhD Candidate: _____ Josephine Ryan Murphy ___ **Date:** 04/12/2025

I confirm that the information provided by the candidate is correct:

Signature of Principal Supervisor: _ **Date:** 04/12/2025

In some cases, it may be appropriate for verification to be given by both the principal supervisor and the lead/corresponding author of the work (where the lead/corresponding author of the work is not the candidate or the principal supervisor):

Signature of Lead/Corresponding Author__ Josephine Ryan Murphy __ **Date:** 04/12/2025

Nature of Current Post/Responsibilities PhD Researcher

Home institution Dublin City University

Paper 2 Declaration of Authorship

Section 1: Candidate's Details	
Candidate's Name	Josephine Ryan Murphy
DCU Student Number	21266615
School	School of Mechanical & Manufacturing Engineering
Principal Supervisor	Prof. Dermot Brabazon

Title of PhD by Publication Thesis	Development of Nickel-Titanium Based Shape Memory Alloy Actuators with Bespoke Thermo-Mechanical Action
Section 2: Paper Details	
Title of co-authored paper included in the thesis under examination	Investigating the Effect of Wire Drawing and Heat Treatment on the Response of Ni50.9Ti49.1 R-phase Actuators.
List of authors as in order given on accepted/published version	Josephine Ryan Murphy, Muhannad A. Obeidi, Inam Ul Ahad, Dermot Brabazon.
Publication Details (e.g. Year of Publication, Journal Name, Issue Number, Page Numbers, Place of Publication, DOI, ISSN, URL etc.)	October 2025, Materials, Volume 18, DOI: https://www.mdpi.com/1996-1944/18/21/4931
Publication Status (e.g. Published, Accepted)	Published
Provide a brief statement here on the disciplinary ranking of this publication and the peer-review process involved (e.g. how many reviewers, single blinded or other, initial decision, revision timeline etc and any other details that speak to the rigour of the peer review process)	Q2 journal, 3 reviewers, 2-month timeline, 2 set of reviews needed.
4	

This paper (Chapter 4) is one of co-authored papers to be submitted as part of the PhD by publication thesis submitted for examination.

Section 3: Candidate's Contribution to the Paper

Provide details below of the **nature** and **extent of your contribution** to the paper (include both your intellectual and practical contributions) and your overall contribution in **percentage terms**. Note that these categories can be customised according to disciplinary norms

Overall contribution: 80 %

Briefly outline your contribution to the **conception** of the work described in this paper:

I am the main contributor to the conception of this work under the guidance of my supervisors.

Briefly outline your contribution to the **literature review** in this paper:

I am the sole author of the literature review.

Briefly outline your contribution to the **methodological design**:

I am the main contributor to the methodological design with guidance from my supervisors.

Briefly outline your contribution to **data collection**:

I am the sole contributor to the data collection.

Briefly outline your contribution to **data analysis**:

I am the main contributor to the data analysis with some assistance from the contributing authors.

Briefly outline your contribution to the **synthesis and summary of findings**:

I am the sole contributor to the synthesis and summary of findings.

Finally, outline your contribution to the **writing** and **revision** of the paper:

90%: I am the main contributor to the writing and revision of this paper with minor edits from my supervisors,

Section 4: Signature and Validation

I confirm that the following statements are true:

(a) the information I have provided in this form is correct
(b) this paper is based on research undertaken during my candidature at DCU

Signature of PhD Candidate: _____ Josephine Ryan Murphy ___ **Date:** 04/12/2025

I confirm that the information provided by the candidate is correct:

Signature of Principal Supervisor: _____ **Date:** 04/12/2025

In some cases, it may be appropriate for verification to be given by both the principal supervisor **and** the lead/corresponding author of the work (where the lead/corresponding author of the work is not the candidate or the principal supervisor):

Signature of Lead/Corresponding Author___Josephine Ryan Murphy__ **Date:** 04/12/2025 Nature of Current Post/Responsibilities PhD Researcher Home institution Dublin City University

Paper 3 Declaration of Authorship

Section 1: Candidate's Details	
Candidate's Name	Josephine Ryan Murphy
DCU Student Number	21266615
School	School of Mechanical & Manufacturing Engineering
Principal Supervisor	Prof. Dermot Brabazon
Title of PhD by Publication Thesis	Development of Nickel-Titanium Based Shape Memory Alloy Actuators with Bespoke Thermo-Mechanical Action
Section 2: Paper Details	
Title of co-authored paper included in the thesis under examination	Effect of PBF-LB Process Parameters and Strut Diameter on the Microstructure and Phase Transformation Behaviour of Ti-rich Nitinol Lattice Structures
List of authors as in order given on accepted/published version	Josephine Ryan Murphy, Nicole Church, Nicholas Jones, Paul Healy, and Dermot Brabazon.

Publication Details (e.g. Year of Publication, Journal Name, Issue Number, Page Numbers, Place of Publication, DOI, ISSN, URL etc.)	June 2026, Springer Nature Progress in Additive Manufacturing, https://doi.org/10.1007/s40964-026-01811-8
Publication Status (e.g. Published, Accepted)	Under Review
Provide a brief statement here on the disciplinary ranking of this publication and the peer-review process involved (e.g. how many reviewers, single blinded or other, initial decision, revision timeline etc and any other details that speak to the rigour of the peer review process)	Q1, 3 reviewers, 2 rounds of reviews, 6 month timeline.

This paper (Chapter 5) is one of 4 co-authored papers to be submitted as part of the PhD by publication thesis submitted for examination.

Section 3: Candidate's Contribution to the Paper

Provide details below of the **nature** and **extent of your contribution** to the paper (include both your intellectual and practical contributions) and your overall contribution in **percentage terms**. Note that these categories can be customised according to disciplinary norms

Overall Contribution: 80 %

Briefly outline your contribution to the **conception** of the work described in this paper:

I am the main contributor to the conception of this work under the guidance of my supervisors.

Briefly outline your contribution to the **literature review** in this paper:

I am the sole author of the literature review.

Briefly outline your contribution to the **methodological design**:

I am the main contributor to the methodological design with guidance from my supervisors.

Briefly outline your contribution to **data collection**:

I am the main contributor to the data collection. I collected all data except the SXRD and DSC which was collected by my co-authors.

Briefly outline your contribution to **data analysis**:

I am the main contributor to the data analysis. I conducted all data analysis except the SXRD which was analysed by my co-author.

Briefly outline your contribution to the **synthesis and summary of findings**:

I am the sole contributor to the synthesis and summary of findings.

Finally, outline your contribution to the **writing** and **revision** of the paper:

I am the main contributor to the writing and revision of this paper with minor edits from my supervisors,

Section 4: Signature and Validation

I confirm that the following statements are true:

(a) the information I have provided in this form is correct

(b) this paper is based on research undertaken during my candidature at DCU

Signature of PhD Candidate: _____Josephine Ryan Murphy___ **Date:** 04/12/2025

I confirm that the information provided by the candidate is correct:



Signature of Principal Supervisor: _____ **Date:** 04/12/2025

In some cases, it may be appropriate for verification to be given by both the principal supervisor **and** the lead/corresponding author of the work (where the lead/corresponding author of the work is not the candidate or the principal supervisor):

Signature of Lead/Corresponding Author___Josephine Ryan Murphy__ **Date:** 04/12/2025

Nature of Current Post/Responsibilities PhD Researcher

Home institution Dublin City University

Paper 4 Declaration of Authorship

Section 1: Candidate's Details

Candidate's Name	Josephine Ryan Murphy
DCU Student Number	21266615
School	School of Mechanical & Manufacturing Engineering
Principal Supervisor	Prof. Dermot Brabazon
Title of PhD by Publication Thesis	Development of Nickel-Titanium Based Shape Memory Alloy Actuators with Bespoke Thermo-Mechanical Action
Section 2: Paper Details	
Title of co-authored paper included in the thesis under examination	Investigating the Effect of VED and Lattice Strut Diameter on the Shape Memory Effect of Nitinol Actuators
List of authors as in order given on accepted/published version	Josephine Ryan Murphy, Josiah Cherian Chekotu, Paul Healy, and Dermot Brabazon.
Publication Details (e.g. Year of Publication, Journal Name, Issue Number, Page Numbers, Place of Publication, DOI, ISSN, URL etc.)	December 2025, Journal of Materials Research and Technology
Publication Status (e.g. Published, Accepted)	Accepted
Provide a brief statement here on the disciplinary ranking of this publication and the peer-review process involved (e.g. how many reviewers, single blinded or other, initial decision, revision timeline etc and any	Q1, 1 month timeline, 2 reviewers, 1 round of reviews

other details that speak to the rigour of the peer review process)	

This paper (Chapter 6) is one of 4 co-authored papers to be submitted as part of the PhD by publication thesis submitted for examination.

Section 3: Candidate's Contribution to the Paper

Provide details below of the **nature** and **extent of your contribution** to the paper (include both your intellectual and practical contributions) and your overall contribution in **percentage terms**. Note that these categories can be customised according to disciplinary norms

Overall Contribution: 80 %

Briefly outline your contribution to the **conception** of the work described in this paper:

I am the main contributor to the conception of this work under the guidance of my supervisors.

Briefly outline your contribution to the **literature review** in this paper:

I am the sole author of the literature review.

Briefly outline your contribution to the **methodological design**:

I am the main contributor to the methodological design with guidance from my supervisors.

Briefly outline your contribution to **data collection**:

I am the main contributor to the data collection. I collected all data except the DSC which was collected by my co-authors.

Briefly outline your contribution to **data analysis**:

I am the main contributor to the data analysis. I conducted all data analysis with minor input from contributing authors.

Briefly outline your contribution to the **synthesis and summary of findings**:

I am the sole contributor to the synthesis and summary of findings.

Finally, outline your contribution to the **writing** and **revision** of the paper:

I am the main contributor to the writing and revision of this paper with minor edits from my supervisors,

Section 4: Signature and Validation

I confirm that the following statements are true:

(a) the information I have provided in this form is correct
(b) this paper is based on research undertaken during my candidature at DCU

Signature of PhD Candidate: _____ Josephine Ryan Murphy ___ **Date:** 04/12/2025

I confirm that the information provided by the candidate is correct:

Signature of Principal Supervisor: _____ **Date:** 04/12/2025

In some cases, it may be appropriate for verification to be given by both the principal supervisor **and** the lead/corresponding author of the work (where the lead/corresponding author of the work is not the candidate or the principal supervisor):

Signature of Lead/Corresponding Author__Josephine Ryan Murphy__ **Date:** 04/12/2025

Nature of Current Post/Responsibilities PhD Researcher

Home institution Dublin City University